

Reaction Dynamics with Exotic Nuclei

V. Baran^{a,1}, M. Colonna^a, V. Greco^b, M. Di Toro^{a,*},

^a*Laboratori Nazionali del Sud INFN, Via S. Sofia 62, I-95123 Catania, Italy
and Dipartimento di Fisica e Astronomia, Università di Catania*

^b*Cyclotron Institute, Texas A&M Univ., College Station, USA*

*Iste magistrorum locus est simul et puerorum, mittunt quando
volunt hic res quas perdere nolunt [1].*

Abstract

We review the new possibilities offered by the reaction dynamics of asymmetric heavy ion collisions, using stable and unstable beams. We show that it represents a rather unique tool to probe regions of highly Asymmetric Nuclear Matter (*ANM*) in compressed as well as dilute phases, and to test the in-medium isovector interaction for high momentum nucleons. The focus is on a detailed study of the symmetry term of the nuclear Equation of State (*EOS*) in regions far away from saturation conditions but always under laboratory controlled conditions.

Thermodynamic properties of *ANM* are surveyed starting from nonrelativistic and relativistic effective interactions. In the relativistic case the role of the isovector scalar δ -meson is stressed. The qualitative new features of the liquid-gas phase transition, "diffusive" instability and isospin distillation, are discussed. The results of ab-initio simulations of n-rich, n-poor, heavy ion collisions, using stochastic isospin dependent transport equations, are analysed as a function of beam energy and centrality. The isospin dynamics plays an important role in all steps of the reaction, from prompt nucleon emissions to the final fragments. The isospin diffusion is also of large interest, due to the interplay of asymmetry and density gradients. In relativistic collisions, the possibility of a direct study of the covariant structure of the effective nucleon interaction is shown. Results are discussed for particle production, collective flows and iso-transparency.

Perspectives of further developments of the field, in theory as well as in experiment, are presented.

Key words: isospin dynamics, symmetry energy, nucleon effective masses, reaction mechanisms, phase transitions, relativistic collisions, collective flows, isospin diffusion, meson production

PACS: 21.65.+f, 21.30.Fe, 25.70.Pq, 25.75.Dw, 24.10.Cn, 24.10.Jv

Contents

1	Introduction	1
2	Symmetry term effects on compressibility, saturation density and nucleon mean field	7
2.1	The symmetry term of Skyrme forces	10
2.1.1	Mean field and chemical potentials	12
2.2	Effective masses in neutron-rich matter	15
2.2.1	Effective masses and Landau Parameters	17
2.2.2	Energy dependence of the Lane Potential	18
2.3	Isospin effects on the momentum dependence of the mean field	20
3	Instabilities in Two-component Fluids: the Liquid-Gas Phase Transition in Asymmetric Matter	25
3.1	Thermodynamical study	25
3.1.1	Isoscalar-like and isovector-like instabilities	29
3.1.2	Nuclear matter instabilities	30
3.2	Dynamical analysis	33
3.2.1	Illustrative results for liquid-gas phase transitions	36
3.2.2	Coulomb effects on instabilities	36
3.2.3	Isospin distillation	38
3.3	Simulation results: heated nuclear matter in a box	40
4	Symmetry term effects on fast nucleon emission and collective flows	46
4.1	Pre-equilibrium dynamics	46
4.1.1	Average emission times	47
4.2	Nucleon-nucleon correlation functions	49
4.2.1	Isospin Momentum Dependence	52

* ditoro@lns.infn.it

¹ On leave from NIPNE-HH and Bucharest University, Romania

4.2.2	Light Clusters	53
4.3	Collective Flows	54
4.3.1	Definitions	55
4.3.2	Collective Flows at the Fermi Energies	56
4.3.3	Isospin effects around the Balance Energy	57
4.3.4	Differential Flows	59
4.4	Effective Mass Splitting and Collective Flows	61
4.4.1	Tranverse flows	61
4.4.2	Elliptic flows	64
4.4.3	Changing the stiffness of the symmetry term	66
5	Isospin Dynamics at the Fermi energies	68
5.1	Stochastic BNV transport theory	68
5.2	Main mechanisms of dissipative collisions: Fusion vs. Deep-Inelastic Competition	70
5.3	Isospin in Fragmentation Dynamics: Survey of experimental results	72
5.3.1	Isospin equilibration and fragment production	72
5.3.2	Isospin Distillation and Isoscaling	73
5.3.3	Isospin Dynamics for Neck Fragmentation in Semiperipheral Collisions	75
5.3.4	Isospin Diffusion	77
5.4	Theoretical interpretation: overview.	78
5.5	From central to semi-central collisions: bulk fragmentation.	78
5.5.1	Fragmentation dynamics	78
5.5.2	Isospin distillation	80
5.5.3	Isoscaling analysis	81
5.5.4	Symmetry Energy effects	84

5.6	From semicentral to peripheral collisions: neck fragmentation	84
5.6.1	Neck dynamics and IMF properties: the iso-migration	85
5.6.2	Neck dynamics at lower energy	88
5.6.3	Analysis of kinematical observables	90
5.6.4	Symmetry term effects	92
5.6.5	Isoscaling analysis	93
5.7	Charge Equilibration in Peripheral Collisions	94
5.7.1	Isospin diffusion in presence of inhomogenous density distributions	94
5.7.2	Isospin diffusion and EOS dependence	96
6	Effective interactions in the isovector channel: relativistic approach and the role of the δ meson	100
6.1	QHD effective field theory	101
6.1.1	Relativistic transport equations with Fock terms	102
6.1.2	Equilibrium properties: the nuclear Equation of State	104
6.1.3	Symmetry energy	106
6.1.4	Symmetry Pressure and Symmetry Incompressibility	109
6.1.5	Finite Temperature Effects	111
6.2	Mechanical and chemical instabilities	111
6.3	Nucleon Effective Mass Splitting	116
6.3.1	Dirac and Schrödinger Nucleon Effective Masses in Asymmetric Matter	117
6.3.2	The Dirac-Lane Potential	119
7	Collective modes of asymmetric nuclear matter in the relativistic approach	122
7.1	Linear Response Equations	122
7.2	The Role of Scalar/Vector Fields in the Dynamical Response	124

7.2.1	Isovector Response	124
7.2.2	Isoscalar Response	125
7.2.3	Landau Parameters	127
7.3	Isovector Collective Modes in Asymmetric Nuclear Matter	128
7.3.1	Disappearance of the Isovector Modes	130
7.4	Isoscalar Collective Modes in Asymmetric Nuclear Matter	132
7.4.1	Exotic high baryon density modes	132
7.4.2	Isospin Distillation in Dilute Matter	133
7.5	General comments from the ANM collective response	134
8	Relativistic Heavy Ion Collisions: the covariant structure of the symmetry term	136
8.1	Relativistic transport simulations	139
8.2	Collective flows	140
8.3	π^-/π^+ Ratios	143
8.4	Isospin Transparency	147
9	Conclusion and outlook	152
9.1	Outlook: The Eleven Observables	153
	References	156

1 Introduction

A key question in the physics of unstable nuclei is the knowledge of the *EOS* for asymmetric nuclear matter (*ANM*) away from normal conditions. We recall that the symmetry energy at low densities has important effects on the neutron skin structure, while the knowledge in high densities region is crucial for supernovae dynamics and neutron star properties. The paradox is that while we are planning second and third generation facilities for radioactive beams our basic knowledge of the symmetry term of the *EOS* is still extremely poor. Effective interactions are obviously tuned to symmetry properties around normal conditions and any extrapolation can be quite dangerous. Microscopic approaches based on realistic NN interactions, Brueckner or variational schemes, or on effective field theories show a rather large variety of predictions. As an example, in Fig.1-1 we collect the isospin dependence of some *EOS*'s which have *the same saturation properties for symmetric NM* (top): *SKM** [2,3], *SLy230b (SLy4)* [4,5,6] and *BPAL32* [7,8,9].

In Fig.1-1 (bottom) we report the density dependence of the potential symmetry contribution for the three different effective interactions. While all curves obviously cross at normal density ρ_0 , quite large differences are present for values, slopes and curvatures in low density and particularly in high density regions.

Moreover even at the relatively well known “crossing point” at normal density the various effective forces are presenting controversial predictions for the momentum dependence of the fields acting on the nucleons and consequently for the splitting of the neutron/proton effective masses, of large interest for nuclear structure and dynamics.

In the recent years under the stimulating perspectives offered from nuclear astrophysics and from the new Radioactive Ion Beam (*RIB*) facilities a relevant activity has started in the field of the isospin degree of freedom in heavy ion reactions, see the refs.[14,15,16]. Here we review the field trying to pin down the most interesting theory questions and eventually the related key observables. We will follow non-relativistic and relativistic approaches to construct effective interactions. In general the physics is not dependent on the theoretical framework, however we will see some genuine pure relativistic effects in the dynamics of the isovector part of the *EOS*.

In Section 2, we look at the density dependence of the symmetry term around saturation in order to relate slope and curvature to physics properties of exotic nuclei, bulk densities, neutron distributions and monopole frequencies. The momentum dependence of the interactions in the isovector channel is thoroughly analysed discussing the expected effects on the energy-slope of the

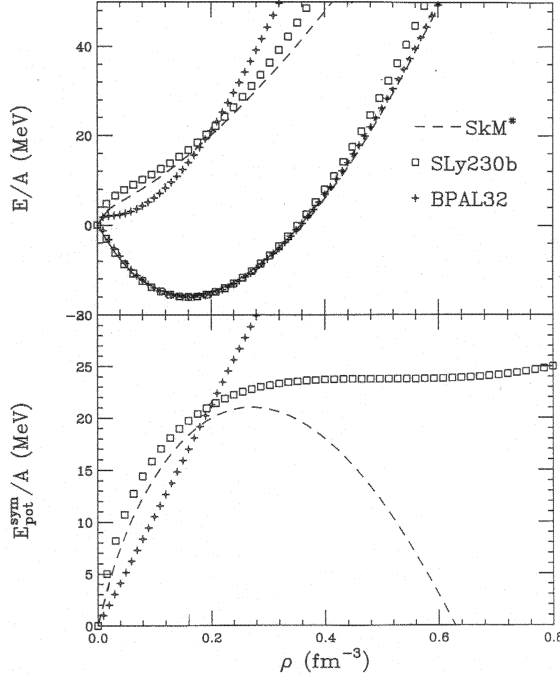


Fig. 1-1. *EOS* for various effective forces. Top: neutron matter (up), symmetric matter (down); Bottom: potential symmetry term.

Lane Potential at normal density and on the symmetry field seen by high momentum nucleons.

Section 3 is devoted to the study of symmetry properties at low density, i.e. to the Liquid-Gas Phase Transition in Asymmetric Matter. We start with a thermodynamical approach to the mechanical (vs. density variations) and chemical (vs. concentration variations) instability regions. We show then that the line of maximum instability for a two component system goes along a mixing of the two directions with a “mixing angle” that depends on microscopic properties of the interaction among the components.

We pass then to a dynamical approach of great relevance since it leads to the space-time properties of the unstable normal modes which give rise to fragments inside the extended spinodal boundary. Characteristic coupled dispersion relations must be solved. We remind that the coupling of the isoscalar and isovector collective response is well known for stable modes [17,18] in neutron rich exotic nuclei, with transition densities that show a mixed nature. Here we extend the same results to the unstable responses of interest in fragmentation reactions. The mixed nature of the unstable density oscillations will naturally lead to the *isospin distillation* effect, i.e. a different *concentration* (N/Z) between the liquid and the gas phase [19,20,21,22,23]. This is indeed the main new feature of the liquid-gas phase transition which is behind the cluster formation in the expansion stage of the reaction dynamics. We can expect that quantitatively this effect will be dependent on properties of the

symmetry energy in very dilute matter, well below the saturation point.

The early emission of particles in heavy ion collisions is relevant for understanding both the reaction dynamics and the mechanism for particle production. As discussed before, the density behavior of the symmetry potential is strictly related to the value of the pressure that one obtains in asymmetric nuclear matter. The early reaction dynamics is mainly governed by the pressure of the excited nuclear matter produced during the initial stage of the collision [24,25,26]. Therefore we can expect important symmetry effects on transport properties (fast particle emission, collective flows) in the asymmetric NM that will be probed by Radioactive Beam collisions at Fermi and intermediate energies. In Section 4 we review several observables that are related to the early particle emission: two-nucleon correlation functions, light cluster formation, transverse and elliptic collective flows and we will focus on the difference observed between neutron and proton behavior. Results of collision simulations based on microscopic kinetic equation are discussed, starting from realistic effective interactions widely used for symmetric systems. Different parametrizations in the momentum dependence of the isovector channel are tested, taking care that the symmetry energy, including its density dependence, will be not modified. We study in particular the transport effect of the sign of the n/p effective mass splitting $m_n^* - m_p^*$ in asymmetric matter at high baryon and isospin density.

In Section 5, we continue the discussion of nuclear reactions in the Fermi energy domain. We remind that this is the transition region between a dynamics mainly driven by the mean-field, below $15 - 20$ $AMeV$, and the one where the nucleon-nucleon collisions play a central role, above 100 $AMeV$. We can have then a very rich variety of dissipative reaction mechanisms, with related different isospin dynamics. One of the new distinctive features is the enhanced production of Intermediate Mass Fragments ($IMF, 3 \leq Z \leq 20$). We analyse then with great detail the isovector channel effect on the onset of the fragmentation mechanism and on the isotopic content of the produced fragments. In the reaction simulations it is essential the use of a *Stochastic Transport Approach* since fluctuations, instabilities and dynamical branchings are very important in this energy range.

As we may see, even from Fig.1-1, the potential symmetry term for various effective interactions shows quite different behaviors in the region around normal density and at very low densities, where we enter the spinodal zone and the cluster formation initiates. While around ρ_0 the density dependence becomes steeper when we go from asy-soft (Skyrme-like) to asy-superstiff (this suggests the names) at subsaturation densities it manifests an opposite trend. We will see that with the centrality of the collision we can have different scenarios for fragment production, from the growing instabilities of dilute matter in central reactions to the cluster formation at the interface between low and

normal density regions in semicentral collisions. We can then expect a large variety of isospin effects, probing different regions of the symmetry energy below saturation.

The traditional approach to nuclear physics starts from non-relativistic formalisms in which non-nucleonic degrees of freedom are integrated out giving nucleon-nucleon potentials. Then nuclear matter is described as a collection of quantum nonrelativistic nucleons interacting through an instantaneous effective potential. Although this approach has had a great success, a more appropriate set of degrees of freedom consists of strongly interacting effective hadron fields, mesons and baryons. These variables are the most efficient in a wide range of densities and temperatures and they are the degrees of freedom actually observed in experiments, in particular in Heavy Ion Collisions at intermediate energies. Moreover this framework appears in any case a fundamental “Doorway Step” towards a more microscopic understanding of the nuclear matter. Relativistic contributions to the isospin physics for static properties and reaction dynamics will be discussed in the second part of the report, Sections 6, 7 and 8.

The *QHD* (Quantum-Hadro-Dynamics) effective field model represents a very successful attempt to describe, in a fully consistent relativistic picture, equilibrium and dynamical properties of nuclear systems at the hadronic level [27,28,29]. In this report we mostly focus our attention on the dynamical response of Asymmetric Nuclear Matter (*ANM*). We present a relativistic kinetic theory with the aim of a transparent connection between the collective and reaction dynamics and the coupling to various channels of the nucleon-nucleon interaction. We show that the same isospin physics described in detail at the non-relativistic level can be naturally reproduced. Moreover some new genuine relativistic effects will be revealed, due to the covariant structure of the effective interactions.

One of the main points of our discussion is the relevance of the coupling to a scalar isovector channel, the effective $\delta[a_0(980)]$ meson, not considered in the usual nuclear structure studies [12,13]. A related feature of interest is the dynamical treatment of the Fock terms. We like to note that recently , see the conclusions of the refs. [30,31], the δ -field coupling has been reconsidered as an interesting improvement of covariant approaches, in the framework of an *Effective Field Theory* as a relativistic *Density Functional Theory*, since contribution to this channel are mainly coming from correlation effects. One of the main tasks of our work is just to try to select the dynamical observables more sensitive to it.

In Section 6, this extension of the *QHD* model is presented. Equilibrium properties are discussed, like the nuclear *EOS* and the corresponding thermodynamical instabilities. Particular attention is devoted to the expectations

for the splitting of the nucleon effective masses in asymmetric matter, with a detailed analysis of the relationship between the Dirac masses of the effective field approach and the Schrödinger masses of the non-relativistic models. A relativistic Dirac-Lane potential is deduced, which shows a structure very similar to the Lane potential of the non-relativistic optical model, but now in terms of isovector self-energies and coupling constants. As a general trend we have a close parallelism between relativistic and non-relativistic results, as it should be since the main physics is the same. We always note this point but we also stress several new features coming from a consistent use of a field theory approach.

We follow a Relativistic Mean Field (*RMF*) approximation that is allowing more physics transparent results, often even analytical. We will always keep a close connection to the more microscopic Dirac-Brueckner-Hartree-Fock (*DBHF*) approaches, in their extension to asymmetric matter, [32,33,34,35] It is well known that correlations are naturally leading to a density dependence of the coupling constants, see ref.[33] for the *DBHF* calculations and ref.[36] just for the basic Fock correlations. Within the *RMF* model we can get a clear qualitative estimation of the contribution of the various fields to the nuclear dynamics. The price to pay is that when we try to get quantitative effects we are forced to use different sets of couplings in different baryon density regions. In this case we use the *DBHF* results as guidelines. In particular for the controversial δ -meson field, expected to be important at densities above saturation, we fix the corresponding coupling from the analysis of refs.[34,35], where it actually appears not strongly density dependent in a wide range of baryon densities.

An important outcome of our work is to show that the two effective couplings, vector and scalar, in the isovector channel are influencing in a different way the static (symmetry energy) and dynamic (collective response, reaction observables) properties of asymmetric nuclear matter. All that will open new possibilities for a phenomenological determination of these fundamental quantities.

In Section 7, we discuss a fully relativistic Landau Fermi liquid theory based on the Quantum Hadro-Dynamics (*QHD*) effective field picture of Nuclear Matter. From the linearized kinetic equations we get the dispersion relations of the propagating collective modes. The relation between static properties and the collective response is analysed stressing the different role of the various channels present in the effective nuclear interaction. We focus our attention on the dynamical effects of the interplay between scalar and vector field contributions. An interesting “mirror” structure in the form of the dynamical response in the isoscalar/isovector degree of freedom is revealed, with a complete parallelism in the role respectively played by the compressibility and the symmetry energy. In particular we study the influence of a scalar-isovector

channel (coupling to a δ -meson-like effective field) on the collective response of asymmetric nuclear matter (*ANM*). Interesting contributions are found on the propagation of isovector-like modes at normal density and on an expected smooth transition to isoscalar-like oscillations at high baryon density.

Important “chemical” effects on the neutron-proton structure of the normal modes are shown. For dilute *ANM* we have the isospin distillation mechanism of the unstable isoscalar-like oscillations, as already shown in Section 3 in a non-relativistic frame, while at high baryon density we predict an almost pure neutron wave structure of the propagating sounds.

Results for relativistic Heavy Ion Collisions (*HIC*) in the *AGeV* beam energy region are presented in Section 8. We recall that intermediate energy *HIC*’s represent the only way to probe in terrestrial laboratories the in-medium effective interactions far from saturation, at high densities as well as at high momenta. Within a relativistic transport model it is shown that the isovector-scalar δ -meson, which affects the high density behavior of the symmetry term and the nucleon effective mass splitting, influences the isospin dynamics. The effect is largely enhanced by a relativistic mechanism related to the covariant nature of the fields contributing to the isovector channel. The possibility is emerging of a direct measurement of the Lorentz structure of the effective nuclear interaction in the isovector channel.

Quantitative calculations are discussed for collective flows, charged pion production and isospin stopping. Asymmetric systems where some data are available have been studied. Although the data are mostly of inclusive type (and the colliding nuclei not very neutron rich), quite clearly a dependence of some observables on charge asymmetry is emerging. Very sensitive quantities appear to be the elliptic flow, related to the time scale of the particle emissions, and the isospin transparency in central collisions.

Finally in Section 9 a general outlook for theory and experiment is presented. Particular attention is paid to a selection of the expected most sensitive observables to the isospin dynamics, in heavy ion reactions from low to relativistic energies.

2 Symmetry term effects on compressibility, saturation density and nucleon mean field

In asymmetric matter the energy per nucleon, i.e. the equation of state, will be a functional of the total ($\rho = \rho_n + \rho_p$) and isospin ($\rho_3 = \rho_n - \rho_p$) densities. In the usual parabolic form in terms of the asymmetry parameter $I \equiv \rho_3/\rho = (N - Z)/A$ we can define a symmetry energy $\frac{E_{sym}}{A}(\rho)$:

$$\frac{E}{A}(\rho, I) = \frac{E}{A}(\rho) + \frac{E_{sym}}{A}(\rho) I^2. \quad (2-1)$$

The symmetry term gets a kinetic contribution directly from the basic Pauli correlations and a potential contribution from the properties of the isovector part of the effective nuclear interactions in the medium. Since the kinetic part can be exactly evaluated we can separate the two contributions, reducing the discussion just to a function $F(u)$ of the density $u \equiv \rho/\rho_0$ linked to the interaction:

$$\epsilon_{sym} \equiv \frac{E_{sym}}{A}(\rho) = \frac{\epsilon_F(\rho)}{3} + \frac{C}{2} F(u), \quad (2-2)$$

with $F(1) = 1$, where ρ_0 is the saturation density and the parameter C is of the order $C \simeq 32 \text{ MeV}$ to reproduce the a_4 term of the Bethe-Weiszäcker mass formula. The validity of the parabolic form Eq.(2-1) comes directly from the isospin structure of the nucleon-nucleon interaction. The effects of many-body correlations are not much affecting this behaviour, see ref.[32,37], well verified in the nuclear data systematics [38]. Corrections are negligible up to very high densities, of the order of $5\rho_0$. The corrections in the kinetic term are also exactly evaluated to be of 4% for any density.

A traditional expansion to second order around normal density is used [39,40,12]

$$\epsilon_{sym} \equiv \frac{E_{sym}}{A}(\rho) = a_4 + \frac{L}{3} \left(\frac{\rho - \rho_0}{\rho_0} \right) + \frac{K_{sym}}{18} \left(\frac{\rho - \rho_0}{\rho_0} \right)^2, \quad (2-3)$$

in terms of a slope parameter

$$L \equiv 3\rho_0 \left(\frac{d\epsilon_{sym}}{d\rho} \right)_{\rho=\rho_0} = \frac{3}{\rho_0} P_{sym}(\rho_0) \quad (2-4)$$

simply related to the *symmetry pressure* $P_{sym} = \rho^2 d\epsilon_{sym}/d\rho$ at ρ_0 , and a curvature parameter

$$K_{sym} \equiv 9\rho_0^2 \left(\frac{d^2\epsilon_{sym}}{d^2\rho} \right)_{\rho=\rho_0}, \quad (2-5)$$

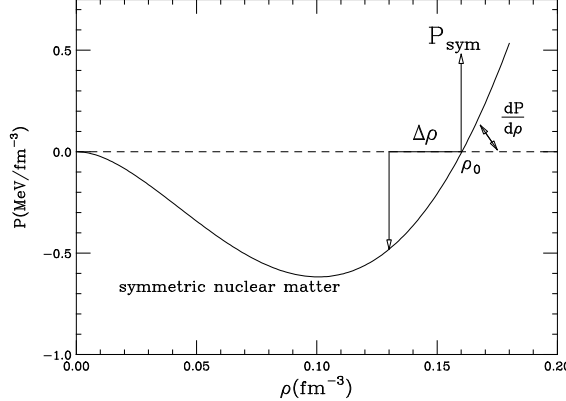


Fig. 2-1. Geometric picture of the lowering of the saturation density in asymmetric matter, Eq.(2-6).

a kind of symmetry compressibility. We remark that our present knowledge of these basic properties of the symmetry term around saturation is still very poor, see the recent analysis in ref.[30] and refs. therein. In particular we note the uncertainty on the symmetry pressure at ρ_0 , of large importance for structure calculations. These points, in connection to the possibility of getting a new insight from reaction data, will be largely discussed in this report.

We first mention some simple considerations on asymmetry effects on equilibrium density and compressibility, observables related respectively to bulk densities and monopole resonances in medium heavy nuclei [10]. From a linear expansion around the value at symmetry, $I = 0$, we get for the variation of saturation density

$$\begin{aligned} \Delta\rho_0(I) &= -\frac{9\rho_0^2}{K_{NM}(I=0)} \frac{d}{d\rho} \epsilon_{sym}(\rho) \Big|_{\rho=\rho_0} I^2 \\ &= -\frac{3\rho_0 L}{K_{NM}(I=0)} I^2 < 0, \end{aligned} \quad (2-6)$$

where $K_{NM}(I = 0)$ and ρ_0 are respectively compressibility and saturation density of symmetric NM .

The Eq.(2-6) has an intuitive *geometrical* meaning, which is qualitatively shown in Fig.2-1. Asymmetry brings an extra pressure $P_{sym} = \rho^2 d\epsilon_{sym}/d\rho$ that can be compensated just moving to the left the saturation point ($P = 0$) of the quantity $P_{sym}/(dP/d\rho)$ at ρ_0 (we recall that, for symmetric matter at ρ_0 , $9(dP/d\rho) = K_{NM}(I = 0)$). For the compressibility shift we have, after some algebra,

$$\Delta K_{NM}(I) = 9\rho_0 \left[\rho_0 \frac{d^2}{d\rho^2} - 2 \frac{d}{d\rho} \right] \epsilon_{sym}(\rho) \Big|_{\rho=\rho_0} I^2$$

Table 1
Symmetry term at saturation

$F(u)$	L	K_{sym}	$[K_{sym} - 6L]$
$const = 1$	$+25\text{MeV}$	-25MeV	-125MeV
\sqrt{u}	$+49\text{MeV}$	-61MeV	-355MeV
u	$+75\text{MeV}$	-25MeV	-475MeV
$u^2/(1+u)$	$+100\text{MeV}$	$+50\text{MeV}$	-550MeV

$$= [K_{sym} - 6L]I^2 < 0, \quad (2-7)$$

where we note the interplay between slope and curvature of the symmetry term.

The Eq.(2-6), and the related geometrical interpretation Fig.2-1, is a particular case (for $P = 0$) of the general variation of the density in asymmetric matter corresponding to a fixed pressure P , see the discussion in refs.[41,42]. The corresponding compressibility shift, Eq.(2-7), is also evaluated in the isobaric case, where there is the possibility to have some experimental information from Giant Monopole Resonance (*GMR*) data in charge asymmetric nuclei. Actually Eq.(2-7) represents an approximate form where higher order terms in density variations are neglected, see refs.[41,42]. The general negative sign of the compressibility shift, Eq.(2-7), is a natural consequence of Eq.(2-6), i.e. of the fact that the saturation density is decreasing with charge asymmetry.

In order to have a quantitative idea, we now show explicitly the influence on the L, K_{sym} parameters of a different density dependence in the potential part of the symmetry energy around saturation, i.e. of the function $F(u)$ of Eq.(2-2):

$$L = \frac{2}{3}\epsilon_F + \frac{3}{2}C \frac{d}{du}F(u) \Big|_{u=1}$$

$$K_{sym} = -\frac{2}{3}\epsilon_F + \frac{9}{2}C \frac{d^2}{du^2}F(u) \Big|_{u=1}$$

We obtain the very instructive Table 1 for various functional forms $F(u)$, $u \equiv \rho/\rho_0$, around ρ_0 .

The choices in the table of the $F(u)$ behaviors are in fact not arbitrary. They reflect the wide spectrum of theory predictions for effective forces in the isovector channel, as discussed in detail in the rest of the report. The constant trend of the first row (around saturation density) is typical of Skyrme-like forces, the \sqrt{u} behavior is obtained in variational approaches with realistic NN interactions [43,44], the linear dependence in Brueckner-Hartree-Fock (*BHF*) non relativistic calculations [7,8,37] as well as in Relativistic Mean Field (*RMF*),

[10], and Dirac-Brueckner-Hartree-Fock (*DBHF*), [32], approaches. Finally the more repulsive, nearly parabolic, dependence of the fourth row, [45,46], can be related to non-relativistic predictions with three-body forces, either extended *BHF* or variational [37,47] as well as to other relativistic *DBHF* estimations, refs. [33,34], or *RMF* with scalar isovector meson-like contributions [12,13].

Fixing the same compressibility at saturation for symmetric matter $K_{NM}(I=0)$, the relativistic effective forces always predict larger shifts in both equilibrium density and compressibility for asymmetric matter. This can be seen also in the comparison with Skyrme-like interactions in the finite nuclei calculations shown in ref.[10], even at relatively small charge asymmetries. There are therefore good chances of obtaining some direct experimental indications from *GMR* measurements in $N \neq Z$ nuclei. A recent systematic study of the isospin dependence of *GMR*'s in *Sn* isotopes, [48], seems to reveal a relatively large decrease of the Giant Monopole centroid with increasing asymmetry, more in agreement with a *stiff* behavior of the symmetry term around saturation, as expected in the relativistic models. We note that the relation between the “symmetry compressibility”, Eq.(2-5), and the variation of the compressibility of asymmetric matter is not trivial: we can have cases where an increase of K_{sym} actually corresponds to a softening of the Equation of State of asymmetric matter.

It is finally instructive to evaluate the density gradient of the symmetry pressure as a function of the slope and curvature of the symmetry term:

$$\frac{d}{d\rho}P_{sym} = \frac{2}{3}L + \frac{1}{9}K_{sym}, \quad (2-8)$$

that around normal density gives

$$\frac{d}{d\rho}P_{sym} = \frac{10}{27}\epsilon_F + C\left[\frac{d}{du} + \frac{1}{2}\frac{d^2}{du^2}\right]F(u)\Big|_{u=1}$$

A stiffer symmetry term in general enhances the pressure gradient of asymmetric matter. We can expect direct effects on the nucleon emissions in the reaction dynamics, fast particles and collective flows. Moreover due to the different fields seen by neutrons and protons, we shall observe even specific isotopic effects. This point will be analysed in detail in Sect.4.

2.1 The symmetry term of Skyrme forces

Since in this report we will often show reaction results from non-relativistic kinetic equations with Skyrme forces [2], we will expand a little the discussion

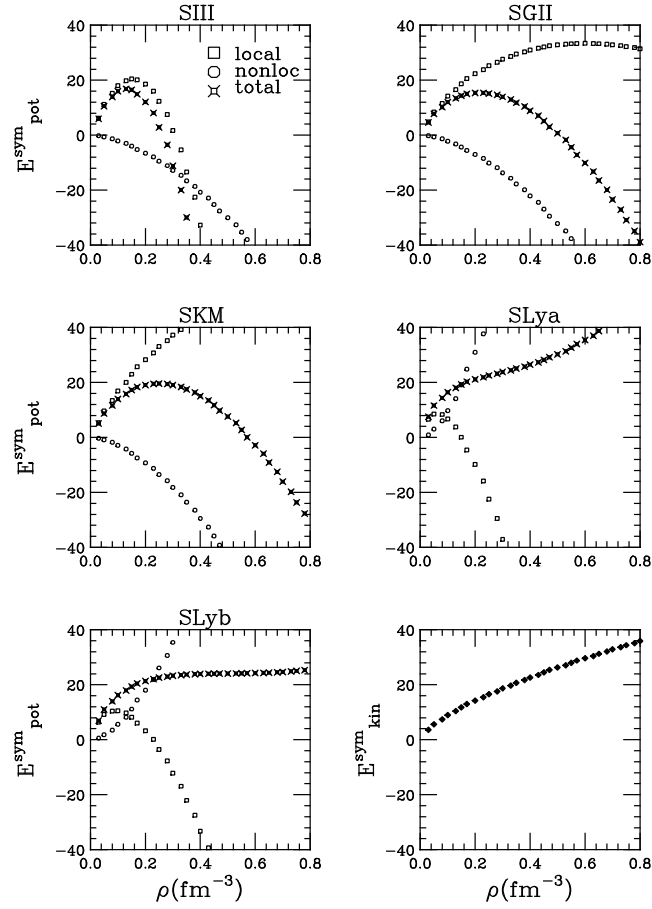


Fig. 2-2. Density dependence of the potential symmetry term for various Skyrme effective forces, see text. The bottom right panel shows the kinetic contribution on the isospin dependence of these widely used effective interactions. In a Skyrme-like parametrization the symmetry term has the form:

$$\epsilon_{sym} \equiv \frac{E_{sym}}{A}(\rho) = \frac{\epsilon_F(\rho)}{3} + \frac{C(\rho)}{2} \frac{\rho}{\rho_0} \quad (2-9)$$

with the function $C(\rho)$, in the potential part, given by:

$$\begin{aligned} \frac{C(\rho)}{\rho_0} = & -\frac{1}{4} \left[t_0(1 + 2x_0) + \frac{t_3}{6}(1 + 2x_3) \rho^\alpha \right] \\ & + \frac{1}{12} \left[t_2(4 + 5x_2) - 3t_1x_1 \right] \left(\frac{3\pi^2}{2} \right)^{2/3} \rho^{2/3} \end{aligned} \quad (2-10)$$

with $\alpha > 0$ and the usual Skyrme parameters. We remark that the second term is related to isospin effects on the momentum dependence [4]. In the Fig. 2-2 we show the density dependence of the potential symmetry term of various Skyrme interactions, *SIII*, *SGII*, *SKM** (see [3] and refs. therein) and the

Table 2
Parameters of Skyrme Forces

Force	<i>SIII</i>	<i>SGII</i>	<i>SkM*</i>	<i>SLya</i>	<i>SLy4</i>	<i>SLy7</i>
$t_0(MeV fm^3)$	-1128.75	-2645.0	-2645.0	-2490.3	-2488.91	-2482.41
$t_3(MeV fm^{3+3\alpha})$	14000.0	15595.0	15595.0	13803.0	13777.0	13677.0
x_0	0.45	0.09	0.09	1.1318	0.8340	0.846
x_3	1.0	0.06044	0.0	1.9219	1.3539	1.391
$t_1(MeV fm^5)$	395.0	340.0	410.0	489.53	486.82	457.97
$t_2(MeV fm^5)$	-95.0	-41.9	-135.0	-566.58	-546.39	-419.85
x_1	0.0	-0.0588	0.0	-0.8426	-0.3438	-0.511
x_2	0.0	1.425	0.0	-1.0	-1.0	-1.0
α	1	1/6	1/6	1/6	1/6	1/6

more recent Skyrme-Lyon forms, *SLya* and *Slyb* (or *Sly4*), see [4,5]. We also separately present the local and non-local contributions, first and second term of the Eq.(2-10). We clearly see a sharp change from the earlier Skyrme forces to the Lyon parametrizations, with almost an inversion of the signs of the two contributions. The important repulsive non-local part of the Lyon forces leads to a completely different behavior of the neutron matter *EOS*, of great relevance for the neutron star properties. Actually this substantially modified parametrization was mainly motivated by a very unpleasant feature in the spin channel of the earlier Skyrme forces, the collapse of polarized neutron matter, see discussion in [49,4,5,6].

In the Table 2 we collect the parameters, of interest for Nuclear Matter properties, of the various Skyrme forces used here, where we have also included the recent *Sly7* force particularly tuned for neutron rich systems [6]. Note the transition to $x_2 = -1$ values in the Skyrme-Lyon Forces just to cure the collapse of ferromagnetic neutron stars discussed before. In correspondence the predictions on the isospin effects on the momentum dependence of the symmetry term are quite different, see Fig.2-2. A very important consequence for the reaction dynamics is the expected inversion of the sign of the n/p effective mass splitting, which will be widely discussed in the next sections.

2.1.1 Mean field and chemical potentials

We can derive a general Skyrme-like form for neutron and proton mean field potentials [50,51]:

$$\begin{aligned}
U_q &\equiv \frac{\partial \epsilon_{pot}(\rho_q, \rho_{q'})}{\partial \rho_q} \\
&= A \left(\frac{\rho}{\rho_0} \right) + B \left(\frac{\rho}{\rho_0} \right)^{\alpha+1} + C(\rho) \left(\frac{\rho_3}{\rho_0} \right) \tau_q + \frac{1}{2} \frac{\partial C}{\partial \rho} \frac{\rho_3^2}{\rho_0} ,
\end{aligned} \tag{2-11}$$

ϵ_{pot} being the potential energy density. Here $\rho \equiv \rho_n + \rho_p$ and $\rho_3 \equiv \rho_n - \rho_p$ are respectively isoscalar and isovector densities, and $q = n, p$, $\tau_q = +1$ ($q = n$), -1 ($q = p$).

In the following we will always compare results obtained with forces that have *the same saturation properties for symmetric NM* [52]. We will refer to an "*asy-stiff*" *EOS* (e.g. like *BPAL32* of Fig.1) when we are considering a potential symmetry term linearly increasing with nuclear density and to a "*asy-soft*" *EOS* (e.g. like *SKM** of Fig.1) when the symmetry term shows a saturation and eventually a decrease above normal density. In some cases, in order to enhance the dynamical effects, we will consider also "*asy-superstiff*" behaviours, i.e. with a roughly parabolic increase of the symmetry term above normal density [9,45,46]. We focus our discussion on single particle properties since in this case the symmetry contribution will be linearly dependent on the asymmetry of the matter.

In Figs.2-3, 2-4 we report, for an asymmetry $(N-Z)/A = 0.2$ representative of ^{124}Sn , the density dependence of the symmetry contribution to the mean-field potential (Fig.2-3, second part of Eq.(2-11)) and of the chemical potentials (Fig.2-4) for neutrons (top curves) and protons (bottom curves), for the different effective interactions in the isovector channel.

From Fig.2-3 we note that in regions just off normal density the field "seen" by neutrons and protons in the three cases is very different, in particular below saturation density. We thus expect important transport effects during reactions at intermediate energies (prompt particle emissions, collective flows, n/p interferometry): the interacting asymmetric nuclear matter will experience compressed and expanding phases before forming fragments around normal density.

A transparent picture of the isospin dynamics can be obtained from the analysis of the density dependence of the "*local*" values of the neutron/proton chemical potentials $\mu_q \equiv \partial \epsilon(\rho_q, \rho_{q'}) / \partial \rho_q$, ϵ being the energy density. We remind that the chemical potentials contain all the contributions to the energy per particle, including the isoscalar part and the kinetic symmetry term. In non-equilibrium processes the mass flow is determined by the differences in the local values of chemical potential and it is directed from the regions of higher chemical potential to regions of lower values until equalization.

From Fig.2-4 we can already predict the *Isospin Distillation* effect and even

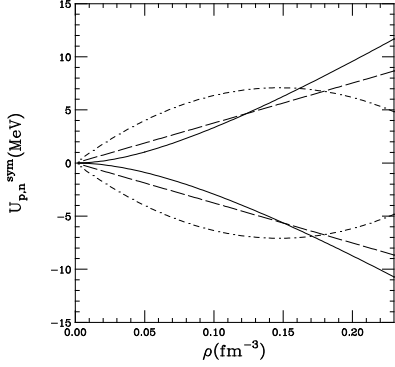


Fig. 2-3. Symmetry contribution to the mean field at $I = 0.2$ for neutrons (upper curves) and protons (lower curves): dashed lines "asy-soft", long dashed lines "asy-stiff", solid lines "asy-superstiff"

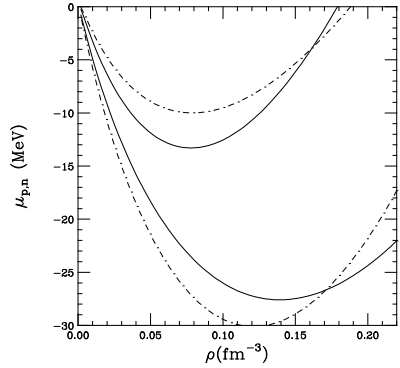


Fig. 2-4. Density dependence, for $I = 0.2$, of neutron (upper curves) and proton (lower curves) chemical potentials for asy-superstiff (solid lines) and asy-soft (dashed line) EOS.

the differences between the results in the isospin dynamics during fragment formation obtained using different symmetry terms, see Sects.3 and 5. The chemical potential for protons in a system having the ^{124}Sn asymmetry, $I = 0.2$, is below the corresponding value of symmetric nuclear matter while for neutrons is above, indeed $\mu_n - \mu_p = 4\epsilon_{sym}(\rho)I$. From the density dependence in the low densities region we see that when the inhomogeneities develop both neutrons and protons have the tendency to move in phase from lower to higher density regions. This is in qualitative agreement with the rigorous proof of the fact that the system is unstable against isoscalar-like fluctuations, see next section. Since the variations of the two chemical potentials are different (larger for protons) we expect a lower asymmetry in the liquid phase, i.e. in the clusters formed through such bulk instability mechanism. Moreover from the larger difference in the neutron/proton slopes in dilute matter, around $1/3\rho_0$, for the *asysoft* case (dashed lines of Fig.2-4) we can even expect a larger Isospin Distillation mechanism with such symmetry term.

In the case of a clusterization in presence of a contact between more dilute and "normal" density regions in order to understand the isospin dynamics we have to look at the density dependence of proton/neutron chemical potentials in the region between 0.08 fm^{-3} and 0.16 fm^{-3} . We see from Fig.2-4 that in this range the neutrons have the tendency to move towards more dilute regions producing a n -enrichment while the protons will migrate in opposite direction. Such mechanism is present in the "neck fragmentation", [53,54,55,56]: the neck IMF 's will be always more n -rich compared to the fragments produced in the case of bulk fragmentation. This effect, clearly seen in experiments, will be discussed in detail in Sect.5 since naturally it appears very sensitive to the stiffness of the symmetry term around saturation density.

2.2 Effective masses in neutron-rich matter

In the Fig.2-2 we have noticed a dramatic change in the local vs. non-local contributions to the symmetry energy going from the *old* to the *new* Skyrme forces of the Lyon type, explicitly built for asymmetric matter. A related interesting effect can be seen on the neutron/proton effective masses.

In asymmetric matter we consistently have a splitting of the neutron/proton effective masses given by:

$$m_q^{*-1} = m^{-1} + g_1\rho + g_2\rho_q, \quad (2-12)$$

with

$$\rho_{q=n,p} = \frac{1 + \tau_q I}{2} \rho \quad .$$

The g_1 , g_2 coefficients are simply related to the momentum dependent part of the Skyrme forces:

$$\begin{aligned} g_1 &= \frac{1}{4\hbar^2} [t_1(2 + x_1) + t_2(2 + x_2)] \\ g_2 &= \frac{1}{4\hbar^2} [t_2(1 + 2x_2) - t_1(1 + 2x_1)] \end{aligned} \quad (2-13)$$

This result derives from a general q – *structure* of the momentum dependent part of the Skyrme mean field

$$U_{q,MD} = m(g_1\rho + g_2\rho_q)E \quad (2-14)$$

where E is the nucleon kinetic energy.

In the Fig. 2-5 we show the density behavior of $m_{n,p}^*$ in neutron rich matter $I = 0.2$ for the same effective interactions. From the Eqs.(2-12, 2-13) we see that the sign of the g_2 univocally assigns the sign of the splitting, i.e. $g_2 < 0$ gives larger neutron masses $m_n^* > m_p^*$ while we have the opposite for $g_2 > 0$.

In the Table 3 we report some results obtained with various Skyrme forces for quantities of interest, around saturation, for the present discussion. We show also the E – *slope* of the corresponding Lane Potential, see later, simply related to the isospin dependent part of Eq.(2-14). For the effective mass parameters of Eq.(2-12) we observe that while the g_1 coefficients are always positive, corresponding to a decrease of the nucleon mass in the medium, the isospin dependent part shows different signs. In particular we see that in the Lyon forces the g_2 values are positive, with neutron effective masses below the proton ones for n-rich matter as shown in Fig. 2-5.

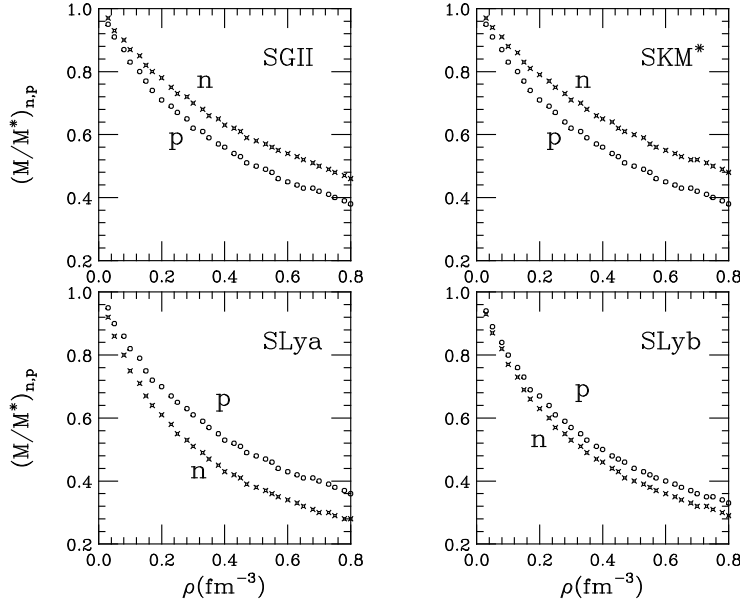


Fig. 2-5. Density dependence of the neutron/proton effective mass splitting for various Skyrme effective forces, see text. The asymmetry is fixed at $I = 0.2$, not very exotic.

Table 3
Properties at saturation

Force	<i>SIII</i>	<i>SGII</i>	<i>SkM*</i>	<i>SLya</i>	<i>SLy4</i>	<i>SLy7</i>
$g_1 (10^{-3})(MeV^{-1} fm^3)$	+3.85	+3.31	+3.53	+10 ⁻⁵	+1.67	+1.70
$g_2 (10^{-3})(MeV^{-1} fm^3)$	-3.14	-2.96	-3.50	+5.78	+2.53	+2.76
$\rho_0(fm^{-3})$	0.150	0.1595	0.1603	0.160	0.1595	0.1581
$a_4(MeV)$	28.16	26.83	30.03	31.97	32.01	32.01
$C(\rho_0)(MeV)$	31.72	29.06	35.46	39.40	39.42	39.42
$E - \text{slope}(LanePot.)$	-0.22	-0.21	-0.26	+0.43	+0.19	+0.20

In general we obtain a splitting of the order of 10 – 15% at normal density ρ_0 , and increasing with baryon density. Unfortunately from the present nuclear data we have a very little knowledge of this effect, due to the low asymmetries available. This issue will be quite relevant in the study of drip-line nuclei.

The sign itself of the splitting is very instructive. Passing from Skyrme to Skyrme-Lyon we see a dramatic inversion in the sign of the n/p mass splitting. The Lyon forces predict in n -rich systems a neutron effective mass always smaller than the proton one. We will come back to this point. Here we just note that the same is predicted from microscopic relativistic Dirac-Brueckner calculations [34] and in general from the introduction of scalar isovector virtual

mesons in *RMF* approaches [12,13]. At variance, non-relativistic Brueckner-Hartree-Fock calculations are leading to opposite conclusions [57,58]. We remind that a comparison between relativistic effective (*Dirac*) masses and non-relativistic effective masses requires some attention. This point will be carefully discussed later in the effective field theory approach to the in-medium interactions, Sect.6.

2.2.1 Effective masses and Landau Parameters

The quasiparticle nucleon energies in a general Skyrme form are given by:

$$\epsilon_q(\rho_q, \rho_{q'}, p) = \frac{p^2}{2m} + \int \frac{d^3 p'}{(2\pi\hbar)^3} (p - p')^2 [g_1 f(p') + g_2 f_q(p')] + U_q(\rho_q, \rho_{q'}) \quad (2-15)$$

where $U_q(\rho_q, \rho_{q'})$ is the local part of the mean field, Eq.(2-11), and $f(p), f_q(p)$ are the nucleon momentum distributions. The corresponding Landau parameters defined by:

$$\delta\epsilon_q \equiv \frac{2}{N_q} \int \frac{d^3 p'}{(2\pi\hbar)^3} [F_{qq}(p, p') \delta f_q(p') + F_{qq'}(p, p') \delta f_{q'}(p')] \quad (2-16)$$

have the form:

$$\begin{aligned} F_{qq}(p, p') &= N_q \left(\frac{g_1}{2} (p - p')^2 + \frac{g_2}{2} (p - p')^2 + \frac{\partial U_q}{\partial \rho_q} \right) \\ F_{qq'}(p, p') &= N_q \left(\frac{g_1}{2} (p - p')^2 + \frac{\partial U_q}{\partial \rho_{q'}} \right) \end{aligned} \quad (2-17)$$

where $N_q \equiv \frac{m_q^* p_q}{\pi^2 \hbar^3}$ is the energy level density of the q -nucleons.

From the expansion:

$$F_{qq'} = F_{qq'}^0 + F_{qq'}^1 (\hat{p} \cdot \hat{p}') \quad (2-18)$$

we get, at the Fermi momentum, the explicit Skyrme form of the “local” and “non-local” Landau parameters:

$$\begin{aligned} F_{qq}^0 &= N_q(p_F) \left[(g_1 + g_2) p_{Fq}^2 + \frac{\partial^2 U_q}{\partial \rho_q^2} \right] \\ F_{qq'}^0 &= N_q(p_F) \left[g_1 p_{Fq}^2 + \frac{\partial^2 U_q}{\partial \rho_q \partial \rho_{q'}} \right] \end{aligned}$$

$$\begin{aligned}
F_{qq}^1 &= -N_q(p_F)(g_1 + g_2)p_{Fq}^2 \\
F_{qq'}^1 &= -N_q(p_F)g_1p_{Fq}p_{Fq'}
\end{aligned} \tag{2-19}$$

The (n,p) effective masses have the compact form:

$$\frac{m_q^*}{m} = 1 + \frac{1}{3} \left[F_{qq}^1 + \left(\frac{p_{Fq'}}{p_{Fq}} \right)^2 F_{qq'}^1 \right] \tag{2-20}$$

which nicely leads to the $(1 + \frac{1}{3}F^1)$ result for symmetric matter [59]. For the (n,p) mass splitting in asymmetric matter we have the expression:

$$\frac{m_n^* - m_p^*}{m} = \frac{1}{3} \left[F_{nn}^1 - F_{pp}^1 + \left(\frac{p_{Fp}}{p_{Fn}} \right)^2 F_{np}^1 - \left(\frac{p_{Fn}}{p_{Fp}} \right)^2 F_{pn}^1 \right]. \tag{2-21}$$

Since all the $F_{qq'}^1$ are negative this result has been used to predict a larger m_n^* mass in n-rich systems due to the larger neutron Fermi momentum, see the recent ref.[60]. However this is actually not generally correct because in fact all the F^1 Landau parameters also depend on Fermi momenta and the final balance will be fixed by the microscopic structure of the effective interaction, i.e. by the interplay between the g_1 and g_2 quantities in the case of Skyrme-like forces, Eq.(2-19). In particular, we see that when we pass from the “old” Skyrme to the “Lyon” parametrizations, i.e. from $g_2 < 0$ to $g_2 > 0$, the combination $g_1 + g_2$ becomes much larger and the F_{nn}^1 term is dominant in the n-rich case, see Eq.(2-21), leading to a $m_n^* < m_p^*$ mass splitting, as already discussed.

2.2.2 Energy dependence of the Lane Potential

We note that the sign of the splitting will directly affect the energy dependence of the Lane Potential, i.e. the difference between (n, p) optical potentials on charge asymmetric targets, normalized by the target asymmetry [61]. From the Eqs.(2-11, 2-14) we obtain the explicit Skyrme form of the Lane Potential:

$$U_{Lane} \equiv \frac{U_n - U_p}{2I} = C(\rho_0) + \frac{m\rho_0}{2}g_2E \tag{2-22}$$

where $C(\rho_0)$ gives the potential part of the a_4 parameter in the mass formula, see Eq.(2-2). We see that the $E - slope$ has just the sign of the g_2 parameter, and so we have opposite predictions from the various Skyrme forces analysed here. The change in the energy slope is reported in the last row of the Table

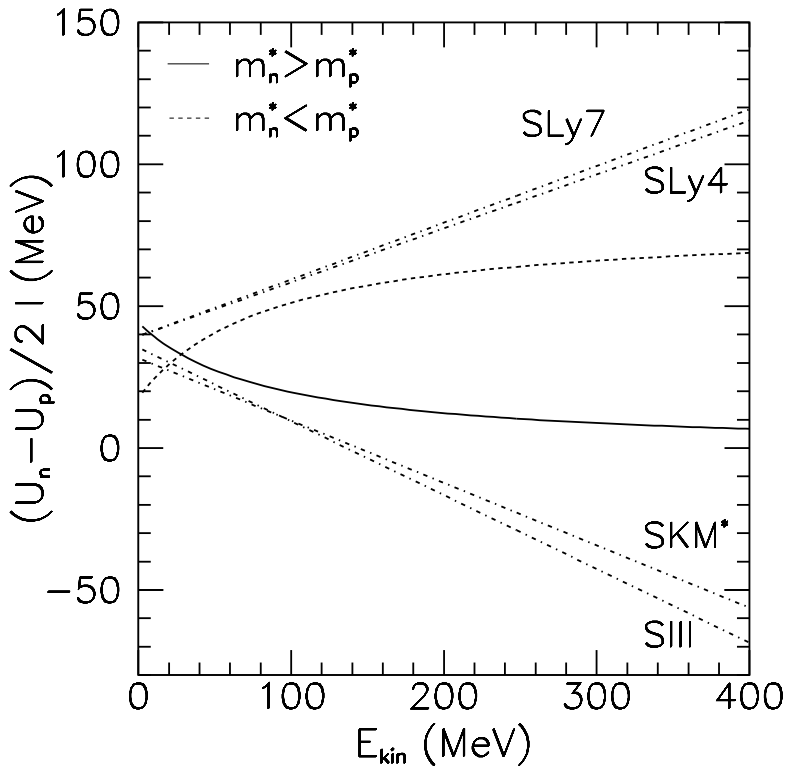


Fig. 2-6. Energy dependence of the Lane Potential for different Skyrme forces. The dotted ($m_n^* < m_p^*$) and solid ($m_n^* > m_p^*$) curves correspond to the more general momentum dependent mean fields $BGBD - 1, 2$ of the ref.[65], see text.

3. The difference in the energy dependence of the Lane Potential is quite dramatic, as we can see from Fig.2-6.

An important physical consequence of the negative slopes is that the isospin effects on the optical potentials tend to disappear at energies just above 100 MeV (or even change the sign for “old” Skyrme-like forces). Unfortunately results derived from neutron/proton optical potentials at low energies are not conclusive, [61,62,63], since the effects appear of the same order of the uncertainty on the determination of the local contribution. More neutron data are needed at higher energies, in particular a systematics of the energy dependence.

Moreover we can expect important effects on transport properties (fast particle emission, collective flows) of the dense and asymmetric NM that will be reached in Radioactive Beam collisions at intermediate energies. Indeed at supra-saturation density the difference in the predictions will be enhanced.

2.3 Isospin effects on the momentum dependence of the mean field

In presenting the symmetry energy results of various effective Skyrme forces we have stressed the conflicting predictions on the isospin dependence of the effective masses, i.e. on Isospin Momentum Dependent, *Iso-MD*, effects. This will be one of the main questions to address in the reaction dynamics of exotic nuclear systems, in particular for the close connection to fundamental properties of the nuclear interaction in the medium.

We will review some results on this direction using non-relativistic and relativistic (later in Sects. 6 and 8) microscopic kinetic approaches. Starting from realistic effective interactions widely used for symmetric systems we will test very different parametrizations in the momentum dependence of the isovector channel, taking care that the symmetry energy, including its density dependence, will be not modified. We study in particular the transport effect of the sign of the n/p effective mass splitting $m_n^* - m_p^*$ in asymmetric matter at high baryon and isospin density.

In a non-relativistic frame we can extend the general form of effective momentum dependent interactions first introduced by Bombaci et al. [64,57] for astrophysical and heavy ion physics applications. The isovector part can be modified in order to get new parametrizations with different n/p effective mass splittings while keeping the same symmetry energy at saturation, including a very similar overall density dependence, see ref.[65].

The energy density as a function of the asymmetry parameter reads: $I \equiv \frac{N-Z}{A}$:

$$\varepsilon(\rho_n, \rho_p) = \varepsilon_{kin} + \varepsilon_A + \varepsilon_B + \varepsilon_{MD} \quad (2-23)$$

$$\begin{aligned} \varepsilon_{kin}(\rho_n, \rho_p) &= \frac{2}{(2\pi)^3} \int d^3k f_n(k) \frac{\hbar^2}{2m} k^2 + \frac{2}{(2\pi)^3} \int d^3k f_p(k) \frac{\hbar^2}{2m} k^2 \\ \varepsilon_A(\rho, I) &= \frac{A}{2} \frac{\rho^2}{\rho_0} - \frac{A}{3} \frac{\rho^2}{\rho_0} \left(\frac{1}{2} + x_0 \right) I^2 \\ \varepsilon_B(\rho, I) &= \frac{B}{\sigma+1} \frac{\rho^{\sigma+1}}{\rho_0^\sigma} - \frac{2}{3} \frac{B}{\sigma+1} \frac{\rho^{\sigma+1}}{\rho_0^\sigma} \left(\frac{1}{2} + x_3 \right) I^2 \\ \varepsilon_{MD}(\rho_n, \rho_p, I) &= C \frac{\rho}{\rho_0} (\mathcal{I}_n + \mathcal{I}_p) + \frac{C - 8z_1}{5} \frac{\rho}{\rho_0} I (\mathcal{I}_n - \mathcal{I}_p) \end{aligned}$$

where the integrals $\mathcal{I}_\tau(\Lambda) = \frac{2}{(2\pi)^3} \int d^3k f_\tau(k) g(k, \Lambda)$ include the momentum dependent part of the mean field $g(k, \Lambda) = \left[1 + \left(\frac{k - \langle k \rangle}{\Lambda} \right)^2 \right]^{-1}$; the subscript $\tau = n, p$ stands for neutrons and protons respectively; $\rho_0 = 0.16 \text{ fm}^{-3}$ is the

normal density of nuclear matter. We refer to this parametrization as the *BGBD – EOS*. For symmetric nuclear matter ($I = 0$), the energy density Eq.(2-23) reduces to the parametrization proposed by Gale, Bertsch and Das Gupta (*GBD* interaction, [66]). In a sense this interaction represents an extension of the Gogny non locality since it gives very similar results in the range $\rho/\rho_0 \leq 1.5$ and $k < 4fm^{-1}$, see refs. [67,68] where nice applications in the Fermi energy region can be found.

The parameters A, B, C, σ and Λ take the same values as in [66] ($A = -144 MeV$, $B = 203.3 MeV$, $C = -75 MeV$, $\sigma = \frac{7}{6}$, $\Lambda = 1.5 p_F^{(0)}$, where $p_F^{(0)}$ is the Fermi momentum at normal density), and provide a soft *EOS* for symmetric matter, with a compressibility $K_{NM} \simeq 210 MeV$. The value of z_1 sets the strength of the momentum dependence (*MD*) in the isospin channel; the remaining parameters x_0 and x_3 can be set to fix the symmetry energy.

Taking the functional derivative of the energy density with respect to the distribution function f_τ , we obtain, apart from the kinetic term ε_{kin} , the mean field potential for neutrons and protons:

$$U_\tau(k; \rho, I) = A \left(\frac{\rho}{\rho_0} \right) + B \left(\frac{\rho}{\rho_0} \right)^\sigma - \frac{2}{3}(\sigma - 1) \frac{B}{\sigma + 1} \left(\frac{1}{2} + x_3 \right) \left(\frac{\rho}{\rho_0} \right)^\sigma I^2$$

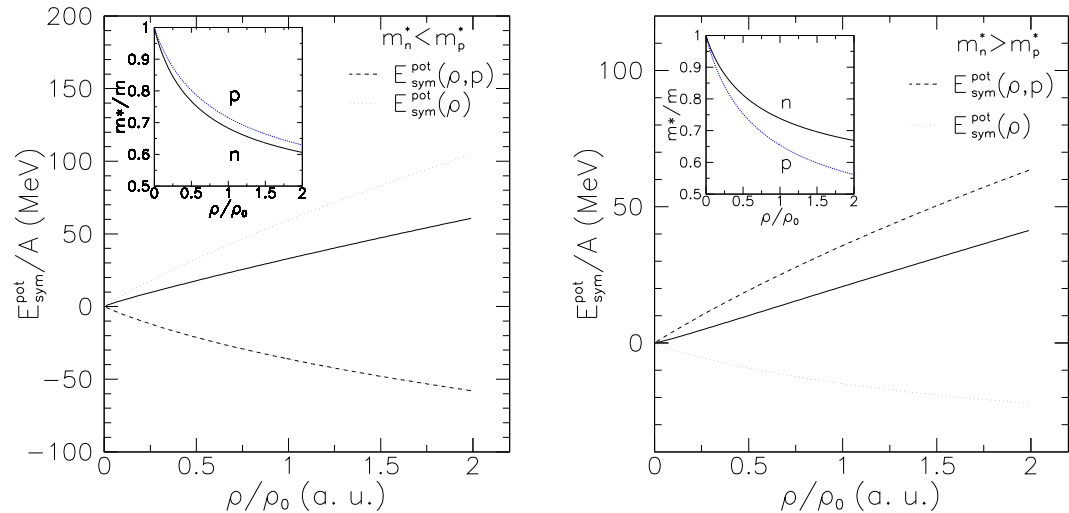


Fig. 2-7. Potential symmetry energy as a function of density (solid line) for $m_n^* < m_p^*$ (*BGBD – 1 set*, left) and $m_n^* > m_p^*$ (*BGBD – 2 set*, right). Dotted lines refer to density-dependent contributions, dashed-dotted to momentum dependent ones. Small panels indicate the corresponding behaviour of proton and neutron effective masses as a function of density, with $I = 0.2$.

$$\begin{aligned}
& \pm \left[-\frac{2}{3}A\left(\frac{1}{2} + x_0\right)\left(\frac{\rho}{\rho_0}\right) - \frac{4}{3}\frac{B}{\sigma+1}\left(\frac{1}{2} + x_3\right)\left(\frac{\rho}{\rho_0}\right)^\sigma \right] I^{2-24} \\
& + \frac{4}{5\rho_0} \left\{ \frac{1}{2}(3C - 4z_1)\mathcal{I}_\tau + (C + 2z_1)\mathcal{I}_{\tau'} \right\} \\
& + \left(C \pm \frac{C - 8z_1}{5}I \right) \left(\frac{\rho}{\rho_0}\right) g(k)
\end{aligned}$$

where the subscripts in the integrals are $\tau \neq \tau'$; the upper signs refer to neutrons, the lower ones to protons.

The last $BGBD$ term includes, besides the usual GBD momentum dependence, an isospin-dependent part from which we can get different effective masses for protons and neutrons. In fact, the effective mass is defined as:

$$\frac{m_\tau^*}{m} = \left\{ 1 + \frac{m}{\hbar^2 k} \frac{dU_\tau}{dk} \right\}_{k=k_F^{[\tau]}}^{-1} \quad (2-25)$$

and we see that mass splitting is determined not only by different momentum dependence of mean field, but also by Fermi momenta of neutrons and protons.

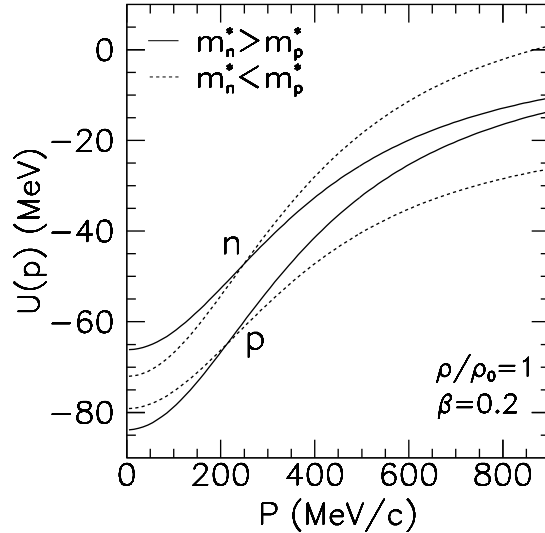


Fig. 2-8. Mean field potential as a function of momentum at normal density, for an asymmetry $I = 0.2$. Solid lines refer to the case $m_n^* > m_p^*$ ($BGBD - 1$ set), dashed lines to $m_n^* < m_p^*$ ($BGBD - 2$ set).

In the case considered here we have:

$$\frac{m_\tau^*}{m} = \left\{ 1 + \frac{-\frac{2m}{\hbar^2} \frac{1}{\Lambda^2} \left(C \pm \frac{C-8z_1}{5} I \right) \frac{\rho}{\rho_0}}{\left[1 + \left(\frac{k_{F0}}{\Lambda} \right)^2 (1 \pm I)^{(2/3)} \left(\frac{\rho}{\rho_0} \right)^{(2/3)} \right]^2} \right\}^{-1}$$

In order to investigate the effects of mass splitting on non-relativistic heavy ion collisions two sets of parameters (*BGBD* – 1, 2 shown in Table 4) which give opposite splitting, but quite similar behaviour of the symmetry energy, will be considered:

force	mass splitting	z_1	x_0	x_3
BGBD-1	$m_n^* < m_p^*$	28	1.925	0.41
BGBD-2	$m_n^* > m_p^*$	-36.75	-1.477	-1.01

Table 4

Values of the parameters z_1 , x_0 and x_3 , for opposite mass splitting but giving the same $E_{sym}(\rho_0) = 33 \text{ AMeV}$, which characterize the two used effective forces.

Figure 2-7 shows the potential part of the symmetry energy as a function of density (solid line) for the two choices of mass splitting. We remark the very similar overall density dependence. The dashed-dotted and dotted lines indicate respectively the contributions from the momentum dependent and density-dependent part of the *EOS*. A change in the relative sign of mass splitting is related to opposite behaviours of these two contributions, exactly as already noticed in the Introduction for the Skyrme-like forces. The small panels on the top left of each graph illustrate the corresponding mass splitting as a function of density for an asymmetry $I = 0.2$ (the ^{197}Au asymmetry).

We finally discuss the relation between effective mass and momentum dependence. From the definition Eq.(2-25) we see that the effective mass is inversely proportional to the slope of mean field at the Fermi momentum:

- For n-rich systems the n/p mean field potential difference $U_n - U_p$ will increase with nucleon momentum in the $m_n^* < m_p^*$ case and decrease in the opposite $m_n^* > m_p^*$ case.
- For nucleons with smaller effective masses the potential will be more repulsive at momenta higher than the Fermi one, and more attractive at low momenta.

Mean field potentials at normal density as a function of momentum are shown in Fig.2-8 for asymmetry $I = 0.2$. As we can see, the parametrizations described here give rise to opposite behaviors for low and high momentum particles. This is a very general feature, due to the meaning itself of effective mass Eq.(2-25). As we will see in the reaction dynamics this behavior can give rise

to some compensation effects between low and high momenta contributions. This will lead to an expected larger *isospin* – MD sensitivity of more exclusive measurements, in particular with a tranverse momentum selection of the nucleons emitted for a given rapidity.

3 Instabilities in Two-component Fluids: the Liquid-Gas Phase Transition in Asymmetric Matter

Since the fragment production represents a relevant dissipation mechanism for intermediate energy reactions and since it is seen as a consequence of the liquid-gas phase transition in Asymmetric Nuclear Matter (*ANM*), we are devoting one section to a detailed discussion of it. In this way we set some guidelines in order to understand the physics behind the transport simulation results of Sect.5, in particular on the possibility of extracting some information on the nuclear effective forces in the isovector channel. A very transparent picture of the *Isospin Distillation*, actually *Neutron Distillation*, effect is emerging.

One-component systems may become unstable against density fluctuations as the result of the strong attraction between constituents. In symmetric binary systems, like Symmetric Nuclear Matter (*SNM*), one may encounter two kinds of density fluctuations: i) isoscalar, when the densities of the two components oscillate in phase with equal amplitude, ii) isovector when the two densities fluctuate still with equal amplitude but out of phase. Then mechanical instability is associated with instability against isoscalar fluctuations leading to cluster formation while chemical instability is related to instability against isovector fluctuations, of repulsive character, leading to species separation. Turning now to asymmetric binary systems, as the *ANM* of interest here, this direct correspondence between the nature of fluctuations and the occurrence of mechanical or chemical instabilities is lost and we face a more complicated scenario, where isoscalar and isovector instabilities are coupled [19,20,22].

An appropriate framework for the study of instabilities is provided by the Fermi liquid theory [69], which has been applied, for instance, to symmetric binary systems as *SNM* (the two components being protons and neutrons) [70] and the liquid ^3He (spin-up and spin-down components) [71,72].

3.1 Thermodynamical study

Let us first discuss the thermodynamical stability of *ANM* at $T = 0$. We will review here the results obtained in [20] with some more discussion on the physics observables. The introduction of finite temperatures is straightforward.

The starting point is an extension to the asymmetric case of the formalism introduced in [71]. The distribution functions for protons and neutrons are:

$$f_q(\epsilon_p^q) = \Theta(\mu_q - \epsilon_p^q) , \quad q = n, p \quad (3-1)$$

where μ_q are the corresponding chemical potentials. The nucleon interaction is characterized by the Landau parameters:

$$F^{q_1 q_2} = N_{q_1} V^2 \frac{\delta^2 H}{\delta f_{q_1} \delta f_{q_2}} = N_{q_1} \frac{\delta^2 H}{\delta \rho_{q_1} \delta \rho_{q_2}}, \quad N_q(T) = \int \frac{-2 d\mathbf{p}}{(2\pi\hbar)^3} \frac{\partial f_q(T)}{\partial \epsilon_p^q} \quad (3-2)$$

where H is the energy density, V is the volume and N_q is the single-particle level density at the Fermi energy. At $T = 0$ this reduces to

$$N_q(0) = mp_{F,q}/(\pi^2 \hbar^3) = 3\rho_q/(2\epsilon_{F,q}),$$

where $p_{F,q}$ and $\epsilon_{F,q}$ are Fermi momentum and Fermi energy of the q -component. Thermodynamical stability for $T = 0$ requires the energy of the system to be an absolute minimum for the undistorted distribution functions, so that the relation:

$$\delta H - \mu_p \delta \rho_p - \mu_n \delta \rho_n > 0 \quad (3-3)$$

is satisfied when we deform proton and neutron Fermi seas.

Only monopolar deformations will be taken into account, since we consider here momentum independent interactions, so that $F_{l=0}^{q_1 q_2}$ are the only non-zero Landau parameters. In fact, for momentum independent interactions, all the information on all possible instabilities of the system is obtained just considering density variations. However one should keep in mind that in the actual dynamical evolution of an unstable system in general one observes deformations of the Fermi sphere, hence the direction taken by the system in the dynamical evolution is not necessarily the most unstable one defined by the thermodynamical analysis.

Then, up to second order in the variations, the condition Eq.(3-3) becomes

$$\delta H - \mu_p \delta \rho_p - \mu_n \delta \rho_n = \frac{1}{2}(a\delta\rho_p^2 + b\delta\rho_n^2 + c\delta\rho_p\delta\rho_n) > 0 \quad (3-4)$$

where

$$\begin{aligned} a &= N_p^{-1}(0)(1 + F_0^{pp}) \quad ; \quad b = N_n^{-1}(0)(1 + F_0^{nn}) \quad ; \\ c &= N_p^{-1}(0)F_0^{pn} + N_n^{-1}(0)F_0^{np} = 2N_p^{-1}(0)F_0^{pn}. \end{aligned} \quad (3-5)$$

The r.h.s. of Eq.(3-4) is diagonalized by the following transformation:

$$\begin{aligned} u &= \cos\beta \delta\rho_p + \sin\beta \delta\rho_n, \\ v &= -\sin\beta \delta\rho_p + \cos\beta \delta\rho_n, \end{aligned} \quad (3-6)$$

where the *mixing* angle $0 \leq \beta \leq \pi/2$ is given by

$$\tg 2\beta = \frac{c}{a-b} = \frac{N_p^{-1}(0)F_0^{pn} + N_n^{-1}(0)F_0^{np}}{N_p^{-1}(0)(1+F_0^{pp}) - N_n^{-1}(0)(1+F_0^{nn})}. \quad (3-7)$$

Then Eq.(3-4) takes the form

$$\delta H - \mu_p \delta \rho_p - \mu_n \delta \rho_n = Xu^2 + Yv^2 > 0 \quad (3-8)$$

where

$$\begin{aligned} X &= \frac{1}{2} (a + b + \text{sign}(c) \sqrt{(a-b)^2 + c^2}) \\ &\equiv \frac{(N_p(0) + N_n(0))^{-1}}{2} (1 + F_{0g}^s) \end{aligned} \quad (3-9)$$

and

$$\begin{aligned} Y &= \frac{1}{2} (a + b - \text{sign}(c) \sqrt{(a-b)^2 + c^2}) \\ &\equiv \frac{(N_p(0) + N_n(0))^{-1}}{2} (1 + F_{0g}^a), \end{aligned} \quad (3-10)$$

defining the new generalized Landau parameters $F_{0g}^{s,a}$.

Hence, thanks to the rotation Eq.(3-6), it is possible to separate the total variation Eq.(3-3) into two independent contributions, the "normal" modes, characterized by the "mixing angle" β , which depends on the density of states and the details of the interaction.

In the symmetric case, $N_p = N_n \equiv N$, $F_0^{nn} = F_0^{pp}$ and $F_0^{np} = F_0^{pn}$, Eq.(3-4) reduces to

$$\begin{aligned} \delta H - \mu_p \delta \rho_p - \mu_n \delta \rho_n &= \frac{N(0)^{-1}}{2} (1 + F_0^s) (\delta \rho_p + \delta \rho_n)^2 \\ &\quad + \frac{N(0)^{-1}}{2} (1 + F_0^a) (\delta \rho_p - \delta \rho_n)^2 \end{aligned} \quad (3-11)$$

where $F_0^s \equiv F_0^{nn} + F_0^{np}$ and $F_0^a \equiv F_0^{nn} - F_0^{np}$ are symmetric and antisymmetric (or isoscalar and isovector) Landau parameters, and the usual Pomeranchuk stability conditions for pure isoscalar/isovector fluctuations are recovered [51].

In the general case u - and v -variations, Eq.(3-6), can be interpreted as new independent *isoscalar*-like and *isovector*-like directions appropriate for asymmetric systems and F_{0g}^s and F_{0g}^a , defined by Eqs. (3-9,3-10), can be considered

as generalized symmetric and antisymmetric Landau parameters. Now, the instability of the system can be studied completely just looking at the curvatures along the u and v directions. If the system is stable against these two directions, it cannot be unstable in any other directions. On the contrary, if the system is unstable against u or v direction, or both, it can be unstable also in other directions of the $(\delta\rho_n, \delta\rho_p)$ plane.

Thus the thermodynamical stability requires $X > 0$ and $Y > 0$. Equivalently, the following conditions have to be fulfilled:

$$1 + F_{0g}^s > 0 \quad \text{and} \quad 1 + F_{0g}^a > 0, \quad (3-12)$$

They represent Pomeranchuk stability conditions extended to asymmetric binary systems.

As one can intuitively expect, the new stability conditions, Eq.(3-12), are equivalent to mechanical and chemical stability of a thermodynamical state, [73], i.e.

$$\left(\frac{\partial P}{\partial \rho}\right)_{T,y} > 0 \quad \text{and} \quad \left(\frac{\partial \mu_p}{\partial y}\right)_{T,P} > 0 \quad (3-13)$$

where P is the pressure and y the proton fraction. In fact, mechanical and chemical stability are very general conditions, deduced by requiring that the curvatures of thermodynamical potentials, such as the free energy (or the entropy) with respect to the extensive variables are positive (negative). In the case discussed here, it can be proven that [20]:

$$\begin{aligned} XY &= N_p^{-1}(0)N_n^{-1}(0)[(1 + F_0^{nn})(1 + F_0^{pp}) - F_0^{np}F_0^{pn}] \\ &= \frac{1}{(1 - y)\rho^2} \left(\frac{\partial P}{\partial \rho}\right)_{T,y} \left(\frac{\partial \mu_p}{\partial y}\right)_{T,P} \end{aligned} \quad (3-14)$$

and:

$$\begin{aligned} \left(\frac{\partial P}{\partial \rho}\right)_{T,y} &= \rho y(1 - y)(t a + \frac{1}{t} b + c) \\ &\propto X(\sqrt{t} \cos \beta + \frac{1}{\sqrt{t}} \sin \beta)^2 + Y(\sqrt{t} \sin \beta - \frac{1}{\sqrt{t}} \cos \beta)^2 \\ &\quad \text{with} \quad t = \frac{y}{1 - y}. \end{aligned} \quad (3-15)$$

Moreover, from Eq.3-15 (first line), it is possible to see that $(dP/d\rho)_{T,y}$ is proportional to the variation of the energy along the direction $\delta\rho_n/\delta\rho_p = 1/t = (1-y)/y = \rho_n/\rho_p$. In fact, from Eq.(3-4), along the direction $\delta\rho_p = t \delta\rho_n$, one has: $\delta H - \mu_p \delta\rho_p - \mu_n \delta\rho_n = \frac{1}{2}t (at + b/t + c) \delta\rho_n^2$. Thus the sign of $(dP/d\rho)_{T,y}$ gives information about the stability (or the instability) of the system against variations that preserve the initial proton to neutron density ratio. However, as we have seen, this is not the isoscalar-like direction of the normal mode, that is given by u .

3.1.1 Isoscalar-like and isovector-like instabilities

From Eq.s (3-8,3-9,3-10,3-12), one can define as isoscalar-like instability the case when the state is unstable against u -fluctuations, i.e. when $1 + F_{0g}^s < 0$ (or $X < 0$). The name isoscalar-like comes from the fact that since the mixing angle is in the interval $0 \leq \beta \leq \pi/2$ the neutron and proton oscillations are in phase in the normal-mode u -direction. Analogously we deal with isovector-like instability when the system is unstable against v -fluctuations i.e. when $1 + F_{0g}^a < 0$ (or $Y < 0$).

Let us consider first the case when $X < 0$. Since, as seen before, the mechanichal instability $((dP/d\rho)_{T,y} < 0)$ is not along the normal-mode u -direction, when the isoscalar-like instability starts to appear ($X = 0$), it cannot be a mechanical instability, so it corresponds to a chemical instability. On the contrary, when the isoscalar-like instability becomes stronger, we will have mechanical instabilities and the chemical instability will in turn disappear. However the nature of the unstable mode has not changed. So the distinction between mechanical and chemical instabilities is purely semantic. This was shown for the first time in ref.[20] for nuclear matter and confirmed in the case of finite nuclear systems in ref.[21].

It is also interesting to observe that when $(dP/d\rho)_{T,y}$ changes the sign, passing through zero, the quantity $\left(\frac{\partial\mu_p}{\partial y}\right)_{T,P}$ changes also the sign, but passing through infinity. In fact, from Eq.(3-14), one sees that the product $\left(\frac{\partial\mu_p}{\partial y}\right)_{T,P} \left(\frac{\partial P}{\partial\rho}\right)_{T,y} \propto XY$ is a finite negative number, since $X < 0$ and $Y > 0$.

The case of symmetric nuclear matter is easily recovered. In fact, as expected, now the isoscalar instability, ($X < 0, Y > 0$), appears as mechanical instability and the isovector instability, ($X > 0, Y < 0$), as chemical instability. Indeed we have $t = 1$, $a = b$, $\beta = \pi/4$ and so X and $\left(\frac{\partial P}{\partial\rho}\right)_{T,y}$ are proportional (see Eq.(3-15)) in this case.

A more quantitative analysis can be performed in the case of asymmetric nuclear matter considering that the quantities a and b remain positive. In this

way one can study the effect of the interaction between the two fluids, given by c , on the instabilities of the mixture. If $c < 0$, i.e. for an attractive interaction between the two components, from Eq.(3-10) one sees that the system is stable against isovector-like fluctuations but it becomes isoscalar unstable if $c < -2\sqrt{ab}$ (see Eq.(3-9)). However thermodynamically this instability against isoscalar-like fluctuations will show up as a chemical instability if $(-ta - b/t) < c < -2\sqrt{ab}$ or as a mechanical instability if $c < (-ta - b/t) < -2\sqrt{ab}$ (see Eq.(3-15)). So the distinction between the two kinds of instability (mechanical and chemical) is not really relevant since the nature of density fluctuations is essentially the same, i.e. isoscalar-like. If $c > 0$, i.e. when the interaction between the components is repulsive, the thermodynamical state is always stable against isoscalar-like fluctuation, but can be isovector unstable if $c > 2\sqrt{ab}$. Since the system is mechanically stable ($a, b, c > 0$, see Eq. (3-15)), the isovector instability is now always associated with chemical instability. Such situation will lead to a component separation of the liquid mixture. Following this line a complete analysis of the instabilities of any binary system can be performed, in connection to signs, strengths and density dependence of the interactions.

3.1.2 Nuclear matter instabilities

We show now quantitative calculations for asymmetric nuclear matter which illustrate the previous general discussion on instabilities. Let us consider a potential energy density of Skyrme type, [50,51],

$$H_{pot}(\rho_n, \rho_p) = \frac{A}{2} \frac{(\rho_n + \rho_p)^2}{\rho_0} + \frac{B}{\alpha + 2} \frac{(\rho_n + \rho_p)^{\alpha+2}}{\rho_0^{\alpha+1}} + (C_1 - C_2 \left(\frac{\rho}{\rho_0}\right)^\alpha) \frac{(\rho_n - \rho_p)^2}{\rho_0} \quad (3-16)$$

where $\rho_0 = 0.16 \text{ fm}^{-3}$ is the nuclear saturation density. The values of the parameters $A = -356.8 \text{ MeV}$, $B = 303.9 \text{ MeV}$, $\alpha = 1/6$, $C_1 = 125 \text{ MeV}$, $C_2 = 93.5 \text{ MeV}$ are adjusted to reproduce the saturation properties of symmetric nuclear matter and the symmetry energy coefficient.

We focus on the low density region, where phase transitions of the liquid-gas type are expected to happen, in agreement with the experimental evidences of multifragmentation [74,75]. Since $a, b > 0$ and $c < 0$, we deal only with instability against isoscalar-like fluctuations, as for symmetric nuclear matter. In Fig.3-1 the circles represent the spinodal line corresponding to isoscalar-like instability, as defined above, for three values of the proton fraction. For asymmetric matter, $y < 0.5$, under this border one encounters either chemical instability, in the region between the two lines, or mechanical instability, under

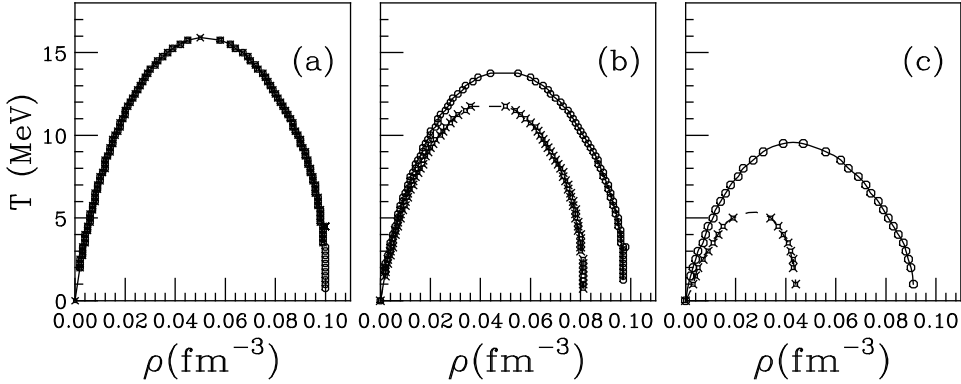


Fig. 3-1. Spinodal line corresponding to isoscalar-like instability of asymmetric nuclear matter (circles) and mechanical instability (crosses) for three proton fractions: $y = 0.5$ (a), $y = 0.25$ (b), $y = 0.1$ (c).

the inner line (crosses). The latter is defined by the set of values (ρ, T) for which $\left(\frac{\partial P}{\partial \rho}\right)_{T,y} = 0$. We observe that the line defining chemical instability is more robust against the variation of the proton fraction in comparison to that defining mechanical instability: reducing the proton fraction it becomes energetically less and less favoured to break in clusters with the same initial asymmetry.

However, we stress again the unique nature of the isoscalar-like instability. The change from the chemical to the mechanical character along this border line is not very meaningful and does not affect the properties of the system. Later we will show a quantitative realistic case of the clusterization of a dilute and heated asymmetric nuclear matter in a box, Subsect. 3.3. As seen before, in

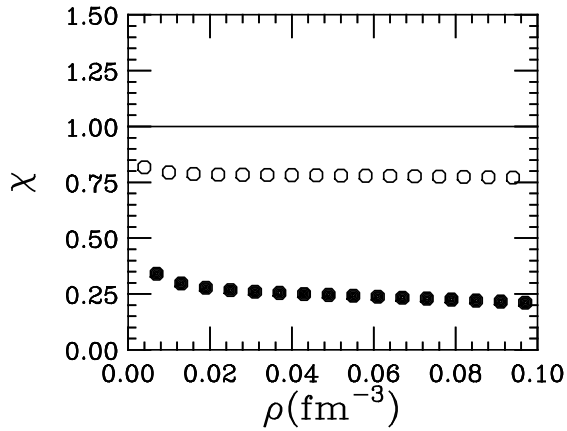


Fig. 3-2. Density dependence of the function χ , see text, for three proton fractions, $y = 0.5$ (solid), $y = 0.4$ (open circles), and $y = 0.1$ (full circles) at $T = 1 MeV$.

ANM isoscalar-like fluctuations are always associated with a chemical effect (change of concentration), which is responsible for the Isospin Distillation in

phase transitions [74]. Indeed the variation of the asymmetry ($I = 1 - 2y$) = $(\rho_n - \rho_p)/(\rho_n + \rho_p)$ is

$$\delta I = \delta \rho_p \left[\frac{(1 - I_0)}{(1 + I_0)} \operatorname{tg} \beta - 1 \right] \equiv \delta \rho_p [\chi - 1] \quad (3-17)$$

where I_0 is the initial asymmetry. The defined function $\chi(\rho)$ is reported in Fig.3-2 for different asymmetries. For $y = 0.5$, $\delta I = 0$, but for an initial proton fraction $y < 0.5$, one finds $\chi < 1$. Therefore $\delta I < 0$ if $\delta \rho_p > 0$, thus when the density increases (liquid phase), the asymmetry decreases.

The effect of the isospin distillation can be connected to the strength of the symmetry energy and, in particular, to the derivative of the symmetry energy coefficient with respect to ρ . This is easy to demonstrate if we adopt the simplest form for the symmetry energy: $E_{sym} = \frac{1}{2}C \frac{\rho}{\rho_0} I^2 = \frac{1}{2}C_{sym}(\rho)I^2$. According to Eq.(3-7), the ratio $\delta \rho_p / \delta \rho_n$, can be expressed as: $\delta \rho_p / \delta \rho_n = \operatorname{tg} \beta' = 1 / \operatorname{tg} \beta$, with $\operatorname{tg}(2\beta') = -\operatorname{tg}(2\beta) = -c/(a - b)$. The difference $(a - b)$ can be written as: $(a - b) = (N_p^{-1} - N_n^{-1}) + (N_p^{-1}F_0^{pp} - N_n^{-1}F_0^{nn})$. For the simple interaction considered, the second term of the sum vanishes and $(a - b)$ is equal to the difference of the inverse of proton and neutron single-particle level density, which is positive in n-rich matter. The quantity c is the derivative of the proton potential $U_p = \frac{\delta H}{\delta \rho_p}$ (see Eq.(3-2)) with respect to the neutron density. This is equal to the sum of a negative term coming from the isoscalar part of the considered effective interaction and a negative term $(-C/\rho_0)$, that comes from the symmetry energy. Hence the term $-c$ is positive and increases when C increases. In this case $\operatorname{tg} 2\beta'$ becomes larger and consequently $\delta \rho_p / \delta \rho_n$ increases leading to a larger distillation effect. One can easily notice that C/ρ_0 coincides with the derivative of C_{sym} with respect to ρ , hence the distillation effect is related to the derivative of the symmetry energy coefficient.

Within this simple model even the effect of the Coulomb repulsion on the distillation effect can be easily understood. Taking into account the Coulomb interaction, the term $(N_p^{-1}F_0^{pp} - N_n^{-1}F_0^{nn})$ does not vanish anymore, but it is equal to the derivative of the Coulomb potential with respect to the proton density, that is a positive term. Hence the difference $(a - b)$ increases and consequently the distillation effect decreases when including the Coulomb interaction, as intuitively expected.

Investigations on instabilities in nuclear matter can be extended also to the high density region. Fig.3-3 shows the density dependence of the generalized Landau parameters Eqs.(3-9), (3-10). For the interaction considered here the system exhibits another instability at high density, around 1.5 fm^{-3} (far away from the validity of this NM model), where the quantity c is positive and $1 + F_{0g}^a < 0$ (or $Y < 0$). From Eq.(3-14) one finds that this is again a chemical instability. However now it results from isovector-like fluctuations, in contrast

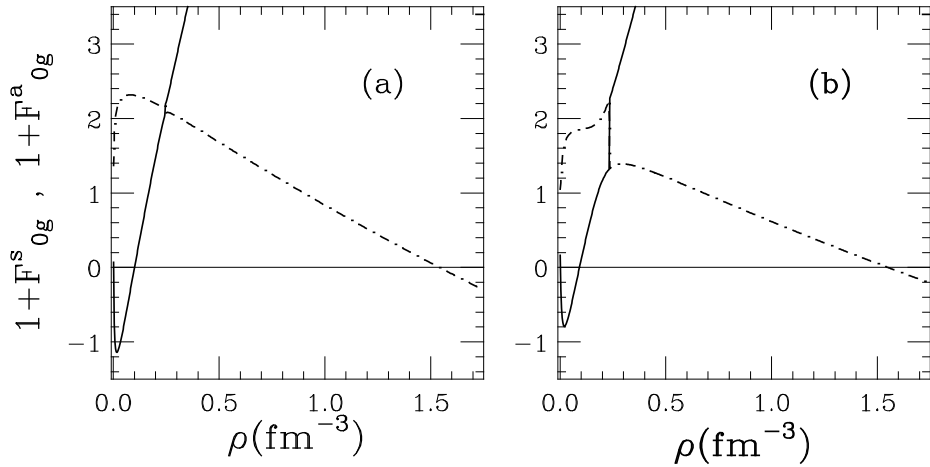


Fig. 3-3. Density dependence of the generalized Landau parameters for two proton fractions, $y = 0.4$ (a) and $y = 0.1$ (b) (symmetric, solid, and antisymmetric, dashed) at $T = 1 MeV$.

to the low density instability. The reason is the change in the character of the interaction between the two components. Since the interaction becomes repulsive the nuclear phase can become unstable against proton-neutron separation. We also notice in Fig.3-3 that the generalized Landau parameters display a discontinuity where the quantity c changes the sign. Other effective forces, with more repulsive symmetry terms, will not show this high density chemical instability [50], that actually could be of interest for other many body systems.

3.2 Dynamical analysis

The dynamical behaviour of a two-fluid system can be described, at the semi-classical level, by considering two Vlasov equations, for neutrons and protons in the nuclear matter case [76,77,50,51], coupled through the self-consistent nuclear field :

$$\frac{\partial f_q(\mathbf{r}, \mathbf{p}, t)}{\partial t} + \frac{\mathbf{p}}{m} \frac{\partial f_q}{\partial \mathbf{r}} - \frac{\partial U_q(\mathbf{r}, t)}{\partial \mathbf{r}} \frac{\partial f_q}{\partial \mathbf{p}} = 0 , \quad q = n, p. \quad (3-18)$$

For simplicity effective mass corrections are neglected. In fact in the low density region, of interest for our analysis of spinodal instabilities, effective mass corrections should not be large.

$U_q(\mathbf{r}, t)$ is the self-consistent mean field potential in a Skyrme-like form [50,51] :

$$U_q = \frac{\delta H_{pot}}{\delta \rho_q} = A \left(\frac{\rho}{\rho_0} \right) + B \left(\frac{\rho}{\rho_0} \right)^{\alpha+1} + C \left(\frac{\rho_3}{\rho_0} \right) \tau_q + \frac{1}{2} \frac{dC(\rho)}{d\rho} \frac{\rho_3^2}{\rho_0} - D \Delta \rho + D_3 \tau_q \Delta \rho_3 , \quad (3-19)$$

where

$$H_{pot}(\rho_n, \rho_p) = \frac{A}{2} \frac{\rho^2}{\rho_0} + \frac{B}{\alpha+2} \frac{\rho^{\alpha+2}}{\rho_0^{\alpha+1}} + \frac{C(\rho)}{2} \frac{\rho_3^2}{\rho_0} + \frac{D}{2} (\nabla \rho)^2 - \frac{D_3}{2} (\nabla \rho_3)^2 \quad (3-20)$$

is the potential energy density (see Eq.3-16), where also surface terms are included; $\rho = \rho_n + \rho_p$ and $\rho_3 = \rho_n - \rho_p$ are respectively the total (isoscalar) and the relative (isovector) density; $\tau_q = +1$ ($q = n$), -1 ($q = p$).

The value of the parameter $D = 130$ MeV·fm⁵ is adjusted to reproduce the surface energy coefficient in the Bethe-Weizsäcker mass formula $a_{surf} = 18.6$ MeV. The value $D_3 = 40$ MeV·fm⁵ $\sim D/3$ is chosen according to Ref. [78], and is also close to the value $D_3 = 34$ MeV·fm⁵ given by the SKM* interaction [3].

Let us now discuss the linear response analysis to the Vlasov Eqs. (3-18), corresponding to a semiclassical *RPA* approach. For a small amplitude perturbation of the distribution functions $f_q(\mathbf{r}, \mathbf{p}, t)$, periodic in time, $\delta f_q(\mathbf{r}, \mathbf{p}, t) \sim \exp(-i\omega t)$, Eqs. (3-18) can be linearized leading to the following form:

$$-i\omega \delta f_q + \frac{\mathbf{p}}{m} \frac{\partial \delta f_q}{\partial \mathbf{r}} - \frac{\partial U_q^{(0)}}{\partial \mathbf{r}} \frac{\partial \delta f_q}{\partial \mathbf{p}} - \frac{\partial \delta U_q}{\partial \mathbf{r}} \frac{\partial f_q^{(0)}}{\partial \mathbf{p}} = 0 , \quad (3-21)$$

where the superscript (0) labels stationary values and δU_q is the dynamical component of the mean field potential. The unperturbed distribution function $f_q^{(0)}$ is a Fermi distribution at finite temperature :

$$f_q^{(0)}(\epsilon_p^q) = \frac{1}{\exp(\epsilon_p^q - \mu_q)/T + 1} . \quad (3-22)$$

Since we are dealing with nuclear matter, $\nabla_r U_q^{(0)} = 0$ in Eq. (3-21) and $\delta f_q \propto \exp(-i\omega t + i\mathbf{kr})$. Following the standard Landau procedure [72,50], one can derive from Eqs. (3-21) the following system of two equations for neutron and proton density perturbations :

$$[1 + F_0^{nn} \chi_n] \delta \rho_n + [F_0^{np} \chi_n] \delta \rho_p = 0 , \quad (3-23)$$

$$[F_0^{pn} \chi_p] \delta \rho_n + [1 + F_0^{pp} \chi_p] \delta \rho_p = 0 , \quad (3-24)$$

where:

$$\chi_q(\omega, \mathbf{k}) = \frac{1}{N_q(T)} \int \frac{2 d\mathbf{p}}{(2\pi\hbar)^3} \frac{\mathbf{kv}}{\omega + i0 - \mathbf{kv}} \frac{\partial f_q^{(0)}}{\partial \epsilon_p^q}, \quad (3-25)$$

is the long-wavelength limit of the Lindhard function [72], $\mathbf{v} = \mathbf{p}/m$ and

$$F_0^{q_1 q_2}(k) = N_{q_1}(T) \frac{\delta U_{q_1}}{\delta \rho_{q_2}}, \quad q_1 = n, p, \quad q_2 = n, p \quad (3-26)$$

are the usual zero-order Landau parameters, as already introduced in Eq.(3-2), where now the k -dependence is due to the presence of space derivatives in the potentials (see Eq.(3-19)). For the particular choice of potentials given by Eq.(3-19), the Landau parameters are expressed as:

$$F_0^{q_1 q_2}(k) = N_{q_1}(T) \left[\frac{A}{\rho_0} + (\alpha + 1)B \frac{\rho_0^\alpha}{\rho_0^{\alpha+1}} + Dk^2 + \left(\frac{C}{\rho_0} - D'k^2 \right) \tau_{q_1} \tau_{q_2} + \frac{dC}{d\rho} \frac{\rho'}{\rho_0} (\tau_{q_1} + \tau_{q_2}) + \frac{d^2C}{d\rho^2} \frac{\rho'^2}{2\rho_0} \right]. \quad (3-27)$$

Multiplying the first equation by $N_n^{-1} \chi_p$ and the second one by $N_p^{-1} \chi_n$, we are led to define the following functions:

$$\begin{aligned} a(k, \omega) &= N_p^{-1} (1 + F_0^{pp} \chi_p) \chi_n; \quad b(k, \omega) = N_n^{-1} (1 + F_0^{nn} \chi_n) \chi_p; \\ c(k, \omega) &= (N_p^{-1} F_0^{pn} + N_n^{-1} F_0^{np}) \chi_n \chi_p = 2N_p^{-1} F_0^{pn} \chi_n \chi_p, \end{aligned} \quad (3-28)$$

in some analogy with Eqs.(3-5) and we obtain the following system of equations:

$$\begin{aligned} a\delta\rho_p + c/2 \delta\rho_n &= 0; \\ c/2 \delta\rho_p + b\delta\rho_n &= 0 \end{aligned} \quad (3-29)$$

The system can be diagonalized with eigenvalues λ_s and λ_i solutions of the equation:

$$(a - \lambda_{s,i})(b - \lambda_{s,i}) - c^2/4 = 0.$$

Formally we obtain for $\lambda_{s,i}$ the same expressions as given in Eqs.(3-9,3-10) for X and Y , but now a, b and c depend on ω . The unstable solutions for ω are obtained by solving the equations: $\lambda_s = 0$ (for isoscalar-like fluctuations), $\lambda_i = 0$ (for isovector-like fluctuations). This problem is completely equivalent to solve the equation: $c^2(\omega, k) = 4a(\omega, k)b(\omega, k)$, i.e. the dispersion relation

$$(1 + F_0^{nn} \chi_n)(1 + F_0^{pp} \chi_p) - F_0^{np} F_0^{pn} \chi_n \chi_p = 0, \quad (3-30)$$

that is also obtained directly by imposing the determinant of the system of Eqs.(3-23), (3-24) equal to zero.

The dispersion relation is quadratic in ω and one finds two independent solutions (isoscalar-like and isovector-like solutions): ω_s^2 and ω_i^2 . Then the structure of the eigenmodes can be determined and one finds:

$$\delta\rho_p/\delta\rho_n = -2b(\omega_s, k)/c(\omega_s, k),$$

for the isoscalar-like modes and

$$\delta\rho_p/\delta\rho_n = -2b(\omega_i, k)/c(\omega_i, k),$$

for isovector-like oscillations. However, it is important to notice that the corresponding angles $\beta_{s,i}$ are not equal to the angle β determined in the thermodynamical analysis, Eq.(3-7), because of the ω dependence in a, b and c . They only coincide with β when $\omega = 0$ (and thus $\chi_{n,p} = 1$), i.e. at the border of the unstable region.

3.2.1 Illustrative results for liquid-gas phase transitions

The dispersion relation, Eq.(3-30), have been solved for various choices of the initial density, temperature and asymmetry of nuclear matter. Fig.3-4 reports the growth rate $\Gamma = \text{Im } \omega(k)$ as a function of the wave vector k , for three situations inside the spinodal region. Results are shown for symmetric ($I = 0$) and asymmetric ($I = 0.5$) nuclear matter. The growth rate has a maximum $\Gamma_0 = 0.01 \div 0.03$ c/fm corresponding to a wave-vector value around $k_0 = 0.5 \div 1$ fm $^{-1}$ and becomes equal to zero at $k \simeq 1.5k_0$, due to k -dependence of the Landau parameters, as discussed above. One can see also that instabilities are reduced when increasing the temperature, an effect also present in the symmetric $N = Z$ case [79,80,23].

At larger initial asymmetry the development of the spinodal instabilities is slower, decrease of the maximum of the growth rate. One should expect also an increase of the size of the produced fragments, decrease of the wave number corresponding to the maximum growth rate. From the long dashed curves of Fig.3-4 we can predict the asymmetry effects to be more pronounced at higher temperature, when in fact the system is closer to the boundary of the spinodal region.

3.2.2 Coulomb effects on instabilities

The influence of Coulomb effects on the growth rates can be easily investigated within the formalism outlined above, as done in [81]. It suffices to add to the energy density, Eq.(3-20), the Coulomb energy density, that can be calculated

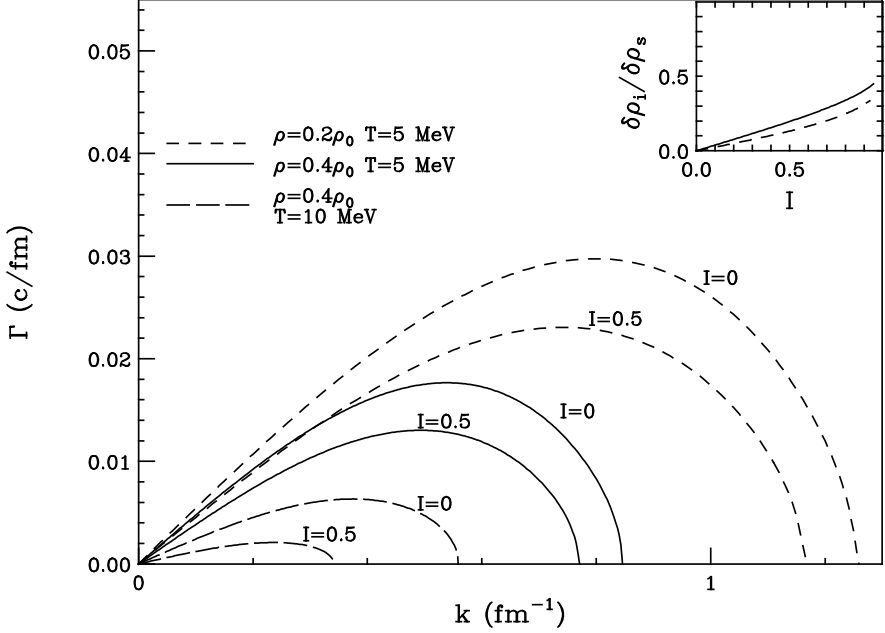


Fig. 3-4. Growth rates of instabilities as a function of the wave vector, as calculated from the dispersion relation Eq.(3-30), for three situations inside the spinodal region. Lines are labelled with the asymmetry value I . The insert shows the asymmetry of the perturbation $\delta\rho_i/\delta\rho_s$, as a function of the asymmetry I of the initially uniform system, for the most unstable mode, in the case $\rho = 0.4\rho_0$, $T = 5$ MeV.

in the Hartree-Fock approximation, with the Fock term evaluated in the local density approximation:

$$H^{(C)}(\mathbf{r}) = \frac{e^2}{2} \rho_p(\mathbf{r}) \int d\mathbf{r}' \frac{\rho_p(\mathbf{r}')}{|\mathbf{r} - \mathbf{r}'|} - \frac{3}{4} \left(\frac{3}{\pi}\right)^{\frac{1}{3}} e^2 \rho_p^{\frac{4}{3}}. \quad (3-31)$$

This only modifies the F_0^{pp} Landau parameter, implemented by adding the term:

$$\frac{4\pi e^2}{k^2} - \frac{1}{3} \left(\frac{3}{\pi}\right)^{\frac{1}{3}} e^2 \rho_p^{-\frac{2}{3}} \quad (3-32)$$

Fig.3-5 shows a comparison between the results obtained with and without the Coulomb interaction, for density $\rho = 0.4\rho_0$ and $T = 0$. The Coulomb force causes an overall decrease of growth rates. This decrease is almost independent of the asymmetry. Moreover, as discussed in [81], it depends only slightly on the temperature. It is also observed that, when the Coulomb force is included, the wave vector k must exceed a certain value k_{min} in order to observe instabilities. The two effects (the decrease of the growth rate and the appearance of k_{min}) are due to the competition between the Coulomb and the nuclear forces. In fact, the Coulomb forces push the protons towards regions of lower density, the nuclear forces instead push the neutrons in this direction

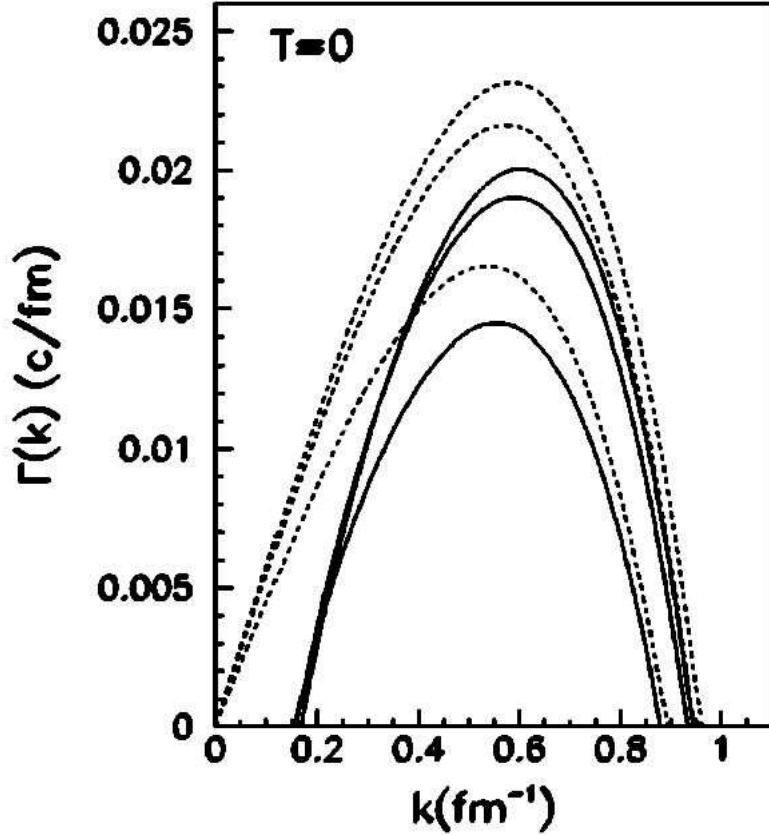


Fig. 3-5. Growth rates of the unstable modes for $T=0$, $\rho = 0.4 \rho_0$ and three different values of the asymmetry parameter I (from top to bottom $I = 0, 0.3, 0.6$). Results including the Coulomb interaction (full line) and without the Coulomb interaction (dashed) are shown. Taken from [81]

(neutron distillation).

3.2.3 Isospin distillation

A better understanding of liquid-gas phase transitions in a two-component system can be achieved by studying the chemical composition of the growing mode. This is shown in the insert of Fig.3-4, where the asymmetry of the perturbation $I_{pt} = (\delta\rho_n - \delta\rho_p)/(\delta\rho_n + \delta\rho_p) = \delta\rho_I/\delta\rho_S$, as obtained by solving the system of Eqs.(3-23), (3-24), is displayed as a function of the asymmetry of the initially uniform system $I = (\rho_n^{(0)} - \rho_p^{(0)})/(\rho_n^{(0)} + \rho_p^{(0)})$, for the dominant (most unstable) mode (for the case $\rho = 0.4 \rho_0$, $T = 5$ MeV). Without any chemical processes it should be $I_{pt} = I$. However one obtains $I_{pt} \leq 0.5 I$. This means that a growing mode produces more symmetric high-density regions (liquid phase) and less symmetric low-density regions (gas phase). Hence, during the fragmentation, a collective diffusion of protons from low-density regions to high-density regions takes place. This is the isospin fractionation (distillation)

effect already discussed in the context of liquid-gas phase transitions in two-component systems. This is essentially due to the increasing behaviour of the symmetry energy per nucleon with density, in the density region considered here. The distillation effect is represented in Fig.3-6, where the ratio $\delta\rho_n/\delta\rho_p$, as obtained by solving the dispersion relation, is displayed (direction and magnitude of the arrows) for some points of the (ρ_p, ρ_n) plane inside the spinodal region. One observes that the distillation effect is more pronounced at large asymmetry (i.e. smaller proton fraction y).

We recall that the *Isospin Distillation* has been revealed even in n-rich finite nuclei, performing quantal *RPA* calculations [21] (see also [23] for a thorough discussion on instabilities in finite systems).

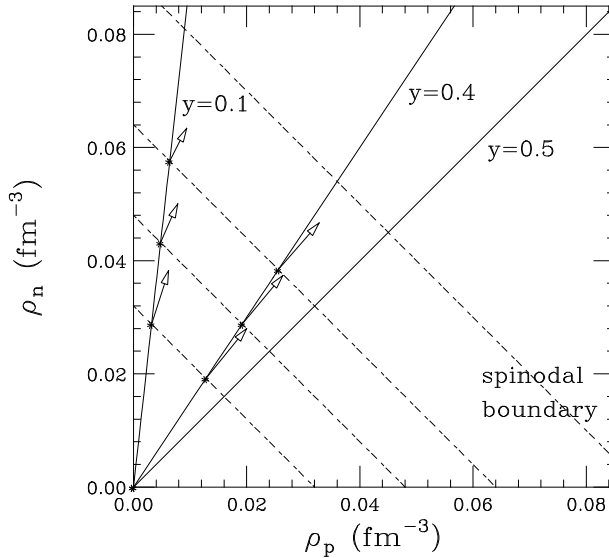


Fig. 3-6. Direction of $\delta\rho_n/\delta\rho_p$ in several points of the (ρ_p, ρ_n) plane.

As discussed before, the size of the effect is related to the stiffness of the symmetry energy, as illustrated in Table 5, where the ratio $\delta\rho_n/\delta\rho_p$, as obtained using a stiff or a soft (in brackets) parameterization of the symmetry energy, is reported. As expected, the neutron distillation effect (reduction of the asymmetry in the formed clusters) is systematically larger at lower densities in the asy-soft case while the opposite is seen already at $\rho = 0.4\rho_0$. This is nice evidence of the dependence on the *slope* of the symmetry term in the low density region (see Fig.1, Sect.1).

ρ/ρ_0	$I = 0.2$ ($N/Z = 1.5$)	$I = 0.8$ ($N/Z = 9.0$)
0.2	1.23 (1.2)	3.15 (2.61)
0.3	1.19 (1.186)	2.44 (2.4)
0.4	1.15 (1.18)	1.99 (2.32)

Table 5

Isospin content of the clusters, density variations $\delta\rho_n/\delta\rho_p$, formed in dilute matter at different initial densities for two initial asymmetries, $N/Z = 1.5$ and 9.0 . The values in brackets are obtained with a softer symmetry term (asy-soft *EOS*)

3.3 Simulation results: heated nuclear matter in a box

The previous analytical study is restricted to the onset of Fragmentation, and related Isospin Distillation, in Nuclear Matter, in a linearized approach. Numerical calculations have been performed in order to study all stages of the fragment formation process [51,85]. We report on the results of ref.[51] where the same effective Skyrme interactions have been used.

In the numerical approach the dynamical response of nuclear matter is studied in a cubic box of size L imposing periodic boundary conditions. The Landau-Vlasov dynamics is simulated following a phase-space test particle method, using gaussian wave packets [86,87,88]. The dynamics of nucleon-nucleon collisions is included by solving the Boltzmann-Nordheim collision integral using a Monte-Carlo method [87]. The width of the gaussians is chosen in order to correctly reproduce the surface energy value in finite systems. In this way a cut-off appears in the short wavelength unstable modes, preventing the formation of too small, unphysical, clusters [79]. The calculations are performed using 80 gaussians per nucleon and the number of nucleons inside the box is fixed in order to reach the initial uniform density value. An initial temperature is introduced by distributing the test particle momenta according to a Fermi distribution.

We have followed the space-time evolution of test-particles in a cubic box with side $L = 24\text{fm}$ for three values of the initial asymmetry $I = 0$, 0.25 and 0.5 , at initial density $\rho^{(0)} = 0.06\text{fm}^{-3} \simeq 0.4\rho_0$ and temperature $T = 5$ MeV. The initial density perturbation is created automatically due to the random choice of test-particle positions. Results for the initial asymmetries $I = 0$ and $I = 0.5$, are reported in Fig. 3-7, (a) and (b) respectively. The figure shows density distributions in the plane $z = 0$, which contains the center of the box, at three time steps $t = 0$, 100 and 200 fm/c, corresponding respectively to initial conditions, intermediate and final stages of the cluster formation. Clearly, a growth of the small initial density perturbations takes place, this time non-linear and hard particle collision effects are included.

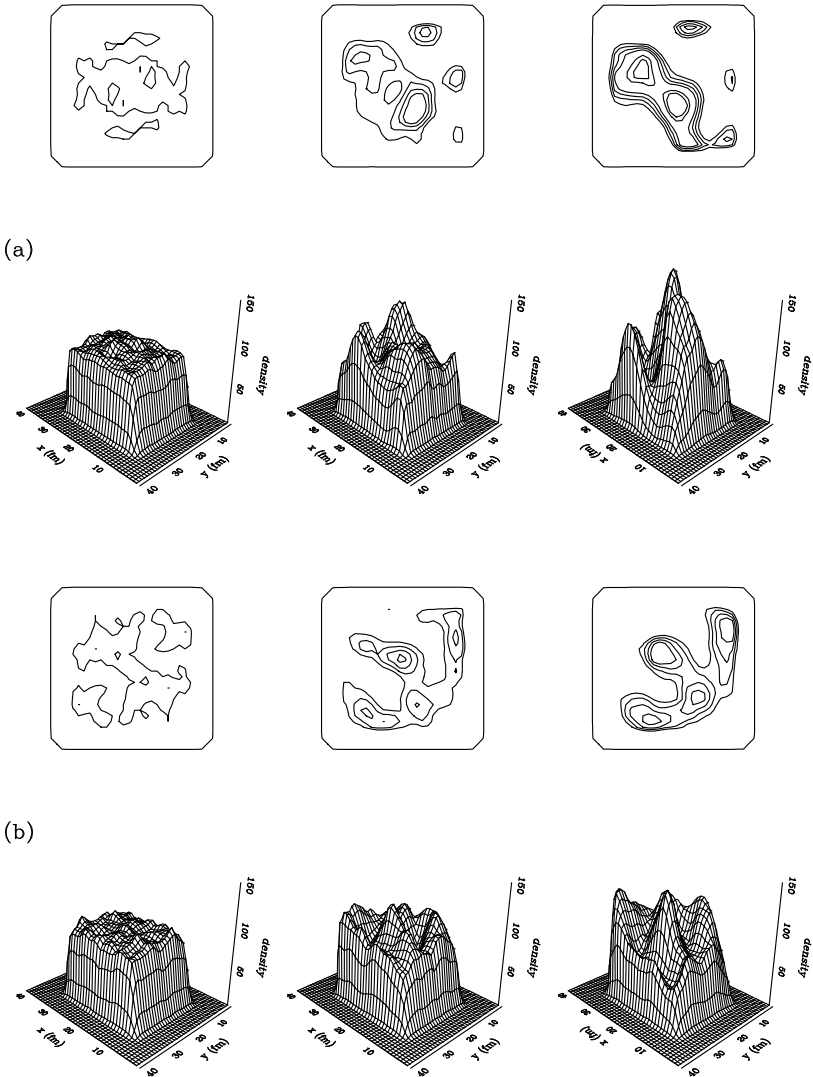


Fig. 3-7. Time evolution ($t = 0.0, 100.0$ and 200.0 fm/c) of the density $\rho(x, y)$ in the plane $z = 0$. Initial conditions: $\rho = 0.06\text{fm}^{-3}$, $T = 5\text{MeV}$ and asymmetries $I = 0.0$ (a); $I = 0.5$ (b). Upper panels: contour plots; Lower panels: corresponding two-dimensional surfaces. Densities in fm^{-3} .

We can compare the dynamical evolution with the analytical predictions of the previous sections. To do this, two variables are constructed: the total density variance (see [82])

$$\sigma = <(\rho - \rho^{(0)})^2>_{all} \quad (3-33)$$

and the correlation function between proton and neutron density perturba-

tions, normalized to the neutron density variance,

$$R_{pn} = \frac{\langle (\rho_p - \rho_p^{(0)})(\rho_n - \rho_n^{(0)}) \rangle_{all}}{\langle (\rho_n - \rho_n^{(0)})^2 \rangle_n}. \quad (3-34)$$

In Eqs. (3-33),(3-34) $\langle \dots \rangle_{all}$ denotes the average over all test particles, while $\langle \dots \rangle_n$ denotes the average over neutrons only. The densities ρ , ρ_n and ρ_p are calculated in the position of the test particle considered by taking contributions from gaussians of all test particles. For a dominant plane-wave perturbation we have the limit:

$$\sigma \propto \exp(2\Gamma t), \quad R_{pn} = \frac{\delta \rho_p}{\delta \rho_n}. \quad (3-35)$$

Fig.3-8 shows the evolution of σ (a) and of the (test-particle) perturbation asymmetry $I_{pt} = (1 - R_{pn})/(1 + R_{pn})$ (b) for the same initial conditions discussed above, i.e. $T = 5 MeV$, $\rho^{(0)} = 0.4\rho_0$ and asymmetries $I = 0.0, 0.25, 0.5$. A general feature is the clear linear increase of $\ln(\sigma)$ in the time interval

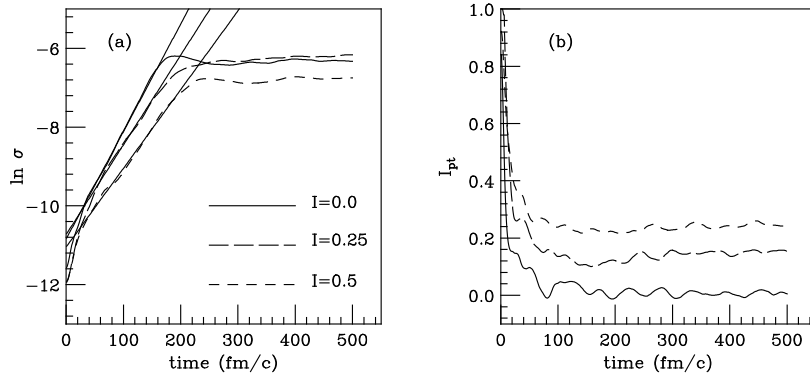


Fig. 3-8. Time evolution of the density variance (a) and of the perturbation asymmetry (b) (see text) for the box simulations at initial density $\rho = 0.06 fm^{-3}$, $T = 5 MeV$ and asymmetries $I = 0.0, 0.25, 0.5$. The straight lines in (a) show linear logarithmic fits in the initial stage of the cluster formation.

$50 < t < 150 fm/c$. During the first $50 fm/c$ the system is quickly "self-organizing", selecting the most unstable normal mode. Afterwards the variance (Eq. (3-33)) increases exponentially with a time scale given by $\Gamma = \text{Im } \omega(k)$, finally it saturates. In correspondence (see Fig.3-8b), the perturbation asymmetry I_{pt} reveals also a quick saturation at $t \sim 50 fm/c$. At times before $50 fm/c$ the proton and neutron density perturbations are not correlated

$(I_{pt}(t = 0) \simeq 1.0$ since nicely $R_{pn}(t = 0) \simeq 0.0$) , but at $t > 50$ fm/c the correlation of plane-wave type ($\delta\rho_p/\delta\rho_n = \text{const} > 0$) develops.

We notice that the time scales necessary to reach the asymmetry value characteristic of the most important growing modes, which are quite short in our calculations, generally depend on the structure of the initial noise put in the neutron and proton densities. In our calculations all modes are nearly equally excited. This causes the quick appearance of the features associated with the dominant mode. In agreement with analytical calculations, the instability grows slower in the case of larger asymmetry.

For an initial asymmetry $I = 0.5$, the extracted values of growth time $\Gamma \simeq 0.01$ c/fm and perturbation asymmetry $I_{pt} \simeq 0.24$ (see Fig.3-8), and of wavelength $\lambda \simeq 12$ fm (from the distance between the density distribution maxima in Fig.3-7b), are in good agreement with the analytical results presented before.

The Spinodal Decomposition Mechanism, *SD*, leads to a fast formation of the liquid (high density) and gaseous (low density) phases in the matter. Indeed this dynamical mechanism of clustering will roughly end when the variance (Eq. (3-33)) saturates [83], i.e. around 250 fm/c in the asymmetric cases (see Fig.3-8a). We also discuss the "chemistry" of the liquid phase formation. In

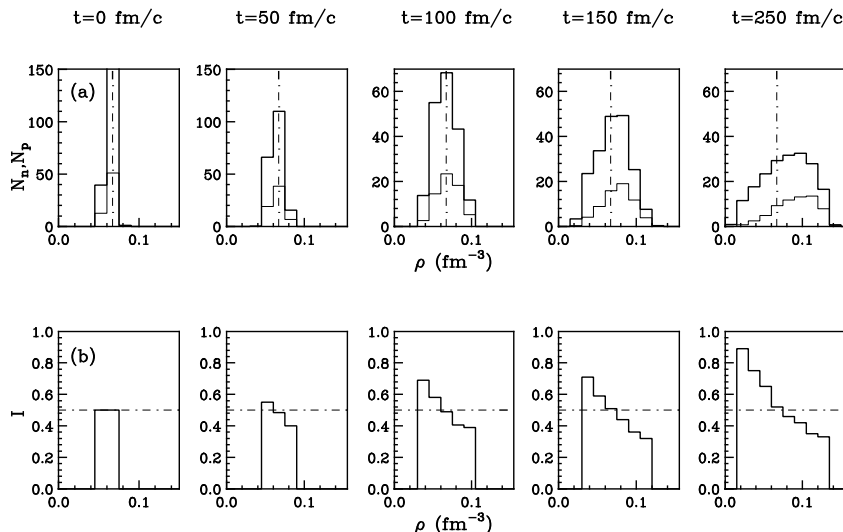


Fig. 3-9. Time evolution of neutron (thick lines) and proton (thin lines) abundances (a) and of asymmetry (b) in different density bins. The calculation refers to the case of $T = 5$ MeV, with initial average density $\rho = 0.06$ fm $^{-3}$ and asymmetry $I = 0.5$ (see the first panel of the (b) plots).

Fig.3-9 we report the time evolution of neutron (thick histogram in Fig. 3-9a) and proton (thin histogram in Fig.3-9a) abundances and of asymmetry (Fig.3-9b) in various density bins. The dashed lines respectively shows the initial uniform density value $\rho \simeq 0.4\rho_0$ (Fig.3-9a) and the initial asymmetry

$I = 0.5$ (Fig.3-9b). The drive to higher density regions is clearly different for neutrons and protons: at the end of the dynamical clustering mechanism we have very different asymmetries in the liquid and gas phases (see the panel at $250 fm/c$ in Fig.3-9b).

It was shown in Refs. [78,19,84], on the basis of thermodynamics, that the two phases should have different asymmetries, namely, $I_{gas} > I_{liquid}$, and actually a pure neutron gas was predicted at zero temperature if the initial global asymmetry is large enough ($I > 0.4$) [78]. Here we are studying this chemical effect in a non-equilibrium clustering process, on very short time scales, and we confirm the predictions of a linear response approach discussed before.

We can directly check the important result on the unique nature of the most unstable mode, independent of whether we start from a *mechanical* or from a *chemical* instability region. The isospin distillation dynamics presented in the Fig.3-9 refers to the initial conditions of $T = 5 MeV$, average density $\rho = 0.06 fm^{-3}$ and asymmetry $I = 0.5$, i.e. we start from a point well inside the *mechanical* instability region of the used *EOS*, see Fig.3-1(b). We can repeat the calculation at the same temperature and initial asymmetry, but starting from an initial average density $\rho = 0.09 fm^{-3}$, i.e. inside the *chemical* instability region of Fig.3-1(b). The results for the *Isospin Distillation Dynamics* are shown in the Fig.3-10. The trend is the same as in the previous Fig.3-9.

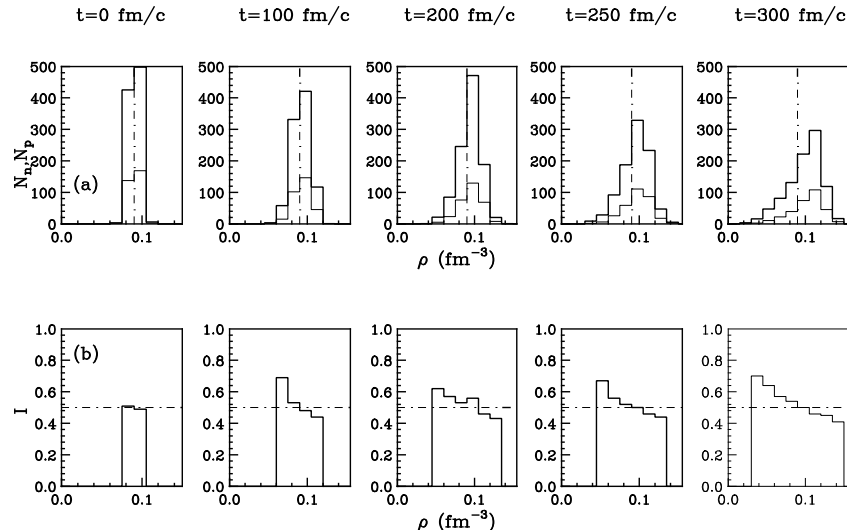


Fig. 3-10. Same calculation as in Fig.3-9 but with initial average density $\rho = 0.09 fm^{-3}$, inside the *chemical* instability region.

This nicely shows the uniqueness of the unstable modes in the spinodal instability region, as discussed in detail in the previous subsection. Such result is due to gross properties of the n/p interaction, thus it should be not dependent on the use of a particular effective force. This has been clearly shown recently in the linear response frame, [22], and in full transport simulations, [85].

As intuitively expected, and as confirmed by the *RPA* analysis (see [51]), the isospin distillation effect becomes more important when increasing the initial asymmetry of the system. At the same time, the instability growth rates become smaller for the more asymmetric systems, see Fig.3-4.

Moreover it is possible to observe a rather smooth and continuous transition from the trend observed at $\rho = 0.06 fm^{-3}$ (mechanical unstable region) to the trend observed at $\rho = 0.09 fm^{-3}$ (chemical unstable region), thus indicating that there is no qualitative change between the two kinds of instabilities. In fact they actually correspond to the same mechanism, the amplification of isoscalar-like fluctuations, with a significant chemical component (change of the concentration).

The conclusion is that the fast spinodal decomposition mechanism in neutron-rich matter will dynamically form more symmetric fragments surrounded by a less symmetric gas. Some recent experimental observations from fragmentation reactions with neutron rich nuclei at the Fermi energies seem to be in agreement with this result on the fragment isotopic content : nearly symmetric Intermediate Mass Fragments (*IMF*) have been detected in connection to very neutron-rich light ions [74], [75]. This will be extensively discussed in Sect.5.

4 Symmetry term effects on fast nucleon emission and collective flows

4.1 Pre-equilibrium dynamics

The early reaction dynamics is mainly governed by the pressure of the excited nuclear matter formed in the initial stage of the collision, [24,25,26]. We recall that a *stiff* symmetry energy gives a larger gradient of pressure than the *asy – soft* case, as shown in Sect.2, Eq.(8). This should result in an overall faster emission of particles. Moreover, the soft behaviour of the symmetry energy leads (at low density) to a larger repulsion of neutrons, with respect to the stiff case (see Fig.2-3 of Sect.2). Thus neutrons are expected to be emitted at earlier times, with respect to protons, in the *asy – soft* case. The isotopic content of the pre-equilibrium emission is also sensitive to the symmetry part of the *EOS*. For the same reasons explained above more neutrons are emitted in the soft case.

These ideas have lead to investigate the effect of the symmetry energy on the nucleon emission. Of course we do not have direct access to the particle emission time experimentally, but two-particle correlation functions, through final-state interactions and quantum statistics effects, have been shown to be a sensitive probe to the temporal and spatial distribution of emission sources during the reaction dynamics of heavy ion collisions at incident energies ranging from intermediate [89,90,91] to RHIC energy [92].

To discuss isospin effects on pre-equilibrium emission, we will review the results obtained by Chen et al., [93,94], using an isospin dependent transport code, *IBUU*. This is a one-body dynamics approach without fluctuating terms [149] but the results discussed here can be reliable since mainly due to the average nuclear dynamics.

We will consider a typical reaction with radioactive beams: $^{52}\text{Ca} + ^{48}\text{Ca}$ at $E = 80$ MeV/nucleon [95], central collisions. This study has been performed for two kinds of density dependence, labelled as “soft” and “stiff”, that correspond to $\gamma = 0.5$ and $\gamma = 2.0$ respectively, in the parametrization of the symmetry energy (total, kinetic + potential)

$$E_{\text{sym}}(\rho) = E_{\text{sym}}(\rho_0) \cdot u^\gamma.$$

It is important to note that, in this case, “soft” refers to a slope around normal density $L = 52$ MeV, which is close to the common value, while in the stiff case the slope is $L = 210$ MeV, which is much larger than what has been labelled as “super-stiff” ($L \simeq 100$ MeV) in the previous Sect.2.

4.1.1 Average emission times

For the two symmetry energy parametrizations we report in Fig. 4-1 (*soft*: squares, *stiff*: triangles) the average emission time of protons and neutrons as a function of their momenta. It is seen that the average emission time of nucleons with a given momentum is earlier for the stiff symmetry energy than for the soft one. This is expected because of the overall larger pressure gradient in the stiff case. We also notice that the relative emission sequence of neutrons and protons is, however, determined by the difference in their symmetry potentials. In other words if we average over neutron and proton the emission time is faster for the stiff case, but, on top of this there is a difference in the neutron-proton emission that is driven by the symmetry potential which is more attractive for protons causing an emission delay with respect to neutrons.

The neutron-proton difference is larger for the soft case because the isovector mean field at low densities, where most nucleons are emitted, is larger for the soft symmetry energy than for the stiff symmetry potential. In such a reasoning we have disregarded the effect of Coulomb interaction which reduces the delay of protons with respect to neutrons. For $^{52}\text{Ca} + ^{48}\text{Ca}$ the effect is quite small, but it grows with the size of the colliding system modifying the $p-n$ difference in the emission time, $|t_p - t_n|$. Therefore for heavier systems one can expect a reduction of the $|t_p - t_n|$ for the soft case and an increase of the difference for the stiff case, because the stronger Coulomb effect will shift down the proton average emission time. We will discuss the consequences on the correlation functions and the cluster formation in the corresponding subsections.

We notice the relation between larger momenta and earlier emission. For the reaction considered here, it is shown that most of the particles with momentum $P \geq 250$ MeV/c are emitted within $t \leq 70$ fm/c. This allows to connect the momenta of the emitted particles with the time evolution of the reaction, giving hints also about the average density at which particles are emitted. The crossing point between the neutron-proton emission time is connected to the crossing in the symmetry potential, including Coulomb, at density around $0.8\rho_0$. We can say, for example, that particles with momenta of the order of 300 MeV show features of the interaction already at density around and below the saturation one.

Using a coalescence model also the emission time of light clusters, such as d , t , ^3He has been studied [96]. The authors have found that light cluster production occurs mainly from the pre-equilibrium stage and has a shorter duration than nucleon emission. We notice that this is different from the cluster formation at lower energies, where the multifragmentation process is dominant, see the previous Sect.3. A stiffer symmetry energy causes an earlier emission of nucleons that reflects the earlier formation of clusters. The average emission

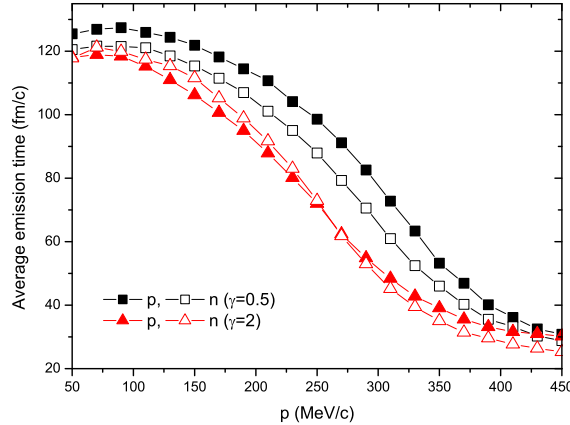


Fig. 4-1. Average emission times of protons and neutrons as functions of their momenta for different symmetry energies, for $^{52}\text{Ca} + ^{48}\text{Ca}$ at 80 MeV/nucleon $b=0$ fm, see text (from [94]).

time decreases with increasing kinetic energy as for the nucleons, moreover the heavier is the cluster and earlier it is formed. This has a simple explanation: the probability to coalesce decreases with the average density, moreover we can have a cluster break-up in the expansion phase. The dependence is stronger for clusters with more nucleons.

Therefore the study of cluster isobars has two advantages: they are easier to detect with respect to neutrons and they carry information from higher density. However the influence of the symmetry energy on the average emission time is reduced with respect to the nucleon one. This leads to a reduced sensitivity of observables like the correlation function of light clusters, see next subsections.

In summary a simple analysis of the average emission time nicely shows how the particle emission is regulated by the symmetry potential. However, as mentioned above, the particle emission time cannot be directly accessed by experiments, but the nucleon emission function can be extracted from two-particle correlation functions, see, e.g., Refs. [89,90,91,92] for reviews. In most studies, only the two-proton correlation function has been measured [97,98,99,100,24]. In particular, the correlation function of two nonidentical particles has been found to depend on their relative space-time distributions at freeze out and thus provides a useful tool for measuring the emission sequence, time delay, and separation between the emission sources for different particles [101,102,103,104,105,106]. Recently, data on two-neutron and neutron-proton correlation functions have also become available. The neutron-proton correlation function is especially useful as it is free of correlations due to wavefunction anti-symmetrization and Coulomb interactions. Indeed, Ghetti *et al.* have deduced from measured neutron-proton correlation function the time sequence of neutron and proton emissions [107,108].

4.2 Nucleon-nucleon correlation functions

In the standard Koonin-Pratt formalism [109,110,111], the two-particle correlation function is obtained by convoluting the emission function $g(\mathbf{p}, x)$, i.e., the probability for emitting a particle with momentum \mathbf{p} from the space-time point $x = (\mathbf{r}, t)$, with the relative wave function of the two particles, i.e.,

$$C(\mathbf{P}, \mathbf{q}) = \frac{\int d^4x_1 d^4x_2 g(\mathbf{P}/2, x_1) g(\mathbf{P}/2, x_2) |\phi(\mathbf{q}, \mathbf{r})|^2}{\int d^4x_1 g(\mathbf{P}/2, x_1) \int d^4x_2 g(\mathbf{P}/2, x_2)}. \quad (4-1)$$

In the above, $\mathbf{P}(= \mathbf{p}_1 + \mathbf{p}_2)$ and $\mathbf{q}(= \frac{1}{2}(\mathbf{p}_1 - \mathbf{p}_2))$ are, respectively, the total and relative momenta of the particle pair; and $\phi(\mathbf{q}, \mathbf{r})$ is the relative two-particle wave function with \mathbf{r} being the relative position, i.e., $\mathbf{r} = (\mathbf{r}_2 - \mathbf{r}_1) - \frac{1}{2}(\mathbf{v}_1 + \mathbf{v}_2)(t_2 - t_1)$. This approach has been very useful in studying effects of nuclear equation of state and nucleon-nucleon cross sections on the reaction dynamics of intermediate energy heavy-ion collisions [90]. The extension to the study of symmetry energy from a theoretical point of view is instead quite recent [93,94].

Shown in Fig. 4-2 are two-nucleon correlation functions gated on total momentum P of nucleon pairs from central collisions of $^{52}\text{Ca} + ^{48}\text{Ca}$ at $E = 80$ MeV/nucleon. The left and right panels are for $P < 300$ MeV/c and $P > 500$ MeV/c, respectively. Both neutron-neutron (upper panels) and neutron-proton (lower panels) correlation functions peak at $q \approx 0$ MeV/c. The proton-proton correlation function (middle panel) is, however, peaked at about $q = 20$ MeV/c due to the strong final-state s-wave attraction, but is suppressed at $q = 0$ as a result of Coulomb repulsion and anti-symmetrization of two-proton wave function. These general features are consistent with those observed in experimental data from heavy ion collisions [107].

Since emission times of low-momentum nucleons do not change much with the different $E_{\text{sym}}(\rho)$ used in IBUU model as shown in Fig. 4-1, two-nucleon correlation functions are not much affected by the stiffness of the symmetry energy. On the other hand, the emission times of high-momentum nucleons, which are dominated by those with momenta near 250 MeV/c, differ appreciably for the two symmetry energies considered here. Correlation functions of high-momentum nucleon pairs thus show an important dependence on nuclear symmetry energy. Gating on nucleon pairs with high total momentum allows one to select those nucleons that have short average spatial separations at emission and thus exhibit enhanced correlations. The strength of the correlation function is stronger for the stiff symmetry energy than for the soft symmetry energy: about 30% and 20% for neutron-proton pairs and neutron-neutron pairs at low relative momentum $q = 5$ MeV/c, respectively, and 20% for proton-proton pairs at $q = 20$ MeV/c.

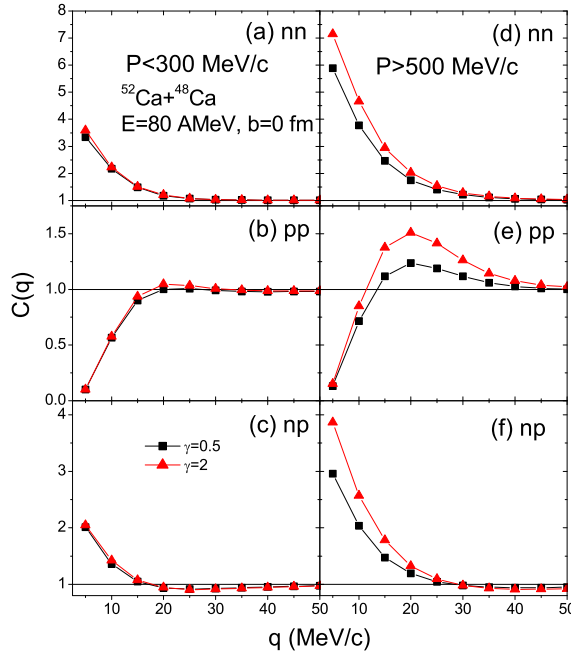


Fig. 4-2. Two-nucleon correlation functions gated on total momentum of nucleon pairs using the soft (filled squares) or stiff (filled triangles) symmetry energy. Left panels are for $P < 300$ MeV/c while right panels are for $P > 500$ MeV/c (from [93]).

The neutron-proton correlation function thus exhibits the highest sensitivity to variations of $E_{\text{sym}}(\rho)$, however one should heed that proton-proton correlation function is much easier to measure thanks to the proton charge and to the larger relative momentum at which the effect is expected. As shown in Fig. 4-1 and discussed earlier, the emission sequence of neutrons and protons is sensitive to $E_{\text{sym}}(\rho)$. With a stiff $E_{\text{sym}}(\rho)$, high momentum neutrons and protons are emitted almost simultaneously, and they are thus temporally strongly correlated, leading to a larger neutron-proton correlation function. At variance in the case of soft $E_{\text{sym}}(\rho)$ we have a delay in the proton emission, larger attractive field, which reduces the temporal correlation with neutrons.

Furthermore, both neutrons and protons are emitted earlier with stiff $E_{\text{sym}}(\rho)$, so they have smaller spatial separation. This demonstrates that correlation functions of nucleon pairs with high total momentum can indeed reveal sensitively the effect of nuclear symmetry energy on the temporal and spatial distributions of emitted nucleons. However, one must be aware that such an effect is delicate and can vanish as a function of impact parameter, beam energy, colliding system.

The impact parameter dependence has been studied again for the $^{52}\text{Ca} + ^{48}\text{Ca}$ at $E = 80$ MeV/nucleon. It is seen that the symmetry energy effect is stronger in central and semi-central collisions and becomes weaker in semi-peripheral

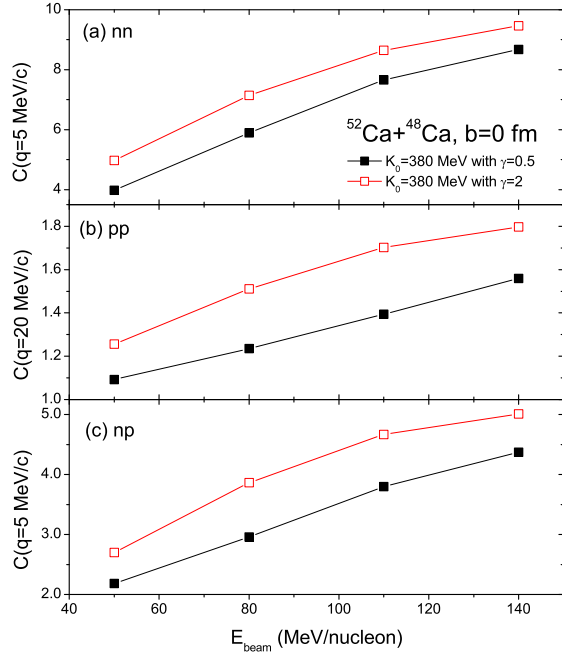


Fig. 4-3. Dependence of nucleon-nucleon correlation functions on the incident energy for high total momentum ($P > 500$ MeV) neutron-neutron (a) and neutron-proton (c) pairs with relative momentum $q = 5$ MeV/c and proton-proton (b) pairs with relative momentum $q = 20$ MeV/c by using $K_0 = 380$ MeV and free N - N cross sections with the soft (filled squares) or stiff (open circles) symmetry energy. (from [94]).

and peripheral collisions. This reflects the decrease in nuclear compression with the consequent change in the reaction mechanism.

The dependence of nucleon-nucleon correlation functions on the incident energy of heavy ion collisions is shown in Fig.4-3. It is seen that the values of nucleon-nucleon correlation functions increase with increasing incident energy. This is understandable since nuclear compression increases with increasing incident energy, and nucleons are also emitted earlier, leading to a smaller source size. The difference due to the symmetry energy does not change significantly with the incident energy at least in the range 50 – 150 MeV/nucleon.

A dependence on the mass of the colliding system has been already studied in Ref.[94] for central collisions. The authors have looked at $^{132}\text{Sn} + ^{124}\text{Sn}$ at $E = 80$ MeV/nucleon. It is seen that, even if the isospin asymmetry is similar to $^{52}\text{Ca} + ^{48}\text{Ca}$ system, the effect is reduced by about a factor two for pp and np , while nn is less affected. This can be understood with the increased Coulomb potential which is expected to reduce the difference in C_{pn} . Considering the emission times in $^{52}\text{Ca} + ^{48}\text{Ca}$ as a reference, for heavier systems the Coulomb potential increases the correlation for the soft case but decreases it for the stiff case, where for $^{52}\text{Ca} + ^{48}\text{Ca}$ neutrons and protons

have almost equal emission times.

In conclusion the symmetry term effect on nucleon nucleon correlation functions shows up only if particular conditions of impact parameter and colliding systems are matched. An experimental plan to pursue the investigation of such an observable needs a careful choice of the system and the possibility to have a good centrality selection. Furthermore it is important to choose the various colliding systems in such a way that the isospin asymmetry is as much different as possible while the total mass is unchanged [112,113]. Moreover this kind of comparative analysis is in general more reliable than the study of absolute values of correlation functions, which themselves are not perfectly reproduced by *BUU* simulations already for isospin symmetric systems, see ref.[24].

4.2.1 Isospin Momentum Dependence

During the preparation of this report, phenomenological potentials extracted from the Gogny effective interaction [114] or extensions of the Bertsch-Gale-Das Gupta (*BGBD*) [65,115] have been considered to improve *IBUU* and *BNV* transport codes, to include the effect of a momentum dependence in the isovector channel, namely a splitting of the effective masses of neutrons and protons, see the discussion in Sect.2. A detailed study of particle emission with a momentum dependent mean field was firstly done in [67,68], but without including isospin effects. Generally the momentum dependence causes a faster and richer pre-equilibrium emission. This reflects in an increasing of the two nucleon correlation function and of the yield of the clusters formed.

A first analysis of the effect of the momentum dependence on the particle emission has shown a weakening of the role of the symmetry energy leading to a weaker dependence of the correlation function on the symmetry energy [116]. In fact such a study has employed an effective interaction with a splitting of the effective masses as $m_n^*(\rho) > m_p^*(\rho)$, which leads to a reduction of the effective action of the symmetry energy at higher density. Indeed the difference of the neutron-proton potentials decreases with momentum [65,114], see Fig.2-8 of Sect.2. However, if a momentum dependence in the isovector channel corresponding to a splitting in the opposite direction is considered, $m_n^*(\rho) < m_p^*(\rho)$, a strong effect on the correlation function can be envisaged, as we will see in the results concerning collective flows discussed later in the Section.

Since this is a stimulating open problem, directly related to the E –slope of the Lane Potential of Sect.2, a systematic study of the beam energy dependence of the (n, p) correlation functions appears to be very promising. A related interesting observable would also be just the isotopic content of the free nucleon emissions and/or of light isobars, see following.

4.2.2 Light Clusters

Another observable of interest for the $E_{sym}(\rho)$ search is the yield and the energy spectrum of light clusters that differ in the isospin content. As mentioned above, the light clusters (isobars) offer the possibility of having particles with different isospin that are charged and therefore can be detected in a much simpler way with respect to neutrons. Moreover, as already discussed, their production time is shorter and they represent good probes of the higher density phase.

Isospin effects on cluster production and isotopic ratios in heavy ion collisions have been previously studied using either the lattice gas model [119] or a hybrid of *IBUU* and statistical multifragmentation model [120]. These studies are, however, at lower energies, where multifragmentation processes, as a result of possible liquid-gas phase transition, play an important role, see Sect.3.

Except deuterons, both tritons and 3He are only a small fraction of the total multiplicity in heavy ion collisions at beam energy around 100 AMeV. In this energy range the reaction dynamics can be described in terms of a relatively large compression followed by a faster expansion and vaporization. In such a case it is quite suitable to apply a coalescence model for determining the cluster production. However a simple coalescence model can only be applied if the role of correlations play a negligible role and the binding energy of the formed clusters can be discarded. The last issue is expected to affect more the absolute value of the yields and can be overtaken looking at the ratios of particle yields or spectra. In fact the $t/{}^3He$ ratio which is relevant for the isospin physics is expected to be independent on the binding energy effect, that is quite similar for the two clusters.

Within a coalescence model, using the freeze-out distributions obtained in *IBUU*, the behavior of d , t , 3He production has been studied again for the ${}^{52}\text{Ca} + {}^{48}\text{Ca}$ system in central collisions, ref.[116]. The feed-down from heavier fragments is not taken into account, however especially at large kinetic energies, its contribution is less relevant. It is found that the yield of light clusters is quite sensitive to the symmetry potential. As it can be inferred from the result on the particle emission the stiff symmetry energy leads to a larger yield of clusters, in particular the yield of 3He can be a factor two larger than in the soft case. The stiff symmetry energy induces a stronger pressure gradient causing an earlier emission of neutrons *and* protons. Furthermore in the stiff case neutrons and protons are more correlated in time, see Fig.4-1 and 4-2, enhancing the probability of 3He formation in phase space. If one looks at the $t/{}^3He$ ratio, the effect of the symmetry energy is reduced because both yields are modified so that the increase in the ratio is just about 15%.

In Ref.[117] the ratio of neutron to proton as a function of their kinetic energies

was found to be quite sensitive to the symmetry energy. This appears also in the light cluster production as recently found by Chen et al. [118,116]. In particular the $t/{}^3He$ ratio shows a quite different qualitative behaviour: while it increases with the kinetic energy for the soft symmetry energy, it decreases for the stiff one. This is due to the fact that, using a soft symmetry energy, a larger number of neutrons is emitted during the early stage of the collision, thus enhancing the production of tritons with high kinetic energy.

Since clusters are expected to be good probes of the high density region reached during the reaction dynamics all the previous features will be very sensitive to the Momentum Dependence (*MD*) of the effective forces in the isovector channel. For the same ${}^{52}\text{Ca} + {}^{48}\text{Ca}$ system in ref.[118] it has been shown that symmetry energy effects on the $t, {}^3He$ yields are largely reduced when a Gogny effective interaction is used. This is not surprising since the isospin-*MD* is in the $m_n^* > m_p^*$ direction, which implies a quenching of symmetry effects for high momentum nucleons. Of course an enhancement is expected in the case of an opposite effective nucleon mass splitting. Similar information can be obtained from the beam energy dependence of the yields.

4.3 Collective Flows

In the search for the EOS of the nuclear matter in various conditions of density and temperature a chief role is played by the study of the collective flow, which is a motion characterized by space-momentum correlation of dynamical origin.

The build up of sideward and elliptic flow is realized around the higher density stage of the reaction and thus it is a powerful tool for the search of the high density behaviour of the symmetry energy. It represents a mean of investigation very general, giving information on the dynamical response of excited nuclear matter in heavy-ion collisions, from the Fermi energies up to the ultrarelativistic ones, in the search for a phase transition to QGP, [121,122,123,26,124,125]. The collective motion can be characterized in several ways that pin down different kind of space-momentum correlation that can be generated by the dynamics. The kind of collective flows that have been suggested and employed to get information on the equation of state can be divided into three categories: radial, sideward and elliptic.

The sideward and elliptic flow have been and are currently useful tools for the study of the compressibility of symmetric nuclear matter. In the search for the density behaviour of the symmetry energy similar concepts can be exploited but highlighting the difference between neutrons and protons or light clusters with different isospin. We will define now the different types of collective flow and we will discuss the current status of the effects expected due

to different $E_{sym}(\rho)$, and related momentum dependence. We will see that first experimental results with stable beam already show hint of the effect of the symmetry energy. Thus future, more exclusive, experiments with radioactive beams should be able to set stringent constraints on the density dependence of the symmetry energy far from ground state nuclear matter.

4.3.1 Definitions

Sideward flow is a deflection of forwards and backwards moving particles, within the reaction plane [126]. It is formed because for the compressed and excited matter it is easier to get out on one side of the beam axis than on the other. The sideward flow is often represented in terms of the average in-plane component of the transverse momentum at a given rapidity $\langle p_x(y) \rangle$:

$$F(y) \equiv \frac{1}{N(y)} \sum_{i=1}^{N(y)} p_{x_i} \equiv \langle \frac{p_x}{A} \rangle \quad (4-2)$$

The particular case in which the slope of the transverse flow is vanishing in a region around midrapidity is referred as balance energy. It comes out from a balance between the attraction of the mean field and the repulsion of the two-body collisions.

For the isospin effect the sum over the particles in Eq.4-2 is separated into protons and neutrons. In Ref.[127] also the neutron-proton differential flow $F_{pn}(y)$ has been suggested as very useful probe of the isovector part of the *EOS* since it appears rather insensitive to the isoscalar potential and to the in medium nuclear cross section and, as we will discuss, it combines the isospin distillation effects with the direct dynamical flow effect. The definition of the differential flow $F_{pn}(y)$ is

$$F_{pn}(y) \equiv \frac{1}{N(y)} \sum_{i=1}^{N(y)} p_{x_i} \tau_i \quad (4-3)$$

where $N(y)$ is the total number of free nucleons at the rapidity y , p_{x_i} is the transverse momentum of particle i in the reaction plane, and τ_i is +1 and -1 for protons and neutrons, respectively.

The flow observables can be seen respectively as the first and second coefficients from the Fourier expansion of the azimuthal distribution [128]:

$$\frac{dN}{d\phi}(y, p_t) = 1 + V_1 \cos(\phi) + 2V_2 \cos(2\phi)$$

where $p_t = \sqrt{p_x^2 + p_y^2}$ is the transverse momentum and y the rapidity along beam direction.

The transverse flow can be also expressed as:

$$V_1(y, p_t) = \left\langle \frac{p_x}{p_t} \right\rangle$$

It provides information on the azimuthal anisotropy of the transverse nucleon emission and has been used to study the *EOS* and cross section sensitivity of the balance energy [127].

The second coefficient of the expansion defines the elliptic flow v_2 that can be expressed as

$$V_2(y, p_t) = \left\langle \frac{p_x^2 - p_y^2}{p_t^2} \right\rangle$$

It measures the competition between in-plane and out-of-plane emissions. The sign of V_2 indicates the azimuthal anisotropy of emission: particles can be preferentially emitted either in the reaction plane ($V_2 > 0$) or out-of-plane (*squeeze-out*, $V_2 < 0$) [128,129].

The p_t -dependence of V_2 , which has been recently investigated by various groups [124,129,130,131], is very sensitive to the high density behavior of the *EOS* since highly energetic particles ($p_t \geq 0.5$) originate from the initial compressed and out-of-equilibrium phase of the collision, see e.g. ref.[131]. Also at high energy it is allowing to get insight of the partonic stage and hadronization mechanism in ultrarelativistic heavy-ion collisions [125].

4.3.2 Collective Flows at the Fermi Energies

The isospin dependence of the transverse collective flow near the balance energy was first pointed out in Ref.[132], where it is shown that the reactions involving neutron-rich nuclei have a significant stronger attractive flow and consequently a higher balance energy. A discussion of the effect of a different density dependent symmetry energy started only some year later [113,46,25]. It was also stressed that the effects are expected to be more evident for semi-peripheral collisions (see also Fig. 4-5) around the balance energy. Clear signals of the mean field momentum dependence (*MD*) were also revealed ([113,133,129]). In the range of the Fermi energies it is indeed essential an appropriate treatment of the momentum dependence of the mean field [123].

Further studies that look at more n-rich systems investigating the effect of different density behaviour of the symmetry energy and based on a more exclusive analysis (like p_t dependence), have shown that isospin effects on collective flows can be found also at higher energies up to beam energies of

1 AGeV [134,135,65].

The search for the density dependence of $E_{sym}(\rho)$ has also to disentangle effects coming from the isospin dependence of the nucleon-nucleon cross sections [136,137]. In fact little has been done till now to address quantitatively this problem, the best strategy is of course to look for observables that mainly depend on the collision rate. A possibility is offered by the pre-equilibrium gamma radiation, as mentioned in Ref.[67]. Another possibility is the measurement of the radial flow for system with the same mass but different isospin asymmetry. Some observables have been found to be weakly sensitive to an overall change of the absolute value of the pp , nn , pp cross sections. We will pay particular attention at these features.

4.3.3 Isospin effects around the Balance Energy

In Ref.[113] the investigation of the isospin effect on transverse flows at Fermi energies has been carried out, including also a momentum dependence of the mean field. The main structure of this interaction has been already introduced in Sect.2. It is a $GBD - MD$ form in a Skyrme-like effective mean field, [66,138]. For a large dynamical range, in particular at the Fermi energies, it gives results quite similar to non-local forces of Gogny type [139], that well describe collective flows in symmetric systems with realistic compressibilities around $K \simeq 220\text{MeV}$, [138,140]. For the local part a general *Skyrme* form is used, with two choices for the symmetry term: i) *asysoft* with the $SIII-C(\rho)$ parametrization and ii) *asytiff* with the choice $C(\rho) = \text{const} = 32\text{MeV}$ (see Sect.2). In this calculation isospin effects on the momentum dependence are not included.

The microscopic transport *BNV* equations are solved following a test particle evolution on a lattice [113,67,141]. Isospin effects on nucleon cross sections and Pauli blocking are consistently evaluated. Medium effects on the NN cross sections are included following the prescriptions of ref.[136]. A dependence on σ_{NN} variations is also analysed.

We present (p, n) transverse flow results for the collisions $^{58}Fe + ^{58}Fe$ (n-rich) and $^{58}Ni + ^{58}Ni$ (n-poor) in the energy range $55 - 105\text{ AMeV}$ where nice data are available for $Z = 1, 2, 3$ flows [142,143,144] and some other calculations are existing for the proton flows [14,144]. Certainly the asymmetry $(N - Z)/A$ of ^{58}Fe is quite small, nonetheless isospin effects have been found both experimentally [142,143,144] and theoretically to be sizeable. In particular the comparison of *iso-transport* simulations with experimental results seem to show that a stiff behaviour of $E_{sym}(\rho)$ can give a good description of the difference in the proton transverse flows between $^{58}Fe + ^{58}Fe$ (n-rich) and $^{58}Ni + ^{58}Ni$.

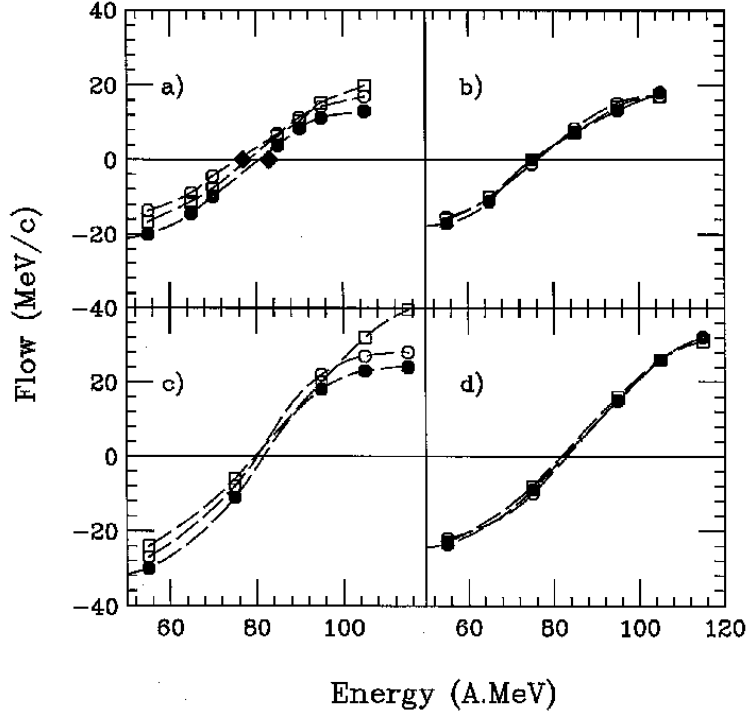


Fig. 4-4. Energy dependence of flows at $b_{red} = 0.45$ [145]: (full circles) $Fe - Fe$ protons; (open circles) $Ni - Ni$ protons; (squares) $Fe - Fe$ neutrons - (a) *asystiff*; (b) *asysoft*; (c),(d) same for $\sigma_{NN} = 2 fm^2$ no isospin dep. - The full diamonds in (a) represent the proton balance energy data of ref.[142] for the $Fe - Fe$ (right) and $Ni - Ni$ systems

In Figs.4-4, 4-5 we clearly see the isospin effects on the transverse flows, in particular the sensitivity to the density dependence of the symmetry term of the nuclear *EOS*: an *asystiff* behavior, more attractive for protons above normal density for the Fe asymmetric case, gives a clear shift in the balance energy as well as a larger (negative) flow at 55 A.MeV. i.e. below the balance. Both effects are in agreement with the data and are disappearing in the *asysoft* choice. Of course also the isospin and density dependence of the NN cross sections is important (see the (c) plots) but we note that a noticeable sensitivity to the isovector part of the *EOS* is still present. In particular we see that the isospin dependence of the mean field is able to keep the transverse flow difference between protons in $Fe - Fe$ and $Ni - Ni$. However a systematic study over different systems with more “exotic” isospin content is necessary to confirm this result.

An important effect predicted by the simulations is the clear difference between neutron and proton flows. Due to the difficulties in measuring neutrons this should be seen in a detailed study of light isobar flows. Moreover we like to recall that clusters are better probing the higher density regions. This point is quantitatively shown in the Fig.(4-6) where we present the transverse momentum vs. rapidity distributions for $^3He - Triton$ clusters in semicen-

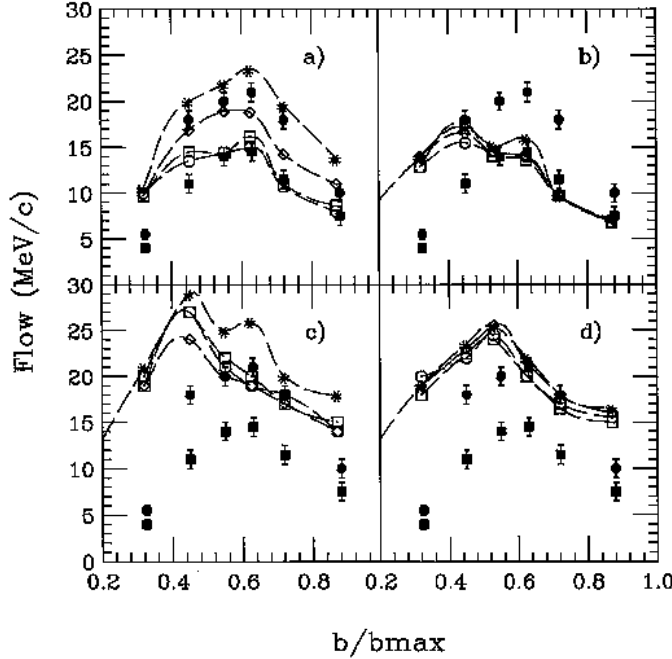


Fig. 4-5. Centrality dependence of flows at beam energy 55 AMeV: (stars) $Fe - Fe$ protons; (open circles) $Ni - Ni$ protons; (open diamonds) $Fe - Fe$ neutrons; (open squares) $Ni - Ni$ neutrons - (a) asystiff; (b) asysoft; (c),(d) same for $\sigma_{NN} = 2 fm^2$ no isospin dep. - Experimental points: (full circles) $Fe - Fe$ protons; (full squares) $Ni - Ni$ protons.

tral $Fe - Fe$ collisions at 55 AMeV, i.e. below the balance energy [113]. We can estimate a 20% larger (negative) flow for the 3He ions, just opposite to what expected from Coulomb effects. This appears to be a clear indication of the contribution of a much reduced (negative) neutron flow in the case of an *asystiff* force, i.e. a more repulsive symmetry term just above ρ_0 . The effect would disappear in an *asysoft* choice. Of course even for this observable the *Isospin-MD* will modify the symmetry energy dependence, as already noted before for the cluster yields.

4.3.4 Differential Flows

It has been suggested that in the study of symmetry energy by mean of the neutron and proton collective flow one can even exploit the difference in the so called isospin fractionation, i.e. the difference in the neutron-proton pre-equilibrium emission. In fact it has been pointed out that a soft/stiff symmetry energy leads to a different N/Z emission [112,46,55], see also previous section. This can be attributed to the density pressure gradient, which is quite different in the two cases.

We note that the gradient of the pressure should not be confused with the

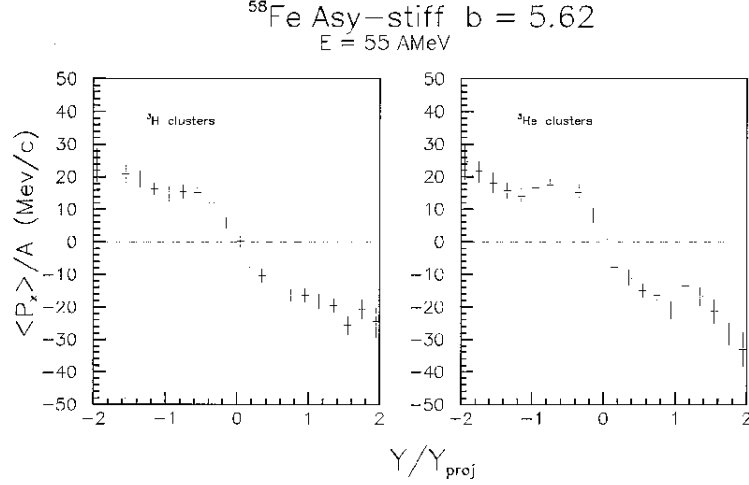


Fig. 4-6. Mean transverse momentum in the reaction plane vs. reduced rapidity for light ^3He – ^3H isobars in the Fe – Fe collisions at 55 AMeV beam energy (i.e. below the balance) for semicentral impact parameter, $b_{red} = 0.6$. Asystiff parametrization.

so called K_{sym} , see also the discussion in Sect.2. Therefore the interpretation given in [46] which relies entirely of the different K_{sym} , around saturation, for the two used parametrization (from –69 to +61 MeV) should be taken with caution. In fact between the soft and stiff symmetry energy there is, at the same time, a change in the slope L , from 54 to 95 MeV, that indeed gives a larger contribution to the pressure gradient, according to :

$$\frac{dP_{asy}}{d\rho} = \left(2\rho \frac{d(E/A)_{sym}}{d\rho} + \rho^2 \frac{d^2(E/A)_{sym}}{d\rho^2} \right) I^2 = \left(\frac{2}{3}L + \frac{1}{9}K_{sym} \right) I^2 \quad (4-4)$$

where $I \equiv (N - Z)/A$ is the asymmetry parameter.

Despite the possible interpretation, in order to make the analysis of collective flow more sensitive to the symmetry potential, the *neutron–proton* differential flow, defined in Eq.4-3, has been introduced [127]. In such a way one combines constructively the difference in the neutron-proton collective flow and the difference in the number of protons and neutrons emitted. At the same time the influences of the isoscalar potential and the in-medium nucleon-nucleon cross sections are also reduced. However the measurement of such a differential flow demands not only for the measurement of neutron collective flow but also for a precise assessment of their number, which most likely is impossible. On the other hand the idea to combine more than one isospin contribution in one observable is certainly important for elusive effects as those coming from the symmetry energy. Moreover the usual problems caused by the neutrons can be overtaken looking at clusters. For example one can use the definition of differential collective flow and apply it to the ^3H – ^3He isospin doublet, see previous subsection.

4.4 Effective Mass Splitting and Collective Flows

The problem of momentum dependence in the isospin channel is still open. Intermediate energies are important in order to have high momentum particles and to test regions of high baryon (isoscalar) and isospin (isovector) density during the reactions dynamics. Now we present some qualitative features of the dynamics in heavy ion collisions related to the splitting of nucleon effective masses.

We report here on expected effects of the isospin MD , studied by means of the Boltzmann-Nordheim-Vlasov BNV transport code, Ref. [67], implemented with a $BGBD$ –*like* mean field with a different (n, p) momentum dependence, as already introduced in Sect.2, see ref.[65]. Free (isospin dependent) isotropic cross sections are used in the collision term. In order to enhance the role of the energy dependence of the mean field we focus on semi-peripheral $Au + Au$ collisions at the energy of 250 AMeV and on transverse and elliptic flows of neutrons and protons in high rapidity regions, see [146].

4.4.1 Tranverse flows

The evaluation of the balance energy for the proton more inclusive *Directed Flow*, integrated over all transverse momenta, in $Au + Au$ collisions represents a very good test for the used effective interactions at lower energies. The

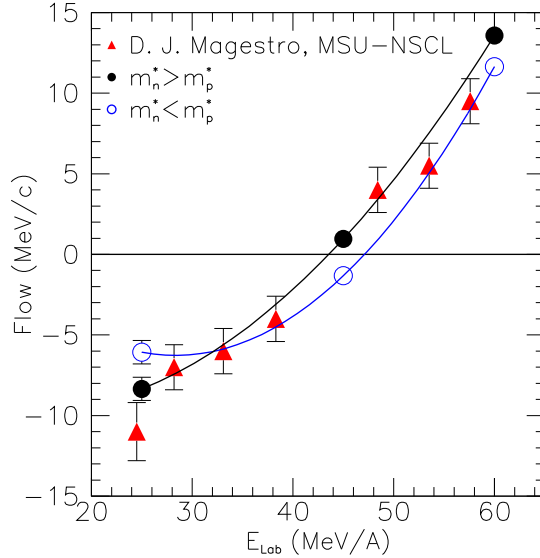


Fig. 4.7. Balance energy in $Au + Au$ collisions for intermediate impact parameters. Solid circles refer to the case $m_n^* > m_p^*$, empty circles to $m_n^* < m_p^*$. Triangles represent the data from ref.[147]

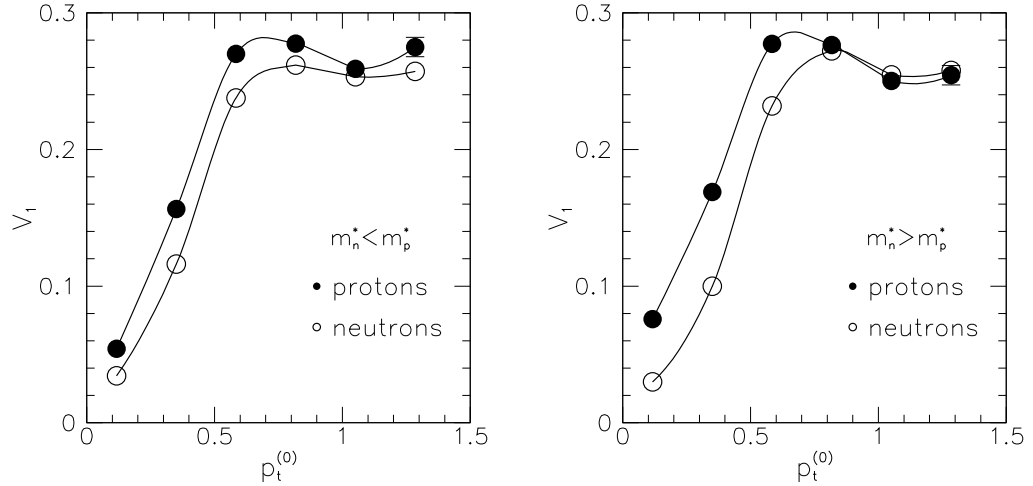


Fig. 4-8. Transverse flow of protons and neutrons for Au+Au reactions at 250 AMeV, $b/b_{max} = 0.5$, in the rapidity interval $0.7 \leq |y^{(0)}| \leq 0.9$.

results are shown in Fig. 4-7 and compared with NSCL-MSU data. The proton directed flows are calculated for semicentral collisions, i.e. $b_{red} = 0.5$ [145].

Both parametrizations are well reproducing the experimental balance energy region. As expected we see a slightly earlier balance of the flow in the $m_n^* > m_p^*$ case due to some more repulsion for fast protons but the effect is hardly appreciable at these energies, see also the previous subsection. We will now look more carefully at the mass-splitting effects with increasing beam energy and for more exclusive observables.

n/p transverse flow results for semicentral $^{197}Au + ^{197}Au$ collisions at 250 AMeV beam energy, for particles in regions of relatively high rapidities are shown in Fig. 4-8 where the left and right panels illustrate the two $m_n^* < m_p^*$ and $m_n^* > m_p^*$ cases. It is useful to work with momenta and rapidities normalized to projectile ones in the center of mass system (cm), defined as $y^{(0)} \equiv (y/y_{proj})_{cm}$ and $p_t^{(0)} \equiv (p_t/p_{proj})_{cm}$.

High rapidity selections allow us to find effects of the mean field MD , which become more important with increasing momenta. Indeed the different behaviour of mean field depending on mass splitting is evident all over the range of transverse momentum shown here. We emphasize that the average momentum of these particles is generally beyond the Fermi momentum. Indeed a rough estimate in the center of mass system gives already for the beam parallel component

$$p_z \approx m_0 \cdot 0.8(y_{proj})_{cm} \simeq 260 - 280 \text{ MeV}/c$$

In this momentum region a smaller effective mass determines greater repulsive interaction. When $m_n^* < m_p^*$ neutrons feel greater repulsion than protons and their deflection in the reaction plane for $p_t^{(0)} \leq 0.6$ is close to protons, where

the Coulomb field is also acting. At variance in the case $m_n^* > m_p^*$ the proton flow is greatly enhanced if compared with neutrons.

We like to note that in both plots of Fig. 4-8 the proton flow is above the neutron one, particularly at low transverse momenta. This is a clear effect of the Coulomb repulsion. This is also responsible for the non-symmetric behavior of neutron and proton flows in the two cases of opposite mass splitting.

At high transverse momentum we must take into account the increase of the out-of-plane component, so in this case increased repulsion determines a greater reduction of transverse flow. It causes a crossing between proton and neutron flow in the case $m_n^* > m_p^*$. This behaviour is clearly seen if we look at the different slope of the curves in Fig. 4-8 (right panel) around $p_t^{(0)} \geq 0.6$.

A quite suitable way to observe such effective mass splitting effect on the transverse flows is to look directly at the difference between neutron and proton flows

$$V_1^{p-n}(y, p_t) \equiv V_1^p(y, p_t) - V_1^n(y, p_t)$$

shown in Fig.4-9.

The variation due to the mass splitting choice is quite evident in the whole p_t range of emitted nucleons. Since the statistics is much smaller at high p_t 's (large error bars in the evaluation) the effect should be mostly observed in the $p_t^{(0)} \leq 0.5$ range.

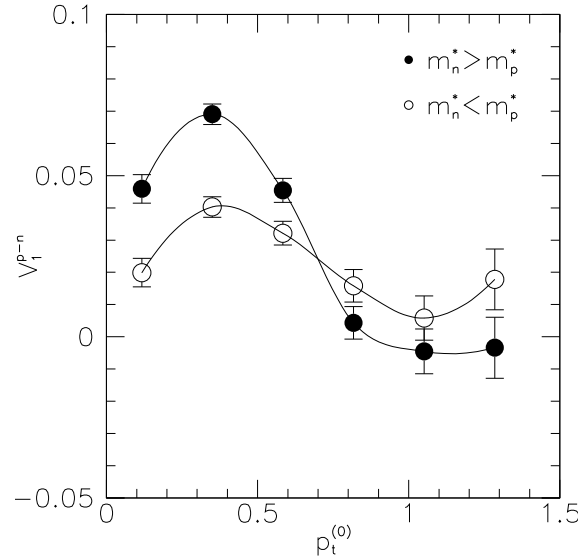


Fig. 4-9. p_t dependence of the difference between neutron and proton transverse flows in $Au + Au$ collisions, same energy, centrality and rapidity selection as in Fig.4-8. Solid circles refer to the case $m_n^* > m_p^*$, empty circles to $m_n^* < m_p^*$.

4.4.2 Elliptic flows

Also in this case a good check of our effective interaction choices is provided by some more inclusive data in the medium energy range. In Fig.4-10 we report a comparison with the *FOPI – GSI* data in the interesting beam energy region of the change of sign of the elliptic flow for protons, integrated over large transverse momentum contributions. The agreement is reasonable for both parametrizations. Also in this case we see a slightly larger overall repulsion (earlier zero-crossing) for the $m_n^* > m_p^*$ case.

Results on the p_t dependence of the neutron/proton elliptic flows in $Au + Au$ reactions at 250 AMeV are shown in Fig. 4-11. We can see that the p_y component rapidly grows at momenta $p_t^{(0)} > 0.6$, causing the flows to fall down towards negative values. At low momenta, emitted particles undergo a deflection in the reaction plane, more pronounced for nucleons with smaller effective mass. In fact, comparing the two panels of Fig.4-11 we see that around the maximum in-plane deflection $0.4 \lesssim p_t^{(0)} \lesssim 0.8$ neutron and proton flows are inverted. We also find different slopes for protons and neutrons around $p_t^{(0)} \geq 0.7$, depending on the relative sign of mass splitting, in agreement with the previous results in the transverse flows. Around $p_t^{(0)} \simeq 1$, i.e. projectile momentum in the *cm*, the elliptic flow finally takes negative values, with slight differences for the two parametrizations. Again the proton and neutron behaviors are not perfectly inverted in the two cases because of the proton Coulomb repulsion, in particular at low p_t . Also in this case the best observable

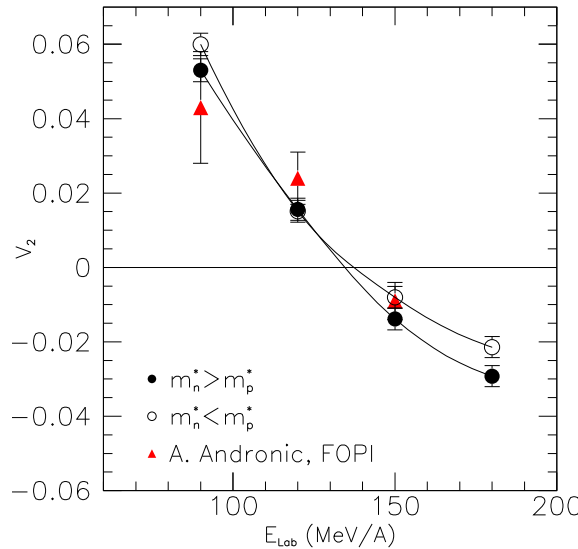


Fig. 4-10. Energy dependence of the elliptic flow in $Au + Au$ semicentral collisions at mid-rapidity, $|y^{(0)}| \leq 0.1$, integrated over the $p_t^{(0)} \geq 0.8$ range. *FOPI* data with similar selections, see ref. [148], are given by the full triangles. Solid circles refer to the case $m_n^* > m_p^*$, empty circles to $m_n^* < m_p^*$.

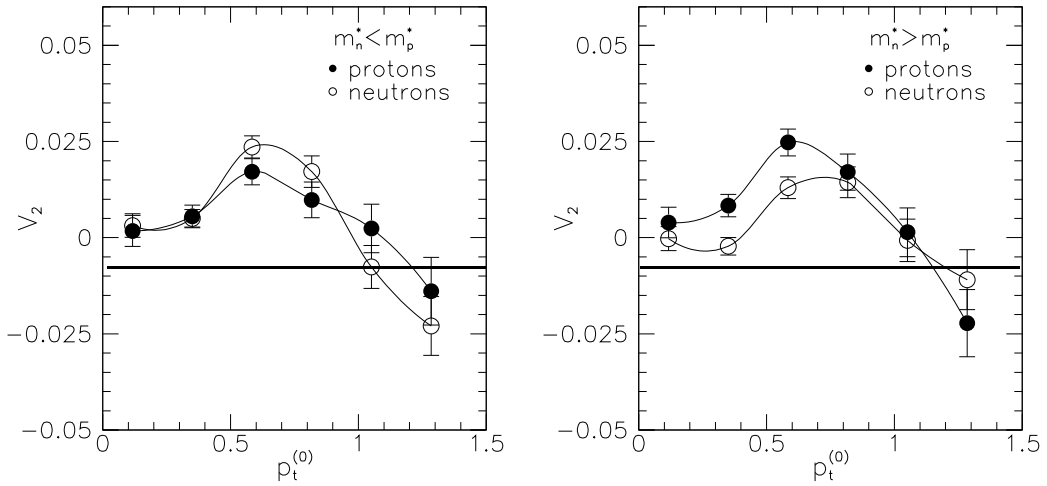


Fig. 4-11. Elliptic flow of protons and neutrons in Au+Au reaction at 250 AMeV, $b/b_{max} = 0.5$, in the rapidity interval $0.7 \leq |y^{(0)}| \leq 0.9$.

to look at is the p_t dependence of the difference between neutron and proton elliptic flows

$$V_2^{p-n}(y, p_t) \equiv V_2^p(y, p_t) - V_2^n(y, p_t)$$

shown in the Fig.4-12.

Again the difference is quite evident in the whole p_t range of emitted nucleons. We note that also here the statistics is much smaller at high p_t 's (large error bars in the evaluation). Anyway the mass splitting effect appears very clearly

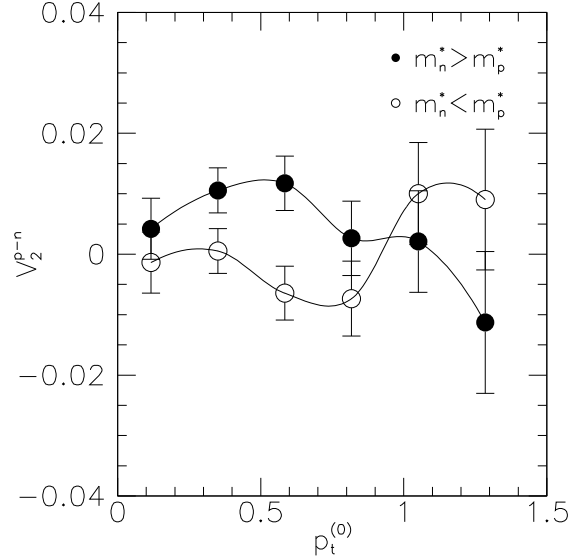


Fig. 4-12. p_t dependence of the difference between neutron and proton transverse flows in $Au + Au$ collisions, same energy, centrality and rapidity selection as in Fig.4-11. Solid circles refer to the case $m_n^* > m_p^*$, empty circles to $m_n^* < m_p^*$.

in the low $p_t^{(0)} \leq 0.5$ range where the results are more reliable.

As a general comment we stress the importance of more exclusive data, with a good p_t selection. Indeed from Figs. 4-8, 4-9 (for V_1) and Figs. 4-11, 4-12 (for V_2) we clearly see that more inclusive $V_1(y)$, $V_2(y)$ data, integrated over all p_t 's of the emitted nucleons at a given rapidity, will appear to be less sensitive to *isospin – MD* effects. As already discussed from general features of the mean field *MD* we expect a kind of compensation between low and high p_t contributions. As already remarked the Coulomb repulsion acting on protons in this heavy system tends to reduce the dynamical effects of nucleon mass splitting, in particular for low momentum particles. In spite of that the signals appear quite clear in the simulations. In any case this represents a further indication of the importance of momentum selections.

4.4.3 *Changing the stiffness of the symmetry term*

It is well known that the collective flows for asymmetric systems are sensitive to the density dependence of the symmetry term of the nuclear EOS, in particular at high transverse momentum [113,46,25]. For this reason it is important to be sure that signals previously discussed are mainly due to the n/p effective mass splitting and not strictly depending on the choice of the stiffness of the symmetry energy. In order to check this point we show some calculations using a symmetry energy with a density behaviour very different from the one used before, *but keeping the same n/p-effective mass splittings*. We refer to it as *asy-soft*, compared with the *asy-stiff* previously used. For details see ref.[65]. Our results show that while the nucleon flows are depending on the stiffness of the symmetry term, like in other calculations [113,46,25], the transverse momentum behavior of the differences keeps the same sensitivity to the effective mass splittings. Fig. 4-13 illustrates the n/p -flow differences as a function of transverse momentum for the same energy, impact parameter and high rapidity selections used before. Both transverse $V_1^{p-n}(y, p_t)$ and elliptic $V_2^{p-n}(y, p_t)$ flow differences show very small variations from the *asy – stiff* case (i.e. Figs. 4-9 and 4-12) over the whole $p_t^{(0)}$ range, in particular in the region $p_t^{(0)} \leq 0.5$, of interest for the better statistics. This result represents an important indication that we are selecting experimental observables that directly probe the isospin effects on the momentum dependent part of the nuclear *EOS*.

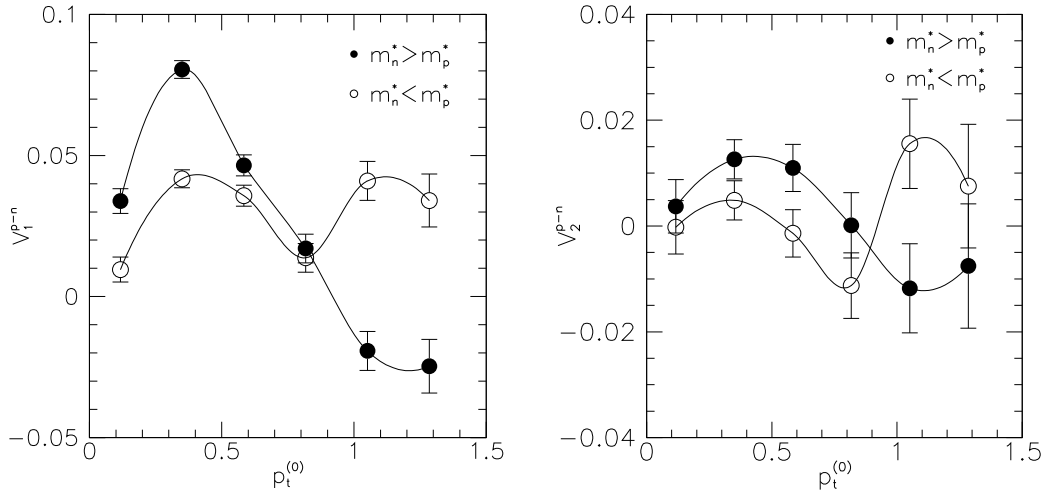


Fig. 4-13. p_t dependence of the difference between neutron and proton transverse (left panel) and elliptic flow (right panel) in $Au + Au$ collisions at $250 AMeV$, $b/b_{max} = 0.5$, in the rapidity interval $0.7 \leq |y^{(0)}| \leq 0.9$. Calculations are performed using the *asy - soft* symmetry energy. Solid circles refer to the case $m_n^* > m_p^*$, empty circles to $m_n^* < m_p^*$.

5 Isospin Dynamics at the Fermi energies

5.1 Stochastic BNV transport theory

We will show that Heavy Ion Collisions in the Fermi energy domain are rather sensitive to the different density/momentum dependences of the symmetry term in a quite transparent way. We present studies with stable and unstable ions in order to increase the asymmetry range of the nuclear systems.

Since dynamical instabilities are playing an essential role in the reaction dynamics at Fermi energies it is essential to employ a stochastic transport theory. An approach has been adopted based on microscopic transport equations of Boltzmann-Nordheim-Vlasov (*BNV*) type [86,149,150,151,141] where asymmetry effects are suitably accounted for [112,113] and the dynamics of fluctuations is included [52,154].

The transport equations, with Pauli blocking consistently evaluated, are integrated following a test particle evolution on a lattice [141,156,67]. A parametrization of free NN cross sections is used, with isospin, energy and angular dependence. The same symmetry term is utilized even in the initialization, i.e. in the ground state construction of two colliding nuclei.

We consistently include isospin effects in the treatment of the stochastic term of the transport equation. Indeed the evolution under the influence of fluctuations is described by a transport equation with a stochastic fluctuating term, the so-called Boltzmann-Langevin equation (*BLE*) [157,158,159,79,160]. We follow two methods to include the fluctuations effects. The Stochastic Mean Field (*SMF*) approach, [52,154,155], and a simplified procedure, computationally much easier [83,156,161,162], based on the introduction of density fluctuations by a random sampling of the phase space, (Phase Space Sampling, *PSS*). The amplitude of the noise is gauged to reproduce the dynamics of the most unstable modes [83].

The *SMF* method is based on a fully self-consistent dynamical treatment of the fluctuations during the time evolution. We notice that $\sigma^2 = <(f - \bar{f})^2>$, the variance around the mean trajectory of the system, given by the Boltzmann-Vlasov evolution in phase space $\bar{f}(\mathbf{r}, \mathbf{p}, t)$, in each phase space cell obeys the equation of motion [80,154]:

$$\frac{d}{dt}\sigma^2 = -\frac{2}{\tau(t)}\sigma^2 + 2 D(t). \quad (5-1)$$

with $2 D(t)$ the correlation function of the fluctuating term and the relaxation

time $\tau(t) = 1/(w^+ + w^-)$, where w^+ and w^- are the transition probabilities into and out of the cell. The statistical value $\sigma_0^2 = f_0(t_{eq})(1 - f_0(t_{eq}))$ at equilibrium suggests an ansatz for the correlation function of the fluctuation term of the form:

$$2D(t) = (1 - \bar{f})w^+ + \bar{f}w^- \quad (5-2)$$

i.e. the magnitude of the fluctuations is given by the total number of collisions (fluctuation-dissipation theorem) [159]. Then we obtain for the time evolution of the difference relative to local statistical fluctuations $\Delta \equiv \sigma^2 - \bar{f}(1 - \bar{f})$:

$$\frac{d}{dt}\Delta = -\frac{2}{\tau(t)}\Delta. \quad (5-3)$$

Since $\Delta = 0$ is a solution of Eq.(5-3), if the variance is initially locally set equal to its statistical value, it will always follow the evolution of the average distribution function according to the relation $\sigma^2 = \bar{f}(1 - \bar{f})$. Thus from our knowledge of the mean “trajectory” $\bar{f}(\mathbf{r}, \mathbf{p}, t)$, at any time step we can extract local statistical fluctuations in each phase space cell.

From a projection over coordinate space we derive local density variances which are implemented with a Montecarlo method at suitably chosen time intervals, see ref.[155]. In this way we can have also the trajectory branchings in regions of instability. The procedure is correct if we assume a *local* thermal equilibrium in each phase space cell. This is appropriate for the problems discussed here, namely fragment production in the expansion/separation phase, and it can be tested numerically.

For each system we have checked the equivalence of the *SMF* approach with the sampling *PSS* method in the description of the collision dynamics, from fast particle emissions to the fragment production. The analysis of the results, presented in the following, is based on events collected with both numerical procedures. We note that in this way the transport simulation will represent a kind of event generator. In general we have accumulated $400 - 500$ events for each physical case.

In order to simplify the analysis of the observables most sensitive to isospin effects we keep fixed the isoscalar part of the *EOS*, corresponding to a *soft* behavior of symmetric nuclear matter(*SNM*) with compressibility $K = 201\text{MeV}$. We will usually consider three choices for the density dependence of the symmetry term. From Fig.2-3 of Sect.2 these are *asy-soft* (dashed line), *asy-stiff* (solid line) and *asy-superstiff* (long-dashed line). In this way we try to disentangle dynamical symmetry term effects.

5.2 Main mechanisms of dissipative collisions: Fusion vs. Deep-Inelastic Competition

We start the analysis at relatively low energies. Moreover we will also consider medium-light unstable beams eventually available in this energy range from *SPIRAL/I – II* and other new Radioactive Ion Beam (*RIB*) facilities. Here we investigate isospin effects on the competition between binary events and heavy residue formation which occurs at intermediate impact parameter $b \simeq 0.4b_{max}$.

In Fig.5-1 we show plots, for two choices of the symmetry term, of the time-evolution of the density projection on the reaction plane for the mean trajectory (averaged over several events) in semicentral collisions ($b = 4fm$) of neutron rich ($^{46}Ar(N/Z = 1.56) + ^{64}Ni(N/Z = 1.29)$) and $N = Z$, neutron poor ($^{46}V + ^{64}Ge$) ions at $30AMeV$ [112].

The effect on the main reaction mechanism of the different density dependences of the symmetry term is quite evident in Figs.5-1(*a, b*). It can be understood in terms of the amount of repulsion present during the interaction of the two surfaces, i.e. in a region below normal density. For neutron rich colliding ions the asy-soft choice in general leads to a less repulsive dynamics since the symmetry field for protons is more attractive, see Fig.3 of Sect.2. We see a stronger interaction between the two partners, a larger dissipation of the relative energy, and thus the system will more likely enter a fusion path, Fig.5-1(*a*). Experimentally this means a larger incomplete fusion cross section at medium energies.

For neutron poor systems, Figs.5-1(*c, d*) we see just the opposite. Naively we would expect more repulsion since we have larger Coulomb and direct $n - p$ collision contributions. Actually in the asy-soft case we have now a dominant binary deep-inelastic mechanism, Fig.5-1(*c*). At variance, in the asy-stiff choice Fig.5-1(*d*) we get a clear fusion dominance. This result is amazing for two reasons: i) The dynamics of a symmetric $N = Z$ system appears to be isospin-dependent; ii) The stiffer symmetry term leads to a larger attraction. A way to understand this is that the two exotic neutron poor systems develop a “proton skin” which is overlapping in the interaction zone. The protons in the asy-stiff case see a stronger repulsive field and are more easily promptly emitted. As a consequence the two partners feel a smaller Coulomb repulsion and more likely fusion can be reached. Consistently a larger yield of fast proton emission is predicted with the asy-stiff parametrization [112]. We like to recall that some sensitivity to isospin effects in deep inelastic collisions was already shown in ref. [153] from Landau-Vlasov simulations of *Ca*-isotope collisions at $15AMeV$.

These results suggest that in low energy dissipative collisions an observable

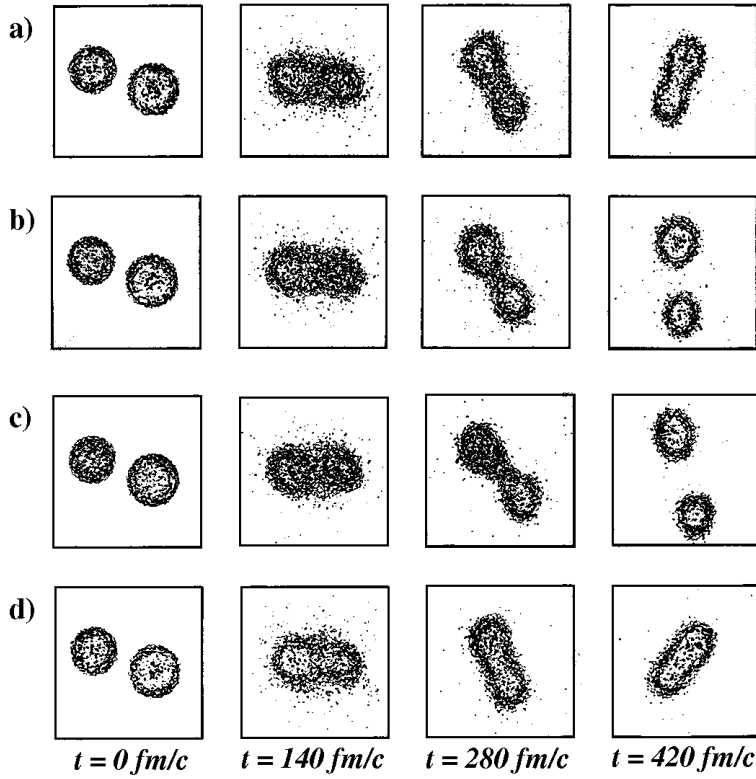


Fig. 5-1. Density plots at different times in a reaction between neutron-rich ions ($a, b : {}^{46}Ar + {}^{64}Ni$) and neutron-poor ions ($c, d : {}^{46}V + {}^{64}Ge$). (a, c): *asysoft* symmetry term; (b, d): *asystiff*. See text

sensitive to the stiffness of the symmetry term can be just the relative yield of incomplete fusion vs. deep-inelastic events. Moreover for n-rich systems in the asy-soft case we expect more interaction time available for charge equilibration. This means that even the binary events will show a sensitivity through a larger isospin diffusion. At variance, in the asy-stiff case the two final fragments will keep more memory of the initial conditions. This point will be further discussed later in the Section.

The dependence of the interaction time on the stiffness of the symmetry term will also influence the competition between binary and *neck – fragmentation* events [163,53], where Intermediate Mass Fragments (*IMF*, in the range $3 \leq Z \leq 10$) are formed in the overlapping region, roughly at mid-rapidity in semicentral reactions. This represents the new leading dissipative mechanism at the Fermi energies, as we will discuss in detail later on. Therefore the expected sensitivity to the isovector *EOS* appears very stimulating.

5.3 Isospin in Fragmentation Dynamics: Survey of experimental results

In the last decade the experimental interest on the isospin dynamics in heavy ions collisions at Fermi energies and *EOS* symmetry term effects on various reaction mechanisms has been steadily rising, largely stimulated by the perspective of the second generation radioactive beam facilities.

A large variety of systems and phenomena have been investigated. This clearly shows the richness of the field but also reveals some uncertainty in focussing on the most relevant physics questions. One of the aims of this report is just to contribute on that direction, even trying to select the most sensitive observables. In this respect we will first organize a discussion of the performed experiments, in a precise correspondence to theoretical analyses and suggestions presented in the following subsections.

5.3.1 Isospin equilibration and fragment production

The systems ^{40}Ca , ^{40}Ar , $^{40}Cl + ^{58}Fe$, ^{58}Ni have been among the first devoted to study the role of the isospin degree of freedom at Fermi energies [164]. Let us note that the Cl -projectile is a radioactive secondary beam. The total mass of composite system (CS) is the same in all cases allowing to explore the effects of the N/Z content on the *IMF* production. At $53AMeV$, the isotopic ratios of $^{11}B/^{10}B$, $^{8}Be/^{7}Be$, $^{7}Li/^{6}Li$, exhibit an increasing trend with the $(N/Z)_{CS}$. Differences in the yield in central selections, formed with the two beam-target combinations, $^{40}Ar + ^{58}Ni$ and $^{40}Ca + ^{58}Fe$, show that the *IMF* emission occurs before the isospin degree of freedom is fully equilibrated. Similar studies were performed at lower energies, at 33 and $45AMeV$, in ref. [165], for n-rich vs. n-poor isobaric *IMF* ratios. Differences in the isotopic ratios were seen at $45AMeV$ but not at $33AMeV$. The authors claim that with increasing beam energy we see a transition from a regime in which the isospin equilibration is reached before fragment production to one when *IMF* emission happens before charge equilibration. This could be a nice evidence of isospin transparency for these medium-light systems, but a more accurate analysis of the reaction mechanism would be required (centrality cuts).

An example of the importance of the centrality cuts can be seen from the results obtained at low energy, $E_{beam} = 30AMeV$, for the heavier $A = 58$ systems $^{58}Fe(n-rich)/^{58}Ni(n-poor)$, in various projectile/target combinations. The isobaric and isotopic ratios $^{11}B/^{11}C$, $^{10}Be/^{10}B$, $^{7}Li/^{7}Be$, $^{12}C/^{11}C$, $^{11}B/^{10}B$, $^{7}Li/^{6}Li$, measured at various laboratory angles scale approximately with the $(N/Z)_{CS}$, [166], clearly showing that both projectile and target nucleons contribute to the source composition. However, for the $^{58}Ni + ^{58}Fe$ and $^{58}Fe + ^{58}Ni$ mixed cases, different values of $^{12}C/^{11}C$ or $^{11}B/^{11}C$ at 40^0

seems to suggest an incomplete charge equilibration even at this energy for the source situated at midrapidity. We will see from the transport simulations that at these forward angles in semicentral collisions we can have fragments produced in the neck region but still driven from the projectile remnants, so the discussion on isospin equilibration is more involved.

For the same Fe, Ni systems the correlation between the mean number of $IMFs$ and charged particle multiplicity, a rough indication of centrality, has been investigated as a function of incident energy in [167]. Neutron rich combinations systematically produce more $IMFs$ for the same value of charged particle multiplicity. The effect is robust at the three lower energies, $45, 55, 75AMeV$, as clearly evidenced when an appropriate normalization to the system total charge, accounting for the larger number of protons in the Ni case, is introduced. However at higher energy, $105AMeV$, the isospin dependence of multifragment production appears much weakened. This could be an interesting indication of the onset of different mechanisms for fragment production at higher energies, well above the Fermi region discussed in this section.

5.3.2 Isospin Distillation and Isoscaling

In other collisions the formed composite systems differ not only in N/Z but also in mass. In these cases, for a proper interpretation of isospin effects, attention is payed even to the mass dependence of observables. The n-rich/n-poor $^{124}Sn/^{112}Sn$ systems have been extensively investigated with outstanding results.

The first evidence of the Isospin Distillation (i.e. different asymmetry in the liquid and gas phases) in central collisions was in fact observed in $^{124}Sn + ^{124}Sn$ and $^{112}Sn + ^{112}Sn$ reactions at $40AMeV$, [168], where the correlations between the average number $\langle N_{IMF} \rangle$ of $IMFs$ and the multiplicities of charged particles N_C , of light-charged particles N_{LC} ($Z \leq 2$), and neutrons N_n were measured. It was shown, [168,169], that in the n-rich $^{124}Sn + ^{124}Sn$ case the multiplicity of the emitted neutrons N_n for the maximum value of $\langle N_{IMF} \rangle$ was much larger than expected from the neutron excess of the 124+124 system. A clear *Neutron Distillation* effect was seen for the first time, associated to the largest yield of fragment formation: very n-rich gas phase coexisting with a more symmetric cluster phase, the so-called *healthier fragments* of ref.[169].

The Sn reactions in all possible n-rich/n-poor target/projectile combinations have been extensively studied at the Cyclotron Lab. of MSU at the beam energy $E_{beam} = 50AMeV$, [74,170]. The Isospin Distillation in central collisions was observed and analysed using an approach aimed to reduce as much as possible the effects of sequential decays by normalizing the isotopic yield from different $Sn + Sn$ systems to that of the more charge-symmetric case. It was

then realised that the yield ratio of a given isotope in two different reactions $R_{21}(N, Z) = Y_2(N, Z)/Y_1(N, Z)$ obey an *Isoscaling* law: its logarithm is a linear function on the number of neutrons and protons, with the slope given by the the isoscaling parameter α and β respectively, [74,170].

The double ratio of the measured isotope and isotone yields can be used, in a grand-canonical statistical approach, to extract the isospin composition of the free nucleons, i.e. the proton/neutron density ratios.. Observing its dependence on the asymmetry of the composite system, $(N/Z)_{CS}$, it was clearly established that a neutron enrichment of the free nucleonic gas takes place. Within the same thermodynamical model the absolute value of ρ_n/ρ_p in the nucleonic gas can be evaluated. The output is in fact significantly larger than the initial neutron to proton ratio: between 1.7 to 3.4 for $^{112}Sn + ^{112}Sn$ (initial 1.24) and 2.8 to 8.2 for $^{124}Sn + ^{124}Sn$ (initial 1.48). This effect is certainly present but it appears overestimated within the grand canonical picture. In the same scheme the isoscaling parameters, being related to the difference of neutron and proton chemical potentials, can provide an evaluation of the symmetry term of the *EOS* in dilute matter [170,120]. Very low values are deduced, with a large uncertainty due to the determination of the temperature of the equilibrated source. Alternative interpretations have been recently proposed, e.g. see ref. [171], were the isospin dynamical aspects play a greater role and no global equilibration is required. Information even on the density gradient of the symmetry energy can be reached, see the following discussions based on transport simulations.

Reactions for similar systems, $^{124}Sn, ^{124}Xe + ^{124}Sn, ^{112}Sn$, have been recently studied at lower energies, 28AMeV [172]. Isotopic yield ratios measured at 40 0 laboratory angle show a reduced isospin distillation effect. This could be an indication of the quenching at lower energies of the liquid-gas transition for the fragment production. However the centrality selection of the events should be accurately checked since in semiperipheral collisions other mechanisms, with different isospin dynamics, can produce fragments in the same angular range, as discussed below. In any case we expect a rise and fall of the liquid-gas mechanism with increasing beam energy for central collisions, and consequently of the related isoscaling signal. This trend has been recently observed for the $^{58}Fe, ^{58}Ni$ reactions systematically studied at 30, 40 and 47AMeV beam energies, [75,173,174].

Isoscaling behaviour and neutron enrichment of the free nucleon gas have been revealed also for $^{112,124}Sn + ^{58,64}Ni$ central collisions at 35AMeV [175]. Finally we have to note that the isospin distillation was also noticed in multifragmentation reactions induced by high energy protons [176].

5.3.3 Isospin Dynamics for Neck Fragmentation in Semiperipheral Collisions

It is now quite well established that the largest part of the reaction cross section for dissipative collisions at Fermi energies goes through the *Neck Fragmentation* channel, with *IMFs* directly produced in the interacting zone in semiperipheral collisions on very short time scales. We can expect different isospin effects for this new fragment formation mechanism since cluster are formed still in a dilute asymmetric matter but always in contact with the regions of the Projectile-Like and Target-Like remnants almost at normal densities.

A first evidence of this new dissipative mechanism was suggested at quite low energies, around $19AMeV$, in semicentral $^{100}Mo + ^{100}Mo$, $^{120}Sn + ^{120}Sn$ reactions [177,178]. A transition from binary, deep-inelastic, to ternary events was observed, with a fragment formed dynamically that influences the fission-like decay of the primary projectile-like (*PLF*) and target-like (*TLF*) partners. From in-plane fragment angular distribution a decrease of scission-to-scission lifetimes with the mass asymmetry of the *PLF/TLF* “fission-fragments” from $3000fm/c$ down to $200fm/c$ was deduced. Similar conclusions were reached in [179]. Consistent with the dynamical scenario was the anisotropic azimuthal distribution of IMF’s. In fact the *IMF alignement* with respect to the (*PLF**) velocity direction has been one clear property of the “neck-fragments” first noticed by Montoya et al.[180] for $^{129}Xe + ^{63,65}Cu$ at $50AMeV$.

A rise and fall of the neck mechanism for mid-rapidity fragments with the centrality, with a maximum for intermediate impact parameters $b \simeq \frac{1}{2}b_{max}$, as observed in [181], suggests the special physical conditions required. The size of the participant zone is of course important but it also appears that a good time matching between the reaction and the neck instabilities time-scales is required, as suggested in refs. [163,53]. In fact a simultaneous presence, in noncentral collisions, of different *IMF* production mechanisms at midrapidity was inferred in several experiments [182,183,184,185,186,188].

An accurate analysis of charge, parallel velocity, and angular distributions has been extended to high fragment multiplicities in [186] by Colin et al. They have noticed a ”hierarchy effect”: the ranking in charge induces on average a ranking in the velocity component along the beam, v_{par} , and in the angular distribution. This means that the heaviest *IMF* formed in the mid-rapidity region is the fastest and the most forward peaked, consistently with the formation and breakup of a neck structure or a strongly deformed quasiprojectile. A very precise and stimulating study of the time scales in neck fragmentation can be carried out using the new 4π detectors with improved performances on mass resolution and thresholds for fragment measurements. Such kind of data are now appearing from the *CHIMERA* collaboration [187,188].

We have reported here the experimental evidences for “neck fragmentation” since we can immediately expect large isospin dynamical effects from the presence of large density gradients and from the possibility of selecting various time-scales for the fragment formation. This will be widely discussed in the theory part of this Section. The first evidences of isospin effects in neck fragmentation were suggested by Dempsey et al. in [189] from semiperipheral collisions of the systems $^{124,136}Xe + ^{112,124}Sn$ at $55AMeV$, where correlations between the average number of *IMF*’s, N_{IMF} , and neutron and charged particle multiplicities were measured. The variation of the relative yields of $^6He/^{3,4}He$, $^6He/Li$ with v_{par} for several Z_{PLF} gates shows that the fragments produced in the midvelocity region are more neutron rich than are the fragments emitted by the *PLF*. Enhanced *triton* production at midrapidity was considered in ref.[181], and more recently in [190], as an indication of a neutron neck enrichment.

P.M. Milazzo et al. [191,192] analyzed the the *IMF* parallel velocity distribution for $^{58}Ni + ^{58}Ni$ semiperipheral collision at $30AMeV$. The two-bumps structure for *IMFs* with $5 \leq Z \leq 12$, located around the center of mass velocity and close to the quasiprojectile (*PLF* *) source respectively, was explained assuming the simultaneous presence of two production mechanisms: the statistical disassembly of an equilibrated *PLF* * and the dynamical fragmentation of the participant region. The separation of the two contributions allows for several interesting conclusions. The average elemental event multiplicity $N(Z)$ exhibits a different trend for the two processes: in particular, the fragments with $5 \leq Z \leq 11$ are more copiously produced at the midvelocity region. This experiment has a particular importance since isospin effects were clearly observed, *in spite of the very low initial asymmetry*. The measured isotopic content of the fragments is clearly different in the two mechanisms. The experimental heavy isotope/light isotope yield ratios, $^{14}C/^{12}C$, $^{12}B/^{10}B$, $^{10}Be/^{7}Be$, $^8Li/^6Li$, show a systematic decreasing trend as a function of parallel velocity from c.m. to *PLF* values. All these results indicate a neutron enrichment of the neck region, *even when initially the system N/Z is close to unity*.

Plagnol et al. [193] have examined, for the system $Xe + Sn$ between 25 and $50AMeV$, the competition between midvelocity dynamical emission and equilibrium evaporation as well as its evolution with incident energy. The onset of the neck emission takes place around $25AMeV$ and rises with the energy while the evaporative part remains quite invariant for a selected centrality. Neck matter is found to be more charge asymmetric: more neutron rich isotopes are favored at midvelocity in comparison to evaporation. Evidence of a neck-like structure and its neutron enrichment has been seen even in collisions with a rather light symmetric target, $^{58}Ni + ^{12}C$, ^{24}Mg , at $34.5AMeV$ [194]. The average N/Z ratio for isotopes with $Z = 3, 4$ exhibits a clear increase from the *PLF* to the midrapidity zone.

We close with a couple of comments that indicate the need of new, possibly more exclusive, data. The reasons for a preponderance of neutron-rich isotopes emitted from the neck region are a matter of debate. Possible explanations being, apart the density dependence of symmetry energy, also a fast light cluster production, especially of α -particles, which promptly leads to an amplification of neutron excess in the participant matter [195]. For completeness we have to mention that different analyses even give conflicting results on the n-enrichement of the clusters produced at mid-rapidity [196,197]. This shows that the reaction dynamics is in general very complicated, and we can have different isospin effects even in competition. The point will be clarified in the next subsections.

5.3.4 Isospin Diffusion

The isospin equilibration appears of large interest also for more peripheral collisions, where we have shorter interaction times, less overlap and a competition between binary and neck-fragmentation processes. The specific feature at Fermi energies is that the interaction times are close to the specific time scales for isospin transport allowing a more detailed investigation of isospin diffusion and equilibration in reaction between nuclei with different N/Z asymmetries. The low density neck formation and the preequilibrium emission are adding essential differences with respect to what is happening in the lower energies regime. Tsang et al. [198] probed the isospin diffusion mechanism for the systems $^{124}Sn + ^{112}Sn$ at $E = 50AMeV$ in a peripheral impact parameter range $b/b_{max} > 0.8$, observing the isoscaling features of the light isotopes $Z = 3 - 8$ emitted around the projectile rapidity. An incomplete equilibration was deduced. The value of the isoscaling parameter $\alpha = 0.42 \pm 0.02$ for $^{124}Sn + ^{112}Sn$ differs substantially from $\alpha = 0.16 \pm 0.02$ for $^{112}Sn + ^{124}Sn$. The isospin imbalance ratio [199], defined as

$$R_i(x) = \frac{2x - x^{124+124} - x^{112+112}}{x^{124+124} - x^{112+112}} \quad (5-4)$$

($i = P, T$ refers to the projectile/target rapidity measurement, and x is an isospin dependent observable, here the isoscaling α parameter) was estimated to be around $R_P(\alpha) = 0.5$ (vs. $R_P(\alpha) = 0.0$ in full equilibration). The authors pointed out that this quantity can be sensitive to the density dependence of symmetry energy term since the isospin transfer takes place through the lower density neck region.

The isoscaling analysis of heavy residues identified in peripheral reactions $^{86}Kr + ^{124,112}Sn$ at $E = 25AMeV$ was employed to trace the degree of N/Z equilibration as a function of the excitation energy of the primary residue, [200]. The evolution of isospin exchange with the centrality or interaction

time, can be established. It was concluded that for the most damped binary events, corresponding to the largest excitation energies, charge equilibration could be attained.

5.4 *Theoretical interpretation: overview.*

Using the above described Stochastic Mean Field (*SMF*) approach dissipative collisions of Sn, Sn and Sn, Ni isotopes at Fermi energies, in various asymmetry combinations, have investigated in great detail. In the transport simulations the isovector part of the effective forces is only modified, following the general philosophy of the research project which is behind this report. We have seen before the amazing richness of the data on isospin effects in reactions, still remaining in the stable beam sector. Here we will try to select the key observables in order to extract precise information on the isovector part of the nuclear *EOS* in regions far from the normal conditions. In particular we report on a study of the 50 *AMeV* collisions of the systems $^{124}Sn + ^{124}Sn$ $^{112}Sn + ^{112}Sn$ and $^{124}Sn + ^{112}Sn$, [55], where data are available from *NSCL – MSU* exps. for fragment production and isospin diffusion, [74,170,198].

We also analyse the neutron rich, mass asymmetric reaction $^{124}Sn + ^{64}Ni$, at 35 *AMeV* bombarding energy, and the corresponding neutron poor reaction $^{112}Sn + ^{58}Ni$, to look in detail at the neck fragmentation dynamics and its isoscaling properties, [56]. These reactions have been experimentally studied with the *CHIMERA* detector at *LNS*, Catania [187,188]. As already remarked, the great advantage of the *CHIMERA* detector for semicentral collision studies is the possibility of measuring target-rapidity data, due to the low threshold of the detection telescopes, together with a large precision in *IMF* mass separation. As we will see this will allow new correlation measurements of fundamental importance for understanding the reaction mechanism and the related isospin dynamics.

5.5 *From central to semi-central collisions: bulk fragmentation.*

5.5.1 *Fragmentation dynamics*

At central impact parameters in this energy range the reaction mechanism manifests the features of bulk fragmentation, as observed in various dynamical simulations, [201,54,202]. One can identify quite generally three main stages of the collision, as observed also from the density contour plot of a typical event at $b = 2fm$ displayed in Fig. 5-2: (1.) In the early compression stage, during the first $40 - 50 fm/c$, the density in the central region can reach values around $1.2 - 1.3$ normal density; (2.) The expansion phase, up to $110 - 120 fm/c$,

brings the system to a low density state. The physical conditions of density and temperature reached during this stage correspond to an unstable nuclear matter phase; (3.) In the further expansion fragmentation is observed.

According to stochastic mean field simulations, the fragmentation mechanism can be understood in terms of the growth of density fluctuations in the presence of instabilities. The volume instabilities have time to develop through spinodal decomposition leading to the formation of a liquid phase in the fragments and a gas of nucleons and light clusters. As seen in the Figure, the fragment formation process typically takes place up to a *freeze-out* time (around $260 - 280 \text{ fm}/c$). This time is well defined in the simulations since as the time of saturation of the average number of excited primary fragments. The clusters are rather far apart with a negligible nuclear interaction left among them.

An intermediate behaviour, between the fragmentation mechanism illustrated above and the formation of an elongated “neck” region between the two collisional partners, extensively discussed later, is observed at $b = 4 \text{ fm}$ (see also Fig. 5-8). The “*Freeze-Out time*”, when the nuclear interaction among clusters disappears, is decreasing with impact parameter. This gradual transition suggests that it may be unappropriate to think in terms of a unique fragmentation mechanism and more so to assign a fixed size or shape for a multifragmenting source, even passing from $b = 1 - 2 \text{ fm}$ to $b = 4 - 5 \text{ fm}$.

Guided by the density contour plots we can investigate the behaviour of some characteristic quantities which give information on the isospin dynamics in fragment formation.

In many of the following figures (i.e. see Fig.5-3) we report as a function of time:

- (a) *Mass A* in the liquid phase (solid line and dots) and gas phase (solid line and dots).
- (b) *The asymmetry parameter* $I = (N - Z)/(N + Z)$ in the gas “central” (solid line and squares), gas total (dashed+squares), liquid “central” (solid+circles) and *IMF*’s (clusters with $3 < Z < 15$, stars). The horizontal line indicates the initial average asymmetry. “Central” means a box of dimension 20 fm around the *C.M.* of the total system.
- (c) *Mean fragment multiplicity* $Z \geq 3$ whose saturation defines the freeze-out time and configuration.

Moreover we show properties of the “primary” fragments in the *Freeze-Out Configuration*:

- (d) *Charge distribution probability* $P(Z)$,
- (e) *Average asymmetry distribution* $I_{av}(Z)$ and
- (f) *Fragment multiplicity distribution* $P(N)$ (normalized to 1).

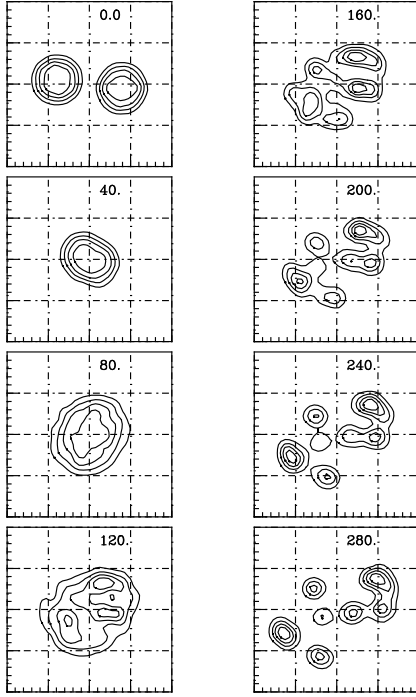


Fig. 5-2. $^{124}Sn + ^{124}Sn$ collision at $50AMeV$: time evolution of the nucleon density projected on the reaction plane. Central $b = 2fm$ collision: approaching, compression and separation phases. The times are written on each figure. The iso-density lines are plotted every $0.02fm^{-3}$ starting from $0.02fm^{-3}$.

5.5.2 Isospin distillation

We look first at the influence of the mass-to-charge ratio of the colliding ions on fragment production comparing, for a fixed asy-EOS (asy-stiff), the neutron-rich and neutron-poor $Sn + Sn$ systems. The results are plotted in the Figures 5-3 and 5-4. For $^{124}Sn + ^{124}Sn$ we notice a neutron dominated pre-equilibrium particle emission during the first $50fm/c$. The liquid phase becomes more symmetric during the compression and expansion. At variance, the system $^{112}Sn + ^{112}Sn$ is on the p-rich side of the valley of stability and along the fast nucleon emission the asymmetry of the liquid increases. Hence the pre-equilibrium stage appears very important to assess the effective asymmetry of the system that will eventually fragment.

From the beginning of the fragment formation phase of the evolution, between 110 and $280fm/c$, the trends of the liquid and gas phase asymmetry of the two systems become similar, Fig. 5-3, 5-4(b). In the "central region" the liquid asymmetry decreases while an *isospin burst* of the gas phase is observed. This behaviour is consistent with the kinetic spinodal mechanism in dilute asymmetric nuclear matter leading to the *Isospin Distillation* between the liquid and the gas phase.

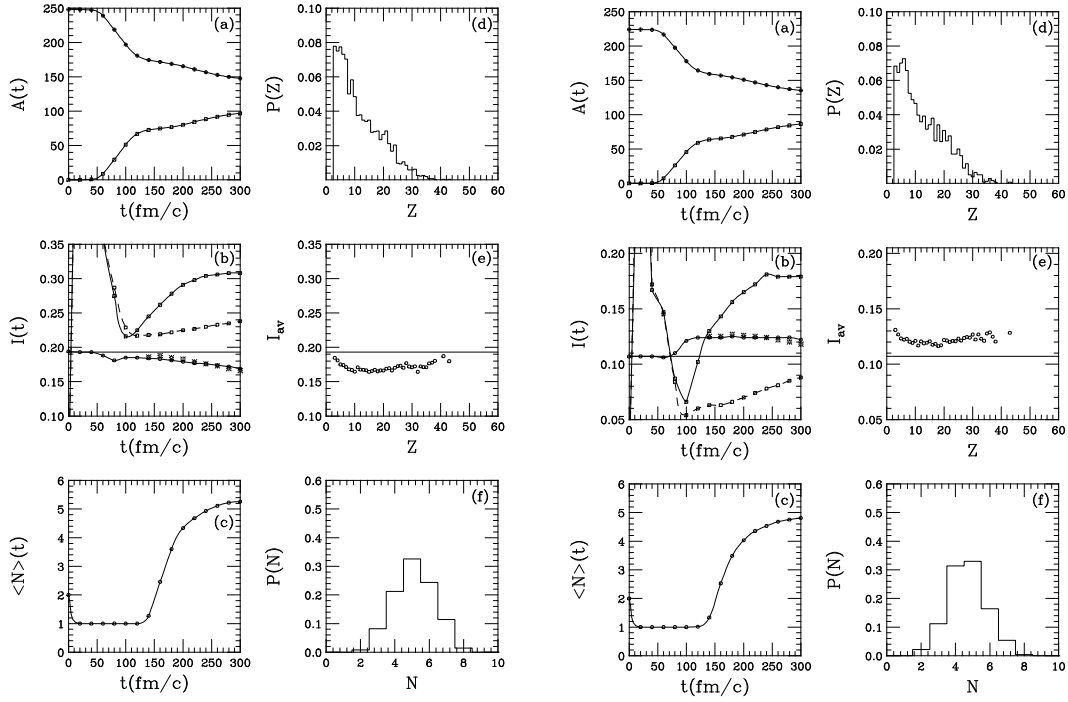


Fig. 5-3. $^{124}Sn + ^{124}Sn$ $b = 2fm$ collision:time evolution (left) and freeze-out properties (right), ASY-STIFF EOS.

Fig. 5-4. $^{112}Sn + ^{112}Sn$ $b = 2fm$ collision:time evolution (left) and freeze-out properties (right), ASY-STIFF EOS.

The effects of this process are clearly seen in the *IMF* isospin content, in both cases lower than at the beginning of the spinodal decomposition, Fig. 5-3,5-4(e). Opposite trends for fragments with charge above and below $Z \approx 15$ can be observed. For heavier products the average asymmetry increases with the charge, a Coulomb related effect. However, the asymmetry rises again for lighter fragments. This can be a result of the differences in density and isospin between the regions in which the fragments grow, due to the fact that not all of them form simultaneously, as shown in the density contour plot.

The charge distribution of primary fragments has a rapidly decreasing trend, typical of a multifragmentation process, Fig. 5-3, 5-4(d). The neutron rich system favors events with larger *IMF*'s multiplicities, see Fig. 5-3, 5-4(c, f). This feature was evidenced also in experiments, as discussed before.

5.5.3 Isoscaling analysis

In recent years isospin effects on fragment production have been discussed in terms of an isoscaling behaviour, revealed first in multifragmentation data [74,170]. It was experimentally observed that comparing two different reactions, one neutron rich (label 2) and one neutron poor (label 1), the ratio

between the yields of a given N, Z isotope $R_{21} = Y_2(N, Z)/Y_1(N, Z)$ follows the relation:

$$\ln R_{21} = C + N\alpha + Z\beta \quad (5-5)$$

with α, β isoscaling parameters and C a constant.

Much work has been done on the interpretation of the isoscaling parameters in the framework of statistical approaches and the relation to the value of the symmetry energy coefficient. For instance, in a grand-canonical statistical approach, these parameters are related to the neutron (proton) chemical potential differences in the nuclear environments, assumed to be at the same temperature, where the fragments are created in the two reactions. It can be also related to the ratio of the free neutron (proton) density in the two sources:

$$\alpha \equiv \frac{\Delta\mu_n}{T} \quad , \quad \beta \equiv \frac{\Delta\mu_p}{T} \quad , \quad (5-6)$$

In turn, these are related to the symmetry energy properties:

$$\begin{aligned} \Delta\mu_n &= \rho \frac{\partial\epsilon_{sym}}{\partial\rho} (I_2^2 - I_1^2) + 2\epsilon_{sym}[(I_2 - I_1) - \frac{(I_2^2 - I_1^2)}{2}] \\ \Delta\mu_p &= \rho \frac{\partial\epsilon_{sym}}{\partial\rho} (I_2^2 - I_1^2) - 2\epsilon_{sym}[(I_2 - I_1) + \frac{(I_2^2 - I_1^2)}{2}] \end{aligned}$$

where ϵ_{sym} is the symmetry energy per nucleon (see Sect.2). We note that only in the limit $\frac{\partial\epsilon_{sym}}{\partial\rho} \simeq 0$ we get the “liquid-drop” results used in refs.[203,204]:

$$\begin{aligned} \Delta\mu_n &= 4\epsilon_{sym}[(\frac{Z_1}{A_1})^2 - (\frac{Z_2}{A_2})^2] \quad and \quad \Delta\mu_p = 4\epsilon_{sym}[(\frac{N_1}{A_1})^2 - (\frac{N_2}{A_2})^2] \\ &\quad with \quad |\Delta\mu_p| > |\Delta\mu_n| \end{aligned} \quad (5-7)$$

Since we have always the relation:

$$\ln\left(\frac{N_2/Z_2}{N_1/Z_1}\right) \equiv \alpha - \beta = \frac{4}{T}\epsilon_{sym}(\rho)(I_2 - I_1) \quad (5-8)$$

a large interest is rising on the possibility of a direct measurement of the symmetry energy in the fragment source from the isoscaling α, β parameters [203,204].

However, it appears that an isoscaling behavior does not necessarily require the existence of a fully equilibrium, i.e. a grand canonical ensemble formula.

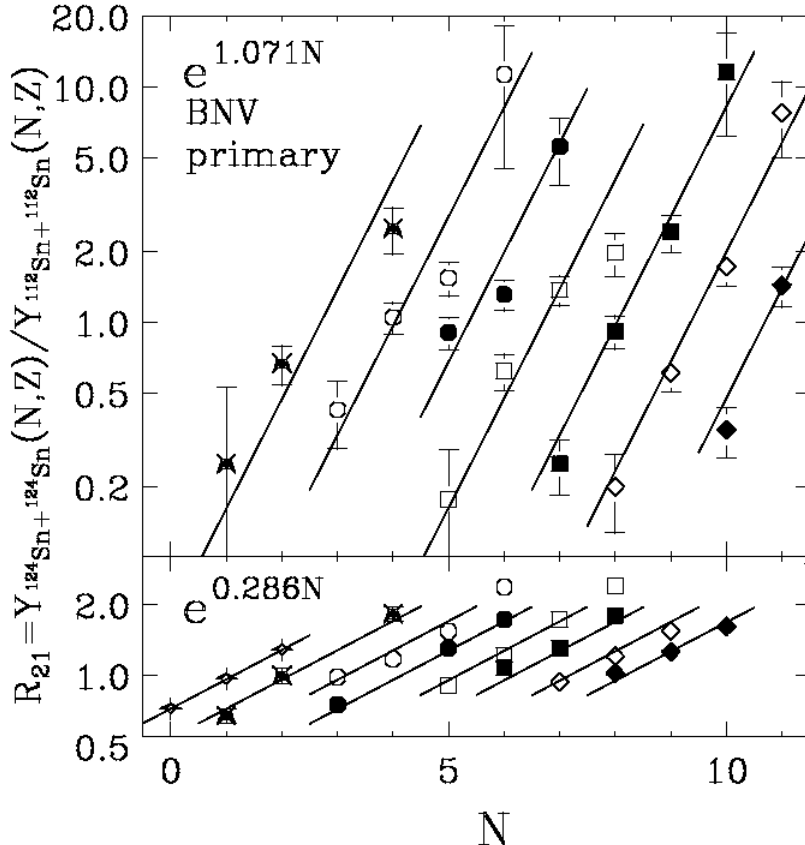


Fig. 5-5. Stochastic transport simulations of $Sn + Sn$ central collisions at $50 AMeV$. Isoscaling behaviors: primary fragments (upper curves); after sequential decays (lower curves).

An isoscaling law is in fact observed also in dynamical simulations of the stochastic mean-field type [171]. In Fig.5-5 we report the isoscaling behavior of primary fragments observed in stochastic transport simulations of central $Sn + Sn$ collisions at $50 AMeV$. In the lower part the isoscaling plots are shown after a secondary evaporation calculation. It is seen that the sequential neutron emission reduces the α slope considerably.

Actually one can easily show that isoscaling is expected also in the case where the fragment isotopic distributions in the two reactions have a gaussian shape around a given average asymmetry. Then the isoscaling parameters are determined by the difference of those averages divide by the widths of the distributions. The isoscaling parameters are expected to be larger in the dynamical relatively to the statistical approach, since the widths of the isotopic distributions are smaller than the ones obtained at equilibrium.

5.5.4 Symmetry Energy effects

Let us now investigate how different assumptions on the density dependence of the symmetry energy may influence the observables discussed above. In Figs. 5-6, 5-7 we report the results obtained respectively with the asy-soft and the asy-superstiff symmetry term. We see that the average value of N/Z of the fast particles emitted during the expansion phase is affected by the symmetry term. In the asy-soft case, below ρ_0 , neutrons are less bound than in the asy-superstiff case (opposite for protons). A more neutron-rich prompt particle emission with the soft asy-*EOS* leads to a lower asymmetry of the initial dilute matter undergoing spinodal decomposition. This is seen from Figs.5-6(b) (asy-soft) and 5-7(b) (asy-superstiff). As expected the results of Fig.5-3 (b) (asy-stiff) are somewhat in between.

The influence of the symmetry term is clearly seen in the isospin content of the primary intermediate mass fragments. The asy-soft choice is more effective for the isospin distillation effect, producing the most symmetric *IMF*'s, as the comparison of Figs. 5-6 ,5-7(b),(e) shows. This can be explained energetically observing that this choice has a larger symmetry energy at very low densities. The differences between the results observed using the two parametrizations can also be directly interpreted in terms of the corresponding density behaviours of the n, p -chemical potentials, see the comments on Fig.2-4 of Sect.2.

5.6 From semicentral to peripheral collisions: neck fragmentation

Summarizing the main experimental observations, we would like to stress the following peculiarities of a "dynamical" *IMF* production mechanism in semi-peripheral collisions:

1. An enhanced emission is localized in the mid-rapidity region, intermediate between *PLF* and *TLF* sources, especially for *IMF*'s with charge Z from 3 to 15 units.
2. The *IMF*'s relative velocity distributions with respect to *PLF* (or *TLF*) cannot be explained in terms of a pure Coulomb repulsion following a statistical decay. A high degree of decoupling from the *PLF* (*TLF*) is also invoked.
3. Anisotropic *IMF*'s angular distributions are indicating preferential emission directions and an alignment tendency.
4. For charge asymmetric systems the light particles and *IMF* emissions keep track of a neutron enrichment process that takes place in the neck region.

A fully consistent physical picture of the processes that can reproduce observed characteristics is still a matter of debate and several physical phenomena can

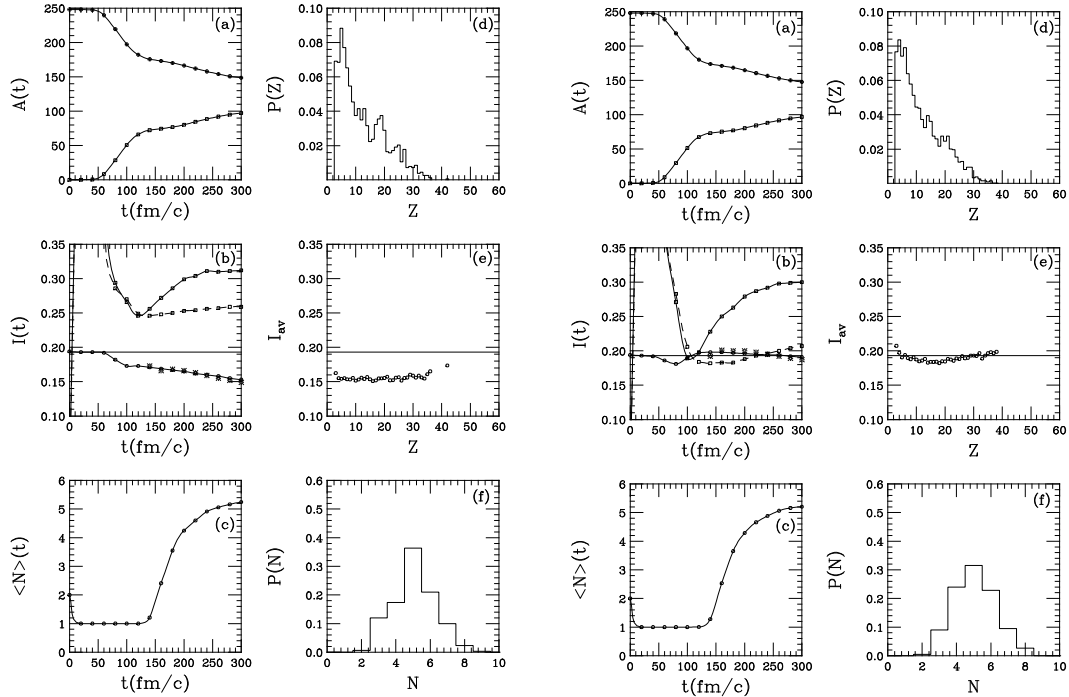


Fig. 5-6. $^{124}Sn + ^{124}Sn$ $b = 2 fm$ collision:time evolution (left) and freeze-out properties (right), ASY-SOFT EOS.

Fig. 5-7. $^{124}Sn + ^{124}Sn$ $b = 2 fm$ collision:time evolution (left) and freeze-out properties (right), ASY-SUPERSTIFF EOS.

be envisaged, ranging from the formation of a transient neck-like structure that would break-up due to Rayleigh instabilities or through a fission-like process, to the statistical decay of a hot source, triggered by the proximity with PLF and TLF [209,205,206]. Dynamical transport models suggest since long time the possibility of observing neck emission [163,207,53,208], [189,181,195]. We show in Fig. 5-8 the density contour plots of a neck fragmentation event at $b = 6 fm$, for the reaction $^{124}Sn + ^{124}Sn$ at $50 AMeV$, obtained from the numerical calculations based on the stochastic transport approach described before, [56].

5.6.1 Neck dynamics and IMF properties: the iso-migration

In the following we will review results regarding the fragmentation mechanism in semiperipheral collisions, as well as the related isospin dynamics and effects of the symmetry term density dependence. First we examine again the $Sn + Sn$ collisions at $50 AMeV$, but at impact parameter $b = 6 fm$. We discuss the same observables as in central collisions.

The development of a neck structure in the overlap region of the two colliding nuclei is evidenced in Fig. 5-8. During the interaction time this zone heats and

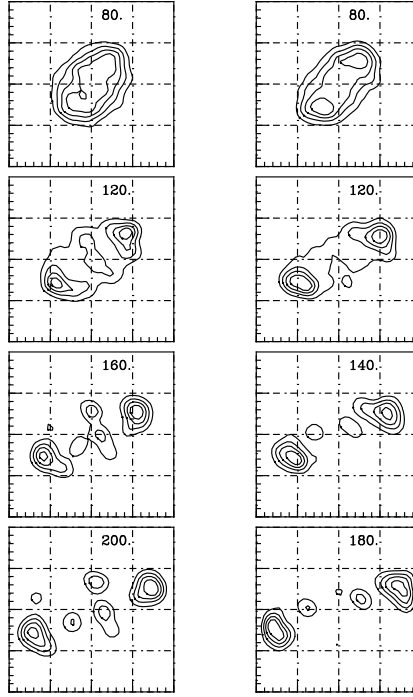


Fig. 5-8. $^{124}Sn + ^{124}Sn$ collision at 50AMeV: time evolution of the nucleon density projected on the reaction plane. Left column: $b = 4fm$. Right column: $b = 6fm$.

expands but remains in contact with the denser and colder regions of *PLF* and/or *TLF*. The surface/volume instabilities of a cylindrically shaped neck region and the fast leading motion of the *PLF* and *TLF* will play an important role in the fragmentation dynamics. At the freeze-out time, with the neck rupture at about $140fm/c$, intermediate mass fragments are produced in the mid rapidity zone. In some events fragments form very early while, in others, they can remain for a longer time attached to the leading *PLF*'s or *TLF*'s. In the same figure we note an intermediate behavior between multifragmentation and neck fragmentation at $b = 4fm$.

In the Figs.5-9, 5-10 we plot the same quantities as before (Sect.5.5.2) for n-rich and n-poor $Sn + Sn$ collisions for impact parameter $b = 6fm$ (asy-stiff *EOS*). In the charge distribution probability, Figs. (5-9, 5-10)(d), one can clearly separate the *PLF/TLF* residues and the *IMF*'s with upper limit charge $Z \approx 15$. We call the *IMF*'s produced by such a mechanism Neck Intermediate Mass Fragments (*NIMF*'s). For neutron-rich systems events with two or even three *NIMF*'s appear, are slightly more likely, Figs. (5-9, 5-10)(f). The isospin content reveals new distinctive features as seen in Figs. (5-9, 5-10)(e). The *IMF*'s formed in the neck region are much more neutron rich than the corresponding fragments produced in semicentral collisions. Moreover the *PLF* and *TLF* residues have definitely a lower asymmetry than *NIMF*'s. To interpret this behaviour we have to keep in mind that the neck region is always in contact

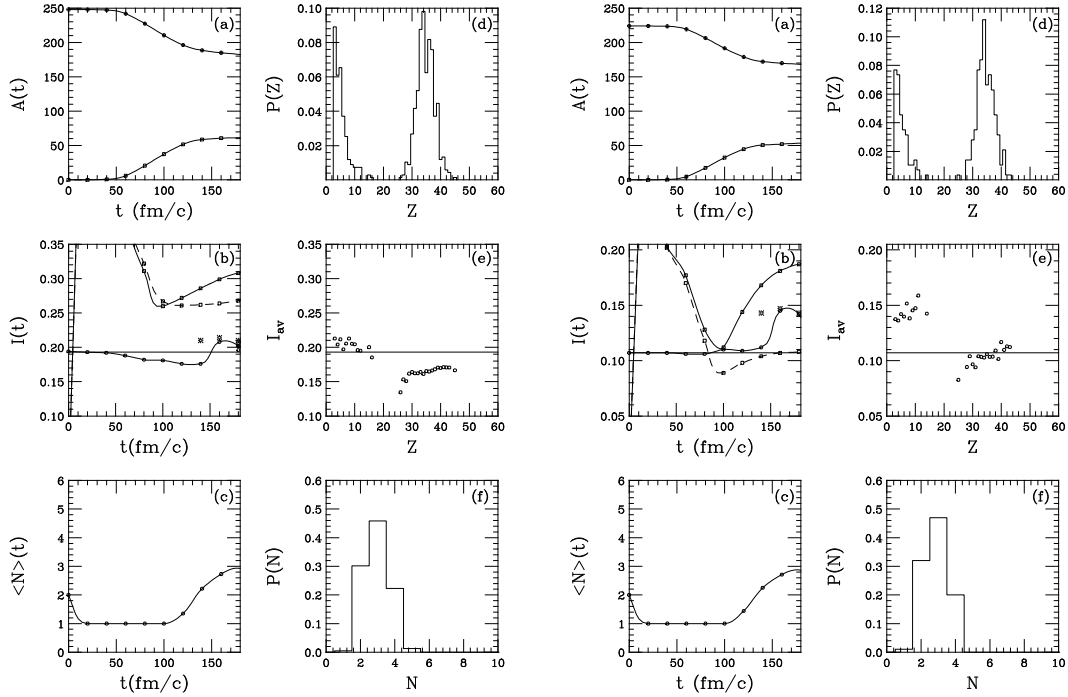


Fig. 5-9. $^{124}Sn + ^{124}Sn$ $b = 6 fm$ collision:time evolution (left) and freeze-out properties (right), ASY-STIFF EOS.

Fig. 5-10. $^{112}Sn + ^{112}Sn$ $b = 6 fm$ collision:time evolution (left) and freeze-out properties (right), ASY-STIFF EOS.

with a normal-density phase (the spectators) during the fragment formation and this determines a different isospin dynamics. Moreover the clusters are formed in a nuclear matter not very dilute relative to saturation density. We also notice that the neck breaking leads, in some events, to fragments closer to one of the spectators with increased interaction between the two. Thus there should be a smooth transition to *PLF/TLF* fast-fission type of events.

In neck fragmentation we are testing the symmetry energy in different regions of nucleon density. It is energetically more favorable to have protons (neutrons) migration from (to) the neck region to (from) the more dense spectators, leaving the nuclear matter in the neck neutron-rich at the time of breaking. Clearly the isospin dynamics is ruled by the same energetic arguments as in the case of isospin distillation in central collisions. The main difference relative to bulk fragmentation is related to the density gradient between the lower density neck and the spectators, which can trigger proton and neutron flows in opposite directions (isovector mode). Therefore, we propose to call this phenomenon isospin migration in contradistinction to the distillation phenomenon driven by isoscalar-like unstable fluctuations.

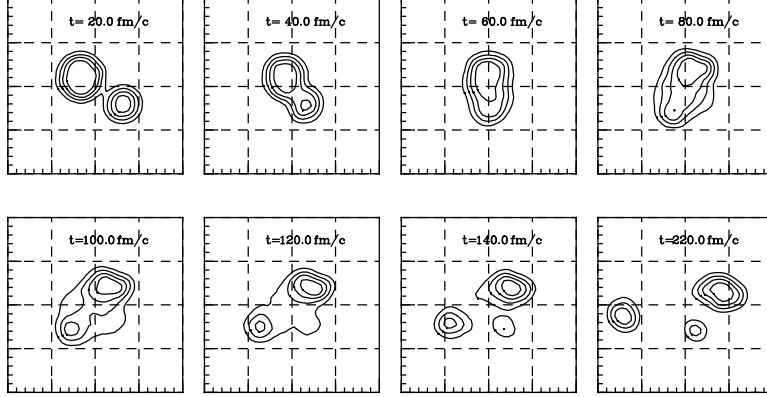


Fig. 5-11. $^{124}Sn + ^{64}Ni$ at $35AMeV$. Typical evolution of the density contour plot for a neck fragmentation event at $b = 6fm$.

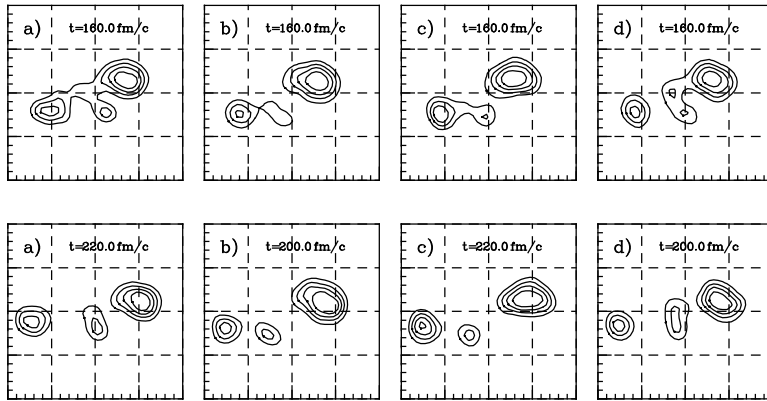


Fig. 5-12. Density contour plots as in Fig.5-11. Early stage of fragment formation (top) and same events close to the freeze-out (bottom) for four ternary cases a), b), c), d) in neck fragmentation.

5.6.2 Neck dynamics at lower energy

It is also interesting to study the features of the neck dynamics at lower energy. Here we consider the $^{124}Sn + ^{64}Ni$ semiperipheral collisions at incident energy around $35AMeV$, where nice data are appearing from the *CHIMERA* collaboration at the *LNS* [187,188]. The reaction evolution at impact parameter $b = 6fm$ is shown in Fig.5-11. Calculations are performed using the asy-stiff parameterization. The dynamics corresponds to a mainly two-center system. We notice the superimposed motion of the *PL* and *TL* pre-fragments linked to the formation of a neck-like structure with a fast changing geometry between $40fm/c$ and $150-160fm/c$.

Neck instabilities favour the appearance of *NIMF*'s, after $150fm/c$, in a variety of places and ways as can be seen by looking at Fig.5-12. For four events, we illustrate two characteristic stages, the early phase of the fragment formation process and the configuration close to freeze-out.

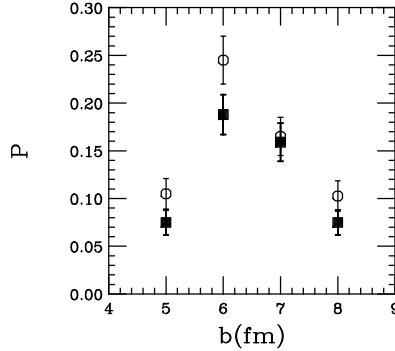


Fig. 5-13. $Sn + Ni$ reactions: Impact parameter dependence of the neck fragmentation probability (ternary events). White circles: neutron rich reaction. Black circles: neutron poor reaction. Asystiff *EOS*.

Apart from the events corresponding to the fast *NIMF* production we have a large fraction of binary events, with a presence in the exit channel of only primary excited *PLF*'s and *TLF*'s. Induced deformations suggest that they can split, also asymmetrically, on time scales long with respect to neck fragmentation, but much shorter than in an equilibrium fission process. In Fig. 5-13 we plot the dependence on the impact parameter of the ternary event probability. The maximum value, about 25%, is attained around mid-centrality, between $b = 6-7\text{ fm}$, decreasing on both sides to about 10% for $b = 5\text{ fm}$ and $b = 8\text{ fm}$. It is even smaller at $b = 4\text{ fm}$, in spite of a stronger dissipation. The longer interaction time favors a reabsorption of the neck matter at this energy. This is a different behaviour in comparison to the dynamics at 50 AMeV , where, as we have already emphasized, the higher available energy makes possible the transition to multifragmentation with increasing centrality. At greater impact parameters, $b = 9\text{ fm}$, a smaller overlap and a faster separation are also suppressing this mechanism.

From the simulations we can extract an interesting information on the time scale of the Neck-*IMF* production. In Fig. 5-14 we show, for different impact parameters, the probability distribution of the time interval between the instant of the first separation of the dinuclear system and the moment when a Neck-*IMF* is identified (scission-to-scission time). A large part of the *NIMFs* are formed in short time intervals, within $50\text{ fm}/c$.

Finally we would like to remark that the neck fragmentation shows a dependence on the nucleon-nucleon cross sections and the *EOS*-compressibility. The latter point is particularly interesting since it seems to indicate the relevance of volume instabilities even for the dynamics of neck. This appears consistent with the short time scales shown before, see also the discussion in ref. [56].

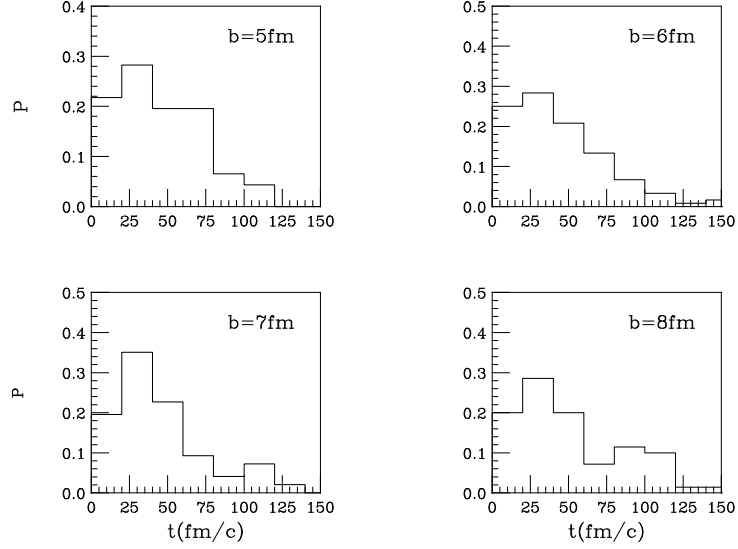


Fig. 5-14. The probability distribution of scission-to-scission time in the neck fragmentation for impact parameters from 5 to 8 fm. Asystiff EOS.

5.6.3 Analysis of kinematical observables

The nonstatistical features of the *NIMF* production are revealed in various kinematic correlations. The corresponding observables can be measured in exclusive experiments.

An interesting kinematical observable is the asymptotic relative velocity of the neck-produced *IMFs* with respect to the *PLF* (*TLF*), $v_{rel}(PLF, TLF) \equiv |\mathbf{v}_{PLF, TLF} - \mathbf{v}_{IMF}|$. This is compared with the relative velocity reached in a pure Coulomb-driven separation, signature of a statistical fission process of a compound *PLF** or *TLF** system, as provided by the Viola systematics [210,211]:

$$v_{viola}(1, 2) = \sqrt{\frac{2}{M_{red}}(0.755 \frac{Z_1 Z_2}{A_1^{1/3} + A_2^{1/3}} + 7.3)} \quad (5-9)$$

where A_1, A_2, Z_1, Z_2 are the mass and charge numbers of the fission products and M_{red} is the corresponding reduced mass.

For each Neck-*IMF* we can evaluate the ratios $r = v_{rel}(PLF)/v_{viola}(PLF)$, $(r_1 = v_{rel}(TLF)/v_{viola}(TLF))$. In Figure 5-15 we plot r_1 against r for each *NIMF*. We call such a representation a *Wilczynski* – 2 plot [212]. The solid lines represent the loci of the *PL*-($r = 1$) and *TL*-($r_1 = 1$) fission events respectively. The values (r, r_1) appear simultaneously larger than 1 suggesting a weak *NIMF* correlation with both *PLF* and *TLF*, in contrast to a statistical fission mechanism. The process has some similarities with the participant-

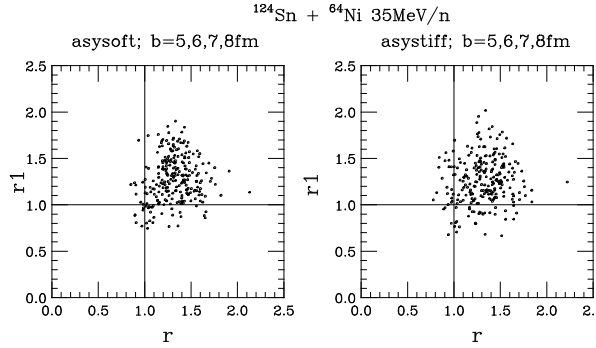


Fig. 5-15. Wilczynski-2 Plot: correlation between deviations from Viola systematics, see text. Results are shown for two *asy* – *EOS*.

spectator scenario. However the dynamics appear much richer than in the simple sudden abrasion model, where the locus of the $r - r1$ correlation should be on the bisectrix, apart the *Goldhaber* widths, see ref.[205]. Here the wide distributions of Fig.5-15 reveal a broad range of fragment velocities, typical of the instability evolution in the neck region that will lead to large dynamical fluctuations on *NIMF* properties.

Another very selective correlation is provided by the anisotropy in the fragment emission, measured by the in-plane azimuthal angle, Φ_{plane} , defined as the angle between the projection of the *PL* – *IMF* scission axis onto the reaction plane and the separation axis between *PLF* and *TLF*, [178]. A $|\Phi_{plane}| \simeq 0$ collects events corresponding to asymmetric “fissions” of the *PL*-system very aligned along the outgoing *PL* – *TL* separation axis. At variance a statistical fission dominance would correspond to a flat Φ_{plane} behavior. The Φ_{plane} distributions, corresponding to the same *NIMF* events analysed before, are covering a quite limited angular window, close to the full alignment configuration, $\Phi_{plane} = 0^\circ$. The distribution becomes wider when we approach the two $r, r1 = 1$ lines of the Fig.5-15.

We can transform in *time – scales* the correlations discussed before. In fact an induced asymmetric, fast fission can also manifest some deviations from Viola systematics. From our simulations, this mechanism takes place on longer time scales compared to neck fragmentation. If a light fragment escapes later from its *PL/TL* partner, friction certainly will attenuate the dynamical effects and relative velocities will deviate less from Coulomb values. In the plane $r - r1$ such events are located closer to the line $r = 1$ or $r1 = 1$. A prolonged contact with the *PLF* or *TLF* will induce also different angular distributions in comparison to the neck fragments (less alignment, wider Φ_{plane} distribution). As a limiting case we recover the statistical fission mechanism for a *IMF* production from an equilibrated *PL/TL* excited residue, with no Viola-deviations and no alignment. We conclude that an analysis based on the Wilczynski-2 plot, Fig.5-15, of the *IMF* produced in semicentral collisions will be able to select and study fragments formed on a large variety of interaction time-scales,

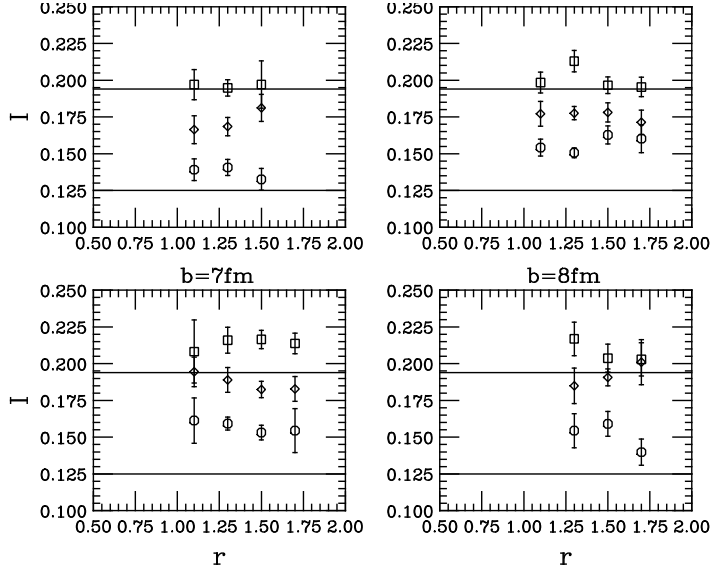


Fig. 5-16. *NIMF* isospin content for *asysoft* (circles), *asystiff* (diamonds) and *supersystiff* (squares) *EOS* as a function of r -deviation from Viola systematics, at impact parameters from $b = 5\text{ fm}$ to 8 fm . The two solid lines represent the mean asymmetries of the projectile (top) and target (bottom).

of particular interest for the mass and isospin dynamics.

5.6.4 Symmetry term effects

From the simulations of ref.[56] for the $^{142}\text{Sn} + ^{64}\text{Ni}$ system it appears that the symmetry term of the *EOS* does not seem to influence sensitively the main features of the neck mechanism, i.e. probability of ternary events, deviations from Viola systematics and *NIMF* angular distributions. However, one has to consider that with the studied system we cannot reach high charge asymmetries, the asymmetry parameter $I \equiv (N - Z)/A$ ranging from 0.193 for the projectile to 0.125 for the target, with an average $I = 0.17$.

A more promising observable seems to be the isotopic content of the Neck-*IMF*. For the three *asy* - *EOSs* introduced in Sect.2 we plot in Fig.5-16 the average isotopic composition I of the *NIMF*'s as a function of the *PLF* r -deviation from Viola systematics. At all impact parameters clear differences are evident. The average asymmetry does not depend strongly on r . We notice however that it increases with the stiffness of the symmetry potential around and below saturation. The *supersystiff* parametrization, i.e. with an almost parabolic increasing behavior around ρ_0 , produces systematically more neutron rich *NIMFs*. This effect is clearly due to a different neutron/proton migration at the interface between *PL/TL* "spectator" zone of normal density and the dilute neck region where the *NIMFs* are formed, as it was already observed for the reactions at 50 $AMeV$.

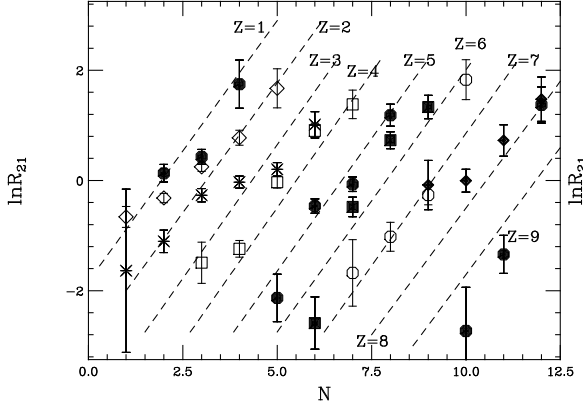


Fig. 5-17. Isoscaling in neck fragmentation: $\ln R_{21}$ dependence on N .

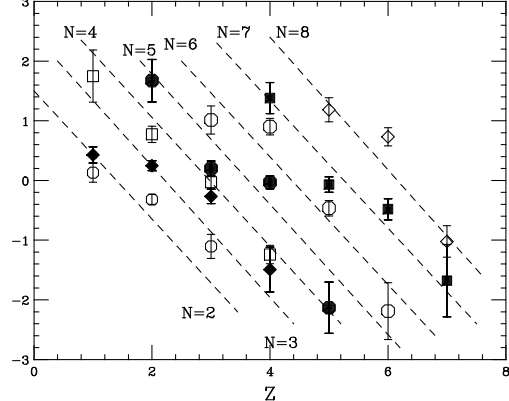


Fig. 5-18. Isoscaling in neck fragmentation: $\ln R_{21}$ dependence on Z .

From the Fig.5-16 we see that the isospin content of *NIMF*'s carries important information on the isovector part of the effective interaction and the related isospin dynamics in the early stages of the reaction. We expect a different isospin pattern for the *IMF*'s produced at later times from induced and/or statistical fission of the more charge symmetric *PLF**'s and *TLF**'s. The Wilczynski-2 plot will help to make the selections. We have to remind that all the results presented here refer to properties of primary (excited) fragments. The neutron excess signal appears likely to be washed out from later evaporation decays. A reconstruction of the primary fragments with neutron coincidence measurements would be very important.

5.6.5 Isoscaling analysis

Relative to the earlier discussion it is of interest to test whether the isoscaling behavior can manifest itself even in the neck-fragmentation, which is a clear dynamical process, related to short characteristic time scales.

In Figs. 5-17, (5-18) is shown the N (Z) dependence of $\ln R_{21}$, for $Z = 1$ to $Z = 9$ light fragments produced in the neck region, as obtained in the simulations with an *asystiff – EOS* parametrization. R_{21} is the yield ratio of the n-rich $^{124}Sn + ^{64}Ni$ vs. the n-poor $^{112}Sn + ^{58}Ni$ system, see before Sect.5.5.3.

We do see the isoscaling signal, an exponential N - and Z - dependence of the yield ratios with quite well defined α, β slopes. Although we cannot use explicit equilibrium relations, like Eq.5-8, we still expect a symmetry energy dependence of the isoscaling parameters. Since the fragment formation takes place in the neck region, we predict that its isospin content will dictate the values of the isoscaling parameters. Indeed, we may assume that for a neutron poor system, closer to the symmetric case, the differences between the various

	<i>asysoft</i>	<i>asystiff</i>	<i>superasystiff</i>
α	0.69	0.95	1.05
β	-0.67	-1.07	-1.18

Table 6

The isoscaling parameters α and β in neck fragmentation for three *asy* – *EOS*.

asy – *EOS* on the isotopic and isotonic distributions are reduced, and in a first approximation, identical. At variance, for the neutron rich system, we have seen that passing from *asysoft*- to *superasystiff*-*EOS* more neutron-rich Neck-*IMFs* are formed. Therefore, the corresponding distributions have to be steeper. As reported in Table 6, a nice increase (in the modulus) of the isoscaling parameters with the increasing stiffness of the symmetry energy is observed.

5.7 Charge Equilibration in Peripheral Collisions

5.7.1 Isospin diffusion in presence of inhomogenous density distributions

We turn now to discuss the isospin equilibration mechanism in even more peripheral collisions where only two primary fragments (*PLF* – *TLF*) are observed in the exit channel. When the ions in the entrance channel have a different N/Z ratio, we expect that isospin diffusion will lead the system towards a more uniform asymmetry distribution. The degree of equilibration, correlated to the interaction time, may provide insights on transport properties of fermionic systems [213,214], in particular on the diffusion coefficient of asymmetric nuclear matter, [215,216].

Here we are focus on a charge asymmetric collision $^{124}Sn + ^{112}Sn$, at $50AMeV$ bombarding energy, to which we refer as the mixed system, (*M*), where some data also exist, [198]. The simulations are performed for peripheral collisions at impact parameters $b = 8, 9, 10 fm$. Binary events are selected. We define the average interaction time, t_c , as the time elapsed between the initial touching and the moment when the *PLF* and *TLF* reseparate. From our simulations we obtain $t_c \approx 120, 100, 80 fm/c$ respectively for the three impact parameters. Typical density contour plots, at $b = 8 fm$ and $b = 10 fm$, are shown in Fig. 5-19. In the overlap region, after around $40 fm/c$, the formation of a lower density interface is evidenced. The isospin migration takes place during the transient contact between the two spectator regions with density close to the normal one, separated by a dilute neck region. Thus we have concentration and density gradients ruling the isospin diffusion. In contrast, in deep-inelastic collisions at lower energies, the isospin equilibration is driven by the N/Z difference between two interacting nuclei with an uniform density

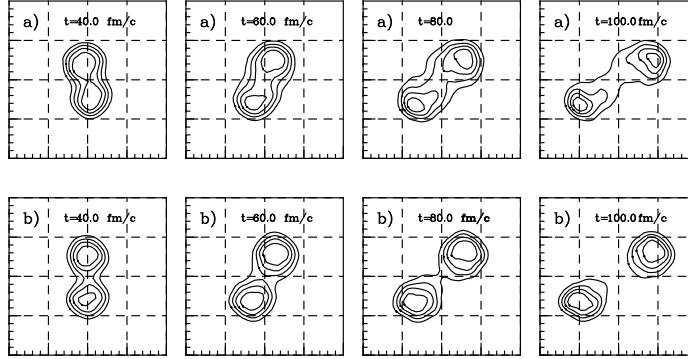


Fig. 5-19. $^{124}Sn + ^{112}Sn$ collision at 50 AMeV, $b = 8 fm$ (up) and $b = 10 fm$ (down): density contour plots.

profile until the separation, i.e. only the concentration gradient is active.

In binary events the charge asymmetry of primary projectile (target)- like fragments, *PLF* and *TLF* provide the essential information about the isospin equilibration rate. At $b = 8 fm$, however, around 25% of the events were ternary and as shown in the previous section for even more central events this mechanism becomes dominant. The *IMF*'s formation in the overlap region will influence the final isospin distribution, rendering more difficult the interpretation of the results. Thus we select here only binary events. We quantify the degree of equilibration through the isospin imbalance ratio R_i Eq.(5-4), [198,199]. The measured isospin dependent quantities are directly the isospin content of the fragments at separation (in the $i = P, T$ rapidity regions), as they result from the mixed reaction 124/112, from the reactions between neutron rich nuclei, (124/124), and between neutron poor nuclei, (112/112), respectively. We report its dependence on t_c for asysoft (squares) and asy-superstiff (circles) *EOS* in Fig. 5-20. A good degree of isospin equilibration corresponds to a “convergence” to 0 of both R_P (upper curves) and R_T (lower curves). From our results we conclude that an asystiff-like *EOS* provides a better agreement to the experimental observations, shown as arrows in Fig.5-20, [198,216]. In fact in the *MSU* experiment there is no particular selection on binary events. We expect that the presence of events with production of Neck-*IMFs* will induce an apparent larger isospin equilibration since more neutrons will migrate to the neck region (and viceversa for protons), as discussed before.

A clear difference between the two equations of state is evident especially for the longer interacting time, $b = 8 fm$ case. Smaller values of the isospin imbalance ratios for asysoft *EOS* point towards a faster equilibration rate. In Refs. [198,216] a possible explanation was proposed related to the observation that below normal density the asysoft *EOS* has a larger value of symmetry energy. Therefore an enhanced isospin equilibration has to be triggered if the diffusion takes place at lower density. In fact the mechanism of charge equilibration is

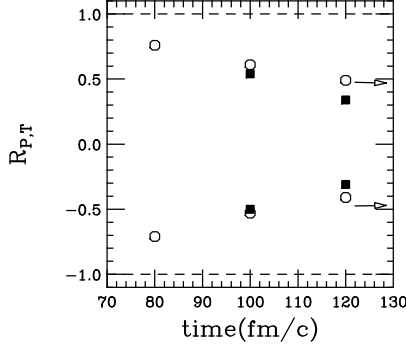


Fig. 5-20. $^{124}Sn + ^{112}Sn$ 50 AMeV collision: interaction time evolution of the projectile (upper) and target (lower) isospin imbalance ratios. Squares: *Asysoft EOS*. Circles: *Superasystiff*. The arrows correspond to the data of Ref.[198].

more complicated at these energies due to reaction dynamics (fast particle emissions, density gradients, etc.), with interesting compensation effects, as shown in the following.

5.7.2 Isospin diffusion and EOS dependence

Let us focus on the “mixed” $^{124}Sn + ^{112}Sn$ case. The isospin content of the two residues at separation is determined by the interplay between the nucleon emission from each ion and by the nucleon transfer through the neck:

$$I_P = \frac{A_{0P}}{A_P} (I_{0P} - \frac{A_{gP}}{A_{0P}} I_{gP} - \frac{A_{PT}}{A_{0P}} I_{PT} + \frac{A_{TP}}{A_{0P}} I_{TP}) \quad (5-10)$$

$$I_T = \frac{A_{0T}}{A_T} (I_{0T} - \frac{A_{gT}}{A_{0T}} I_{gT} + \frac{A_{PT}}{A_{0T}} I_{PT} - \frac{A_{TP}}{A_{0T}} I_{TP}) \quad (5-11)$$

Here I_i, A_i represent asymmetries and masses for: $i = P, T, PLF, TLF$ at separation; $i = 0P, 0T$, initial Projectile/Target; $i = gP, gT$, fast emitted nucleons from Projectile/Target (the label *g* stands for “gas”); $i = PT, TP$, nucleons transferred from projectile (target) to target (projectile).

In Fig. 5-21 we plot the time evolution of the quantities I_{gP}, I_{gT} and A_{gP}, A_{gT} for asysoft and superasystiff *EOS*. We remark that I_{gP} is much larger than $I_{0P} \simeq 0.19$. The same is true for the target but the difference is smaller. Consequently the pre-equilibrium emission reduces the N/Z difference between the two nuclei thus competing with the transfer process.

When the two equations of state are compared a more neutron rich composition of pre-equilibrium is seen in the asysoft case since below normal density, from where most of the emitted nucleons originate, the neutrons (protons) are less (more) bound for this asy-*EOS*. The differences between the two asy-*EOS*

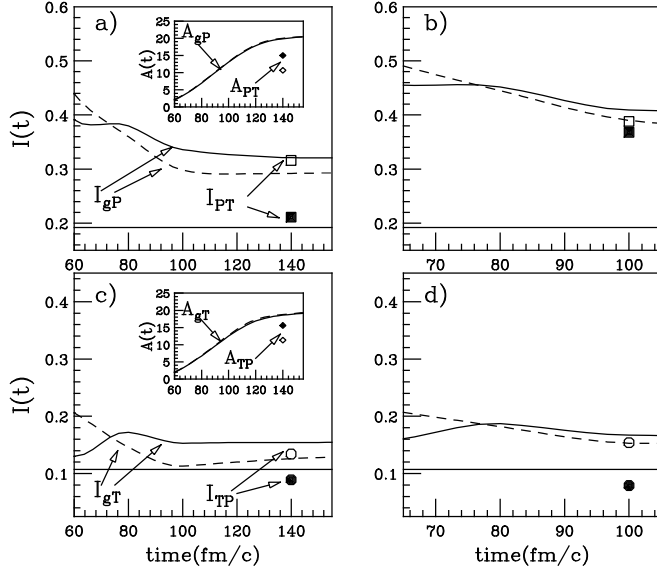


Fig. 5-21. $^{124}Sn + ^{112}Sn$ $b = 8fm$ (left) and $b = 10fm$ (right) collision: time evolution of isospin content and mass of projectile (target) pre-equilibrium emitted particles I_{gP} , A_{gP} (I_{gT} , A_{gT}). The squares (circles) indicate the asymmetry directly transferred from projectile (target) to target (projectile) I_{PT} (I_{TP}), at separation time. Asysoft: full symbols, solid lines. Superasystiff: empty symbols, dashed lines. Horizontal lines give the initial target and projectile asymmetries.

are reduced at larger impact parameters, as seen in the results for $b = 10fm$ in Fig. 5-21. The neutron rich nuclear skin seems to play a more important role for such more peripheral collisions. For the projectile both preequilibrium emission and nucleon transfer drive the system towards a more symmetric configuration. The two processes tend to compensate for the target. Therefore the projectile asymmetry has a more pronounced deviation from the corresponding initial value in comparison to the target.

From the Fig.5-21 we realize that asysoft interactions are very efficient in transferring isospin to the “gas” while the isospin diffusion in the nuclear medium appears more reduced. The opposite is happening with the stiff symmetry term. The final result on isospin equilibration comes out from a kind of compensation, with the asysoft case showing a larger equilibration, see Fig.5-20. The evidence that the isospin content of the free nucleon emission is largely driving the isospin equilibration is extremely important. We can then look for a consistent picture of several observables ranging from isospin effects on fast nucleon emissions and collective flows, see previous Sect.4, to the imbalance ratios of N/Z or other isospin dependent quantities.

Before closing this discussion we would like to elaborate a little more on the physics of isospin diffusion in the nuclear medium at the Fermi energies, and in particular on the conclusion from the simulations of a much stronger effectiveness of a stiff symmetry term. From the Fig.5-21 we see a clear dependence

on the asy-*EOS* of the asymmetry transferred between the two nuclei. In particular, for $b = 8\text{fm}$ we observe that

$$\begin{aligned} I_{PT}^{(supasystiff)} &> I_{PT}^{(asysoft)} > I_{0P} = 0.192 \\ I_{TP}^{(supasystiff)} &> I_{0T} = 0.107 > I_{TP}^{(asysoft)} \end{aligned} \quad (5-12)$$

The origin of these inequalities lies in the presence of density gradients due to the more dilute interface. For the supersystiff *EOS* the neutron migration towards the neck region is favored from both participants. This explains simultaneously $I_{PT}^{(supasystiff)} > I_{0P}$ and $I_{TP}^{(supasystiff)} > I_{0T}$. For the asysoft *EOS* this effect is weakened because the symmetry part of the mean-field for protons and neutrons does not change significantly with density below saturation.

This argument can be made more explicit if we observe that the proton and neutron migration is dictated by the spatial gradients of the corresponding chemical potentials $\mu_n(\rho_p, \rho_n, T)$ and $\mu_p(\rho_p, \rho_n, T)$ [217]. The currents of the two species can be expressed as follows:

$$\begin{aligned} j_n &= -Ct \nabla \mu_n(\rho_p, \rho_n, T) = -Ct \left[\left(\frac{\partial \mu_n}{\partial \rho_n} \right)_{\rho_p, T} \nabla \rho_n + \left(\frac{\partial \mu_n}{\partial \rho_p} \right)_{\rho_n, T} \nabla \rho_p \right] \\ j_p &= -Ct \nabla \mu_p(\rho_p, \rho_n, T) = -Ct \left[\left(\frac{\partial \mu_p}{\partial \rho_n} \right)_{\rho_p, T} \nabla \rho_n + \left(\frac{\partial \mu_p}{\partial \rho_p} \right)_{\rho_n, T} \nabla \rho_p \right], \end{aligned}$$

where C is a constant.

In terms of Landau parameters, i.e.:

$$N_q(T) \frac{\partial \mu_q}{\partial \rho_{q'}} = \delta_{qq'} + F_0^{qq'}, \quad q = n, p \quad q' = n, p \quad (5-13)$$

we obtain:

$$\begin{aligned} j_n &= -Ct \left[\frac{1+I}{2} \frac{1+F_0^{nn}}{N_n} + \frac{1-I}{2} \frac{F_0^{np}}{N_n} \right] \nabla \rho + \frac{\rho}{2} \left[\frac{1+F_0^{nn}}{N_n} - \frac{F_0^{np}}{N_n} \right] \nabla I \\ &= -D_{1n} \nabla \rho - D_{2n} \nabla I \end{aligned} \quad (5-14)$$

$$\begin{aligned} j_p &= -Ct \left[\frac{1+I}{2} \frac{F_0^{pn}}{N_p} + \frac{1-I}{2} \frac{1+F_0^{pp}}{N_p} \right] \nabla \rho + \frac{\rho}{2} \left[\frac{F_0^{pn}}{N_p} - \frac{1+F_0^{pp}}{N_p} \right] \nabla I \\ &= -D_{1p} \nabla \rho - D_{2p} \nabla I \end{aligned} \quad (5-15)$$

In the last expressions we have changed the variables ρ_n, ρ_p to $\rho = \rho_n + \rho_p$ and $I = (\rho_n - \rho_p)/\rho$.

Hence it is clear that not only concentration gradients are important in the dynamics of isospin migration and equilibration, but also density gradients play an essential role. Actually the final result comes out from a delicate balance between the two effects. The stronger density dependence of the stiff symmetry term below normal density enhances the density gradient contribution, finally leading to the larger isospin diffusion of Eqs.(5-12). As already shown the influence of the symmetry term on fast nucleon emissions can partially compensate the effect.

6 Effective interactions in the isovector channel: relativistic approach and the role of the δ meson

The *QHD* effective field model represents a very successful attempt to describe, in a fully relativistic picture, equilibrium and dynamical properties of nuclear systems at the hadronic level [27,28,29]. Consistent results have been obtained for the nuclear structure of finite nuclei [218,219,220], for the *NM* Equation of State and liquid-gas phase transitions [19] and for the dynamics of nuclear collisions [146,221]. Relativistic Random-Phase-Approximation (*RRPA*) theories have been developed to study the nuclear collective response [222,223,77,224,225,226].

This report focusses on the dynamical response and static (equilibrium) properties of Asymmetric Nuclear Matter (*ANM*). We use a relativistic kinetic theory with the aim of a transparent connection between the collective and reaction dynamics and the coupling to various channels of the nucleon-nucleon interaction. One of the main points of discussion is the relevance of the coupling to a scalar isovector channel, the effective $\delta[a_0(980)]$ meson. In fact the scalar-isovector coupling is not necessarily connected to the exchange of a real δ -meson, but such a channel appears automatically in relativistic Hartree-Fock and Dirac-Brueckner-Hartree-Fock treatments from exchange and correlation contributions [33,36].

The introduction of the isovector-scalar channel in covariant approaches should play a key role in the effective interaction in asymmetric matter, see ref.[12,13]. This point has not received great attention before for two main reasons:

- i) The δ -channel has not been considered *a priori*, just on the basis of the weak contribution to the free Nucleon-Nucleon interaction, [227,228]. But in the spirit of the *Effective Field Theory* as a relativistic *Density Functional Theory*, (the *EFT/DFT* framework [229]), the relevance of this channel could be completely different in nuclear matter, due to medium and many-body effects, as noted before. In particular, we expect a large contribution from exchange terms of the strongly coupled isoscalar channels, [36,12,13].
- ii) The extension is not well supported by the existing data on exotic nuclei, as remarked in the refs. [34,220,230,231]. Clearly these conclusions are mainly derived from the lack of information on observables more sensitive to the density dependence of the symmetry term. In particular finite nuclei studies cannot easily disentangle the effects originating from different isovector mesons, since the densities are mainly below saturation, see the discussion in refs.[220,34,232].

We note that recently , see the conclusions of refs. [30,31], the δ -channel has been reconsidered as an interesting improvement of covariant approaches in

the framework of the *EFT/DFT* philosophy. One of the main tasks of our work is then to try to select the dynamical observables more sensitive to it, [12,13].

In this respect the results reported here on the collective response and reaction dynamics can be useful in order to solve the open problem of the determination of the scalar-isovector coupling. Since contributions to this channel are mainly coming from correlation effects [36], the correct microscopic approach should be to derive the relative coupling constant, in a *QHD*-Relativistic Mean Field (*RMF*) framework, from Dirac-Brueckner-Hartree-Fock (*DBHF*) calculations. Several attempts have been recently performed, see [33,34,233,234], but the results are up to now not fully model independent.

An important outcome of our work is to show that the two effective couplings, vector and scalar, in the isovector channel influence in a different way the static (symmetry energy) and dynamic (collective response, reaction observables) properties of asymmetric nuclear matter. This will open new possibilities for a phenomenological determination of these fundamental quantities.

We will often derive transparent analytical results. In order to show also some quantitative effects of the dynamical contribution of the δ -channel we have to fix in some way the corresponding coupling. We have used a constant value (see Table 7) extracted from the *DBHF* analysis of refs.[33,34], where it actually appears not strongly density dependent in a wide range of baryon densities. Some results are also presented with Fock correlations explicitly accounted for (*NLHF* case, see following).

6.1 *QHD effective field theory*

We start from the *QHD* effective field picture of the hadronic phase of nuclear matter [27,28,29]. To include the main dynamical degrees of freedom of the system we will consider the nucleons coupled to the isoscalar scalar σ and vector ω mesons and to the isovector scalar δ and vector ρ mesons.

The Lagrangian density for this model, including non-linear isoscalar/scalar σ -terms [235], is given by:

$$\begin{aligned}
L = & \bar{\psi}[\gamma_\mu(i\partial^\mu - g_\omega V^\mu - g_\rho \mathbf{B}^\mu \cdot \vec{\tau}) - (M - g_\sigma \phi - g_\delta \vec{\tau} \cdot \vec{\delta})] \psi + \\
& \frac{1}{2}(\partial_\mu \phi \partial^\mu \phi - m_s^2 \phi^2) - \frac{a}{3} \phi^3 - \frac{b}{4} \phi^4 - \frac{1}{4} W_{\mu\nu} W^{\mu\nu} + \frac{1}{2} m_v^2 V_\nu V^\nu + \\
& \frac{1}{2}(\partial_\mu \vec{\delta} \cdot \partial^\mu \vec{\delta} - m_\delta^2 \vec{\delta}^2) - \frac{1}{4} \mathbf{G}_{\mu\nu} \mathbf{G}^{\mu\nu} + \frac{1}{2} m_\rho^2 \mathbf{B}_\nu \mathbf{B}^\nu
\end{aligned} \tag{6-1}$$

where $W^{\mu\nu}(x) = \partial^\mu V^\nu(x) - \partial^\nu V^\mu(x)$ and $\mathbf{G}^{\mu\nu}(x) = \partial^\mu \mathbf{B}^\nu(x) - \partial^\nu \mathbf{B}^\mu(x)$.

Here $\psi(x)$ is the nucleon fermionic field, $\phi(x)$ and $V^\nu(x)$ represent neutral scalar and vector boson fields, respectively. $\vec{\delta}(x)$ and $\mathbf{B}^\nu(x)$ are the charged scalar and vector fields and $\vec{\tau}$ denotes the isospin matrices.

From the Lagrangian, Eq.(6-1), with the Euler procedure a set of coupled equations of motion for the meson and nucleon fields can be derived. The basic approximation in nuclear matter applications consists in neglecting all the terms containing derivatives of the meson fields with respect to the mass contributions. Then the meson fields are simply connected to the operators of the nucleon scalar and current densities by the following equations:

$$\hat{\Phi}/f_\sigma + A\hat{\Phi}^2 + B\hat{\Phi}^3 = \bar{\psi}(x)\psi(x) \equiv \hat{\rho}_S \quad (6-2)$$

$$\begin{aligned} \hat{V}^\mu(x) &\equiv g_\omega V^\mu = f_\omega \bar{\psi}(x)\gamma^\mu \psi(x) \equiv f_\omega \hat{j}_\mu, \\ \hat{\mathbf{B}}^\mu(x) &\equiv g_\rho \mathbf{B}^\mu = f_\rho \bar{\psi}(x)\gamma^\mu \vec{\tau} \psi(x), \\ \hat{\vec{\delta}}(x) &\equiv g_\delta \vec{\delta} = f_\delta \bar{\psi}(x)\vec{\tau} \psi(x) \end{aligned} \quad (6-3)$$

where $\hat{\Phi} = g_\sigma \phi$, $f_\sigma = (g_\sigma/m_\sigma)^2$, $A = a/g_\sigma^3$, $B = b/g_\sigma^4$, $f_\omega = (g_\omega/m_\omega)^2$, $f_\rho = (g_\rho/m_\rho)^2$, $f_\delta = (g_\delta/m_\delta)^2$.

For the nucleon fields we get a Dirac-like equation. Indeed after substituting Eqs.(6-2,6-3) for the meson field operators, we obtain an equation which contains only nucleon field operators. The equations can be consistently solved in a Mean Field Approximation (*RMF*), where most applications have been performed, i.e. in a self-consistent Hartree scheme [28,29].

The inclusion of Fock terms is conceptually important [236,237] since it automatically leads to contributions to various meson exchange channels, also in absence of explicit coupling terms. A thorough study of the Fock contributions in a *QHD* approach with non-linear self-interacting terms has been recently performed [238], in particular for asymmetric matter [36].

6.1.1 Relativistic transport equations with Fock terms

We now discuss a kinetic approach consistent with the previous approximation. We are concerned with a semiclassical description of nuclear dynamics, so that the nuclear medium is supposed to be in states for which the nucleon scalar and current densities are smooth functions of the space-time coordinates. Within the *QHD* model we focus our analysis on a description of the many-body nuclear system in terms of one-body dynamics. Correlation effects can be effectively included at the level of coupling constants, as noted in the discussion of the results.

We move to the quantum phase-space introducing the Wigner transform of the one-body density matrix for the fermion field [239,240]. The one-particle Wigner function is defined as:

$$[\hat{F}(x, p)]_{\alpha\beta} = \frac{1}{(2\pi)^4} \int d^4R e^{-ip\cdot R} \langle : \bar{\psi}_\beta(x + \frac{R}{2}) \psi_\alpha(x - \frac{R}{2}) : \rangle ,$$

where α and β are double indices for spin and isospin. The brackets denote statistical averaging and the colons denote normal ordering. The equation of motion is derived from the Dirac field equation by using standard procedures (see e.g.[239,240]), as:

$$\begin{aligned} & \frac{i}{2} \partial_\mu [\gamma^\mu \hat{F}(x, p)]_{\alpha\beta} + p_\mu [\gamma^\mu \hat{F}(x, p)]_{\alpha\beta} - M \hat{F}_{\alpha\beta}(x, p) \\ & - \frac{g_\omega}{(2\pi)^4} \int_R e^{-ip\cdot R} \langle : \bar{\psi}_\beta(x_+) \gamma_{\alpha\gamma}^\mu \psi_\gamma(x_-) V_\mu(x_-) : \rangle \\ & + \frac{g_\sigma}{(2\pi)^4} \int_R e^{-ip\cdot R} \langle : \bar{\psi}_\beta(x_+) \psi_\alpha(x_-) \phi(x_-) : \rangle \\ & - \frac{g_\rho}{(2\pi)^4} \int_R e^{-ip\cdot R} \langle : \bar{\psi}_\beta(x_+) \gamma_{\alpha\gamma}^\mu \psi_\gamma(x_-) \vec{\tau} \cdot \mathbf{B}_\mu(x_-) : \rangle \\ & + \frac{g_\delta}{(2\pi)^4} \int_R e^{-ip\cdot R} \langle : \bar{\psi}_\beta(x_+) \psi_\alpha(x_-) \vec{\delta}(x_-) : \rangle \\ & = 0 \end{aligned} \quad (6-4)$$

with $x_+ = x + \frac{R}{2}$ and $x_- = x - \frac{R}{2}$. When we insert the Eqs.(6-2,6-3) for the meson field operators we clearly see the appearance of Fock contributions (at the lowest order in density matrices).

The Wigner function is a matrix in spin and isospin space; in the case of asymmetric NM it is useful to decompose it into neutron and proton components. Following the treatment of the Fock terms in non-linear QHD introduced in Refs. [238,36], we obtain the kinetic equation:

$$\begin{aligned} & \frac{i}{2} \partial_\mu \gamma^\mu \hat{F}^{(i)}(x, p) + \gamma^\mu p_{\mu i}^* \hat{F}^{(i)}(x, p) - M_i^* \hat{F}^{(i)}(x, p) + \\ & \frac{i}{2} \Delta \left[\tilde{f}_\omega j_\mu(x) \gamma^\mu \pm \tilde{f}_\rho j_{3\mu}(x) \gamma^\mu - \tilde{f}_\sigma \rho_S(x) \mp \tilde{f}_\delta \rho_{S3}(x) \right] \hat{F}^{(i)}(x, p) = 0, \end{aligned} \quad (6-5)$$

where $i = n, p$, and here and in the following upper and lower signs correspond to protons and neutrons, respectively. Here $\Delta = \partial_x \cdot \partial_p$, with ∂_x acting only on the first term of the products and $\rho_{S3} = \rho_{Sp} - \rho_{Sn}$ and $j_{3\mu}(x) = j_\mu^p(x) - j_\mu^n(x)$ are the isovector scalar density and the isovector baryon current, respectively. We have defined the kinetic momenta and effective masses as:

$$\begin{aligned} p_{\mu i}^* &= p_\mu - \tilde{f}_\omega j_\mu(x) \pm \tilde{f}_\rho j_{3\mu}(x) , \\ M_i^* &= M - \tilde{f}_\sigma \rho_S(x) \pm \tilde{f}_\delta \rho_{S3}(x) , \end{aligned} \quad (6-6)$$

with the effective coupling functions given by:

$$\begin{aligned} \tilde{f}_\sigma &= \frac{\Phi}{\rho_S} - \frac{1}{8} \frac{d\Phi(x)}{d\rho_S(x)} - \frac{1}{2\rho_S} \text{Tr} \hat{F}^2(x) \frac{d^2\Phi(x)}{d\rho_S^2(x)} + \frac{1}{2} f_\omega + \frac{3}{2} f_\rho - \frac{3}{8} f_\delta , \\ \tilde{f}_\omega &= \frac{1}{8} \frac{d\Phi(x)}{d\rho_S(x)} + \frac{5}{4} f_\omega + \frac{3}{4} f_\rho + \frac{3}{8} f_\delta , \\ \tilde{f}_\delta &= -\frac{1}{8} \frac{d\Phi(x)}{d\rho_S(x)} + \frac{1}{2} f_\omega - \frac{1}{2} f_\rho + \frac{9}{8} f_\delta , \\ \tilde{f}_\rho &= \frac{1}{8} \frac{d\Phi(x)}{d\rho_S(x)} + \frac{1}{4} f_\omega + \frac{3}{4} f_\rho - \frac{1}{8} f_\delta , \end{aligned} \quad (6-7)$$

where $8 \text{Tr} \hat{F}^2(x) = \rho_S^2 + j_\mu j^\mu + \rho_{S3}^2 + j_{3\mu} j^{3\mu}$. We recall that we are dealing with a transport equation so the currents and densities, in general, are varying functions of the space-time, at variance with the case of nuclear matter at equilibrium. Thus also the effective couplings are space, i.e. density, dependent.

The expression of Eq.(6-6) for the effective mass embodies an isospin contribution from Fock terms even without a direct inclusion of the δ meson in the Lagrangian. As seen from Eqs.6-7 the usual *RMF* approximation (Hartree level) is recovered from the Hartree-Fock results, by changing the effective coupling functions $\tilde{f}_i (i = \sigma, \omega, \rho, \delta)$, Eqs.(6-7), to the the explicit coupling constants f_i .

6.1.2 Equilibrium properties: the nuclear Equation of State

The energy density and pressure for symmetric and asymmetric nuclear matter and the n, p effective masses are self-consistently calculated in terms of the four boson coupling constants, $f_i \equiv (\frac{g_i^2}{m_i^2})$, $i = \sigma, \omega, \rho, \delta$, and the two parameters of the σ self-interacting terms, $A \equiv \frac{a}{g_\sigma^3}$ and $B \equiv \frac{b}{g_\sigma^4}$, [12,13]. Here we will present results at the Hartree level. The extension to Fock contributions is easily performed following the scheme discussed before.

From the Lagrangian, Eq.(6-1), the energy-momentum tensor is derived in the mean field approximation as

$$T_{\mu\nu} = i\bar{\psi}\gamma_\mu\partial_\nu\psi + [\frac{1}{2}m_\sigma^2\phi^2 + U(\phi) + \frac{1}{2}m_\delta^2\vec{\delta}^2]$$

$$-\frac{1}{2}m_\omega^2\omega_\lambda\omega^\lambda - \frac{1}{2}m_\rho^2\mathbf{B}_\lambda\mathbf{B}^\lambda]g_{\mu\nu}. \quad (6-8)$$

with $U(\phi)$, the nonlinear potential of the σ meson $U(\phi) = \frac{1}{3}a\phi^3 + \frac{1}{4}b\phi^4$. By using the field equations for mesons, the equation of state for thermal matter is derived, as in [12], with energy density

$$\begin{aligned} \epsilon = \sum_{i=n,p} 2 \int \frac{d^3k}{(2\pi)^3} E_i^*(k) (n_i(k) + \bar{n}_i(k)) + \frac{1}{2}m_\sigma^2\phi^2 \\ + U(\phi) + \frac{g_\omega^2}{2m_\omega^2}\rho_B^2 + \frac{g_\rho^2}{2m_\rho^2}\rho_{B3}^2 + \frac{g_\delta^2}{2m_\delta^2}\rho_{S3}^2, \end{aligned} \quad (6-9)$$

and pressure

$$\begin{aligned} P = \sum_{i=n,p} \frac{2}{3} \int \frac{d^3k}{(2\pi)^3} \frac{k^2}{E_i^*(k)} (n_i(k) + \bar{n}_i(k)) - \frac{1}{2}m_\sigma^2\phi^2 \\ - U(\phi) + \frac{g_\omega^2}{2m_\omega^2}\rho_B^2 + \frac{g_\rho^2}{2m_\rho^2}\rho_{B3}^2 - \frac{g_\delta^2}{2m_\delta^2}\rho_{S3}^2. \end{aligned} \quad (6-10)$$

where $E_i^* = \sqrt{k^2 + M_i^{*2}}$ and the nucleon effective masses are given in Eq.6-6. The $n_i(k)$ and $\bar{n}_i(k)$ in Eqs.6-9,6-10 are the p,n fermion and antifermion distribution functions:

$$\begin{aligned} n_i(k) &= \frac{1}{1 + \exp\{(E_i^*(k) - \mu_i^*)/T\}}, \\ \bar{n}_i(k) &= \frac{1}{1 + \exp\{(E_i^*(k) + \mu_i^*)/T\}}. \end{aligned} \quad (6-11)$$

The effective chemical potentials μ_i^* are given in terms of the vector meson mean fields

$$\mu_i = \mu_i^* - f_\omega\rho_B \mp f_\rho\rho_{B3}, \quad (6-12)$$

where μ_i are the thermodynamical chemical potentials $\mu_i = \partial\epsilon/\partial\rho_i$, which at zero temperature reduce to the Fermi energies $E_{Fi} \equiv \sqrt{k_{Fi}^2 + M_i^{*2}}$. The baryon densities ρ_B and the scalar densities ρ_S are given by (γ is the spin/isospin degeneracy)

Table 7

Parameter sets of the *QHD* models discussed here

parameter	<i>NLρ</i>	<i>NLρδ</i>	<i>NLHF</i>
f_σ (fm^2)	11.3	<i>same</i>	9.15
f_ω (fm^2)	6.5	<i>same</i>	3.22
f_ρ (fm^2)	1.1	3.15	1.9
f_δ (fm^2)	0.00	2.4	1.4
A (fm^{-1})	0.02	<i>same</i>	0.098
B	-0.004	<i>same</i>	-0.021

$$\begin{aligned} \rho_B &= \gamma \int \frac{d^3k}{(2\pi)^3} (n(k) - \bar{n}(k)), \\ \rho_S &= \gamma \int \frac{d^3k}{(2\pi)^3} \frac{M^*}{E^*} (n(k) + \bar{n}(k)). \end{aligned} \quad (6-13)$$

At the temperatures of interest here the antybaryon contributions are actually negligible.

The isoscalar meson couplings are fixed from symmetric nuclear matter properties at $T = 0$: saturation density $\rho_0 = 0.15 fm^{-3}$, binding energy $E/A = -16 MeV$, nucleon effective mass $M^* = 0.7 M_N$ ($M_N = 939 MeV$) and incompressibility $K_V = 240 MeV$ at ρ_0 . The fitted f_σ, f_ω, A, B parameters are reported in Table 7. They are quite standard for these minimal non-linear *RMF* models, with values compatible with microscopic *DBHF* estimations [33,34] in a wide range of densities. In order to isolate the effects in the isovector channel we will review results obtained using the same isoscalar interaction and with the $\rho(NL\rho)$ – or the $\rho + \delta(NL\rho\delta)$ – couplings in the isovector part (refs.[12,13]. The symmetry energy at saturation is fixed to the Bethe-Weiszäcker fourth parameter $a_4 = 30.5 MeV$. *NLHF* stands for the non-linear Hartree-Fock scheme described before.

6.1.3 Symmetry energy

The symmetry energy in *ANM* is defined from the expansion of the energy per nucleon $E(\rho_B, I)$ in terms of the asymmetry parameter I defined as $I \equiv -\frac{\rho_{B3}}{\rho_B} = \frac{\rho_{Bn} - \rho_{Bp}}{\rho_B} = \frac{N-Z}{A}$. We have

$$E(\rho_B, I) \equiv \frac{\epsilon(\rho_B, I)}{\rho_B} = E(\rho_B) + E_{sym}(\rho_B)I^2 + O(I^4) + \dots \quad (6-14)$$

and so in general

$$E_{sym} \equiv \frac{1}{2} \frac{\partial^2 E(\rho_B, I)}{\partial I^2} \Big|_{I=0} = \frac{1}{2} \rho_B \frac{\partial^2 \epsilon}{\partial \rho_{B3}^2} \Big|_{\rho_{B3}=0} \quad (6-15)$$

In the Hartree case an explicit expression for the symmetry energy is easily derived [11,12,13]:

$$E_{sym}(\rho_B) = \frac{1}{6} \frac{k_F^2}{E_F^*} + \frac{1}{2} f_\rho \rho_B - \frac{1}{2} f_\delta \frac{M^{*2} \rho_B}{E_F^{*2} [1 + f_\delta A(k_F, M^*)]} \\ \equiv E_{sym}^{kin} + E_{sym}^{pot}, \quad (6-16)$$

where k_F is the nucleon Fermi momentum corresponding to ρ_B , $E_F^* \equiv \sqrt{(k_F^2 + M^{*2})}$ and M^* is the effective nucleon mass in symmetric NM , $M^* = M_N - g_\sigma \phi$.

$A(k_F, M^*)$ represents the integral

$$A(k_F, M^*) \equiv \frac{4}{(2\pi)^3} \int d^3k \frac{k^2}{(k^2 + M^{*2})^{3/2}} = 3 \left(\frac{\rho_S}{M^*} - \frac{\rho_B}{E_F^*} \right) \quad (6-17)$$

We remark that $A(k_F, M^*)$ is very small at low densities, and actually can still be neglected up to a baryon density $\rho_B \simeq 3\rho_0$, [12,13]. Then in the density range of interest here we can use, to leading order, a much simpler form of the symmetry energy, with more transparent δ -meson effects:

$$E_{sym}(\rho_B) = \frac{1}{6} \frac{k_F^2}{E_F^*} + \frac{1}{2} \left[f_\rho - f_\delta \left(\frac{M^*}{E_F^*} \right)^2 \right] \rho_B \quad (6-18)$$

We see that, when the δ is included, the empirical a_4 value actually corresponds to the combination $[f_\rho - f_\delta (\frac{M^*}{E_F^*})^2]$ of the (ρ, δ) coupling constants. Therefore if $f_\delta \neq 0$ we have to increase correspondingly the ρ -coupling (see Fig.1 of ref.[11]).

In Table 7 the $NL\rho$ set corresponds to $f_\delta = 0$. In the $NL\rho\delta$ interaction f_δ is chosen as $2.4 fm^2$, roughly derived from the analysis of ref.[34]. As already noted before this choice is not essential for our discussion: the aim of our work is to show the new dynamical effects of the δ -meson coupling and to select the corresponding most sensitive observables.

In order to have the same a_4 at saturation we must increase the ρ -coupling constant by a factor three, up to $f_\rho = 3.15 fm^2$. Now the symmetry energy at saturation density is actually built from the balance of scalar (attractive) and vector (repulsive) contributions, with the scalar channel becoming weaker

with increasing baryon density. This is clearly shown in Fig.6-1. This is indeed the isovector counterpart of the saturation mechanism occurring in the isoscalar channel for symmetric nuclear matter. From this consideration we get a further support to the introduction of the δ -coupling in the symmetry energy evaluation.

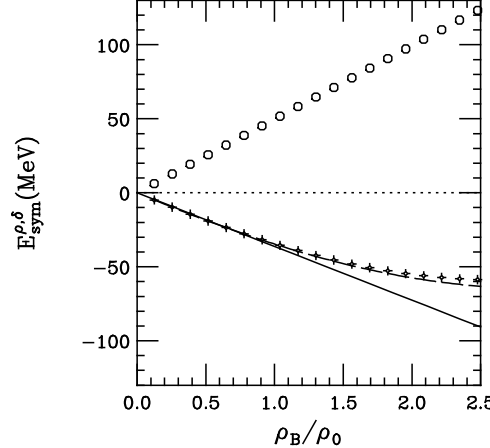


Fig. 6-1. ρ - (open circles) and δ - (crosses) contributions to the potential symmetry energy, second and third terms of Eq.(6-16). The dashed line is the approximate δ -contribution of Eq.(6-18). The solid line is a linear extrapolation of the low density behaviour.

In Fig.6-2 we show the total symmetry energy for the different models. At subnuclear densities, $\rho_B < \rho_0$, in both cases, $NL\rho$ and $NL\rho\delta$, from Eq.(6-18) we have an almost linear dependence of E_{sym} on the baryon density, since $M^* \simeq E_F$ as a good approximation. Around and above ρ_0 we see a steeper increase in the $(\rho + \delta)$ case since M^*/E_F is decreasing.

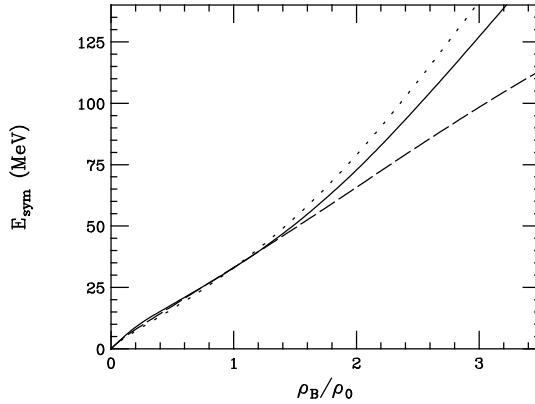


Fig. 6-2. Total (kinetic + potential) symmetry energy as a function of the baryon density. Dashed line ($NL\rho$). Dotted line ($NL\rho\delta$). Solid line $NLHF$.

In conclusion when the δ -channel is included the behaviour of the symmetry energy is stiffer at high baryon density from the relativistic mechanism dis-

cussed before. This is in fact due to a larger contribution from the ρ relative to the δ meson. We expect to see these effects more clearly in the relativistic reaction dynamics at intermediate energies, where higher densities are reached (see Sect.8).

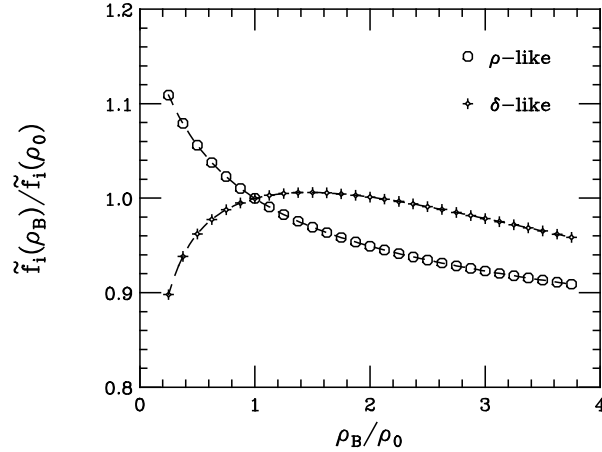


Fig. 6-3. Baryon density variation of the isovector effective coupling when the Fock terms are included, model *NLHF*.

When the Fock terms are evaluated the new “effective” couplings Eqs.(6-7) naturally acquire a density dependence. This is shown in Fig.6-3 for the isovector terms. The decrease of the ρ coupling at high density accounts for the slight softening of the symmetry energy, Fig.6-2, in agreement with *DBHF* expectations, see [34,232]. Details of the calculation can be found in Refs.[36,12].

In Fig.6-4 we show the Equation of State (energy per nucleon) for pure neutron matter ($I = 1$) obtained with the two parameter Sets, $NL\rho$ and $NL\rho\delta$. The values, in particular for the $NL\rho\delta$ case, are in good agreement with recent non-relativistic Quantum-Monte-Carlo variational calculations with realistic 2– and 3–body forces [47]. The inclusion of the δ -coupling leads to a larger repulsion at baryon densities roughly above $1.5\rho_0$. This would be of interest for the structure of neutron stars. It is also relevant for the possibility of a transition to new forms of deconfined nuclear matter [241].

6.1.4 Symmetry Pressure and Symmetry Incompressibility

From the previous analysis we expect to see also interesting δ -effects on the slope (*symmetry pressure*) and curvature (*symmetry incompressibility*) of the symmetry energy around ρ_0 . These quantities and their relevant physical meaning were already discussed in Sect.2 in a non-relativistic framework.

From Eq.(6-18) we get the potential contribution to the density variation of E_{sym} (after some algebra):

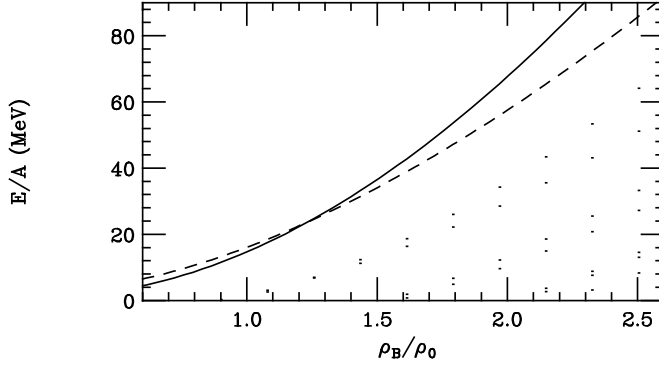


Fig. 6-4. *EOS* for pure neutron matter. Dashed line: $Nl\rho$. Solid line: $NL\rho\delta$).

$$\begin{aligned} \frac{\partial E_{sym}}{\partial \rho_B} \mid_{pot} &= \frac{1}{2} [f_\rho - f_\delta \left(\frac{M^*}{E_F} \right)^2] + \\ &f_\delta \left(\frac{M^* k_F}{E_F^2} \right)^2 \left[\frac{1}{3} - \frac{\rho_B}{M^*} \frac{\partial M^*}{\partial \rho_B} \right]. \end{aligned} \quad (6-19)$$

Around normal density ρ_0 the first term is fixed by the a_4 value (cfr. Eq.(6-18)). The second term (always positive since $(\partial M^* / \partial \rho_B) < 0$) gives a net increase of the slope, due to the δ -field introduction, as seen also in Fig.6-2. To be more quantitative, with our parametrization we get a potential contribution to the slope L of $45 MeV$ from the first term and a genuine δ -contribution of about $20 MeV$ from the second one. When we include also the kinetic part (from the first term of Eq.(6-18)) we have a total slope parameter going from $L(\rho) = +84 MeV$ to $L(\rho + \delta) = +103 MeV$.

We note again that the slope parameter, or equivalently the *Symmetry Pressure* $P_{sym} \equiv \rho_0 L / 3$, is of great importance for structure properties, being linked to the thickness of the neutron skin in n-rich (stable and/or unstable) nuclei [242,243,244,30], and to the position of the drip-line. Moreover the same parameter gives an estimate of the shift of the saturation density with asymmetry (at the lowest order in I^2), easily obtained from a linear expansion around the symmetric value $\rho_0(I = 0)$ as shown in Sect.2, [52].

It is instructive to perform a similar analysis for the curvature parameter K_{sym} . Now the potential contribution is *exclusively* given by the δ -meson, with a definite positive sign, as we can see from the previous discussion. It is a large effect on the total since the kinetic part of the symmetry incompressibility is quite small [245]. Compared to non-relativistic effective parametrizations, in Sect.2, when we add the δ -meson, we move from a linear to a roughly parabolic ρ_B -dependence of the symmetry energy.

With our parameters we pass from a $K_{sym}(\rho) = +7 MeV$ (only kinetic) to a $K_{sym}(\rho + \delta) = +120 MeV$ [245]. Thus this quantity appears extremely interesting to look at experimentally. The problem is that the effect on the total

incompressibility of asymmetric matter, that likely could be easier to measure, is not trivial. What really matters for the total incompressibility is the combination ($K_{sym} - 6L$), as shown in Sect.2, with the possibility of a compensation between the two terms. Just by chance this is actually what is happening in our calculations since for the above combination we get -497MeV in the case of only ρ -coupling, and -504MeV when we add also the δ -field.

6.1.5 Finite Temperature Effects

In the temperature range of interest in this paper, below the critical temperature T_c of the liquid-gas phase transition of the order of $15 - 16$ MeV, temperature effects on the symmetry properties are not expected to be large. Indeed the contributions of antifermions, that could modify all the terms with the scalar densities are still very reduced. For both cases, ρ and $(\rho + \delta)$, the temperature variation of symmetry energy is quite small. We have a reduction mainly coming from the kinetic contribution due to the smoothing of the n/p Fermi distributions. We note that this result is in full agreement with relativistic Brueckner-Hartree-Fock calculations [247].

The temperature effect on the nucleon mass splitting, given by a difference of n/p scalar densities Eq.(6-6), is even smaller. In the following subsection we will study in detail the phase diagram of heated asymmetric nuclear matter, focussing in particular on the instability regions.

6.2 Mechanical and chemical instabilities

Heavy-ion collisions can provide the possibility of studying equilibrated nuclear matter far away from normal conditions, i.e. to sample new regions of the NM phase diagram. In particular the process of multifragmentation allows to probe dilute nuclear matter at finite temperatures. In the symmetric case we expect to see a phase transition of first order of liquid-gas type, as suggested from the very first equations of state built with effective interactions [248,249,250].

As discussed extensively in Sect.3 in a non-relativistic framework, for asymmetric nuclear matter a qualitatively new feature in the liquid-gas phase transition is expected, the onset of a coupling to chemical instabilities (component separation). This will show up in a novel nature of the unstable modes, the mixture of density and charge fluctuations leading to an *Isospin Distillation*. Indeed, equilibrium thermodynamics as well as non-equilibrium kinetics both predict that an asymmetric system will separate into more symmetric larger fragments ("liquid" phase) and into neutron-rich light fragments ("gas" phase). Since the effect is driven by the isospin dependent part of the nuclear

equation of state, here we will look at the influence of the δ -coupling on this new liquid-gas phase transition.

As discussed earlier the instability condition of a two-component, n/p , thermodynamical system is given by

$$\left(\frac{\partial P}{\partial \rho}\right)_{T,y} \left(\frac{\partial \mu_p}{\partial y}\right)_{T,P} < 0, \quad (6-20)$$

where P is the pressure, μ_p is the proton chemical potential and y the proton fraction Z/A , related to the asymmetry parameter $I = 1 - 2y$. Eq.(6-20) is equivalent to constrain the free energy to be a convex function in the space of the n, p density oscillations, $\delta\rho_n, \delta\rho_p$. In charge symmetric matter *isoscalar* (total density) $\delta\rho_n + \delta\rho_p$ and *isovector* (concentration) $\delta\rho_n - \delta\rho_p$ oscillations are not coupled and we have two separate conditions for instability:

$$\begin{aligned} \left(\frac{\partial P}{\partial \rho}\right)_{T,y} &\leq 0, \quad \text{mechanical, i.e. vs. density oscillations, and} \\ \left(\frac{\partial \mu_p}{\partial y}\right)_{T,P} &\leq 0, \quad \text{chemical, i.e. vs. concentration oscillations.} \end{aligned} \quad (6-21)$$

In asymmetric matter the isoscalar and isovector modes are coupled and the two separate inequalities do not anymore maintain a physical meaning, in the sense that they do not select the nature of the instability. Inside the general condition Eq.(6-20) the corresponding unstable modes are a mixing of density and concentration oscillations, very sensitive to the charge dependent part of the nuclear interaction in the various instability regions [20].

In dilute asymmetric NM (n-rich) the normal unstable modes for all realistic effective interactions are still *isoscalar-like*, i.e. in phase $n - p$ oscillations but with a larger proton component. This leads to a more symmetric high density (liquid) phase everywhere under the instability line defined by Eq.(6-20) and consequently to a more neutron-rich gas (*Isospin Distillation*). Such "chemical effect" is driven by the increasing symmetry repulsion going from low to roughly the saturation density and so it appears rather sensitive to the symmetry energy of the used effective interaction at subnuclear densities.

In this section we study the effect of the δ -coupling on the instability region given by Eq.(6-20) in dilute asymmetric nuclear matter and on the structure of the corresponding unstable modes. We start from an identity valid for any binary thermodynamical system

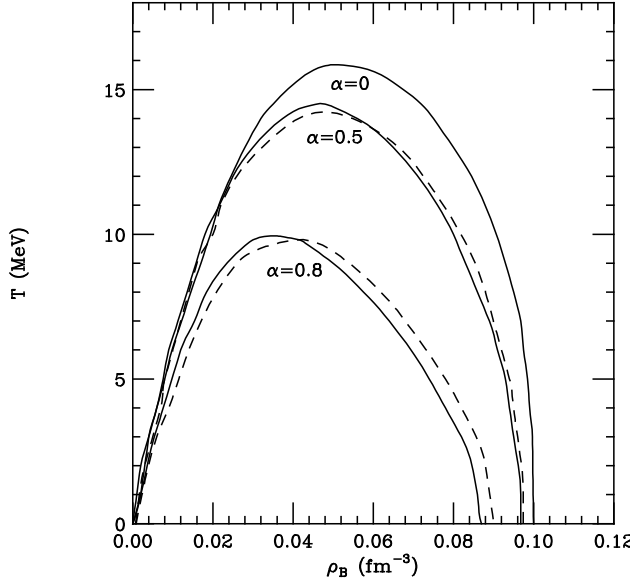


Fig. 6-5. Limits of the instability region in the T, ρ_B plane for various asymmetries. Dashed lines: $NL\rho$). Solid lines: $NL\rho\delta$) [α being the asymmetry parameter].

$$\left(\frac{\partial \mu_p}{\partial \rho_p}\right)_{T, \rho_n} \left(\frac{\partial \mu_n}{\partial \rho_n}\right)_{T, \rho_p} - \left(\frac{\partial \mu_p}{\partial \rho_n}\right)_{T, \rho_p} \left(\frac{\partial \mu_n}{\partial \rho_p}\right)_{T, \rho_n} = \frac{1}{(1-y)\rho^2} \left(\frac{\partial P}{\partial \rho}\right)_{T, y} \left(\frac{\partial \mu_p}{\partial y}\right)_{T, P} \quad (6-22)$$

where μ_q, ρ_q ($q = n, p$) are respectively neutron/proton chemical potentials and densities. Thus from the chemical potential on each isotherm, Eq.(6-12), we can easily compute the limits of the instability region in the T, ρ_B plane for dilute asymmetric NM in the two choices, without and with the δ -meson.

The results are shown in Fig.6-5. The inclusion of a δ -field (solid lines) appears not to affect much the instability limits even at relatively large asymmetry $I = 0.8$ ($N \simeq 9Z$). We notice just a small reduction and a shift to the left (lower densities) of the whole region: this can be related to a slightly larger symmetry repulsion. We can understand the relatively small δ -effect on the stability border by remembering that for low densities, well below ρ_0 , the symmetry term has roughly the same linear behaviour in both (ρ) and $(\rho + \delta)$ schemes, fixed by the a_4 parameter (see the discussion after Eq.(6-18)). Only for very large asymmetries it appears relatively easier in the δ case to be in the stable liquid phase.

A larger difference can be seen in the behavior of the quantity Eq.(6-20) inside the instability region. This is plotted in Fig.6-6 for various asymmetries at zero temperature. The solid curves (with δ -coupling) are systematically above the dashed ones, possible signature of a weaker instability. In fact this is not the

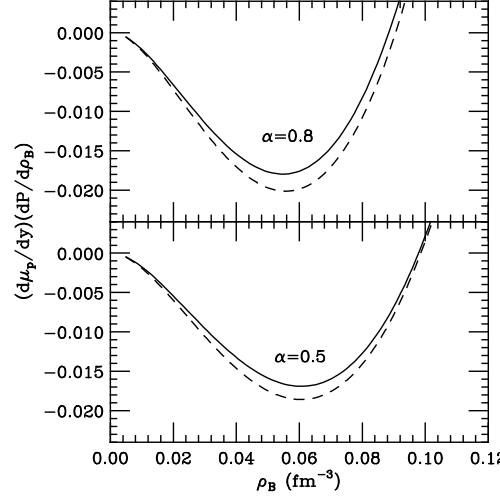


Fig. 6-6. The quantity Eq.(6-20) inside the instability region at $T = 0$ and various asymmetries. Dashed lines: $NL\rho$. Solid lines: $NL\rho\delta$.

case since, as shown in the following, the δ -meson is not affecting the low density unstable modes. In order to better understand the origin of this effect we study the structure of the corresponding unstable modes. We follow the Landau dispersion relation approach to small amplitude oscillations in Fermi liquids, as in Sect.3. For a two component (n, p) matter the interaction is characterized by the Landau parameters $F_0^{q,q'}$, $(q, q') = (n, p)$ defined as

$$N_q(T) \frac{\partial \mu_q}{\partial \rho_{q'}} \equiv \delta_{q,q'} + F_0^{q,q'} \quad (6-23)$$

where $N_q(T)$ represents the single particle level density at the Fermi energy. At zero temperature it has the simple form ($\hbar = c = 1$) $N_q = \frac{k_{Fq} E_{Fq}^*}{\pi^2}$, $q = n, p$.

In the symmetric case ($F_0^{nn} = F_0^{pp}$, $F_0^{np} = F_0^{pn}$), the Eqs.(6-21) correspond to the two Pomeranchuk instability conditions

$$\begin{aligned} F_0^s &= F_0^{nn} + F_0^{np} < -1 & \text{mechanical} \\ F_0^a &= F_0^{nn} - F_0^{np} < -1 & \text{chemical.} \end{aligned} \quad (6-24)$$

From the dispersion relations F_0^s will give the properties of the density (isoscalar) modes while F_0^a is related to the concentration (isovector) modes. For asymmetric NM we have corresponding generalized Landau parameters F_{0g}^s, F_{0g}^a which characterize the asymmetric collective response. They can be expressed as fixed combinations of the $F_0^{q,q'}$ for each baryon density, asymmetry and temperature. This transformation reduces Eq.(6-22) to a "diagonal" form [20]

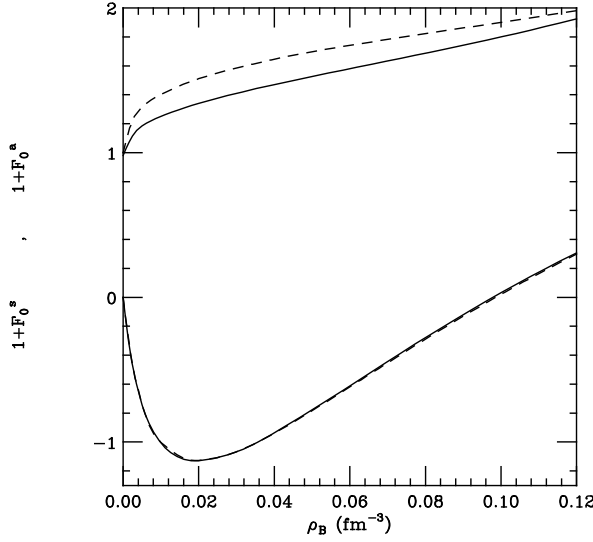


Fig. 6-7. Behaviour of the generalized Landau parameters $F_{0g}^{a,s}$ inside the instability region at zero temperature and asymmetry $I = 0.5$ ($N = 3\bar{Z}$). Dashed lines: $NL\rho$. Solid lines: $NL\rho\delta$.

$$(1 + F_{0g}^s)(1 + F_{0g}^a) = \frac{4}{(1 - y)\rho^2} \left(\frac{N_n N_p}{N_n + N_p} \right)^2 \times \left(\frac{\partial P}{\partial \rho} \right)_{T,y} \left(\frac{\partial \mu_p}{\partial y} \right)_{T,P} \quad (6-25)$$

As already discussed, in the unstable region of dilute asymmetric NM we have *isoscalar-like* unstable modes with $1 + F_{0g}^s < 0$, while the combination $1 + F_{0g}^a$ will always stay positive. In Fig.6-7 we report a full calculation of these two quantities in the unstable region at zero temperature, for asymmetry $I = 0.5$, with and without the δ -coupling. The δ -meson almost does not affect at all the unstable mode, given by the F_{0g}^s parameter. Hence the limits of the instability region, for $I = 0.5$, are not changed (see the Figs.6-5,6-6). We have a larger effect on the F_{0g}^a parameter which describes "stable" *isovector-like* modes, that actually can propagate as good zero-sound collective motions since $F_{0g}^a > 0$. This can be expected from the isovector nature of the δ -meson. From here we get the main differences seen in Fig.6-6 for the Eq.(6-20) inside the instability region, just the product of the two quantities plotted in Fig.6-7 (from Eq.(6-25)).

Another interesting aspect of the comparison between Fig.6-6 and Fig.6-7 is the shift of the "maximum instability" density region. From the thermodynamical condition reported in Fig.6-6 it seems that the largest instability (the

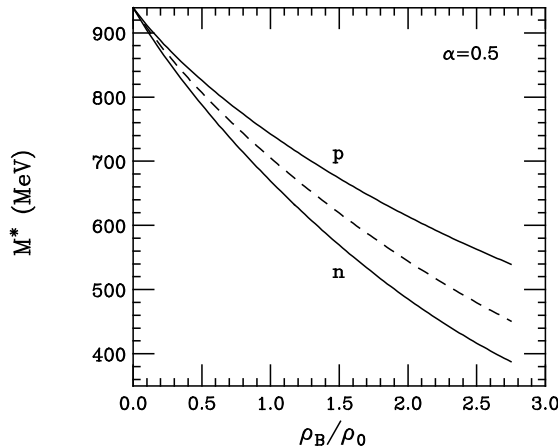


Fig. 6-8. Neutron and proton effective masses vs. the baryon density for $I = 0.5$ ($N = 3Z$), $NL\rho\delta$ parameters. The dashed line corresponds to symmetric nuclear matter.

most negative value) is around $\rho_B = 0.06 fm^{-3}$. In fact from Fig.6-7 we see that the fastest unstable mode, corresponding to the most negative Pomeranchuk condition for $1 + F_{0g}^s$, is actually present for more dilute matter, around $\rho_B = 0.02 fm^{-3}$. This shows the relevance of the linear response analysis.

Finally the fact that the δ -coupling mostly affects the *stable, isovector-like*, modes is of great interest for possible effects on the isovector Giant Dipole Resonances studied around normal density within the *RMF* approach in asymmetric systems. This will be shown in the next Section on the relativistic linear response in asymmetric matter.

6.3 Nucleon Effective Mass Splitting

An important qualitatively new result of the δ -meson coupling is the n/p -effective mass splitting in asymmetric matter [11,12], see Eq.(6-6). In Fig.6-8 we report the baryon density dependence of the n/p effective masses for $I = 0.5$ ($N = 3Z$) asymmetry, calculated with our $NL\rho\delta$ parameters, compared to the symmetric case [246]. We see a splitting of the order of 15% at normal density ρ_0 , increasing with baryon density. Unfortunately, from the present nuclear data we have a very limited knowledge of this effect, due to the low asymmetries available. However we can expect important effects on transport properties (fast particle emission, collective flows) of the dense and asymmetric *NM* that will be reached in Radioactive Beam collisions at intermediate energies.

The sign itself of the splitting would be very instructive, since it is a quite controversial point (see the comments at the end of Sect.2). As we can see from Eq.(6-6), in a relativistic approach in n -rich systems we have a neutron effective mass always smaller than the proton one. We note again that a decreasing neutron effective mass in n -rich matter is a direct consequence of the relativistic mechanism for the symmetry energy, i.e. the balance of scalar (attractive) and vector (repulsive) contributions in the isovector channel.

6.3.1 Dirac and Schrödinger Nucleon Effective Masses in Asymmetric Matter

The prediction of a definite $m_n^* < m_p^*$ effective mass splitting in *RMF* approaches, when a scalar δ – *like* meson is included, is an important result that requires some further analysis, in particular relative to the controversial predictions of non-relativistic approaches, see Sect.2.

Here we are actually discussing the *Dirac* effective masses $m_D^*(n, p)$, i.e. the effective mass of a nucleon in the in-medium Dirac equation with all the meson couplings. The relation to the *Schrödinger* effective masses $m_S^*(n, p)$, i.e. the “k-mass” due to the momentum dependence of the mean field in the non-relativistic in-medium Schrödinger equation is not trivial, see [237,28,252,253]. We will extend the argument of the refs. [252,253] to the case of asymmetric matter.

We start from the simpler symmetric case without self-interacting terms. The nucleon Dirac equation in the medium contains the scalar self-energy $\Sigma_s = -f_\sigma\rho_S$ and the vector self-energy (fourth component) $\Sigma_0 = f_\omega\rho_B$ and thus the corresponding energy-momentum relation reads:

$$(\epsilon + m - \Sigma_0)^2 = p^2 + (m + \Sigma_s)^2 = p^2 + m_D^{*2} \quad (6-26)$$

i.e. a dispersion relation

$$\epsilon = -m + \Sigma_0 + \sqrt{p^2 + m_D^{*2}} \quad (6-27)$$

From the total single particle energy $E = \epsilon + m$ expressed in the form $E = \sqrt{k_\infty^2 + m^2}$, where k_∞ is the relativistic asymptotic momentum, using Eq.(6-26) we can get the relation

$$\begin{aligned} \frac{k_\infty^2}{2m} &= \epsilon + \frac{\epsilon^2}{2m} = \\ \frac{p^2}{2m} + \Sigma_s + \Sigma_0 + \frac{1}{2m}(\Sigma_s^2 - \Sigma_0^2) + \frac{\Sigma_0}{m}\epsilon &\equiv \frac{p^2}{2m} + U_{eff}(\rho_B, \rho_s, \epsilon) \end{aligned} \quad (6-28)$$

i.e. a Schrödinger-type equation with a momentum dependent mean field that with the dispersion relation Eq.(6-27) is written as

$$\begin{aligned} U_{eff} &= \Sigma_s + \frac{1}{2m}(\Sigma_s^2 + \Sigma_0^2) + \frac{\Sigma_0}{m}\sqrt{(p^2 + m_D^{*2})} \\ &\simeq \Sigma_s + \frac{\Sigma_0 m_D^*}{m} + \frac{1}{2m}(\Sigma_s^2 + \Sigma_0^2) + \frac{p^2}{2m} \frac{\Sigma_0}{m_D^*} \end{aligned} \quad (6-29)$$

The relation between Schrödinger and Dirac nucleon effective masses is then

$$m_S^* = \frac{m}{1 + \frac{\Sigma_0}{m_D^*}} = m_D^* \frac{m}{m + \Sigma_s + \Sigma_0} \quad (6-30)$$

Since at saturation the two self-energies are roughly compensating each other, $\Sigma_s + \Sigma_0 \simeq -50\text{MeV}$ the two effective masses are not much different, with the S – mass slightly larger than the D – mass.

In the case of asymmetric matter, neutron-rich as always considered here, we can have two cases:

- *Only ρ meson coupling*

Now the scalar part is not modified, we have the same scalar self energies Σ_s for neutrons and protons and so the same Dirac masses. The vector self energies will show an isospin dependence with a new term $\mp f_\rho \rho_{B3}$, repulsive for neutrons (– sign, since we use the definition $\rho_{(B,S)3} \equiv \rho_{(B,S)p} - \rho_{(B,S)n}$). As a consequence we see a splitting at the level of the Schrödinger masses since Eq.(6-30) becomes

$$m_S^*(n, p) = m_D^* \frac{m}{m + (\Sigma_s + \Sigma_0)_{sym} \mp f_\rho \rho_{B3}} \quad (6-31)$$

in the direction of $m_n^* < m_p^*$ (here and in the following upper signs are for neutrons).

- *$\rho + \delta$ coupling*

The above splitting is further enhanced by the direct effect of the scalar isovector coupling, see Eq.(6-6). Then the Schrödinger masses are

$$m_S^*(n, p) = (m_{D_{sym}}^* \pm f_\delta \rho_{S3}) \frac{m}{m + (\Sigma_s + \Sigma_0)_{sym} \mp (f_\rho \rho_{B3} - f_\delta \rho_{S3})} \quad (6-32)$$

The new term in the denominator will further contribute to the $m_n^* < m_p^*$ splitting since we must have $f_\rho > f_\delta$ in order to get a correct symmetry parameter a_4 . The effect is larger at higher baryon densities because of the decrease of the scalar ρ_{S3} , due to the faster $\frac{m_{Dn}^*}{E_{Fn}^*}$ reduction of ρ_{S3} .

Actually in a non-relativistic limit we can approximate in Eq.(6-28) directly the energy ϵ with the asymptotic kinetic energy leading to the much simpler relation:

$$m_S^* = \frac{m}{1 + \frac{\Sigma_0}{m}} \simeq m - \Sigma_0 = m_D^* - (\Sigma_s + \Sigma_0). \quad (6-33)$$

In the case of asymmetric matter this leads to the more transparent relations

- *Only ρ meson coupling*

$$m_S^*(n, p) = m_D^* - (\Sigma_s + \Sigma_0)_{sym} \pm f_\rho \rho_{B3} \quad (6-34)$$

- *$\rho + \delta$ coupling*

$$m_S^*(n, p) = m_{D_{sym}}^* - (\Sigma_s + \Sigma_0)_{sym} \pm (f_\rho \rho_{B3} - f_\delta \rho_{S3}) \quad (6-35)$$

In conclusion any relativistic effective field model will predict the definite isospin splitting of the nucleon effective masses $m_n^* < m_p^*$ in the non-relativistic limit. We expect an increase of the difference of the neutron/proton mean field at high momenta, with important dynamical contributions that will enhance the transport effects of the symmetry energy.

6.3.2 The Dirac-Lane Potential

In the non-relativistic limit of the Eq.(6-28) we can easily extract the neutron-proton mean optical potential using the isospin dependence of the self-energies

$$\begin{aligned} \Sigma_{0,q} &= \Sigma_{0,sym} \mp f_\rho \rho_{B3} , \\ \Sigma_{s,q} &= \Sigma_{s,sym} \pm f_\delta \rho_{S3} , \end{aligned} \quad (6-36)$$

With some algebra we get a compact form of the *Dirac – Lane Potential*

$$\begin{aligned} U_{Dirac-Lane} &\equiv \frac{U_n - U_p}{2I} = \\ \rho_0 \left[f_\rho \left(1 - \frac{\Sigma_{0,sym}}{m} \right) - f_\delta \frac{\rho_{S3}}{\rho_{B3}} \left(1 + \frac{\Sigma_{s,sym}}{m} \right) \right] + f_\rho \frac{\rho_0}{m} \epsilon \end{aligned} \quad (6-37)$$

It is interesting to compare with the related discussion presented in Sect.2 for the non-relativistic effective forces, mainly of Skyrme-like form. First of all we predict a definite positive $E - slope$ given by the quantity $f_\rho \frac{\rho_0}{m}$, which is actually not large within the simple *RMF* picture described here. This is a obvious consequence of the fact that the “relativistic” mass splitting is always

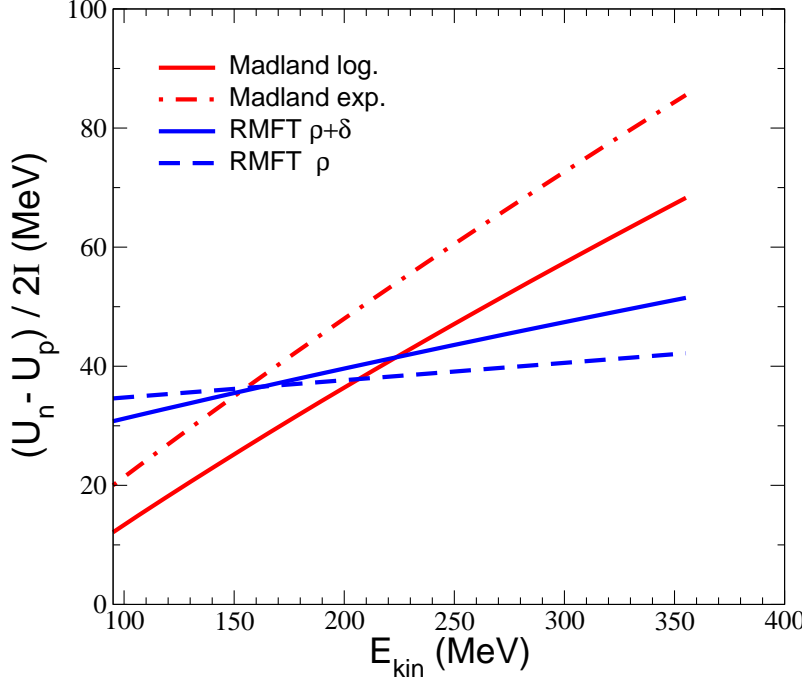


Fig. 6-9. Energy dependence of the Dirac-Lane potential in the *RMF* picture (solid: $NL\rho$; dashed: $NL\rho\delta$) and in the phenomenologic Dirac Optical Model of Madland et al. [254,255], see text.

in the direction $m_n^* < m_p^*$. The realistic magnitude of the effect could be larger if we take into account that some explicit momentum dependence should be included in the scalar and vector self energies, as discussed in ref.[146]. An interesting point in this direction comes from the phenomenological Dirac Optical Potential (*Madland – potential*) constructed in the refs. [254,255], fitting simultaneously proton and neutron (mostly total cross sections) data for collisions with a wide range of nuclei at energies up to 100 *MeV*. Recently this Dirac optical potential has been proven to reproduce very well the new neutron scattering data on ^{208}Pb at 96 *MeV* [256] measured at the Svendberg Laboratory in Uppsala.

The phenomenological *Madland – potential* has different implicit momentum dependences (*exp/log*) in the self-energies, [254,255]. In Fig.6-9 we show the corresponding energy dependences for the *Dirac – Lane* potentials, compared to our $NL\rho$ and $NL\rho\delta$ estimations. When we add the δ -field we have a larger slope since the $\rho – coupling$ should be increased. The slopes of the phenomenological potentials are systematically larger, interestingly similar to the ones of the *Skyrme – Lyon* forces of the Fig.2-6 of Sect.2. We note that in the *Madland – potential* the Coulomb interaction is included, i.e. an extra repulsive vector contribution for the protons. The first, not energy dependent, term of Eq.(6-37) is directly related to the symmetry energy at saturation, exactly like in the non-relativistic case, see Eq.(2-22) of Sect.2.

The conclusion is that a good *systematic* measurement of the Lane potential in a wide range of energies, and particularly around/above 100 *MeV*, would answer many fundamental questions in isospin physics.

7 Collective modes of asymmetric nuclear matter in the relativistic approach

7.1 Linear Response Equations

We discuss here collective oscillations that propagate in cold nuclear matter under the influence of the mean field dynamics. These studies can be considered a relativistic extension of the method introduced by Landau to study liquid- 3He [73,257,71] and recently applied to investigate stable and unstable modes in nuclear matter [72,50,51]. The starting point is the relativistic kinetic transport equation of Sect.6, Eq.(6-5). We look for solutions corresponding to small oscillations of the Wigner function $\hat{F}(x, p)$ around the equilibrium value. Therefore we put

$$\hat{F}(x, p) = \hat{H}(p) + \hat{G}(x, p) \quad (7-1)$$

where $\hat{H}(p)$ is the distribution function at equilibrium and $\hat{G}(x, p)$ represents its fluctuations, ref.[13].

In the linear approximation, i.e. neglecting terms of second order in $\hat{G}(x, p)$, the equations for the Wigner functions become

$$\begin{aligned} \frac{i}{2} \partial_\mu \gamma^\mu \hat{G}_{(i)}(x, p) + (\Pi_\mu \pm \tilde{f}_\rho b_\mu) \gamma^\mu \hat{G}_{(i)}(x, p) - M_i^* \hat{G}_{(i)}(x, p) = \\ (1 - \frac{i}{2} \Delta) (\hat{F}(x) \mp \hat{F}_3(x)) \hat{H}_{(i)}(p) , \end{aligned} \quad (7-2)$$

for neutrons and protons ($i = n, p$, upper/lower signs), where $M_i^* = M - \tilde{f}_\sigma \rho_S \pm \tilde{f}_\delta \rho_{S3}$. The quantities $\hat{F}(x)$ and $\hat{F}_3(x)$ are the isoscalar and the isovector components of the self-consistent field:

$$\begin{aligned} \hat{F}(x) = -8\tilde{f}_\sigma G(x) + 8\tilde{f}_\omega \gamma_\mu G^\mu(x) - 8\frac{\partial \tilde{f}_\sigma}{\partial \rho_S} \rho_S G(x) - 8\frac{\partial \tilde{f}_\sigma}{\partial j_\mu} \rho_S G^\mu(x) \\ - 8\frac{\partial \tilde{f}_\sigma}{\partial \rho_{S3}} \rho_S G_3(x) - 8\frac{\partial \tilde{f}_\sigma}{\partial j_{3\mu}} \rho_S G_3^\mu(x) + 8\frac{\partial \tilde{f}_\omega}{\partial \rho_S} \gamma_\mu j^\mu G(x) , \end{aligned} \quad (7-3)$$

$$\hat{F}_3(x) = -8\tilde{f}_\delta G_3(x) + 8\tilde{f}_\rho \gamma_\mu G_3^\mu(x) - 8\frac{\partial \tilde{f}_\delta}{\partial \rho_S} \rho_{S3} G(x) + 8\frac{\partial \tilde{f}_\rho}{\partial \rho_S} \gamma_\mu j_3^\mu G(x) . \quad (7-4)$$

Following the notation of Sect.6 the coupling functions \tilde{f}_i are in general density dependent due to the Fock contributions. The Hartree approximation is

recovered by vanishing all the derivative terms in the quantities $\hat{F}(x)$ and $\hat{F}_3(x)$ (except $\frac{\partial \tilde{f}_S}{\partial \rho_S}$, since still $\tilde{f}_\sigma = \Phi(\rho_S)/\rho_S$).

We obtain equations for the collective oscillations by multiplying Eqs. (7-2) by γ_λ . After performing the traces, we equate to zero both the real and imaginary parts of the result [222,77]. Furthermore, by Fourier transforming and integrating over four-momentum, we get the set of equations for the scalar and vector fluctuation of each species, [13]. We note that the formalism developed here in Hartree-Fock approximation includes a linear response theory valid also for any other approach to *QHD* beyond *RMF*. Namely when we consider in general a dependence on the baryon density of all meson-nucleon couplings, like in the Density Dependent Hadronic (*DDH*) model [258,259,220,260], inspired by the Dirac-Brueckner-Hartree-Fock (*DBHF*) approach to account for many-body correlations.

The set of equations developed in the Hartree-Fock approximation includes the ones corresponding to the usual Hartree approximation (*RMF*). As already mentioned, it is easily obtained by considering the coupling \tilde{f}_i to each channel equal to the coupling constant of the corresponding meson. The result is of appreciable plainer structure due to the constant value of all couplings, except \tilde{f}_σ [261]. Since the physics results become more transparent, in the following we will stay in the Hartree scheme, keeping well in mind that the Fock contributions can be easily included. In fact they amount to having some extra contributions in the various interaction channels without qualitative modifications of the physical response.

The normal collective modes are plane waves, characterized by the wave vector ($k^\mu = (k^0, 0, 0, |\mathbf{k}|)$). They are determined by solving a set of homogeneous linear equations. The solutions correspond only to longitudinal waves and do not depend on k^0 and $|\mathbf{k}|$ separately, but only on the ratio

$$v_s = \frac{k^0}{|\mathbf{k}|} .$$

The zero-sound velocities are given by those values of v_s for which the relevant determinant of the set of equations vanishes, i.e. by the dispersion relations. Correspondingly the neutron/proton structure of the eigenvectors (normal modes) can be derived. Again it should be noted that in asymmetric nuclear matter isoscalar and isovector components are mixed in the normal modes. Here this can be argued by the fact that in each linearized equation (7-2) both proton/neutron densities and currents are appearing, [13]. However we also recall that one can still identify isovector-like excitations as the modes where neutrons and protons move out of phase, while isoscalar-like modes are characterized by neutrons and protons moving in phase [50,20].

7.2 The Role of Scalar/Vector Fields in the Dynamical Response

Before showing numerical results for the dynamical response of asymmetric nuclear matter in various baryon density regions and using the different effective interactions, we would like to analyse in more detail the structure of the relativistic linear response theory in order to clearly pin down the role of each meson coupling.

7.2.1 Isovector Response

One may perhaps expect that once the asymmetry parameter a_4 is fixed, the velocity of sound is also fixed [263]. On the other hand our results will clearly show a different dynamical response, e.g. with or without the δ -meson channel, for interactions which give *exactly the same a_4 parameter*. Essentially this is due to the fact that the response depends on the slope of the symmetry energy for isovector oscillations around the saturation point. In order to get a complete quantitative understanding of this effect we will first consider the case of symmetric nuclear matter in the Hartree scheme, where the dispersion relations assume a particularly transparent analytical form.

In this case it is also possible to decouple the collective modes into *pure* isoscalar and isovector oscillations, [50,20] as also seen in Sect.3. After a straightforward rearrangement we have a dispersion relation for the isovector modes. Now in order to find the zero-sound velocity one has to evaluate the determinant of a 2×2 matrix (and not a 4×4 , as in the asymmetric NM). After a straightforward rearrangement we have a dispersion relation [13] for the isovector modes

$$1 + N_F \left[f_\rho (1 - v_s^2) - f_\delta \frac{M^{*2}}{E_F^{*2}} \left(1 - f_\delta A(k_F, M^*) - f_\rho \frac{\rho_S}{M^*} v_s^2 \right) \right] \varphi(s) = 0 \quad .(7-5)$$

Here $N_F = \frac{2k_F E_F^*}{\pi^2}$ is the density of states at the Fermi surface and $s \equiv v_s/v_F$. $\varphi(s)$ is the usual Lindhard function of the Landau Fermi Liquid response theory:

$$\varphi(s) = 1 - \frac{s}{2} \ln \left| \frac{s+1}{s-1} \right| + \frac{i}{2} \pi s \theta(1-s)$$

The quantity $A(k_F, M^*)$ is the same integral discussed in the Sect.6, Eq.(6-17).

In fact the structure of the dispersion relation is the same for the isoscalar excitations, of course one has to replace the isovector fluctuations ($\delta\rho_{B3}$, $\delta\rho_{S3}$) with the isoscalar ones ($\delta\rho_B$, $\delta\rho_S$), and the coupling constants of isovector mesons with those of the isoscalar mesons.

At this point we can make the following approximation

$$v_s^2 \simeq v_F^2 = \frac{k_F^2}{E_F^{*2}},$$

to evaluate the expression inside the square brackets in Eq.(7-5). Looking at numerical results shown later (Fig.7-2) this is a good approximation to within 3% for all effective interactions considered. As in Sect.6 we also neglect the integral $A(k_F, M^*)$. Then Eq.(7-5) assumes the transparent form:

$$1 + \frac{6 E_F^*}{k_F^2} \left[E_{sym}^{pot} - \frac{f_\rho}{2} \frac{k_F^2}{E_F^{*2}} \left(1 - f_\delta \frac{M^*}{E_F^{*2}} \rho_S \right) \rho_B \right] \varphi(s) = 0. \quad (7-6)$$

The potential part of the symmetry energy explicitly appears in the dispersion relations, but *together with an important correction term* which exhibits a different f_ρ, f_δ structure with respect to that of E_{sym}^{pot} , Eq.(....) of Sect.6. *We can easily have interactions with the same a_4 value at normal density but with very different isovector response.* E.g. when including the δ channel we have to increase the f_ρ coupling in order to have the same a_4 , as discussed in Sect.6, but now the “restoring force” (coefficient of the Lindhard function in the Eq.(7-6)) will be reduced.

A similar effect has been pointed out in a detailed non-relativistic *Skyrme – RPA* study of the Giant Dipole Resonance in heavy nuclei (^{208}Pb) using effective interactions with various isovector terms [262]. A separate sensitivity of the average resonance frequencies on the symmetry energy a_4 and on its slope has been found. In a covariant scheme we can see from Eq.(7-6) that such behaviour can be achieved only by using two isovector fields, at the lowest order. This result shows more generally that a dynamical observable can be more sensitive to the microscopic structure of the isovector interaction than static properties. For instance in a careful study of the neutron distributions, [30], it is clearly shown that these “equilibrium” observables are almost equally correlated to value, slope and curvature of the symmetry term.

7.2.2 Isoscalar Response

We already noted that for symmetric NM there is a close analogy between the isoscalar and the isovector response in the *RMF* approach. In the isoscalar degree of freedom the compressibility will play the same role of the symmetry energy in the dispersion relation equations. Also in this case we will have an important correction term coming from the interplay of the scalar and vector channel.

The Eq.(7-5) now becomes [261]:

$$1 + N_F \left[f_\omega (1 - v_s^2) - f_\sigma \frac{M^{*2}}{E_F^{*2}} \left(1 - f_\sigma A(k_F, M^*) - f_\omega \frac{\rho_S}{M^*} v_s^2 \right) \right] \varphi(s) = 0 \quad (7-7)$$

that can be reduced with the same approximations to the isoscalar equivalent of the Eq.(7-6):

$$1 + \frac{E_F^*}{3 k_F^2} \left[K_{NM}^{pot} - 9 f_\omega \frac{k_F^2}{E_F^{*2}} \left(1 - f_\sigma \frac{M^*}{E_F^{*2}} \rho_S \right) \rho_B \right] \varphi(s) = 0. \quad (7-8)$$

Here the K_{NM}^{pot} is the potential part of the nuclear matter compressibility that in the Hartree scheme has the simple structure [261](see Eq.(16) of ref. [263])

$$K_{NM}(\rho_B) = \frac{3 k_F^2}{E_F^*} + 9 \left[f_\omega - f_\sigma \left(\frac{M^*}{E_F^*} \right)^2 \right] \rho_B \equiv K_{NM}^{kin} + K_{NM}^{pot}. \quad (7-9)$$

With this analogy, the previous discussion can be transferred to isoscalar oscillations with the role of E_{sym} now “played” by the compressibility. In fact in the isoscalar sector one always takes into account both the scalar and vector fields in any *RMF* model. However, the coupling constant f_ω can assume very different values depending on the chosen value for effective masses M_0^* . This is easy to understand since in the *RMF* limit the saturation binding energy has the simple form

$$E/A(\rho_0) = E_F^* + f_\omega \rho_0 - M_N$$

where M_N is the bare nucleon mass. Thus in order to have the same saturation values of ρ_0 , $E/A(\rho_0)$, when we decrease M_0^* we have to increase f_ω . We then come to the natural conclusion that two *EOS* with different effective masses, even if the compressibilities are the same, are expected to have different dynamical behaviour. This is a very general feature present also in non-relativistic approaches.

From studies in *RMF* on monopole resonances in finite nuclei it seems that a higher value of compressibility is required with respect to non-relativistic calculations. Many authors state that this certainly demands for a clarification [225,226,264,265]. Even if the monopole resonance is not directly connected to the isoscalar collective mode in nuclear matter, our discussion nicely suggests to look at the interplay between effective mass and compressibility. For example we can estimate by means of the dispersion relation Eq.(7-8) that we can have a shift between the compressibility and the “effective compressibility” of the order of ~ 100 MeV. Therefore an effective interaction e.g.

with $K \sim 300 \text{ AMeV}$ can reproduce the same frequencies of another one with $K \sim 200 \text{ AMeV}$ (and a slightly larger M_0^*).

7.2.3 Landau Parameters

Next we discuss the relativistic equations for collective modes in terms of the Landau parameters. Interesting features will appear from the comparison to the analogous non-relativistic case of Sect.3. We will focus first on the isovector response, but, as shown before, the structure of the results will be absolutely similar in the isoscalar channel.

The general non-relativistic expression for dispersion relation of isovector modes can be found in ref.[257]:

$$1 + \left[F_0^a + \frac{F_1^a}{1 + 1/3 F_1^a} s^2 \right] \varphi(s) = 0 \quad (7-10)$$

where F_0^a is the “isovector” combination of the Landau F_0 parameters for neutrons and protons $F_0^a = F_0^{nn} - F_0^{np}$, already introduced in Sect.2. F_1^a are the equivalent quantities for the momentum dependent part of the mean field. In the relativistic approach, for symmetric nuclear matter, we have:

$$\begin{aligned} F_0^a &= F_\rho - F_\delta \frac{M^{*2}}{E_F^{*2}} \frac{1}{1 + f_\delta A(k_F, M^*)} \\ F_1^a &= -F_\rho \frac{v_F^2}{1 + \frac{1}{3} F_\rho v_F^2}, \end{aligned} \quad (7-11)$$

where $F_i = N_F f_i$ ($i = \rho, \delta$) with $N_F = 2N_{n,p}$. Note that the F_1^a contribution results only from the vector coupling. By using the expression of E_{sym}^{pot} (Eq.(6-18) of Sect.6), we can write Eq.(7-10) in the same form of Eqs.(7-5, 7-6). The result is a similar expression but without the term in f_δ inside the brackets in Eq.(7-6). As said before this is not the leading term, however, around saturation density it amounts to about 10% of the total correction.

Moreover turning to the analogy with isoscalar channel, the corresponding term is now the coupling of the σ field, which is much larger. This purely relativistic contribution could be up to a 20%. We underline this point because generally the linear response in *RMF* is discussed calculating the Landau parameters and then using these values directly in the non-relativistic expression for collective modes [263,266].

From the analysis in terms of the Landau parameters, we can describe the effect of the scalar-vector coupling competition previously discussed in the

following way. The symmetry energy fixes the F_0^a , in fact:

$$E_{sym} = \frac{k_F^2}{6 E_F^*} (1 + F_0^a), \quad (7-12)$$

but in the dynamical response also the F_1^a enters, linked to the momentum dependence of the mean field, mostly given by the vector meson coupling. The results are completely analogous in the isoscalar channel, with the compressibility given by

$$K_{NM} = \frac{3 k_F^2}{E_F^*} (1 + F_0^s) \quad (7-13)$$

with the “isoscalar” combination $F_0^s = F_0^{nn} + F_0^{np}$. The relativistic forms of the isoscalar Landau parameters are exactly the same as in Eq.(7-11), just substituting the δ, ρ coupling constants for the σ, ω ones [261].

7.3 Isovector Collective Modes in Asymmetric Nuclear Matter

We now turn to Asymmetric Nuclear Matter. We discuss first results for the isovector collective oscillations, which are driven by the symmetry energy terms of the nuclear *EOS*. The aim is mainly to investigate the effect of the scalar-isovector channel. This is normally not included in studying the isovector modes, or generally the properties of asymmetric matter in a relativistic approach, while it should be naturally present on the basis of the analysis presented in Sect.6. Moreover we emphasize again that a Hartree-Fock scheme leads to the presence of a scalar-isovector channel in any case, *even without the inclusion of the δ -meson field* [238,36].

We will first discuss results obtained in the Non-Linear Hartree scheme (*NLH*) including either both the isovector ($\rho + \delta$) mesons (*NL* $\rho\delta$ parametrization) or only the ρ meson, (*NL* ρ). Even though the Hartree approximation has a simpler structure, it contains all the physical effects we want to point out. Finally from the complete Hartree-Fock (*NLHF*) calculations we will confirm the dynamical contribution of the scalar isovector channel. For *NLH* calculations we use the parametrizations of Table 7, Set(*NL* ρ) and Set(*NL* $\rho\delta$), of Sect.6. In the Hartree-Fock case the coupling constant f_δ is adjusted to the value $\tilde{f}_\delta(\rho_0) = 2.0 \text{ fm}^2$ of the *NLHF* model, Eqs.(6-7) of Sect.6.

In Fig.7-1a we show the sound velocities in the Hartree approximation as a function of the asymmetry parameter I for different baryon densities. We actually plot the sound velocities in units of the neutron Fermi velocities. This is physically convenient: when the ratio is approaching 1.00 we can expect

that this “zero” sound will not propagate due to the strong coupling to the “chaotic” single particle motions (“Landau damping”). This quantity then will also directly give a measure of the “robustness” of the collective mode. Dotted lines refer to calculations including $(\rho + \delta)$ mesons, long-dashed lines correspond to the case with only the ρ meson. Calculations are performed for $\rho_B = \rho_0$ and $\rho_B = 2 \rho_0$. We note that the results of the two models differ already at zero asymmetry, $I = 0$. At normal density (ρ_0 curves), in spite of the fact that the symmetry energy coefficient, $a_4 = E_{sym}(\rho_0)$, is exactly the same in the two cases, significant differences are observed in the response of the system. From Fig. 7-1(a) we expect a reduction of the frequency for the bulk isovector dipole mode in stable nuclei when the scalar isovector channel (δ -like) is present. Moreover we note that, in the $NL\rho$ case, the excitation of isovector modes persists up to higher asymmetries at saturation density. These

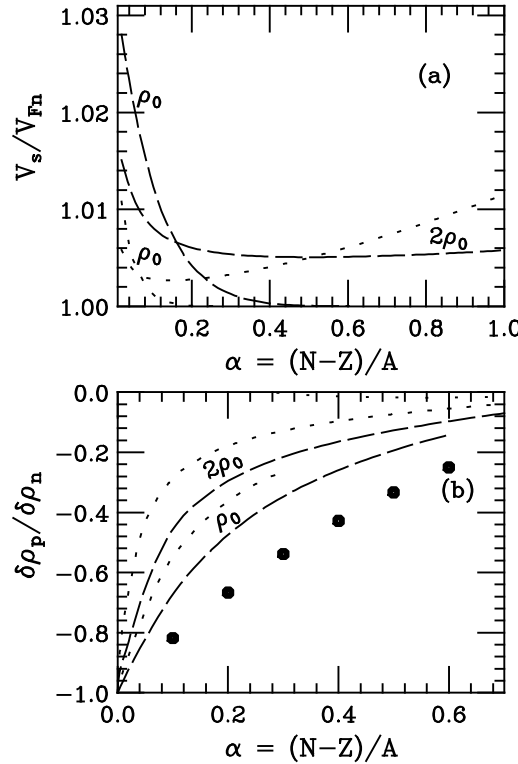


Fig. 7-1. Isovector-like modes: (a) Ratio of zero sound velocities to the neutron Fermi velocity V_{Fn} as a function of the asymmetry parameter I for two values of baryon density. Long dashed line: $NL\rho$. Dotted line: $NL\rho\delta$. (b) Corresponding ratios of proton and neutron amplitudes. All lines are labelled with the baryon density, $\rho_0 = 0.16 \text{ fm}^{-3}$. The full circles in panel (b) represent the trivial behaviour of $-(\rho_p/\rho_n)$ vs. asymmetry parameter.

are non-trivial features, related to the different way scalar and vector fields are entering in the dynamical response of the nuclear system. Such behaviours are therefore present in both collective responses, isoscalar and isovector, as seen in the previous subsection.

Differences are observed even at $\rho_B = 2\rho_0$, where however also the symmetry energy is different. At higher densities a larger E_{sym} is obtained in the case including the δ meson and this leads to a compensation of the effect observed at normal nuclear density. In particular, at higher asymmetries I the collective excitation becomes more robust for $NL\rho\delta$. Differences are observed also in the "chemical" structure of the mode, represented by the ratio $\delta\rho_p/\delta\rho_n$, which is plotted in Fig.7-1(b). The ratio of the out of phase n/p oscillations is not following the ratio of the n/p densities for a given asymmetry, as shown by the full circles in the figure. We systematically see a larger amplitude of the neutron oscillations. The effect is more pronounced when the δ (scalar-isovector) channel is present (dotted lines).

7.3.1 Disappearance of the Isovector Modes

For asymmetric matter it is found that for all interactions with increasing baryon density the isovector modes disappear: we call the density, where this occurs, ρ_B^{cross} . E.g. from Fig.7-1(b) we see that the ratio $\delta\rho_p/\delta\rho_n$ tends very quickly to zero with increasing baryon density, almost for all asymmetries. Around this transition density we expect to have an almost *pure neutron wave* propagation of the sound. In Figs.7-2 and 7-3 we show the results of the $NL\rho$ case, but the effect is clearly present in all the models.

In Fig.7-2 we give the zero-sound velocities as a function of density for a definite asymmetry. For symmetric matter we have a real crossing of the two sound velocities, isoscalar and isovector, as shown in Fig.7-2(a). Above ρ_B^{cross} the isoscalar mode is the most robust.

For asymmetric matter we observe a transition in the structure of the propagating normal mode, from isovector-like to isoscalar-like, Fig.7-2(b,c). Similar effects have been seen in a non-relativistic picture [50]. This mechanism is analysed in Fig.7-3 for the ratio of proton to neutron amplitudes (including the sign). In fact we see that the proton component of the propagating sound is quite small in a relatively wide region around the "transition" baryon density, a feature becoming more relevant with increasing asymmetry, see the open circle line. This is quite interesting since it could open the possibility of observing some experimental signatures of the *neutron wave* effect.

For a given asymmetry I the value of ρ_B^{cross} is different for the models considered, as can be argued by the behaviour of $\delta\rho_p/\delta\rho_n$ at $2\rho_0$ in Fig.7-1(b). E.g. for $I = 0.1$ $NL\rho\delta$ has the lower value ($\rho_B^{cross} \simeq 2.4\rho_0$), while $NL\rho$ has the higher one ($\rho_B^{cross} \simeq 3.0\rho_0$). This is again related to the reduction of the isovector restoring force when the scalar-isovector channel (δ -like) is present, as discussed before.

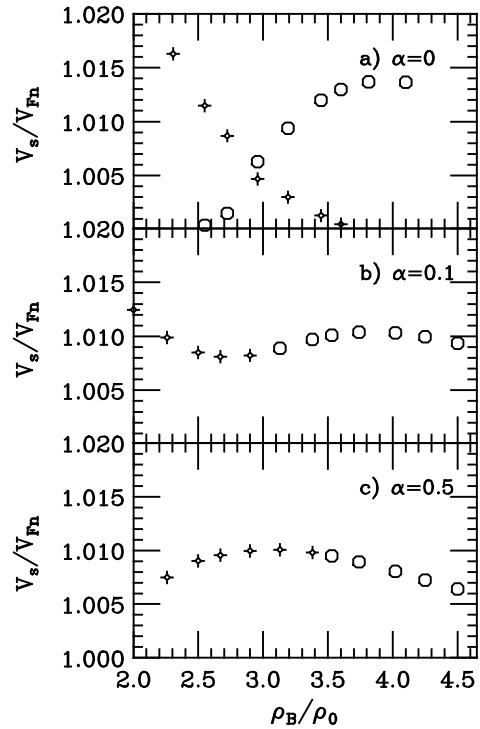


Fig. 7-2. Sound phase velocities of the propagating collective mode vs. the baryon density ($NL\rho$ case). Crosses: isovector-like. Open circles: isoscalar-like. (a): symmetric matter. (b): asymmetric matter, $I = 0.1$. (c): asymmetric matter, $I = 0.5$.

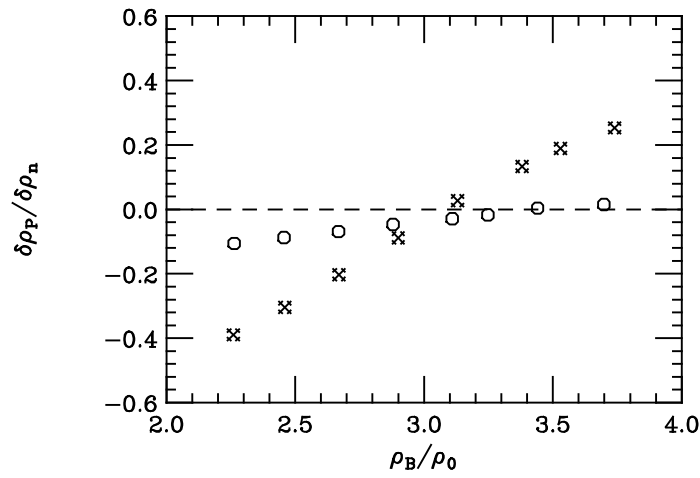


Fig. 7-3. Ratio of protons and neutron amplitudes in the propagating mode, for different asymmetries, as a function of the baryon density around the ρ_B^{cross} ($NL\rho$ case). Crosses: $I = 0.1$, Fig.7-2b. Open circles: $I = 0.5$, Fig.7-2c.

7.4 Isoscalar Collective Modes in Asymmetric Nuclear Matter

7.4.1 Exotic high baryon density modes

From the previous analysis we have seen the isoscalar-like excitations to become dominant at high baryon density, above the ρ_B^{cross} introduced before.

Some results are shown in Fig.7-4. It should be noticed that the frequency of the isoscalar-like modes is essentially related to the compressibility of the system at the considered density. In Fig.7-4(a) we display the sound velocity obtained in Hartree and Hartree-Fock calculations at $\rho_B = 3.5 \rho_0$, as a function of the asymmetry I . The differences observed among calculations performed within the Hartree or Hartree-Fock scheme for symmetric matter are due to a different behaviour of the associated equation of state at high density. At

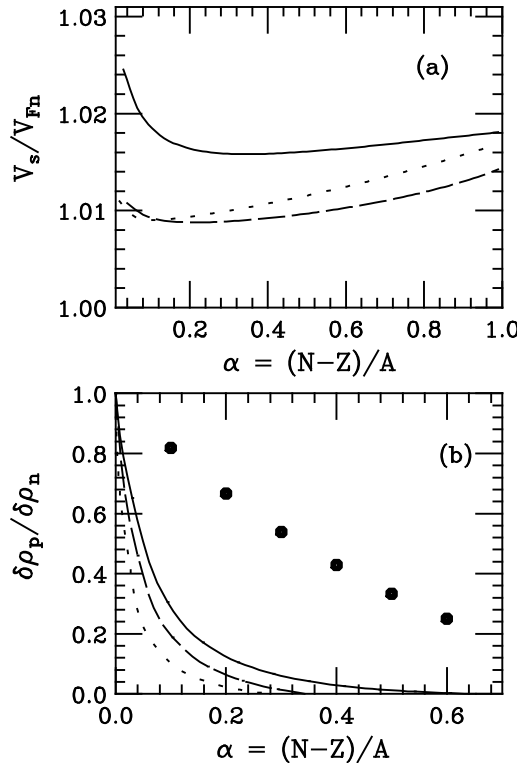


Fig. 7-4. Sound velocity (a) and chemical composition (b) of isoscalar-like modes at $\rho_B = 3.5 \rho_0$. Solid line: $NLHF$. Long dashed line: $NL\rho$. Dotted line: $NL\rho\delta$. The full circles in panel (b) represent the behaviour of ρ_p/ρ_n vs. I .

$I = 0$ the two Hartree models have exactly the same isoscalar mean fields, but for asymmetric nuclear matter the different behaviour of the symmetry energy leads to a different compressibility. The case $NL\rho\delta$, which has the stiffer E_{sym} (resulting in a greater incompressibility for $I > 0$) with respect to $NL\rho$, shows also a larger increase of v_s/v_{Fn} with density.

Differences are also observed in the chemical composition of the mode (Fig.7-4(b)). The black circles show the behaviour of ρ_p/ρ_n vs. α . Note the *almost pure neutron wave* structure of the propagating sound, since the oscillations of protons appear strongly damped ($\delta\rho_p/\delta\rho_n \ll \rho_p/\rho_n$), see the previous comments.

Before closing this discussion we have to remark that the isoscalar-like modes at high baryon density are vanishing if the nuclear *EOS* becomes softer. This is indeed the results of two recent models, [266,267], where the nuclear compressibility is decreasing at high baryon density because of a reduction of the isoscalar vector channel contribution. In ref. [266] this is due to self-interacting high order terms for the ω meson, while in ref.[267] to a decreasing density-dependent f_ω coupling.

Finally we note that all causality violation problems (superluminal sound velocities) observed in the non relativistic results at high baryon density, see ref.[263] and Fig.3c in ref.[50], are completely absent in the relativistic approach, as seen in the high density trends in Fig.7-2.

7.4.2 *Isospin Distillation in Dilute Matter*

As a good check of the relativistic approach we have also investigated the response of the system in the region of spinodal instability associated with the liquid-gas phase transition, which occurs at low densities. In this region an isoscalar unstable mode can be found, with imaginary sound velocity, that gives rise to an exponential growth of the fluctuations. The latter can represent a dynamical mechanism for the multi-fragmentation process observed in heavy-ion collisions, see the discussion in Sects.3 and 5. We find this kind of solution. In Fig.7-5 we show the imaginary sound velocity and the ratio $\delta\rho_p/\delta\rho_n$ as a function of the initial asymmetry for this collective mode. For all the interactions this ratio is different from the corresponding ρ_p/ρ_n of the initial asymmetry. This is exactly the chemical effect associated with the new instabilities in dilute asymmetric matter [19,20]. In particular it is seen that, when isoscalar-like modes become unstable, the ratio $\delta\rho_p/\delta\rho_n$ becomes *larger* than the ratio ρ_p/ρ_n (at variance with the stable modes at high densities, see Fig.7-4). Hence proton oscillations are relatively larger than neutron oscillations leading to a more symmetric liquid phase and to a more neutron rich gas phase, during the disassembly of the system. This is the *Isospin Distillation* effect in fragmentation, as already studied in detail in the previous Sects.3 and 5 in a non-relativistic frame.

In conclusion we note that in dilute asymmetric *NM* we can distinguish two regions of instability, mechanical (cluster formation) and chemical (component separation). There is however no discontinuity in the structure of the unstable modes which are developing. For all realistic effective nuclear interactions (rel-

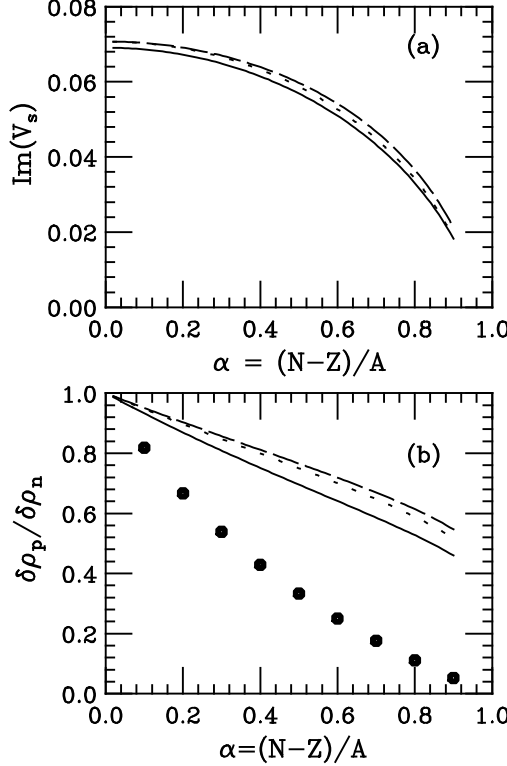


Fig. 7-5. Isoscalar-like unstable modes at $\rho_B = 0.4 \rho_0$: Imaginary sound velocity (a), in c -units, and ratio of proton and neutron amplitudes (b) as a function of the asymmetry. Solid line: $NLHF$. Dotted line: $NL\rho\delta$. Long dashed line: $NL\rho$. The full circles in panel (b) represent the behaviour of ρ_p/ρ_n vs. the asymmetry parameter.

ativistic and not) the nature of the unstable normal modes at low densities is *always isoscalar-like*, i.e. with neutrons and protons oscillating in phase, although with the neutron distillation effect discussed before, refs. [20,268].

7.5 General comments from the ANM collective response

We have shown that from a detailed study of the collective response of asymmetric nuclear systems it would be possible to obtain information on the *Lorentz* structure of the in-medium interaction in the isovector channel. In fact we have singled out some qualitative new effects of the δ -meson-like channel on the dynamical response of *ANM*. Essentially, our investigation indicates that even if the symmetry energy is fixed, the dynamical response is affected by its internal *Lorentz* structure, i.e. the presence or not of an isovector-scalar field. This is implemented by the explicit introduction of an effective δ -meson and/or by the Fock term contributions. Both mechanisms are absent in the present relativistic *RPA* calculations for finite nuclei. In the spirit of the *EFT/DFT* approach [229] it would be interesting to see the effect of an isovector scalar field extension, at the lowest order, on the existing covariant

RPA results. In general we see a close analogy in the structure of the linear response equations for isoscalar/isovector modes:

- Same form of the dispersion relations.
- Parallel role of E_{sym}^{pot} and K_{NM}^{pot} in the determination of the restoring force.
- Parallel structure of the corrections due to the scalar-vector meson competition.

This appears to be a beautiful “mirror” structure of the relativistic approach that seems to nicely support the introduction of a δ -meson-like coupling in the isovector channel, at least from a formal point of view. We like to remind that the same “mirror” structure of the relativistic picture is remarked in Sect.6 for equilibrium properties, saturation binding and symmetry energy, the a_1 and a_4 parameters of the Bethe-Weiszäcker mass formula.

8 Relativistic Heavy Ion Collisions: the covariant structure of the symmetry term

Intermediate energy Heavy Ion Collisions, *HIC*, open the unique possibility to explore the Equation of State (*EOS*) of nuclear matter far from saturation, in particular the density dependence of the symmetry energy $E_{sym}(\rho_B)$. Within a relativistic transport model it is possible to see that the isovector-scalar δ -meson, which affects the high density behavior of the symmetry term, influences the isospin dynamics. The effect is greatly enhanced by a relativistic mechanism related to the covariant nature of the fields contributing to the isovector channel.

An increasing $E_{sym}(\rho_B)$ leads to a more proton-rich neutron star whereas a decreasing one would make it more pure in neutron content. As a consequence the chemical composition and cooling mechanism of protoneutron stars [273,274], mass-radius correlations [275,276], critical densities for kaon condensation in dense stellar matter [277,278] as well as the possibility of a mixed quark-hadron phase [279] in neutrons stars will all be rather different. It has recently been argued by means of simple thermodynamics considerations that even the onset of a quark-deconfined phase at high baryon density could present a sensitivity to the behaviour of $E_{sym}(\rho_B)$ even for not very large asymmetries [241].

In the previous Sections we have seen how the search for $E_{sym}(\rho_B)$ around saturation density has driven a lot of theoretical and experimental efforts. We have seen how *HICs* at Fermi energies can give the possibility to extract some information on the symmetry term of the nuclear Equation of State (*EOS*) in region below and/or slightly above the normal density. Here we will focus our attention on Relativistic *HICs* trying to select reaction observables particularly sensitive to the symmetry energy at higher density, where furthermore we cannot have complementary investigations from nuclear structure like in the case of the low density behaviour. We stress again that *HICs* provide the unique way to create asymmetric matter at high density in terrestrial laboratories. Moreover effective interactions for high momentum nucleons can be probed. Calculations within transport approaches show that *HICs* around $1AGeV$ allow to reach a transient state of matter with more than twice the normal baryon density. Moreover, although the data are mostly of inclusive type (and the colliding nuclei not very neutron rich), quite clearly a dependence of some observables on charge asymmetry is emerging.

Collective flow, particle production and isospin equilibration results for reactions induced by stable and radioactive beams are discussed. The elliptic flows of nucleons and light isobars appear to be quite sensitive to the microscopic structure of the symmetry term, in particular for particles with large transverse momenta, since they represent an earlier emission from a compressed

source. Thus future, more exclusive, experiments with relativistic radioactive beams should be able to set stringent constraints on the density dependence of the symmetry energy far from ground state nuclear matter.

Moreover we show that in fact a *relativistic* description of the nuclear mean field can account for an enhancement of isospin effects during the dynamics of heavy-ion collisions. The isospin dependence of collective flows and pion production has been already discussed in a non-relativistic framework [46,113,280,281] using very different *EOS* with opposite behaviours of the symmetry term at high densities, increasing repulsion (*asy-stiff*) vs. increasing attraction (*asy-soft*). The main new result shown here, in a fully relativistic scheme, is the importance at higher energies of the microscopic covariant structure of the effective interaction in the isovector channel: *effective forces with very similar symmetry terms can give rise to very different isospin effects in relativistic heavy ion collisions.*

In recent years some efforts have been devoted to the effects of the scalar- isovector channel in finite nuclei, [220,230,231]. Such investigations have not shown a clear evidence for the δ -field and this can be understood considering that in finite nuclei one can test the interaction properties mainly below the normal density, where the effect of the δ -channel on symmetry energy and on the effective masses is indeed small [12,13] and eventually could be absorbed into non linear terms of the ρ field. In Sect.7 we have also seen that the dynamical collective response is not much affected, in particular the spinodal instabilities. We can expect just some weak effects on the isovector-like dipole modes.

Here we show that heavy-ion collisions around $1AGeV$ with radioactive beams can provide instead a unique opportunity to spot the presence of the scalar isovector channel. In fact, due to the large counterstreaming nuclear currents one may even exploit the different Lorentz nature of a scalar and a vector field.

When both ρ -like and δ -like channels are considered $E_{sym}(\rho_B)$ can be written as (Sect.6):

$$E_{sym}(\rho_B) = \frac{1}{6} \frac{k_F^2}{E_F^*} + \frac{1}{2} \left[f_\rho - f_\delta \left(\frac{M^*}{E_F^*} \right)^2 \right] \rho_B \equiv E_{sym}^{kin} + E_{sym}^{pot} \quad (8-1)$$

with $E^* = \sqrt{k_F^2 + M^{*2}}$, M^* the effective Dirac mass and $f_{\rho,\delta} = (g_{\rho,\delta}/m_{\rho,\delta})^2$ are the coupling constants of the isovector channels. We see that, when the δ -meson is included, the observed $a_4 = E_{sym}(\rho_0)$ value actually assigns the combination $[f_\rho - f_\delta(\frac{M^*}{E_F^*})^2]$ of the (ρ, δ) coupling constants, [12,13]. In Fig.8-1 we show the density dependence of the symmetry energy for three different

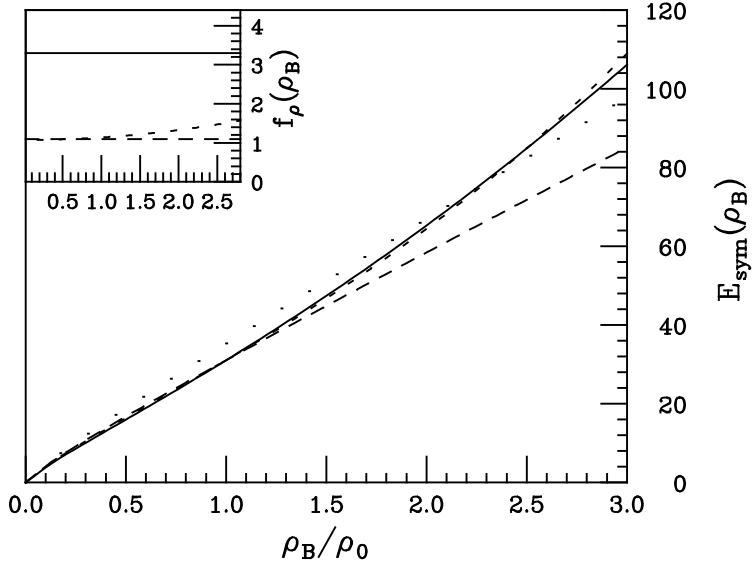


Fig. 8-1. Total (kinetic+potential) symmetry energy (in MeV) as a function of the baryon density. Solid: $NL\rho\delta$. Dashed: $NL\rho$. Short Dashed: $NL - D\rho$. In the insert the density behaviour of the ρ coupling, f_ρ (in fm^2), for the three models is shown.

Non – Linear – RMF models: two of these, one including only the ρ field ($NL\rho$), the other with ρ and δ fields ($NL\rho\delta$), were already introduced in Sect.6 (see Table 7). The last, ($NLD\rho$), includes only a ρ field but with a covariant density dependence of f_ρ , [220,258]. This is tuned to give at high density the same $E_{sym}(\rho_B)$ of the the ($NL\rho\delta$) case. As shown in the following, the latter model is useful for disentagling in the reaction dynamics the effects due to a difference in $E_{sym}(\rho_B)$ from those directly linked to the strength of the ρ vector field [135]. Thus these models parametrize the isovector mean field either by only the vector field with $f_\rho = 1.1 fm^2$, or with a balance between a vector field with $f_\rho = 3.3 fm^2$ and a scalar one with $f_\delta = 2.4 fm^2$, or finally by a normal density coupling $f_\rho(\rho_0) = 1.1 fm^2$, at saturation, but with an increasing density dependence as shown in Fig.8-1 (insert). We stress again that in $NL\rho\delta$ the symmetry energy results from a balance between a scalar attraction, ($\delta - like$), and a vector repulsion, ($\rho - like$), where the ρ -coupling is now roughly three times larger than in the $NL\rho$ case.

The strength of f_δ is fixed relatively well by *DBHF* [34,35] and *DHF* [36] calculations. Therefore the effects described in the following are not artificially enhanced, but based on a reliable estimate available at the moment. In any case the aim of our work is to present some qualitative new features expected in the reaction dynamics, in particular for collective flows, particle production and isospin stopping power, which result from the introduction of a scalar effective field in the isovector channel.

We finally note that the use of a *RMF* approach with fixed couplings in high

density regions generally requires some caution due to the density dependence of the virtual meson couplings because of correlations beyond the mean field scheme. In particular a softer *EOS* for the isoscalar part is favoured, as suggested from experimental analyses [129], from *DBHF* predictions and from reaction simulations for collisions of charge symmetric ions at intermediate energies [131]. In the calculations presented here the (σ, ω) coupling constants have been modified accordingly, see details in ref. [232].

8.1 Relativistic transport simulations

For the theoretical description of heavy ion collisions we solve the covariant transport equation of the Boltzmann type [283,146] within the Relativistic Landau Vlasov (*RLV*) method [259] (for the Vlasov part) and applying a Monte-Carlo procedure for the collision term. *RLV* is a test particle method using covariant Gaussians in phase space for the test particles. The collision term includes elastic and inelastic processes involving the production/absorption of the $\Delta(1232\text{MeV})$ and $N^*(1440\text{MeV})$ resonances as well as their decays into one- and two-pion channels. Details about the cross sections for all the possible channels can be found in ref.[284]. An explicit isospin-dependent Pauli blocking term for the fermions is employed.

For the following discussion it is useful to recall how a relativistic Vlasov equation can be obtained from Wigner Function dynamics of Sect.6. The neutron/proton Wigner functions are expanded in terms of components with definite transformation properties. Consistently with the effective fields included in the minimal model one can limit the expansion to scalar and vector parts:

$$\hat{F}^{(i)}(x, p) = F_S^{(i)}(x, p) + \gamma_\mu F^{(i)\mu}(x, p), \quad i = n, p.$$

From the kinetic equation (6-5) of Sect.6 we obtain after some algebra a relation between the vector and scalar components

$$F^{(i)\mu} \equiv p_i^{*\mu} \frac{F_S^{(i)}}{M_i^*}$$

and thus a transport equation of Vlasov type for the scalar part $f_i(x, p^{*\mu}) \equiv F_S^i/M_i^*$:

$$\{p_{\mu i}^* \partial^\mu + [p_{\nu i}^* F_i^{\mu\nu} + M_i^* (\partial^\mu M_i^*)] \partial_\mu p_i^{*\mu}\} f_i(x, p^{*\mu}) = 0 \quad (8-2)$$

with the field tensors

$$F_i^{\mu\nu} \equiv \partial^\mu p_i^{*\nu} + \partial^\nu p_i^{*\mu}.$$

The trajectories of test particles obey to the following equation of motion:

$$\begin{aligned}\frac{d}{d\tau}x_i^\mu &= \frac{p_i^*(\tau)}{M_i^*(x)} , \\ \frac{d}{d\tau}p_i^{*\mu} &= \frac{p_{i\nu}^*(\tau)}{M_i^*(x)} F_i^{\mu\nu}(x_i(\tau)) + \partial^\mu M_i^*(x) .\end{aligned}\quad (8-3)$$

In order to have an idea of the dynamical effects of the covariant structure of the interactive fields, we write down, with some approximations, the “force” acting on a particle. Since we are interested in isospin contributions we will take into account only the isovector part of the interaction [135]:

$$\begin{aligned}\frac{d\vec{p}_i^*}{d\tau} &= \pm f_\rho \frac{p_{i\nu}}{M_i^*} [\vec{\nabla} J_3^\nu - \partial^\nu \vec{J}_3] \mp f_\delta \nabla \rho_{S3}, \quad (p/n) \\ &\approx \pm f_\rho \frac{E_i^*}{M_i^*} \vec{\nabla} \rho_3 \mp f_\delta \vec{\nabla} \rho_{S3}\end{aligned}\quad (8-4)$$

In the second line we have neglected the contribution coming from the gradient of the current in the transverse direction, i.e. terms like $(\nabla_l J_{3m})$ ($l \neq m = x, y, z$) and the derivative of the current with respect to time. This form will be used below to interpret collective flow.

8.2 Collective flows

Collective flows in heavy ion collisions give important information on the dynamic response of dense, hot and asymmetric nuclear matter [121,123,124,125]. In particular the proton-neutron differential flow $F^{pn}(y)$ [127] has been found to be a very useful probe of the isovector part of the *EOS* since it appears rather insensitive to the isoscalar potential and to the in medium nuclear cross section. The definition of the $F^{pn}(y)$ is

$$F^{pn}(y) \equiv \frac{1}{N(y)} \sum_{i=1}^{N(y)} p_{x_i} \tau_i \quad (8-5)$$

where $N(y)$ is the total number of free nucleons at the rapidity y , p_{x_i} is the transverse momentum of particle i in the reaction plane, and τ_i is +1 and -1 for protons and neutrons, respectively.

A typical result for the very asymmetric $^{132}Sn + ^{132}Sn$ reaction at $1.5AGeV$ (semicentral collisions) is shown in Fig.8-2. The error bars represent the statistical fluctuations due to the Monte-Carlo nature of the simulations. We notice that the differential flow in case of the $NL\rho\delta$ presents a stiffer behaviour relative to the $NL\rho$ model, as expected from the more repulsive symmetry energy

$E_{sym}(\rho_B)$ at high baryon densities, in Fig.8-1. On the other hand it may be surprising that a relatively small difference at $2\rho_0$ results in a such different collective flows.

The calculation can be repeated using the $NLD\rho$ interaction, i.e. with only a ρ contribution *but* tuned to reproduce the same *EOS* of the $NL\rho\delta$ case. The results, short-dashed curve of Fig.8-2, are very similar to the ones of the $NL\rho$ interaction. Therefore we understand the large flow effect as mainly due to the different strengths of the vector-isovector field in the $NL\rho\delta$ and the $NL\rho, NLD\rho$ models. In fact if a source is moving the vector field is enhanced (essentially by the local $\gamma \equiv \frac{E^*}{M^*}$ Lorentz factor) relative to the scalar one.

In the second line of Eq.(8-4) we have written the isovector contribution to the effective force. We are actually interested in the difference between the forces acting on a neutron and on a proton. Oversimplifying the *HIC* dynamics we consider locally neutrons and protons with the same γ factor (i.e. with the same velocity). Then Eq.(8-4) can be expressed approximately in the following transparent form ($\rho_{S3} \simeq \frac{M^*}{E^*} \rho_3$):

$$\frac{d\vec{p}_p^*}{d\tau} - \frac{d\vec{p}_n^*}{d\tau} \simeq 2 \left[\gamma f_\rho - \frac{f_\delta}{\gamma} \right] \vec{\nabla} \rho_3 = \left[\frac{4}{\rho_B} E_{sym}^{pot} + 2(\gamma - 1) f_\rho \right] \vec{\nabla} \rho_3 \quad (8-6)$$

where $\gamma \equiv \frac{E^*}{M^*}$ is the local Lorentz factor of the collective motion and Eq.(8-1) has been used.

Keeping in mind that $NL\rho\delta$ has a three times larger ρ -coupling it is clear that dynamically the vector-isovector mean field acting during the *HIC* is much larger than the one of the $NL\rho, NLD\rho$ cases. Then the isospin effect is mostly caused by the different Lorentz structure of the “interaction” which results in a dynamical breaking of the balance between the ρ vector and δ scalar fields, present in nuclear matter at equilibrium,[135]. This effect is analogous to the interplay between the isoscalar vector- and scalar-fields which is seen in the magnitude and energy dependence of the real part of the optical potential,[131]. To characterize the effect on differential collective flows we have calculated the slope $dF^{pn}(y)/d(y/y_{proj})$ at mid-rapidity. Its value is $46.7 \text{ MeV}/c$ for $NL\rho\delta$ and $23.4 \text{ MeV}/c$ for $NL\rho$, i.e. a factor two difference. Calculations performed at lower beam energies show that below 500 AMeV there is no essential difference in the differential flow predictions among the models discussed here. The effect from the strength of ρ field starts to become important around 1 AGeV , as expected from a relativistic mechanism.

Another interesting observable is the elliptic flow $v_2(y, p_t)$, the second coefficient in a Fourier series expansion of the azimuthal emission distribution, see

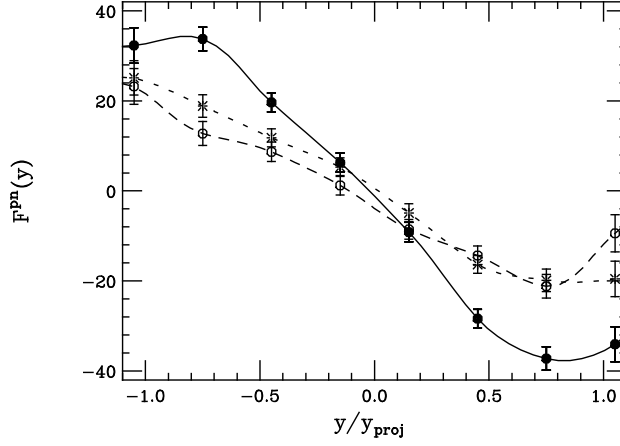


Fig. 8-2. $^{132}Sn + ^{132}Sn$ reaction at 1.5 AGeV ($b = 6\text{ fm}$): Proton-neutron differential transverse collective flow (in MeV/c), vs. rapidity, for the three different models for the isovector mean fields. Full circles and solid line: $NL\rho\delta$. Open circles and dashed line: $NL\rho$. Stars and short dashed line : $NLD\rho$.

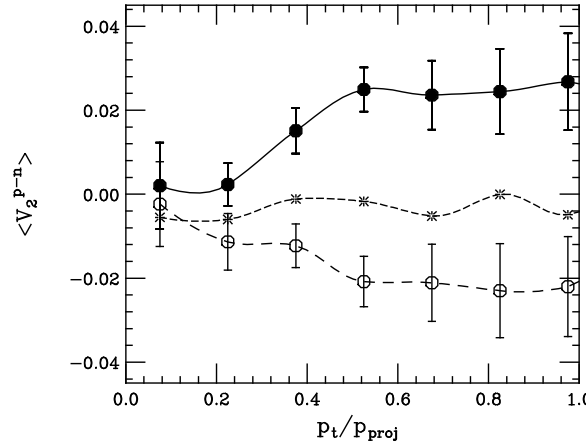


Fig. 8-3. Difference between neutron and proton elliptic flow as a function of the transverse momentum in the $^{132}Sn + ^{132}Sn$ reaction at 1.5 AGeV ($b=6\text{ fm}$) in the rapidity range $-0.3 \leq y/y_{proj} \leq 0.3$. Full circles and solid line: $NL\rho\delta$. Open circles and dashed line: $NL\rho$. Stars and short dashed line: $NLD\rho$. The statistical error bars of the $NLD\rho$ curve are similar to the other cases and not shown.

Sect.4,

$$v_2 = \left\langle \frac{p_x^2 - p_y^2}{p_t^2} \right\rangle$$

where $p_t = \sqrt{p_x^2 + p_y^2}$ is the transverse momentum [128,129]. A negative value of v_2 corresponds to the predominant emission of matter perpendicular to the reaction plane (the so-called *squeeze-out* flow). The p_t -dependence of v_2 , which has been recently investigated by various groups [129,124,130,131] is very sensitive to the high density behavior of the *EOS* since highly energetic particles ($p_t \geq 0.5$) originate from the initial compressed phase of the collision,[131].

In Fig.8-3 we present the p_t dependence of the proton-neutron difference of the elliptic flow in the same very exotic $^{132}Sn + ^{132}Sn$ reaction at $1.5AGeV$ (semi-central collisions) for mid-rapidity emissions. The larger error bars correspond to a reduced statistics when a selection on different p_t bins is introduced, increasing for larger p_t values due to the smaller number of contributions. From Fig.8-3 we see that with the $(\rho + \delta)$ dynamics the high- p_t neutrons show a much larger *squeeze – out*. This is fully consistent with an early emission (more spectator shadowing) due to the larger repulsive ρ -field. We understand this large effect since the relativistic enhancement discussed above is relevant especially at the first stage of the collision. The v_2 observable, which is a good *chronometer* of the reaction dynamics, appears to be particularly sensitive to the Lorentz structure of the effective interaction.

The same set of simulations has been repeated in ref.[135] for the more realistic $^{132}Sn + ^{124}Sn$ reaction at $1.5 AGeV$ ($b = 6fm$), that likely could be studied with the new planned radioactive beam facilities at intermediate energies. The results are shown in Fig.8-4. The effect of the different structure of the isovector channel is still quite clear, of course with a reduction due to the smaller isospin density in the interaction region. Particularly evident is again the splitting in the high p_t region of the elliptic flow.

8.3 π^-/π^+ Ratios

Observable effects originating from the high density symmetry energy are related to differences in neutron and proton densities. Thus, we consider in the following the ratio of neutrons to protons as a function of time and space. One expects isospin effects on the different isospin channels of pions, since they are produced in nn , pp and np collisions via the decay of Δ and N^* resonances. Using the same relativistic transport code the π^- vs. π^+ production for central $Au + Au$ collisions at different energies can be evaluated, see [232]. Results are shown in Fig.8-5. For the $NL\rho\delta$ model the neutrons are emitted much earlier than protons from the high density phase due to a more repulsive mean field together with a lower n -effective mass. This effect is responsible for the reduction of the n/p -ratio in the residual system and, particularly, it influences the particle production,[280,281].

The four isospin states of the Δ -resonance are produced in different scattering channels, when the threshold energy is available, e.g. $nn \rightarrow p\Delta^-, n\Delta^0$, $pp \rightarrow p\Delta^+, n\Delta^{++}, \dots$ Thus $\Delta^{0,-}$ ($\Delta^{+,++}$) resonances are mainly formed in energetic nn - (pp -) collisions. Therefore, the n/p -ratio is indirectly related to that of the particle production.

The n/p effective mass splitting in asymmetric matter can also directly affect

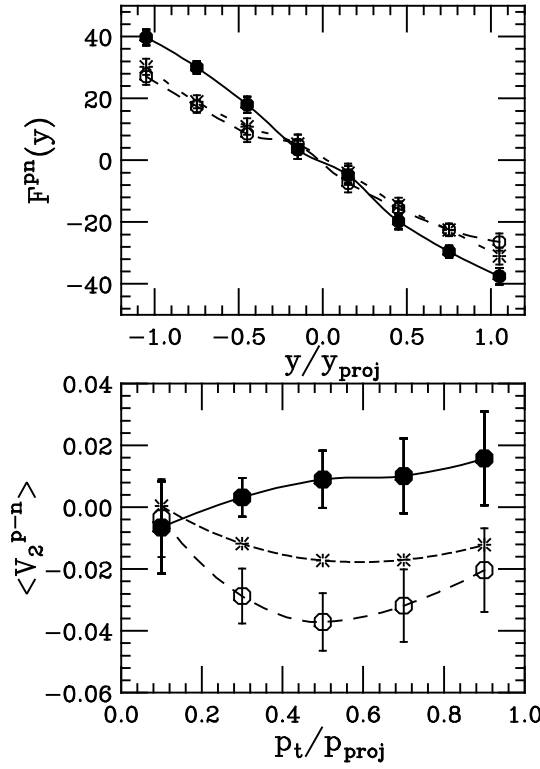


Fig. 8-4. $^{132}\text{Sn} + ^{124}\text{Sn}$ reaction at 1.5 AGeV ($b = 6\text{ fm}$) from the three different models for the isovector mean fields. Top: as in Fig.8-2. Bottom: as in Fig.8-3. Full circles and solid line: $NL\rho\delta$. Open circles and dashed line: $NL\rho$. Stars and short dashed line: $NL - D\rho$. Error bars: see the text and the previous caption.

the resonance production because of threshold effects. We note that resonances will also have isospin dependent in-medium effective masses that can be related to the nucleon effective masses through the isospin coupling coefficients in the process $\Delta \leftrightarrow \pi N$, [134,232]. In terms of the self-energies Σ we have:

$$\begin{aligned}
 \Sigma_i(\Delta^-) &= \Sigma_i(n) \\
 \Sigma_i(\Delta^0) &= \frac{2}{3}\Sigma_i(n) + \frac{1}{3}\Sigma_i(p) \\
 \Sigma_i(\Delta^+) &= \frac{1}{3}\Sigma_i(n) + \frac{2}{3}\Sigma_i(p) \\
 \Sigma_i(\Delta^{++}) &= \Sigma_i(p) \quad \text{and} \\
 \Sigma_i(N^{*(+,0)}) &= \Sigma_i(p, n).
 \end{aligned} \tag{8-7}$$

where $i = \text{scalar and vector}$.

Thus the effective masses of the four isospin states of the Δ -resonance will be different when a δ -meson is included in the calculation. We have seen from general considerations (see Sect.6), that, in n -rich systems, a isovector scalar

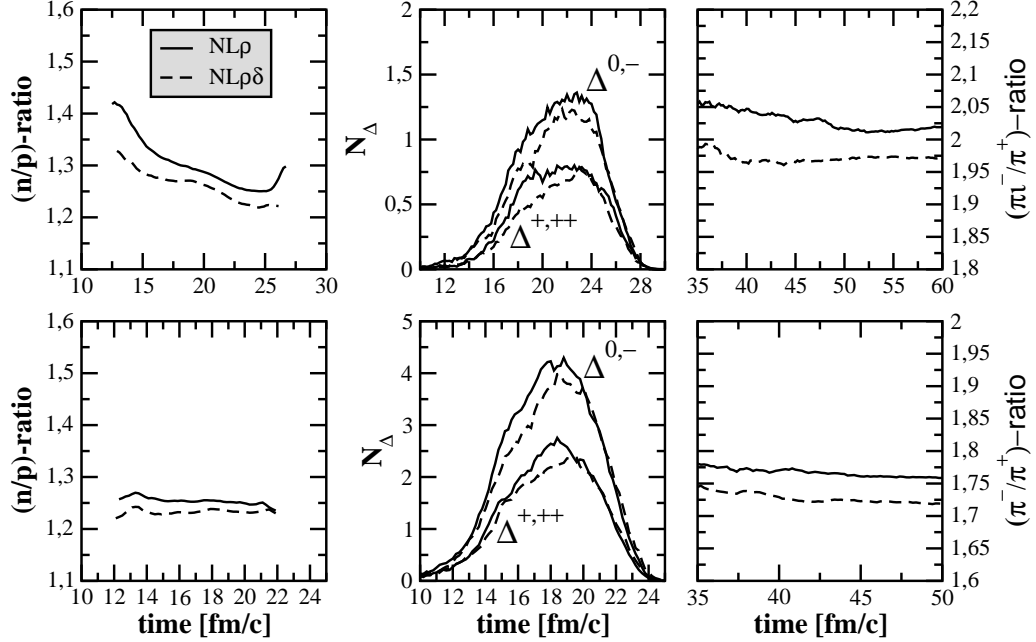


Fig. 8-5. Central $Au + Au$ collisions at $0.6AGeV$ (upper) and $1.0AGeV$ (bottom). Time evolution of n/p ratio and Δ resonance production in high density regions ($\rho/\rho_0 \geq 2.0$) (first two columns) and of the total π^-/π^+ ratio (right). Solid lines: $NL\rho$. Dashed lines: $NL\rho\delta$.

meson field is leading to a neutron effective mass smaller than that for protons, in particular at high baryon densities. Consequently in the process $nn \rightarrow p\Delta^-$ less energy will be available for the Δ^- production in the $NL\rho\delta$ case. We like to note that this mechanism is not strictly linked to the density behavior of the symmetry energy. E.g., in density dependent coupling models we can have at high densities a lower $E_{sym}(\rho)$ because the ρ -meson coupling is decreasing but still a large $m_p^* - m_n^*$ splitting if the δ -meson coupling stays constant or it is slightly increasing, as e.g. in the $DBHF$ calculations of ref.[232].

In the Δ -resonance multiplicities (middle figures) one thus sees a decrease of the $\Delta^{0,-}$ isospin states due to the effect of the isovector-scalar δ -meson. The pions are mainly produced from resonance decays, e.g. as $\Delta^- \rightarrow n\pi^-$, $\Delta^0 \rightarrow p\pi^-$, $\Delta^+ \rightarrow n\pi^+$, \dots . Therefore the decrease of $\Delta^{0,-}$ resonances reduces the production of negative encharged pions which consequently decreases the π^-/π^+ -ratio (right part in Fig. 8-5). This ratio then appears to be sensitive to the isospin term of equation of state at high densities. One should note that both models used here exhibit a similar asy-stiff behavior at high densities (see Fig.8-1). We deduce that the n/p effective mass splitting mechanism described above is very important in inducing isospin effects on the particle production [285].

A comparison of total π^+/π^- ratio with preliminary data, at different energies, is presented in Fig.8-6, in central $Au + Au$ collisions. We note that the δ

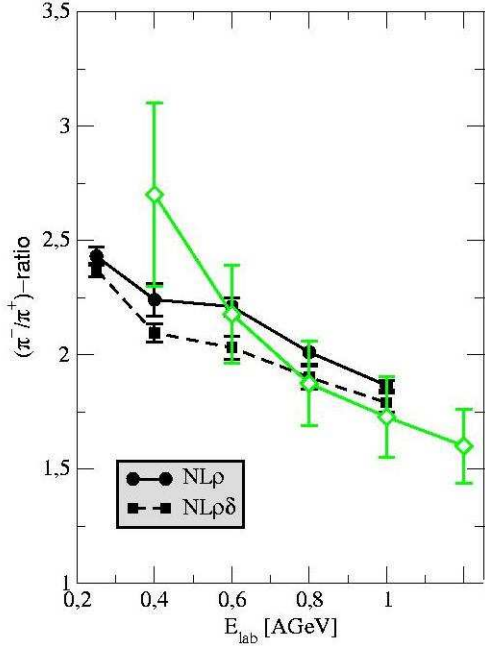


Fig. 8-6. Energy dependence of the (π^-/π^+) -ratio in central $Au + Au$ collisions. Results of $NL\rho$ (solid) and $NL\rho\delta$ (dashed) parametrizations. The grey bars correspond to some very preliminary data from the *FOPI - GSI* collaboration [286].

influence (difference between solid and dashed curves) is slightly decreasing with the beam energy. This is an indication of the n/p effective mass splitting mechanism in Δ^- production, expected to be more important at the threshold.

Generally isospin effects on pion production are decreasing with incident energy, as seen in Fig.8-6, due to secondary collisions, i.e. pion absorption and Δ -rescattering, which are essentially not isospin-dependent. Thus the isospin dependence of pion production will be on average moderated. This trend was already found in earlier studies using a non-relativistic Quantum-Molecular Dynamics (*QMD*) approach [280].

For the same systems new very preliminary data on pion production have recently been reported from the *FOPI*-collaboration at *GSI* [286], shown as grey bars in the Fig.8-6. Generally our simulations provide a qualitative good description of the pion ratio with respect to beam energy, except perhaps at the lower energies. The inclusion of a δ meson in the iso-vector part of the equation of state improves the comparison, at least at higher energies. In any case it appears that π^-/π^+ -ratios might be a probe of the high density symmetry energy and the role of the virtual δ -meson. It would be helpful to look at more exclusive data on pion production in asymmetric systems,[232].

The effect of the δ -field as discussed above is enhanced in the momentum spectra, i.e. the rapidity and transverse momentum distributions, due to the interplay of the isospin effects with the Coulomb interaction which affects

differently the π^+ and π^- distributions. Thus a clearer and more observable effect of the δ -field is predicted in the flow observables of the (π^-/π^+) -ratios, as a function of energy.

8.4 Isospin Transparency

Isospin equilibration is seen in the collisions of systems with different asymmetries. It has been extensively investigated by the *FOPI* collaboration as a signature of transparency [199,289]. Here we investigate it also with respect to the sensitivity to the *iso* – *EOS*. The idea is to study colliding systems with the same mass number but different N/Z ratio. In particular, a combination of $^{96}_{44}Ru$, $N/Z = 1.18$ and $^{96}_{40}Zr$, $N/Z = 1.4$ has been used as projectile/target in experiments at intermediate energies of 0.4 and 1.528 $AGeV$ [199,289]. The degree of stopping or transparency has been determined from the rapidity dependence of the *imbalance ratio* for the mixed reactions $Ru(Zr) + Zr(Ru)$: $R(y^{(0)}) = N^{RuZr}(y^{(0)})/N^{ZrRu}(y^{(0)})$, where $N^i(y^{(0)})$ is the particle yield at a given rapidity for $Ru + Zr$ and $Zr + Ru$ with $i = RuZr, ZrRu$. The observable R is measured for different particle species, like protons, neutrons, light fragments such as t and 3He and produced particles such as pions ($\pi^{0,\pm}$), etc. It characterizes different stopping scenarios.

In the proton case, moving from target to *cm* rapidity, $R(p)$ rises (positive slope) for partial transparency, falls (negative slope) for full rebound scenarios and it is flat when full stopping and total isospin mixing is achieved in the collision. An opposite behavior will appear for neutrons. Indeed we recall that in the full transparency limit R should have the value of $R(p) = Z^{Zr}/Z^{Ru} = 40/44 = 0.91$ and $R(n) = N^{Zr}/N^{Ru} = 56/52 = 1.077$ for protons and neutrons at target rapidity, respectively. Therefore, $R(p)$ can be regarded as a sensitive observable with respect to isospin diffusion, i.e. to properties of the symmetry term.

For the investigation of isospin equilibration we have analyzed transport results obtained in the same way as carried out in the *FOPI* experiment, refs.[287,288]. In particular, central events are selected through the observable *ERAT*, the ratio of the mean transverse to the mean longitudinal kinetic energy. For this a phase space coalescence algorithm for fragment production in the final state is used, and the observable *ERAT* is calculated for each fragment. A detailed description of this analysis can be found in ref.[131], where it was shown that the charged particle multiplicity and *ERAT* distributions fit well the experimental data, as an important check of the phenomenological phase space coalescence model for fragment production. Thus the same centrality cuts as in the *FOPI* experiments [289] can be used.

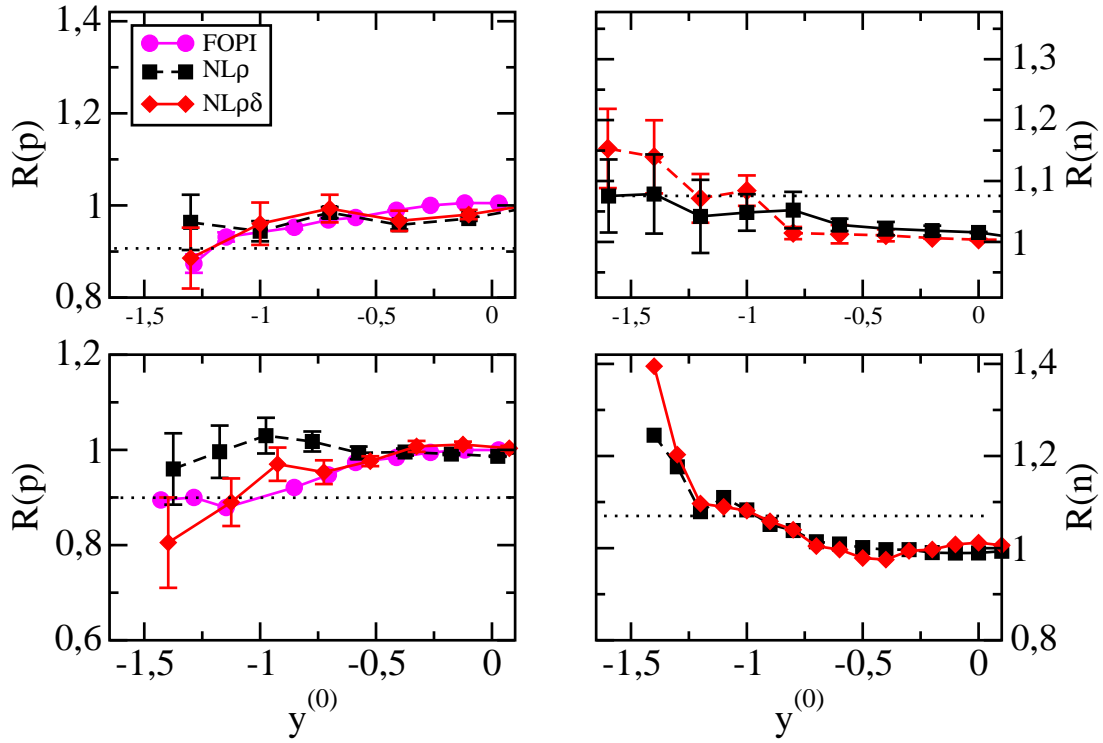


Fig. 8-7. The imbalance ratio $R(y^{(0)}) = \frac{N^{RuZr}(y^{(0)})}{N^{ZrRu}(y^{(0)})}$ as function of the normalized rapidity $y^{(0)} = y/y_{proj}$ of free protons (left panels) and free neutrons (right panels) for the $NL\rho$ and $NL\rho\delta$ models, for central ($b \leq 2 \text{ fm}$) $Ru(Zr) + Zr(Ru)$ -collisions at 0.4 (top) and 1.528 $AGeV$ (bottom) beam energies. The experimental data are taken from the *FOPI* collaboration [289]. The ratio in the initial system is shown by the horizontal dotted line.

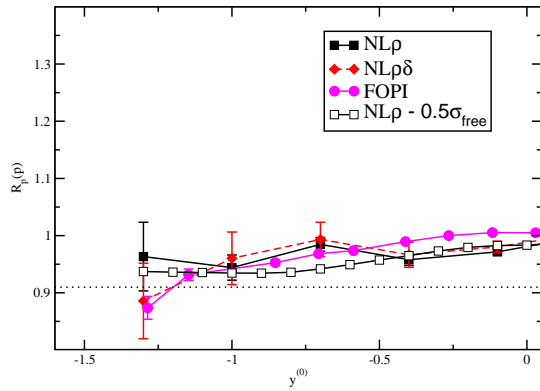


Fig. 8-8. Proton imbalance ratio as function of the normalized rapidity for central ($b \leq 2 \text{ fm}$) $Ru(Zr) + Zr(Ru)$ -collisions at 0.4 $AGeV$ as in the top-left part of Fig.8-7. A curve is added (empty squares) corresponding to a $NL\rho$ calculation with reduced nucleon-nucleon cross sections (half the free values, $\sigma_{NN}(E) = \frac{1}{2}\sigma_{free}$).

In Fig. 8-7 we show the rapidity dependence of the imbalance ratio for free protons ($R(p)$) and free neutrons ($R(n)$) at the two energies 0.4 and 1.528 $AGeV$. The imbalance ratio approaches unity at mid-rapidity for all particle types due to symmetry in the mid-rapidity region, as expected in central collisions.

Going from target- to mid-rapidity the ratio nicely rises for protons, and decreases for neutrons, a good signature of isospin transparency. The effect is more evident for the $NL\rho\delta$ interaction. The observed difference between the two models can be understood since within the $NL\rho\delta$ picture neutrons experience a more repulsive iso-vector mean field, particularly at high densities, than protons, and consequently much less nucleon stopping in the colliding system.

However the influence of the iso-*EOS* on the imbalance ratio of protons and neutrons is not very large. At low intermediate energies (0.4 $AGeV$) one deals with moderate compressions of $\rho_B < 2 \cdot \rho_{sat}$ where the differences in the iso-vector *EOS* arising from the δ meson are small. At higher incident energies (1.528 $AGeV$, Fig.8-7-bottom) where a larger effect is expected, we actually see a slightly higher isospin effect on the imbalance ratios, at least for protons. In fact with increasing beam energy the opening of inelastic channels via the production/decay of Δ resonances through pions, as discussed in the last section, also contribute to the final result. This interpretation is confirmed by other studies [281].

Reduced in-medium Nucleon-Nucleon (NN) cross sections, in particular σ_{np} , will also increase the isospin transparency. This possibility can be investigated considering a factor of two reduction, $\sigma = \frac{1}{2}\sigma_{free}$, of the free NN -cross section values used before, [288]. We note that such a reduction represents rather an upper limit of in-medium effects as compared to recent microscopic Dirac-Brueckner estimations [290]. In Fig.8-8 we show the results for the proton imbalance ratios at 0.4 $AGeV$ with $0.5\sigma_{free}$ in the $NL\rho$ case. We see an overall slightly increased transparency but not enough to reproduce the trend of the experimental values in the target rapidity region. On the other hand the reduction of the NN cross sections, and in particular of $\sigma_{(np)}$, leads too large a transparency in the proton rapidity distributions for central collisions of the charge symmetric $Ru + Ru$ case; as is seen in our simulations and already remarked in previous *IQMD* calculations, [289]. Thus can exclude further reductions of the NN cross sections.

Since the calculations are performed with the same *EOS* for the symmetric nuclear matter, the same compressibility and momentum dependence, the observed transparency appears to be uniquely related to *isovector – EOS* effects, i.e. to the isospin dependence of the nucleon self-energies at high baryon densities. The fact that protons *and* neutrons exhibit an *opposite behavior* for the imbalance ratios at target rapidity suggests that the detection of the

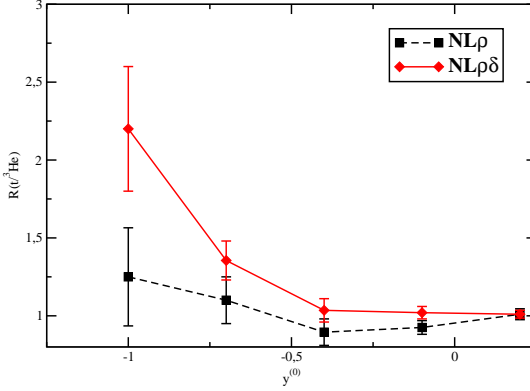


Fig. 8-9. Imbalance ratio of t to 3He for the same collision as in Fig. 8-7 for 0.4 AGeV beam energy.

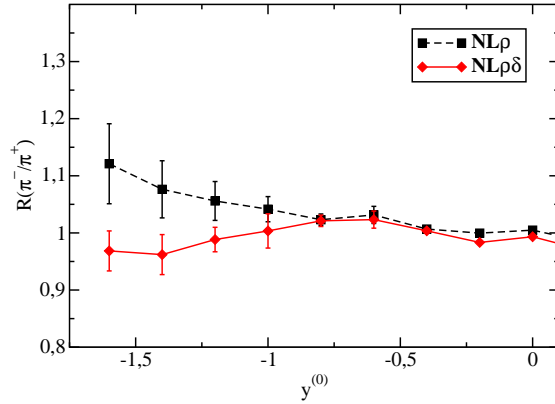


Fig. 8-10. Imbalance ratio for the ratio of negative to positive charged pions for the same collision as in Fig. 8-7 for 0.4 AGeV beam energy.

imbalance observable $R(t/{}^3He)$, i.e. the double ratio of the $t/{}^3He$ yield should reveal a larger sensitivity. The correct and practical method how to properly describe light fragment formation is still controversial. We report here on results obtained in ref. [288] with simplest algorithm, namely a phase space coalescence model [131].

Fig. 8-9 shows the imbalance ratio $R(t/{}^3He)$ for central collisions at 0.4 AGeV incident energy. The isospin effect from the inclusion of the iso-vector, scalar δ meson in the $NL\rho\delta$ model is found to be very large near target rapidities. We note that the effect indeed can be hardly seen from the separate imbalance ratios for protons and neutrons at the same rapidity (see Fig. 8-7 top panels) apart from the difficulties of neutron detections. It would be therefore of great interest to experimentally measure directly this quantity.

Finally, another sensitive observable should be, from the discussion in the last Section, the imbalance ratio of charged pions $R(\pi^-/\pi^+)$ (Fig. 8-10). At variance with the previous results for neutrons and light isobars, this ratio is reduced at target rapidity with the $NL\rho\delta$ model. This effect is consistent with

our understanding of the π^+/π^- - ratios. Pions are produced from the decay of Δ resonances formed during the high density phase, see Fig.8-5. The π^- abundance is then linked to the neutron-excess of the high density matter, as discussed in the previous Section. We recall that the contribution of the δ meson leads to a more repulsive field for neutrons at supra-normal densities and consequently to less neutron collisions and finally to a smaller π^-/π^+ ratio.

We have analyzed the isospin transparency in relativistic collisions. We have observed that this observable is sensitive to the microscopic Lorentz structure of the symmetry term. Effective interactions with symmetry energies which are not much different at 2-3 times normal density ρ_{sat} predict large differences in the *isospin – transparencies*, depending on the relative contribution of the various charged vector and scalar fields. Intermediate energy heavy-ion collisions with radioactive beams can give information on the symmetry energy at high baryon density and on its detailed microscopic structure. We have shown that such experiments provide a unique tool to investigate the strength of the δ – *like* field. The sensitivity is enhanced relative to the static property $E_{sym}(\rho_B)$ because of the covariant nature of the fields involved in collision dynamics.

9 Conclusion and outlook

Nuclear reactions with neutron-rich (or radioactive) nuclei have opened the possibility to learn about the behaviour of the nuclear interaction and, in particular, of the symmetry energy in a wide spectrum of conditions of density and temperature. This study appears extremely important: indeed a deeper understanding of the behaviour of neutrons and protons in a charge asymmetric nuclear medium is essential to test and to extend our present knowledge of the nuclear interaction and is of highest importance for the modelling of astrophysical processes, like supernova explosion or neutron stars.

In the context of nuclear reactions, one has to identify the most sensitive observables that may provide information on the behaviour of the symmetry energy in several conditions of density and temperature. This is the main line followed along this Report.

In Section 2 we discuss the symmetry energy dependence around normal density and how this can affect important properties of neutron-rich nuclei, such as compressibility (and monopole frequency), saturation density and neutron skin.

The behaviour of asymmetric matter at low density has been investigated in Section 3. We discuss in particular the phase diagram of asymmetric matter and the relevant features of instabilities. This subject appears important in connection to the possibility to observe a liquid-gas phase transition in violent heavy ion reactions, where, after the initial collisional shock, low density regions can be easily reached during the expansion phase. New important features, such as the isospin distillation effect, are predicted and some experimental evidences have already appeared along this direction, though a more careful analysis is still needed, to disentangle among other possible contributions to the distillation, such as pre-equilibrium effects, and to really prove the mechanism driving the fragmentation process.

In Section 4 we have focused on features of the early stage of the reaction dynamics between neutron-rich nuclei. Pre-equilibrium emission and collective flows appear particularly sensitive also to the the momentum-dependent part of the interaction. In asymmetric matter a splitting of neutron and proton effective masses is observed. The sign of the splitting is quite controversial, since the behaviour of neutron and proton optical potential at large energy has not been experimentally measured yet. Hence it appears very important to try to extract information on this fundamental question from nuclear collisions, where one can use probes, such as pre-equilibrium particles, particularly sensitive to the high density phase, where also high momenta are reached.

In Section 5, we have explored several fragmentation mechanisms, occurring

at the Fermi energies, in the framework of a stochastic mean-field approach. We discuss the features of multifragmentation in neutron-rich systems, and in particular the isotopic content of fragments. This can be connected to the behaviour (the slope) of the symmetry energy at low density. For semi-peripheral reactions an interesting neutron enrichment of the overlap (“neck”) region appears, due to the neutron migration from higher (spectator regions) to lower (neck) density regions. Also this effect is nicely connected to the slope of the symmetry energy. A careful comparison with experimental data would give important indications on the fragmentation mechanism and on the behaviour of the symmetry energy.

In sections 6-7 we have discussed static properties and dynamical mechanisms in the context of relativistic approaches including isovector, both vector and scalar, channels (the ρ and δ mesons). The contribution of these two channels to static or dynamical properties has a different weight, leading to interesting effects on the frequency of the stable isovector modes, that is not simply related to the value of the symmetry energy (see Sections 6, 7). In the low density region, instabilities and the distillation mechanisms are observed, in close parallelism with the results of the non-relativistic treatment discussed above.

Finally in Section 8 we discuss isospin effects in relativistic heavy ion collisions. The observable consequences of the inclusion of the δ meson are enhanced by the Lorentz structure of the effective nuclear interaction in the isovector channel. In particular, effects on particle production, such as pions or kaons, light particle collective flows and isospin diffusion are investigated. Once again, from the comparison with experimental data, one could get important information on the structure of the isovector interaction.

9.1 Outlook: The Eleven Observables

In conclusion, the study of isospin effects on static and dynamical nuclear properties appears as a very rich and stimulating field. Several probes can be used to get an insight on the behaviour of the symmetry energy in different conditions of density and temperature. A joint effort, from the experimental and theoretical side, should allow to extract relevant information on fundamental properties of the nuclear interaction. We like to suggest a selection of *Eleven Observables*, from low to relativistic energies, that we expect particularly sensitive to the microscopic structure of the *in medium* interaction in the isovector channel, i.e. to the symmetry energy and its “fine structure”:

1. *Competition of Reaction Mechanisms.* Interplay of low-energy dissipative mechanisms, e.g. fusion (incomplete) vs. deep-inelastic vs. neck fragmentation:

a stiff symmetry term leads to a more repulsive dynamics.(Sect.5)

2. *Energetic particle production.* N/Z of fast nucleon emission: symmetry repulsion of the neutron/proton mean field in various density regions. Moreover at the Fermi energies we expect to see also effects from the n/p splitting of the effective masses. Even the spectra and yields of hard photons produced via (n, p) bremmstrahlung should be sensitive to the density and momentum dependence of the symmetry fields.(Sect.4)

3. *Neutron/Proton correlation functions.* Time-space structure of the fast particle emission and its relation to the baryon density of the source. Again combined effects of density and momentum dependence of the symmetry term are expected (Sect.4).

4. *E-slope of the Lane Potential.* A systematic study of the energy dependence of the (n/p) optical potentials on asymmetric nuclei will shed lights on the effective mass splitting, at least around normal density.(Sects.2 and 6)

5. *Isospin Distillation (Fractionation).* Isospin content of the Intermediate Mass Fragments in central collisions. Test of the symmetry term in dilute matter and connection to the possibility to observe a liquid-gas phase transition.(Sect.5)

6. *Properties of Neck-Fragments.* Mid-rapidity *IMF* produced in semicentral collisions: correlations between N/Z , alignment and size. Isospin effects on the reaction dynamics and “Isospin Migration”.(Sect.5)

7. *Isospin Diffusion.* Measure of charge equilibration in the “spectator” region in semicentral collisions. Test of the interplay between concentration and density gradients in the isospin dynamics.(Sect.5)

8. *Neutron-Proton Collective Flows.* Together with light isobar flows. Check of symmetry transport effects. Test of the momentum dependence (relativistic structure) of the interaction in the isovector channel. Measurements also for different p_t selections. (Sects.4 and 8)

9. *Isospin Transparency.* Measure of isospin properties in Projectile/Target rapidity regions in central collisions of “mirror” ions at intermediate energies. Similar effects, but due to the nucleon-nucleon cross section are expected to be smaller (Sect.8).

10. π^-/π^+ *Yields.* Since π^- are mostly produced in nn collisions we can expect a reduction for highly repulsive symmetry terms at high baryon density. Importance of a p_t selection. Similar studies for mesons with smaller rescattering effects would be of great interest. (Sect.8)

11. *Deconfinement Precursors.* Signals of a mixed phase formation (quark-

bubbles) in high baryon density regions reached with asymmetric *HIC* at intermediate energies, versus the properties of the interaction considered (Sect.8).

We stress again the richness of the phenomenology and nice opportunities of getting several cross-checks from completely different experiments.

For the points 3, 5, 6, 7, 8, 9, 10 from the transport simulations discussed here we presently get some indications of *asy-stiff* behaviors, i.e. increasing repulsive density dependence of the symmetry term, but not more fundamental details. Moreover all the available data are obtained with stable beams, i.e. within low asymmetries.

Acknowledgements

This report is deeply related to ideas and results partially reached in very pleasant and fruitful collaborations with very nice people: L.W.Chen, G.Fabbri, G.Ferini, Th.Gaitanos, C.M.Ko, A.B.Larionov, B.A.Li, R.Lionti, B.Liu, S.Maccarone, F.Matera, M.Zielinska-Pfabe', J.Rizzo, L.Scalone and H.H.Wolter. We have learnt a lot from all of them in physics as well as in human relationships.

We are particularly grateful to H.H.Wolter for many stimulating suggestions during the preparation of the report and for a very accurate reading of the manuscript.

Finally we warmly thank our experimental colleagues for the richness of mutual interaction and for the exciting possibility of discussing new results even before publication. We like to mention in particular the Medea/Multics and Chimera Collaboration at the LNS-Catania and the FOPI Collaboration at the GSI-Darmstadt.

References

- [1] *In this same place theachers and pupils are storing topics that they don't like to get lost*
Carved on the stone architrave of the Old Library, Conques Abbey, X^{th} Century, Aveyron (Massif Central), France.
- [2] D.Vautherin and D.M.Brink, Phys.Rev. C3 (1972) 676.
- [3] H.Krivine, J.Treiner and O.Bohigas, Nucl.Phys. A336 (1980) 155.
- [4] E.Chabanat, P.Bonche, P.Haensel, J.Meyer, R.Schaeffer, Nucl.Phys. A627 (1997) 710.
- [5] E.Chabanat, P.Bonche, P.Haensel, J.Meyer, R.Schaeffer, Nucl.Phys. A635 (1998) 231.
- [6] F.Douchin, P.Haensel and J.Meyer, Nucl.Phys. A665 (2000) 419.
- [7] I. Bombaci, T.T.S. Kuo, U. Lombardo, Physics Reports 242 (1994) 165.
- [8] I. Bombaci, Phys.Rev. C55 (1997) 1.
- [9] We remark here that also all relativistic mean field approaches in the presently used approximation scheme are predicting a *stiff-like* simmetry term, proportional to the baryon density, coming from the ρ -meson field contribution, see ref.[10]. Actually a *superstiff-like* behaviour is obtained when a coupling to the scalar charged meson δ is added, see ref.s [11,12,13].
- [10] S.Yoshida, H.Sagawa, N.Takigawa, Phys.Rev. C58 (1998) 2796.
- [11] S.Kubis, M.Kutschera, Phys.Lett. B399 (1997) 191.
- [12] B.Liu, V.Greco, V.Baran, M.Colonna, M.Di Toro, Phys.Rev. C65 (2002) 045201.
- [13] V.Greco, M.Colonna, M.Di Toro, F.Matera, Phys.Rev. C67 (2003) 015203.
- [14] B.-A.Li, C.M.Ko, W.Bauer, Int.J.Mod.Phys. E7 (1998) 147.
- [15] *Isospin Physics in Heavy-ion Collisions at Intermediate Energies*, Eds. Bao-An Li and W. Udo Schröder, Nova Science Publishers (2001, New York).
- [16] M.Di Toro, V.Baran, M.Colonna, V.Greco, S.Maccarone, M.Cabibbo, Eur.Phys.J. A13 (2002) 155
- [17] Contributions of P.G.Reinhard, H.Sagawa, M.Di Toro, G.Colo', E.G.Lanza, in *GR98*, Nucl.Phys. A649 (1999) 1c-446c.
- [18] I.Hamamoto, Phys.Rev. C60 (1999) 031303.
- [19] H.Müller, B.D.Serot, Phys.Rev. C52 (1995) 2072.
- [20] V.Baran, M.Colonna, M.Di Toro, V.Greco, Phys.Rev.Lett. 86 (2001) 4492.

- [21] M.Colonna, Ph.Chomaz, S.Ayik, Phys.Rev.Lett. 88 (2002) 122701.
- [22] J.Margueron, P.Chomaz, Phys. Rev. C67 (2003) 041602.
- [23] Ph.Chomaz, M.Colonna, J.Randrup, Phys.Rep. 389 (2004) 263.
- [24] D.O.Handzy *et al.*, Phys.Rev.Lett. 75 (1995) 2916.
- [25] B.-A.Li, A.T.Sustich, B.Zhang, Phys.Rev. C64 (2001) 054604.
- [26] P.Danielewicz, Nucl.Phys. A685 (2001) 368c.
- [27] J.D.Walecka, Ann.Phys.(N.Y.) 83 (1974) 491.
- [28] B.D.Serot, J.D.Walecka in *Advances in Nuclear Physics* Vol. 16, Eds. J.M.Negele and E.Vogt, Plenum, New York, 1986.
- [29] B.D.Serot, J.D.Walecka, Int.J.Mod.Phys. E6 (1997) 515.
- [30] R.J.Furnstahl, Nucl.Phys. A706 (2002) 85.
- [31] D.G.Madland, T.J.Bürvenich, J.A.Maruhn, P.G.Reinhard, Nucl.Phys. A741 (2004) 52.
- [32] C.H.Lee, T.T.S.Kuo, G.Q.Li, G.E.Brown, Phys.Rev. C57 (1998) 3488.
- [33] F.de Jong, H.Lenske, Phys.Rev. C57 (1998) 3099.
- [34] F.Hofmann, C.M.Keil, H.Lenske, Phys.Rev. C64 (2001) 034314 .
- [35] E.N.E.van Dalen, C.Fuchs, A.Faessler, *The Relativistic Dirac-Brueckner Approach to Asymmetric Nuclear Matter* arXiv:nucl-th/0407070, Nucl.Phys. A, in press.
- [36] V.Greco, M.Colonna, M.Di Toro, G.Fabbri, F.Matera, Phys.Rev. C64 (2001) 045203.
- [37] U.Lombardo, W.Zuo, "EOS of Asymmetric Nuclear Matter", in [15] pp. 1-34 and refs. therein.
- [38] W.D.Myers, *At. Data and Nucl. Data Tables* 17 (1976) 411.
- [39] M.Lopez-Quelle, S.Marcos, R.Niembro, A.Bouyssy, N.Van Giai, Nucl.Phys. A483 (1988) 479.
- [40] Bao-An Li, Nucl.Phys. A681 (2001) 434c.
- [41] M.Prakash, K.S.Bedell, Phys.Rev. C32 (1985) 1118.
- [42] M.Prakash, T.L.Ainsworth, Phys.Rev. C36 (1987) 346.
- [43] R.B.Wiringa, V.Fiks, A.Fabrocini, Phys.Rev. C38 (1988) 1010.
- [44] A.Akmal, V.R.Pandharipande, D.G.Ravenhall, Phys.Rev. C58 (1998) 1804.
- [45] M.Prakash et al., Phys.Rep. 280 (1997) 1.

- [46] Bao-An Li, Phys.Rev.Lett. 85 (2000) 4221.
- [47] S.Fantoni, A.Sarsa, K.E.Schmidt, Phys.Rev.Lett. 87 (2001) 181101.
- [48] Y.-W.Lui, D.H.Youngblood, T.Tokimoto, H.L.Clark, B.John, Phys.Rev. C70 (2004) 014307.
- [49] M.Kutschera, W.Wojcik, Phys.Lett. B325 (1994) 217.
- [50] M.Colonna, M.Di Toro, A.Larionov, Phys.Lett. B428 (1998) 1.
- [51] V.Baran, A.Larionov, M.Colonna, M.Di Toro, Nucl.Phys. A632 (1998) 287.
- [52] M.Di Toro et al., Progr.Part.Nucl.Phys. 42 (1999) 125-136.
- [53] M.Colonna, M.Di Toro, A.Guarnera, Nucl.Phys. A589 (1995) 160.
- [54] M.Di Toro et al., Nucl.Phys. A681 426c (2001) 426c.
- [55] V. Baran, M.Colonna, V.Greco, M.Di Toro, M.Zielinska Pfabé, H.H.Wolter, Nucl.Phys. A703 (2002) 603.
- [56] V.Baran, M.Colonna, M.Di Toro, Nucl.Phys. A730 (2004) 329.
- [57] I.Bombaci, "EOS for isospin-asymmetric nuclear matter for astrophysical applications", in [15] pp. 35-81 and refs. therein.
- [58] W.Zuo, I.Bombaci, U.Lombardo, Phys.Rev. C60 (1999) 24605.
- [59] O.Sjöberg, Nucl.Phys. A265 (1976) 511 and refs. therein.
- [60] Bao-An Li, Phys.Rev. C69 (2004) 064602.
- [61] A.M.Lane, Nucl.Phys. 35 (1962) 676.
- [62] F.D.Becchetti, G.W.Greenless, Phys.Rev. 182 (1969) 1190.
- [63] P.E.Hodgson, *The Nucleon Optical Model*, World Scientific, 1994
- [64] I.Bombaci et al., Nucl.Phys. A583 (1995) 623.
- [65] J.Rizzo, M.Colonna, M.Di Toro, V.Greco, Nucl.Phys. A732 (2004) 202.
- [66] C.Gale, G.F.Bertsch, S.Das Gupta, Phys.Rev. C41 (1990) 1545.
- [67] V.Greco, Diploma Thesis (1997);
V.Greco, A.Guarnera, M.Colonna, M.Di Toro, Phys.Rev. C59 (1999) 810.
Nuovo Cimento A111 (1998) 865.
- [68] P.Sapienza et al., Phys.Rev.Lett. 87 (2001) 2701.
- [69] L.D.Landau, Soviet Physics JETP 5 (1957) 101.
- [70] A.B.Migdal, *Theory of finite Fermi systems and applications to atomic nuclei*, Wiley & Sons, N.Y. 1967.

[71] G.Baym and C.J.Pethick in *The physics of Liquid and Solid Helium* edited by K.H.Bennemann and J.B.Ketterson, Vol 2, (Wiley, New-York, 1978), p.1.

[72] C.J.Pethick, D.G.Ravenhall, Ann.Phys. (N.Y.) 183 (1988) 131.

[73] L.D.Landau and E.M.Lifshitz, *Statistical Physics*, (Pergamon Press, 1989), p. 288.

[74] H.S.Xu et al., Phys.Rev.Lett. 85 (2000) 716.

[75] S.Yennello, Proc.Int.School-Seminar on "Heavy Ion Physics", Ed. Yu.Ts.Oganessian, World Sci. 1997

[76] P.Haensel, Nucl.Phys. A301 (1978) 53.

[77] F.Matera, V.Yu.Denisov, Phys.Rev. C49 (1994) 2816.

[78] G.Baym, H.A.Bethe, C.J.Pethick, Nucl.Phys. A175 (1971) 225.

[79] M.Colonna, Ph.Chomaz, Phys.Rev. C49 (1994) 1908.

[80] M.Colonna, Ph.Chomaz, J.Randrup, Nucl.Phys. A567 (1994) 637.

[81] G.Fabbri, F.Matera, Phys.Rev. C58 (1998) 1345.

[82] M.Colonna, M.Di Toro, A.Guarnera, V.Latora, A.Smerzi, Phys.Lett. 307 (1993) 273.

[83] M.Colonna, M.Di Toro, A.Guarnera, Nucl.Phys. A580 (1994) 312.

[84] B.-A.Li, C.M.Ko, Nucl.Phys. A618 (1997) 498.

[85] B.-A.Li, A.T.Sustich, M.Tilley, B.Zhang, Nucl.Phys. A699 (2002) 493.

[86] Ch.Gregoire et al., Nucl.Phys. A465 (1987) 315.

[87] A.Bonasera, F.Gulminelli, J.Molitoris, Phys.Rep. 243 (1994) 1.

[88] V.Baran, A.Bonasera, M.Colonna, M.Di Toro, A.Guarnera, Prog.Part.Nucl.Phys. 38 (1997) 263.

[89] D.H.Boal, C.K.Gelbke, B.K.Jennings, Rev.Mod.Phys. 62 (1990) 553.

[90] W.Bauer, C.K.Gelbke, S.Pratt, Ann.Rev.Nucl.Part.Sci. 42 (1992) 77.

[91] D.Ardouin, Int.Jour.Phys. E6 (1997) 391.

[92] U.A.Wiedemann, U.Heinz, Phys.Rep. 319 (1999) 145.

[93] L.-W.Chen, V.Greco, C.M.Ko and B.-A.Li, Phys.Rev.Lett. 90 (2003) 162701.

[94] L.-W.Chen, V.Greco, C.M.Ko and B.-A.Li, Phys.Rev. C68 (2003) 014605.

[95] <http://www.nscl.msu.edu/ria/index.php> and <http://www.phy.anl.gov/ria/>

[96] L.-W.Chen, C.M.Ko, and B.-A. Li, Nucl.Phys. A729 (2003) 809.

- [97] W.G.Gong *et al.*, Phys.Rev.Lett. 65 (1990) 2114.
- [98] W.G.Gong, W.Bauer, C.K.Gelbke, S.Pratt, Phys.Rev. C43 (1991) 781.
- [99] W.G.Gong *et al.*, Phys.Rev. C47 (1993) R429.
- [100] G.J.Kunde *et al.*, Phys.Rev.Lett. 70 (1993) 2545.
- [101] C.J.Gelderloos *et al.*, Phys.Rev.Lett. 75 (1995) 3082.
- [102] R.Lednicky, V.L.Lyuboshitz, B.Erazmus and D.Nouais, Phys.Lett. B373 (1996) 30.
- [103] S.Voloshin, R.Lednicky, S.Panitkin and N.Xu, Phys.Rev.Lett. 79 (1997) 4766.
- [104] D.Ardouin *et al.*, Phys.Lett. B446 (1999) 191.
- [105] F.Wang and S.Pratt, Phys.Rev.Lett. 83 (1999) 3138.
- [106] D.Gourio *et al.*, Eur.Phys.J. A7 (2000) 245.
- [107] R.Ghetti *et al.*, Nucl.Phys. A674 (2000) 277.
- [108] R.Ghetti *et al.*, Phys.Rev.Lett. 87 (2001) 102701.
- [109] S.E.Koonin, Phys.Lett. B70 (1977) 43.
- [110] S.Pratt, Phys.Rev.Lett. 53 (1984) 1219;
same Phys.Rev. D33 (1986) 72.
- [111] S.Pratt and M.B.Tsang, Phys.Rev. C36 (1987) 2390.
- [112] M.Colonna, M.Di Toro, G.Fabbri, S.Maccarone, Phys.Rev. C57 (1998) 1410.
- [113] L.Scalone, M.Colonna, M.Di Toro, Phys.Lett. B461 (1999) 9.
- [114] B.-A.Li, C.B.Das, S.Das Gupta, C.Gale, Phys.Rev. C69 (2004) 011603.
- [115] B.-A.Li, C.B.Das, S.Das Gupta, C.Gale, Nucl.Phys. A735 (2004) 563.
- [116] L.-W.Chen, C.M.Ko, and B.-A. Li, Phys.Rev. C69 (2004) 054606.
- [117] B.-A.Li, C.M.Ko, and Z.Z.Ren, Phys.Rev.Lett. 78 (1997) 1644.
- [118] L.-W.Chen, C.M.Ko, and B.-A. Li, Phys.Rev. C68 (2003) 017601.
- [119] Ph.Chomaz and F.Gulminelli, Phys.Lett. B447 (1999) 221.
- [120] W.P.Tan *et al.*, Phys.Rev. C64 (2001) 051901R.
- [121] H.Stöcker and W.Greiner, Phys.Rep. 137 (1986) 277.
- [122] P.Danielewicz and Q.Pan, Phys.Rev. C46 (1992) 2002.
- [123] S.Das Gupta, G.W.Westfall, Physics Today 46 (1993) 34.
- [124] P.Danielewicz, R.Lacey and W.G.Lynch, Science 298 (2002) 1592 and refs. therein.

- [125] V.Greco, C.M.Ko and P.Levai, Phys.Rev. C68 (2003) 034904;
 D.Molnar and S.Voloshin, Phys.Rev.Lett. 91 (2003) 092301;
 B.Zhang, M.Gyulassy and C.M.Ko, Phys.Lett. B455 (1999) 45;
 P.Kolb, J.Sollfrank and U.Heinz, Phys.Rev. C62 (2000) 054909.
- [126] P.Danielewicz and G.Odyniec, Phys.Lett. B157 (1985) 146.
- [127] B.-A. Li and A.T.Sustich, Phys.Rev.Lett. 82 (1999) 5004.
- [128] J.Y.Ollitrault, Phys.Rev. D46 (1992) 229.
- [129] P.Danielewicz, Nucl.Phys. A673 (2000) 375.
- [130] A.B.Larionov, W.Cassing, C.Greiner and U.Mosel, Phys.Rev. C62 (2000) 064611.
- [131] T.Gaitanos, C.Fuchs, H.H.Wolter and A.Faessler, Eur.Phys.J. A12 (2001) 421.
- [132] B.-A. Li, Z.Ren, C.M.Ko, S.J.Yennello, Phys.Rev.Lett. 76 (1996) 4492.
- [133] J.Zhang et al., Phys.Rev. C50 (1994) 1617.
- [134] B.-A. Li, Nucl.Phys. A708 (2002) 365.
- [135] V.Greco, M.Colonna, M.Di Toro, T.Gaitanos, H.H.Wolter and V.Baran, Phys.Lett. B562 (2003) 215;
 V.Greco, Ph.D.Thesis 2002.
- [136] G.Q. Li and R. Machleidt, Phys.Rev. C48 (1993) 1702;
 same Phys.Rev. C49 (1994) 566.
- [137] Q.Li, Z.Li, E.Zhao, Phys.Rev. C69 (2004) 017601.
- [138] M.Prakash, T.T.S.Kuo, S.Das Gupta, Phys.Rev. C37 (1988) 2253.
- [139] J.Decharge and D.Gogny, Phys.Rev. C21 (1980) 1568 and refs. therein.
- [140] V.de La Mota, F.Sebille, M.Farine, B.Remaud, P.Schuck, Phys.Rev. C46 (1992) 677.
- [141] A.Guarnera, *TWINGO Code*, Ph.D.Thesis, Univ.of Caen, July 1996
- [142] G.Westfall, Nucl.Phys. A630 (1998) 27c and refs. therein.
- [143] R.Pak et al., Phys.Rev.Lett. 78 (1997) 1022.
- [144] R.Pak et al., Phys.Rev.Lett. 78 (1997) 1026.
- [145] The reduced impact parameter is defined as $b_{red} \equiv b/b_{max}$ where b_{max} is the sum of the two nuclear radii.
- [146] B.Blättel, V.Koch and U.Mosel, Rep.Prog.Phys. 56 (1993) 1.
- [147] D.J.Magestro et al., Phys.Rev. C61 (2000) 021602.
- [148] A.Andronic et al., Nucl.Phys. A661 (1999) 333c.

- [149] G.F.Bertsch, S.Das Gupta, *Phys.Rep.* 160 (1988) 189.
- [150] A.Bonasera et al., *Phys.Rep.* 244 (1994) 1.
- [151] A.Bonasera, G.F.Burgio, M.Di Toro, *Phys.Lett.* B221 (1989) 233.
- [152] A.Bonasera, F.Gulminelli, *Phys.Lett.* B259 (1991) 399.
- [153] M.Farine, T.Sami, B.Remaud, F.Sebille, *Z.Phys.* A339 (1998) 363.
- [154] M.Colonna et al., *Nucl.Phys.* A642 (1998) 449.
- [155] M.Colonna et al., *Nucl.Phys.* A742 (2004) 337
- [156] A.Guarnera, M.Colonna, Ph.Chomaz, *Phys.Lett.* B373 (1996) 267.
- [157] S.Ayik, C.Gregoire, *Phys.Lett.* B212 (1988) 269.
- [158] S.Ayik, C.Gregoire, *Nucl.Phys.* A513 (1990) 187.
- [159] J.Randrup, B.Remaud, *Nucl.Phys.* A514 (1990) 339.
- [160] Ph.Chomaz, M.Colonna, A.Guarnera, J.Randrup, *Phys. Rev. Lett.* 73 (1994) 3512.
- [161] M.Colonna, G.F.Burgio, Ph.Chomaz, M.Di Toro, J.Randrup, *Phys. Rev. C47* (1993) 1395.
- [162] M. Colonna, *Nucl. Phys. A* 630 (1998) 136c.
- [163] G.F.Bertsch, *Phys.Lett.* B141 (1984) 9.
- [164] S.J.Yennello et al., *Phys.Lett.* B321 (1994) 15.
- [165] H.Johnston et al., *Phys.Lett.* B371 (1996) 186.
- [166] E.Ramakrishnan et al., *Phys.Rev.* C57 (1998) 1803.
- [167] J.Toke et. al., *Phys.Rev.Lett.* 82 (1999) 1399.
- [168] G.J.Kunde et al., *Phys.Rev.Lett.* 77 (1996) 2897.
- [169] G.Kortemeyer, W.Bauer and G.J.Kunde, *Phys.Rev. C55* (1997) 2730.
- [170] M.B.Tsang et al., *Phys.Rev.Lett.* 86 (2001) 5023.
- [171] T.X.Liu et al., *Phys.Rev. C69* (2004) 014603
- [172] D.V.Shetty et al., *Phys.Rev. C68* (2003) 054605.
- [173] D.V.Shetty et al., *Phys.Rev. C68* (2003) 021602(R).
- [174] D.V.Shetty et al., *Phys.Rev. C70* (2004) 011601(R).
- [175] E.Geraci et al., *Nucl.Phys.* A732 (2004) 173.
- [176] E.Martin et al., *Phys.Rev. C62* (2000) 027601.

- [177] G.Casini et al., Phys.Rev.Lett. 71 (1993) 2567.
- [178] A.A.Stefanini et al., Z.Phys. A351 (1995) 167.
- [179] J.Toke et. al., Phys.Rev.Lett. 75 (1995) 2920.
- [180] C.P.Montoya et. al., Phys.Rev.Lett. 73 (1994) 3070.
- [181] J.Lukasik et al., Phys.Rev. C55 (1997) 1906.
- [182] T.Lefort et al., Nucl.Phys. A662 (2000) 397.
- [183] L.Gingras et al., Phys.Rev. C65 (2002) 061604.
- [184] B.Davin et al., Phys.Rev. C65 (2002) 064614.
- [185] F.Bocage et al., Nucl.Phys. A676 (2000) 391.
- [186] J.Colin et al., Phys.Rev. C67 (2003) 064603.
- [187] A.Pagano et al., Nucl.Phys. A681 (2001) 331c.
- [188] A.Pagano et al., Nucl.Phys. A734 (2004) 504c.
- [189] J.F.Dempsey et al., Phys.Rev. C54 (1996) 1710.
- [190] G.Poggi, Nucl.Phys. A685 (2001) 296c.
- [191] P.M.Milazzo et al., Phys.Lett. B509 (2001) 204.
- [192] P.M.Milazzo et al., Nucl.Phys. A703 (2002) 466.
- [193] E.Plagnol et al., Phys.Rev. C61 (1999) 0614606.
- [194] Y.Larochelle et al., Phys.Rev. C62 (2000) 051602(R).
- [195] L.G.Sobotka et al., Phys.Rev. C55 (1997) 2109.
- [196] H.Xu et al., Phys.Rev. C65 (2002) 061602(R).
- [197] L.G.Sobotka et al., Phys.Rev. C62 (2000) 031603(R).
- [198] M.B.Tsang et al., Phys.Rev.Lett. 92 (2004) 062701.
- [199] F.Rami et al., Phys.Rev.Lett. 84 (2000) 1120.
- [200] G.A.Souliotis, M.Velselsky, D.V.Shetty, S.J.Yennello, Phys.Lett. B588 (2004) 35.
- [201] Feng-Shou Zhang et al., Phys.Rev. C 60 (1999) 064604.
- [202] Jian-Ye Liu et al., Nucl.Phys. A726 (2003) 123.
- [203] M.B. Tsang et al., Phys.Rev. C 64 (2001) 054615.
- [204] A. Ono et al., Phys.Rev. C 68 (2003) 051601(R).
- [205] J. Lukasik et al., Phys. Lett. B566 (2003) 76.

[206] A.S. Botvina et al., Phys.Rev. C 59 (1999) 3444.

[207] M.Colonna, N.Colonna, A.Bonasera, M.Di Toro, Nucl.Phys. A541 (1992) 295.

[208] L.G. Sobotka, Phys.Rev. C 50 (1994) 1272R.

[209] U. Brosa, S. Grossman, A. Muller, Phys. Rep. 197 (1990) 167.

[210] V.Viola et al., Phys.Rev. C31 (1985) 1550.

[211] D.J.Hinde et al., Nucl.Phys. A472 (1987) 318.

[212] We like to call the $r - r1$ -correlation plot as *Wilczynski-2 Plot*. Indeed this correlation, very important to rule-out a statistical fission scenario for fragments produced at mid-rapidity, nicely emerged during hot discussions with Janusz the *LNS - INFN*, Catania. As shown in the discussion this correlation represents also a *chronometer* of the fragment formation mechanism. In this sense it is the nice Fermi energy complement of the famous *Wilczynski Plot* which gives the time-scales in Deep Inelastic Collisions.

[213] E.A. Uehling and G.E. Uhlenbeck, Phys.Rev. 43 (1933) 552.

[214] E.J. Hellund and E.A. Uehling, Phys.Rev. 56 (1939) 818.

[215] R.H. Anderson, C.J. Pethick, K.F. Quader, Phys.Rev. B35 (1987) 1620.

[216] L. Shi and P. Danielewicz, Phys.Rev. C 68 (2003) 064604.

[217] R.Balian, *From Microphysics to Macrophysics*, Springer Verlag, Berlin 1992.

[218] M.M.Sharma, M.A.Nagarajan and P.Ring, Ann.Phys.(NY) 231 (1994) 110, G.A.Lalazissis, M.M.Sharma, P.Ring and Y.K.Gambhir, Nucl. Phys. A608 (1996) 202.

[219] P.Ring, Prog.Part.Nucl.Phys. 37 (1996) 193.

[220] S.Typel and H.H.Wolter, Nucl.Phys. A656 (1999) 331.

[221] C.M.Ko and G.Q.Li, J.of Phys. G22 (1996) 1673.

[222] A.Dellafore and F.Matera, Phys.Rev. C44 (1991) 2456.

[223] C.J.Horowitz and K.Wehrberger, Nucl.Phys. A531 (1991) 665.

[224] D.Vretenar, G.A.Lalazissis, R.Behnsch, W.Poeschl and P.Ring, Nucl.Phys. A621 (1997) 853.

[225] Z.Y.Ma , N.Van Giai, H.Toki and M.L'Huillier, Phys.Rev. C55 (1997) 2385.

[226] Z.Y.Ma , N.Van Giai, A.Wandelt, D.Vretenar and P.Ring, Nucl.Phys. A686 (2001) 173 and refs. therein.

[227] B.A.Nikolaus, T.Hoch, D.G.Madland, Phys.Rev. C46 (1992) 1757.

[228] R.J.Furnstahl and J.J.Rusnak, Nucl.Phys. A627 (1997) 495.

[229] R.J.Furnstahl and B.D.Serot, Comm.Nucl.Part.Phys. 2 (2000) A23 and refs. therein.

[230] R.J.Furnstahl and B.D.Serot, Nucl.Phys. A671 (2000) 447.

[231] T.J.Bürvenich, D.G.Madland, J.A.Maruhn and P.G.Reinhard, Phys.Rev. C65 (2002) 044308.

[232] T.Gaitanos et al., Nucl.Phys. A732 (2004) 24.

[233] E.Schiller and H.Muether, Eur.Phys.J. A11 (2001) 15.

[234] Z.Ma and L.Liu, Phys.Rev. C66 (2002) 024321.

[235] J.Boguta and C.E.Price, Nucl.Phys. A505 (1989) 123.

[236] C.J.Horowitz and B.D.Serot, Nucl.Phys. A399 (1983) 529.

[237] A.Bouyssy, J.F.Mathiot, N.Van Giai and S.Marcos, Phys.Rev. C36 (1987) 380.

[238] V.Greco, F.Matera, M.Colonna, M.Di Toro and G.Fabbri, Phys.Rev. C63 (2001) 035202.

[239] S.R.de Groot, W.A. van Lee and Ch.G. van Weert, *Relativistic Kinetic Theory*, North-Holland Amsterdam 1980.

[240] R.Hakim, Nuovo Cimento 6 (1978) 1.

[241] M.Di Toro, A.Drago, V.Greco, A.Lavagno, *Isospin Dependence of the Critical Quark-Deconfinement Densities*, arXiV:nucl-th/0210052.

[242] “It is important to put the properties of *neutron* matter at *subnuclear* densities on as firm a footing as possible not only for astrophysical applications, but also for interpreting terrestrial experiments with coming radioactive beam facilities”, C.J.Pethick and D.G.Ravenhall in *The lives of neutron stars*, NATO ASI Series C Vol.450 (1995) p.59.

[243] B.A.Brown, Phys.Rev.Lett. 85 (2000) 5296.

[244] C.J.Horowitz and J.Piekarewicz, Phys.Rev.Lett. 86 (2001) 5647.

[245] We note that in the non-relativistic case the kinetic contribution to K_{sym} is actually negative, since it has the form $-\pi^2\rho_0/(Mk_F)$ which is of the order $\sim -30\text{MeV}$. In the relativistic case it becomes slightly positive due to the density dependence of the nucleon effective mass.

[246] The solid lines in Fig.4 are not fully symmetric with respect to the $\alpha = 0$ dashed line. This is due to the fact that, for fixed baryon density, the total scalar density which gives the σ field contribution (first part of the Eq.(6)) is also slightly N/Z dependent.

[247] H.Huber, F.Weber, M.K.Weigel, Phys.Rev. C57 (1997) 3484.

[248] G.Sauer, H.Chandra, U.Mosel, Nucl.Phys. A264 (1976) 221.

[249] G.F.Bertsch, P.J.Siemens, Phys.Lett. B126 (1983) 9.

[250] H.R.Jaqaman, A.Z.Mekjian and L.Zamick, Phys.Rev. C29 (1984) 2067.

[251] Of course we can have other asymmetric NM instability regions, at higher baryon densities, with a different structure of the unstable modes [20]. Here some interactions are even predicting quite exciting *isovector-like* (species separation) unstable oscillations. Unfortunately all that appears out of the present experimental possibilities.

[252] M.Jaminon, C.Mahaux, P.Rochus, Phys.Rev. C22 (1980) 2027.

[253] M.Jaminon, C.Mahaux, Phys.Rev. C40 (1989) 354.

[254] R.Kozack, D.G.Madland, Phys.Rev. C39 (1989) 1461.

[255] R.Kozack, D.G.Madland, Nucl.Phys. A509 (1990) 664.

[256] J.Klug et al., Phys.Rev. C67 (2003) 0316001R
ibidem Phys.Rev. C68 (2003) 064605.

[257] A.A.Abrikosov and I.M.Khalatnikov, Rep.Prog.Phys. 22 (1959) 329.

[258] Ch.Fuchs, H.Lenske, H.H.Wolter, Phys.Rev. C52 (1995) 3043.

[259] Ch.Fuchs, H.H.Wolter, Nucl.Phys. A589 (1995) 732.

[260] S.Typel, T.v.Chossy, H.H.Wolter, Phys.Rev. C67 (2003) 034002.

[261] We recall that, when the ϕ field has self-interaction terms, instead of f_σ one has to use $\frac{d\phi}{d\rho_S}$.

[262] P.G.Reinhard, Nucl.Phys. A649 (1999) 305c.

[263] T.Matsui, Nucl.Phys. 365 (1981) 365.

[264] T.Niksic, D.Vretenar, P.Ring, Phys.Rev. C66 (2002) 064302

[265] D.Vretenar, T.Niksic, P.Ring, Phys.Rev. C68 (2003) 024310

[266] J.C.Caillon, P.Gabinski and J.Labarsoque, Nucl.Phys. A696 (2001) 623.

[267] S. Typel and H.H. Wolter, private communication and *Collective Modes of Nuclear Matter in Relativistic Mean Field Theories* Preprint LMU-Physik Sektion, Munich 2002.

[268] M.Di Toro et al., Nucl.Phys. A722 (2003) 129c.

[269] B.Friedam et al., Nucl.Phys. A361 (1981) 502.

[270] B.ter Haar, R. Malfliet, Phys.Rev.Lett. 59 (1987) 1652.

[271] H.Muther, M.Prakash, T.L. Ainsworth, Phys.Lett B199 (1987) 469.

[272] I.Bombaci, U.Lombardo, Phys.Rev. C44 (1991) 1892.

[273] J.M.Lattimer et al., Phys.Rev.Lett. 66 (1991) 2701.

[274] K.Sumiyashi, H.Toki, *Astrophys.J.* 422 (1994) 700.

[275] M.Prakash, T.L.Ainsworth, J.M.Lattimer, *Phys.Rev.Lett.* 61 (1988) 2518.

[276] L.Engivik et al., *Phys.Rev.Lett.* 73 (1994) 2650.

[277] C.H.Lee, *Phys Rep.* 275 (1996) 255 and references there in.

[278] S.Kubis, M.Kutschera, *Acta Phys.Polon.* B30 (1999) 2747.

[279] M.Kutschera, J.Niemic, *Phys.Rev.* C62 (2000) 025802.

[280] V.S.Uma Mashevari et al., *Phys.Rev.* C57 (1998) 922.

[281] B.-A.Li, *Phys.Rev.* C67 (2003) 017601.

[282] T.Gross-Böltzing, C.Fuchs, A.Faessler, *Nucl.Phys.* A648 (1998) 105.

[283] C.M.Ko, Q.Li, R.Wang, *Phys.Rev.Lett.* 59 (1987) 1084

[284] S.Huber, J.Aichelin, *Nucl.Phys.* A573 (1994) 587.

[285] In our framework this is a characteristic relativistic effect that should be somewhat included in the corresponding non-relativistic models. The importance of this contribution was not realized so far in previous non-relativistic studies [281], where no isospin effects were included in the momentum dependent part of the effective forces. In this case the differences in the used symmetry energy parametrizations at supra-normal densities were very pronounced and therefore they resulted in very large effects with respect to earlier neutron emission and particle production.

[286] W.Reisdorf (*FOPI* collaboration), private communication of very preliminary data.

[287] T.Gaitanos, M.Di Toro, G.Ferini, M.Colonna, H.H.Wolter, *Isospin effects in intermediate energy heavy ion collisions*, arXiv:nucl-th/0402041, Proc. XLII International Winter Meeting On Nuclear Physics, Bormio (Italy) 2004.

[288] T.Gaitanos, M.Colonna, M.Di Toro, H.H.Wolter, *Phys.Lett.* B595 (2004) 209

[289] B.Hong et al. (*FOPI* Collaboration), *Phys.Rev* C66 (2002) 034901; and very preliminary data taken from B. Hong, Y.J. Kim, Y. Leifels, et al. (*FOPI* collaboration), *GSI-Report* 2002.

[290] C.Fuchs, A.Faessler, N.El-Shabshiri, *Phys.Rev.* C64 (2001) 024003.